Universidad Carlos III de Madrid
www.uc3m.es

TESIS DOCTORAL

Terahertz Time-Domain Spectroscopy to Characterize Graphene Nanostructures for New Optoelectronic Applications

Autor:

Ehsan Dadrasnia

Director:

Horacio Lamela Rivera

DEPARTAMENTO DE TECNOLOGÍA ELECTRÓNICA

Leganés, Julio 2015

Universidad
Carlos III de Madrid
www.uc3m.es

TESIS DOCTORAL (DOCTORAL THESIS)

Terahertz Time-Domain Spectroscopy to Characterize Graphene Nanostructures for New Optoelectronic Applications

Autor (Candidate):   Ehsan Dadrasnia

Director (Adviser):   Horacio Lamela Rivera

Tribunal (Review Committee):

Firma (Signature)

Presidente (Chair):
Prof. Dr. Ramón Gonzalo García

Vocal (Member):
Prof. Dr. Yahya Moubarak Meziani

Secretario (Secretary):
Prof. Dr. Guillermo Carpintero del Barrio

Título (Degree): *Doctorado en Ingeniería Eléctrica, Electrónica y Automática*

Calificación (Grade):

Leganés, 10 de Julio de 2015

I

Preface

This Ph.D. thesis is the result of research conducted during my time as a researcher Ph.D. student at the Universidad Carlos III de Madrid (UCIIIM) in the period from November 2010 to May 2015. The research was carried out under supervision of Professor Horacio Lamela Rivera, head of the Optoelectrónica y Tecnología Láser (GOTL). All results presented in the thesis were obtained at GOTL, Departamento de Tecnología Electrónica at UCIIIM.

This work is supported with several publications and presentations in the international journals and conferences. The full list is presented in Appendix E.

Ehsan Dadrasnia

Leganés, 10 de Julio de 2015

IV

This thesis is dedicated to my Family, especially…

to my Dad and Mom, for their endless love and support from school to higher education;

to my Sister, Dr. Arezoo Dadrasnia for encouragement and motivation to reach dreams;

to my Grandfathers, who passed away and never managed to see what they wanted me to achieve in life.

Acknowledgements

My heartfelt thanks go to a great number of people who have made this doctoral dissertation work an exceptionally memorable and rewarding experience.

I particularly want to thank my advisor, Professor Horacio Lamela Rivera for introducing me to the world of terahertz and graphene, and also for his encouragement and diligent review of my study and the publications that were inherent in the development of this dissertation throughout the past 5 years.

On the same note, I would like to thank Professors Jean-Louis Coutaz and Frederic Garet in the terahertz spectroscopy field who helped me during my secondment in the Institut de Microélectronique Electromagnétisme et Photonique and LAboratoire d'Hyperfréquences et de Caractérisation (IMEP-LAHC) in France. I have been lucky to work closely with them to carry out the THz-TDS measurements. Also, I acknowledge the contributions of Professor Seunghyun Baik and his PhD student, Dong-Mok Lee, for providing the carbon nanostructure samples from Sungkyunkwan University, South Korea.

I am very thankful the European Community for supporting this work under the project Microwave and Terahertz Photonics (238393 ITN-FP7), in order to develop compact and integrated tunable dual-mode diode lasers for terahertz spectroscopy in sensing, nanotechnology, and biomedical applications.

Though I cannot mention everyone by name, I want to express my thanks to all current and former members of GOTL (Daniel Gallego, MITEPHO and OILTEBIA teams) and administration office OTRI (Myrna Pacheco Bello) at UCIIIM for an always inspiring and very enjoyable environment. A special thanks to Sujitha Puthukodan for carrying out the sub-THz CW measurements and fruitful discussions in the CW results.

Last but not least, I would like to thank my families and friends who have been with me during the whole period of my study and I will forever remember your encouragement and support when I felt depressed and helpless far from my country.

Abstract

Terahertz electromagnetic waves from 0.1 to 30 THz, bounded between the infrared and microwave regions of the spectrum, has been intensively attracted to explore scientific and engineering phenomena for the materials. The graphene, a single layer of carbon atoms in a hexagonal lattice with zero energy band gap, and the carbon nanotube, sheet of graphene rolled into a cylinder, have been widely recognized as the perfect options for next generation ultrafast high performance optoelectronic applications to operate at the sub-THz and THz frequencies. Measuring the electrical conductivity and carriers' responses of such very thin conductance materials in devices could be rather difficult because of the contact issue. The terahertz time-domain spectroscopy (THz-TDS) is a noncontact tool to measure the optical and electrical parameters of the nanometrics semiconductors/semimetals.

This work analysis the THz-TDS signals from the references and samples measurement. It studies the THz frequency-dependent of the electrical and optical properties of the nanostructure graphene-like materials from the transmission and reflection of a home-made THz-TDS, mainly in the frequency range of 0.1-2 THz. The DC conductivity could not be directly determined, as the available THz power decreases sharply and falls below the noise level at lower frequencies. The electrical and optical frequency-dependent parameters are rather noisy due to thickness of thin films compared to the thick substrates and also the limited sensitivity of the THz-TDS set-up over 1.5 THz.

In this thesis results obtained, for the first time, on the characterization and spectroscopic analysis of the graphene-like samples deposited on the top of the quartz substrate, not only at the THz frequencies but also in the zero-frequency, so-achieved DC level, and far-infrared regime are presented. The conductivity values of such fragile materials are extracted from noncontact measurements at THz frequencies using elaborated conductivity Drude and non-Drude models which nicely fit the experimental data, giving information on the physics of electrical conductivity in these materials.

The carrier's transport, scattering and density near the Dirac point of graphene and carbon nanostructure are extracted by combining the measures THZ with the Drude models/non-Drude conductivity. This procedure is validated by the good agreement between the extracted DC conductivity from the THz measurements and the micrometer classical four-point probe in-line contact ones. The extrapolated characteristic length from THz measurement enables us to predict the cut-off frequency of such materials before applying to the optoelectronic devices. This thesis presents a commercially relevant application of noncontact THz-TDS techniques and analysis for the electrical characterization of nanoscale semiconductors and polymers with high mobility in the new generation of optoelectronic devices.

Resumen

Las ondas electromagnéticas en la región de terahercios de 0.1 a 30 THz, cuyo espectro está contenido entre las regiones del infrarrojo y las microondas, han sido intensamente utilizadas en la investigación científica e ingeniería de materiales. El grafeno, una única capa de átomos de carbono constituída por una red hexagonal con banda prohibida de energía cero y lo nanotubo de carbono como una lámina de grafeno enrollado formando un cilindro, han sido ampliamente reconocidos como la opción perfecta para la siguiente generación de aplicaciones optoelectrónicas ultrarrápidas y de alto rendimiento para operar en la región de terahercios. Medir la conductividad eléctrica y la respuesta de las portadoras de materiales tan delgados en dispositivos de medida es difícil debido a los problemas que supone el conectarlos físicamente. La espectroscopia de terahercios en el dominio del tiempo (THz-TDS) es una herramienta que no requiere contacto físico para medir parámetros ópticos y eléctricos de semiconductores y semimetales a escala nanométrica.

En este trabajo se analiza las señales THz-TDS de las referencias y de las mediciones de las muestras. Se estudia la dependencia en frecuencia en el rango de THz, principalmente en las frecuencias de 0,1 a 2 THz, de las propiedades eléctricas y ópticas de nanoestructuras de materiales como el grafeno desde la transmisión y reflexión de un sistema propio de THz-TDS. La conductividad en DC no pudo ser directamente determinada, ya que la potencia disponible en THz decae abruptamente por debajo del nivel de ruido para bajas frecuencias. Los parámetros electrónicos y ópticos dependientes de la frecuencia son ruidosos debido al poco espesor de las láminas en comparación con los gruesos sustratos y también a la limitada sensibilidad del sistema THz-TDS por encima de 1,5 THz.

En esta tesis se obtiene, por primera vez, la caracterización y el análisis espectroscópico de muestras como el grafeno depositado sobre un sustrato de cuarzo, no únicamente en el rango de THz sino también en frecuencia cero, esto es, en DC así como en la región del infrarrojo lejano. Los valores de conductividad de

tan frágiles muestras son extraídos a partir de medidas sin contacto a frecuencias de THz mediante elaborados modelos de Drude y no-Drude que se ajustan a los datos experimentales, proveyéndonos de información de la física y la conductividad eléctrica de dichos materiales.

El transporte, el scattering y la densidad de portadores cercana al punto de Dirac del grafeno y nanoestructuras de carbono son calculadas combinando las medidas en THZ con los modelos de Drude/no-Drude de la conductividad. Este procedimiento es validado mediante la concordancia de la conductividad DC extraída de las medidas de THz con las medidas clásicas de contacto en cuatro puntos a nivel micrométrico. Las características extrapoladas a partir de medidas de THz nos permiten predecir la frecuencia de corte de dichos materiales antes de ser utilizados en dispositivos optoelectrónicos. Esta tesis presenta una aplicación comercialmente relevante de técnicas y análisis THz-TDS sin contacto para la caracterización eléctrica de semiconductores a escala nanométrica y polímeros con alta movilidad en la nueva generación de dispositivos optoelectrónicos.

List of Acronyms

1D	One dimensional
2D	Two dimensional
3D	Three dimensional
AC	Alternating current
AFM	Atomic force microscopy
AgNW	Silver nanowire
Au	Gold
BS	Beam splitter
CNT	Carbon nanotube
CVD	Chemical vapor deposition
CW	Continuous wave
DC	Direct current
DFB	Distributed feedback
DL	Drude-Lorentz
EM	Electromagnetic
EDX	Energy dispersive X-Ray
FP	Fabry-Perot
fs	Femtosecond
FTIR	Fourier transforms infrared spectroscopy
GaAs	Gallium arsenide
GHz	Gigahertz
GOTL	Optoelectronics and Laser Technology Group
GRP	Pristine graphene
InP	Indium phosphide
ITO	Indium tin oxide
LED	Light-emitting diode

LPCVD	Low pressure chemical vapor deposition
MG	Mono-layer graphene
M-G	Maxwell-Garnet
MITEPHO	MIcrowave and TErahertz PHOtonics
mm	Millimeter
MOSFET	Metal oxide semiconductor field effect transistor
MWCNT	Multi walled carbon nanotube
NiCr	Nickel-chromium
nm	Nanometer
NRW	Nicholson-Ross-Weir
PCA	Photoconductive antennae
PMMA	Polymethyl methacrylate
ps	Picosecond
RF	Radio frequency
SEM	Scanning electron microscope
Si	Silicon
SiC	Silicon carbide
SNR	Signal-to-noise ratio
SWCNT	Single wall carbon nanotube
TD	Time delay
TDS	Time domain spectroscopy
THz	Terahertz
Ti	Titanium
VNA	Vector network analyzer
μm	Micrometer
μW	Microwave

Table of Contents

List of Tables

List of Figures

XXVI

XXVII

XXVIII

XXX

Chapter 1: Introduction

Electromagnetic (EM) radiation was described by Maxwell equation in 1865 [1] and afterwards H. Hertz demonstrated the EM field waves in 1888 [2]. Following that, the EM has been presented and characterized in the different electronic and photonic frequency ranges. Bringing the gap between the electronic and photonic technologies has been interested to generate and detect the EM spectrum in the far-infrared range. This gap is known as the terahertz (THz) located in boundary of "electronics" and "photonics" sources [3]. The THz region of the EM spectrum is typically defined as the range from 0.1 to 10 THz, where 1 THz = 10^{12} Hz and corresponds to 33.3 cm^{-1}, 4.14 meV, or a wavelength of 300μm.

The interaction of THz radiation with matter provides a vital low-energy probe of the electronic nature of a system near to its equilibrium state. The THz electromagnetic signals certainly push the border of material study in electronic science and technology in different aspects. The characterization of molecules in the THz band allows investigating the vibrational and rotational modes, validates theoretical molecular structures, carriers' responses, and understanding about electron ionization and collision processes at the picosecond time scale [4].

The THz measurement systems (100 GHz and 5 THz) are in board of resonator (35-144 GHz) and Fourier transformation infrared (5-80 THz) techniques which can be applied for both thin and bulk samples [5]. THz spectroscopy is an absorption method which can enable the precise, simple and exact complex permittivity compared to the far-infrared and microwave spectroscopy. The transmitted or reflected field of the THz pulse from the THz emitter gives details measurement about the field amplitude and phase. They can lead us to obtain the power absorption coefficient and refractive index simultaneously using the coherence radiation with duration pulses of 1-2 ps.

Many materials that are opaque to visible and infrared light are transparent to THz radiation [3, 4]. The characterization of molecules in the THz gap lets studying the vibrational and rotational modes of semiconductor and semimetal samples. Using nondestructive testing and characterization of THz waves on semiconductors gives carriers' lifetime and doping concentrations. The resulting of this application allows investigating on the electron ionization and collision processes at the picosecond time scale.

The THz gap potential has opened the new nondestructive testing and applications in science and industrial fields over the years in different markets: food [6], biomedical and imaging [7], polymers and material characterizations [8], energy, security, safety, defense, biomedical, plasma fusion diagnostics, and electron bunch diagnostics [3, 4].

There are many techniques to generate and radiate the THz EM waves based on the applications and features such as power, tunability, limitation frequency range, and cost of systems. The different generations of THz waves are studied in Appendix A. Among modern THz techniques, terahertz time-domain spectroscopy (THz-TDS) is known for years to be a precise tool for noncontact and nondestructive characterization of samples like semiconductor wafers [4, 9], paint films [10], art and historical pieces [11], biological tissues [12], etc.

The main advantages of coherency, large dynamic, and simultaneously measuring of magnitude and phase of the THz-TDS in a broadband frequency range allow studying propagation and extinction parameters of dielectrics, metals, semiconductors samples precisely. The determination of the refractive index can be obtained with a precision better than 0.1% and absorption measured down to 0.1 cm^{-1} of thick samples using both transmission and reflection modes of the THz-TDS [13, 14]. As the THz-TDS delivers the magnitude and phase of the THz waves transmitted/reflected from samples, the complex permittivity of materials can be obtained from the THz-TDS data. In the case of conductive materials, the THz conductivity can be calculated directly from the Drude complex permittivity.

In optoelectronics and electronic devices, the new materials especially those with high mobility are intensively under investigation to develop transistors with sub-nm channels for operation in the sub-THz and THz frequencies. Graphene-Like materials have been

rapidly growing to be applied in the such optoelectronic devices since they are known as semimetal with zero energy gap which has a fixed nearest-neighbor hopping potential ~2.5-3.1 eV with momentum-independent electronic group velocity of approximately 1/300 of the speed of light in vacuum, resulting particularly high mobility of 10000–15000 cm^2/Vs and micrometer-scale ballistic transport at room temperature [15]. In addition, reasonably priced large-scale production of graphene type materials is now becoming a reality.

It was believed that the synthesis of a single sheet graphene was difficult. But in 2004, Konstantin Novoselov and Andre Geim showed it is possible to isolate monolayer graphene with depositing it on top of a substrate and that the electrical measurements can be performed [15, 16]. High speed electronic devices of carbon based electrodes have already found broad applications such as field-effect transistors [17] and super-capacitors [18]. CNTs and graphene thin films are usually stacked on substrate for different optoelectronic configurations [19, 20]. The high mobility of electrons [21] and optical conductivity [22] in graphene have been experimentally investigated to study the ultrafast intra/inter-band transitions of two-dimensional Dirac fermions and ballistic transport at room temperature [23, 24]. Thus, a profoundly study of the graphene electrical and optical characterization is necessary in order to be applied them in novel optic and electronic applications.

Four-point probe [25] or van der Pauw [26] method, and Hall effect measurements [27-29] have applied to measure the characteristics of the graphene-like materials using direct tools. The Four-point probe and the van der Pauw methods measure only the conductivity or resistivity, while the Hall Effect measurement method measures the carrier density and the carrier mobility. The employ of the four-point probe needs earlier calculation and specific assumption of the sample size, shape and thickness. Also, the four-point probe measures only direct current (DC) value.

The contacting issue may damage such fragile device and thus may prevent a multiple measurement procedure and/or a subsequent use of the tested devices. The importance electrical and optical characteristics (complex functions of the conductivity and refractive index) of graphene devices like other semiconductors have frequency-dependent values. Therefore, a noncontact and nondestructive technique is needed in practice to measure all

aforementioned characterization as functions of frequency. The noncontact method also should give details of physics of samples (e.g., carrier density and mobility) without any energy excitation among the valance and conduction bands.

Graphene has a Fermi level of ~0.2-0.4 eV and high carrier mobility > 2×10^5 cm^2 V^{-1} s^{-1} at room temperature. It is important to note that the electrons in graphene has the long mean free and act as massless two-dimensional particles which yields to a frequency-independent absorption (~2.3% in an ideal case of monolayer graphene sheet) below 3 eV for a normal wave incident. To fully identify the carriers transport, scattering and density at and near the Dirac point, related to the quantum capacitance, we need to apply a low phonon energy wave. THz is characterized by low photon energies sub-millimeter (sub-mm) wavelengths, i.e., 33.3 cm^{-1} or 4.2 meV at 300 μm for 1 THz which is less than corresponding thermal energies (48 K at 1 THz) at room temperature. The electronic transport dynamics of graphene charge carriers are at femtosecond (10^{-15} s) to picosecond time (10^{-12} s corresponding 1 THz).

Microwave [30, 31] and far-infrared [32, 33] noncontact techniques have been used to find alternating current (AC) characterization of graphene-like samples. However, they have limitations because of the complicated numerical transformation process and also low signal-to-noise ratio (SNR). The complex refractive index and electrical conductivity of nanometrics carbon structure and graphene films have been intensively studied by transmission mode of pulsed THz-TDS and continuous wave (CW) vector network analyzer (VNA) [34-36]. These have been done at the low and high THz frequencies instead of the conventional electrochemical conductance measurements. Appendix A compares the advantages and disadvantages of the THz CW and the THz pulsed techniques.

The plasma frequency and damping rate appear between microwave and IR frequencies, commonly named the THz gap [37, 38] with a broad THz absorption peak [39]. There is difficultly due to measuring the dispersion and absorption of such films for high THz frequencies because of excessive attenuation in film coated on top of a bar substrate [40]. The main challenge in such techniques is measuring a separate reference substrate to extract the film parameters precisely. Another significant challenge is at the lowest frequencies because of decreasing the signal to noise ratio due to a drop in THz power. The

DC conductivity cannot be directly determined, as the available THz power decreases sharply and falls below the noise level at lower frequencies (typically below 200 GHz).

The research work presented in this thesis is dedicated to the quantifications and spectra characterizations of the optical and electrical properties of graphene and carbon nanotube (CNT) samples. This thesis has involved the study of THz-TDS based characterization scheme that both quantify and spectrally resolve the optical and electrical parameters (refractive index, absorption and electrical conductivity) over the broadband range frequency from DC (~zero frequency) 0 up to 2 THz. The experimental results of all graphene and CNT samples taken under this study by the transmission and reflection measurement are fitted by alternative Drude and non-Drude (i.e., Drude-Lorentz and Drude-Smith) theories at the low and high frequencies.

As there is difficulty in deposition and integration of such fragile samples to the optoelectronic devices, which may prevent a multiple measurement procedure and/or subsequent use of the tested devices. In this thesis, the electrical conductivity peaks of CNT and graphene samples are also demonstrated by validating the experimental results and the theory parameters not only at THz frequencies but also at far-Infrared regimes (up to 20 THz). Importantly, this thesis directly studies the ultrafast dynamic responses (i.e., carrier density and high mobility) for the graphene-like samples using noncontact THz-TDS without requirement for post process patterning.

Following introduced the research scope and the background as well as the explained objectives in **Chapter 1**, the conceptual study of the noncontact THz-TDS set-up and measurements schemes are presented in **Chapter 2**. This reviews the fundamental of THz-TDS technology in spectroscopy applications. The THz spectroscopy concepts, mainly TDS in comparison with other spectroscopy techniques, in detail is described. This chapter introduces the different THz generation and detection techniques currently employed with importance on the transmission and reflection experimental set-ups designed for this thesis. Detailed information of generation and detection of the THz radiation and the data analysis are presented in this chapter. The delay line scanning in the receiver antenna is explained to measure the THz signals of samples in time domain. The Fourier method is applied to transfer obtained signals from time domain into frequency domain.

The principle of electric field interaction, mainly at THz frequencies, with the nanometrics semiconductors/semimetals is presented in **Chapter 3**. The most important parameters responsible for the spectral behavior of samples, such as raising the plasma frequency and scattering rate at THz regime, along with a review of the most commonly applied theoretical Drude model using Maxwell equation are studied. The dependence of complex permittivity functions to the complex refractive index is aimed studying the electrical conductivity behavior and optical parameters in this chapter. The concepts behind the theoretical background and physics of graphene and carbon nanostructure samples are investigated. This is followed by a description of the absorption and the electrical conductivity engineering bands of graphene and carbon nanotubes samples. This chapter contains a descriptive study on the intraband transition and Fermi level photon energy at THz frequencies. The studies of physical and electronic structure of such samples in the THz range enable not only obtaining the THz conductivity, but also extracting the so-achieved DC conductivity at zero-frequency and also finding the peaks of electrical conductivities at far-infrared regime.

Chapter 4 demonstrates the transmission and reflection THz-TDS set-ups and also the measured THz temporal signals. The measurements steps of references and samples are followed by the experimental results in both time and frequency domains, which here are divided into three different sections: i) transmission signal measurements of SWCNT and MWCNT samples, ii) transmission signal measurements of nanometrics MWCNT and graphene samples, and iii) finally, not only THz transmission signal measurements but also the reflection ones of nanometrics MWCNT, graphene and hybrid silver nano-wire graphene samples deposited over the transparent quartz substrates with thicknesses of several hundred and a few thousand micrometers. The principle of getting the unwrapped phase from the measurement signal is shown in this chapter as well. This unwrapped phase needs to be modified at low frequencies and being start from zero frequencies as there is not enough SNR and power at frequencies below 0.2 THz.

Chapter 5 presents the results and discussion of the achieved experimental studies for different presented samples in Chapter 4. Further to the obtained optical properties of the reference substrates in Chapter 2, the optical and electrical parameters of all CNT and

graphene samples are characterized in Chapter 5. The electrical conductivity of films is extracted from the THz-TDS data using the combined Drude and non-Drude models. The frequency-dependent THz conductivity of the materials in Appendix D with an additional discussion on physics understanding of the samples (electron and phonon parameters) is explained.

Chapter 6 is a further motivation of Chapter 5 results. The whole spectrum analysis obtained from the noncontact THz measurements gives reliable information to find not only the THz conductivity, but also to extrapolate the DC conductivity and the far-infrared conductivity peaks. The agreement between measured THz-TDS optical and electrical values and fitted models are good, thus enforcing the feasibility of such a noncontact and nondestructive technique. To validate our results, the DC electrical conductivity of the films is measured with a classical 4-probe technique. In addition, Chapter 6 exposes the experimental and theoretical results to find the THz sheet conductivity and the dynamic carrier responses of the samples taken within this research for the future optoelectronic applications in nano size.

Chapter 7 finally presents the conclusion of this wok and the potential future works by summarizing significant prospective of this study and ongoing research directions Furtherer more, the complementary studies of chapter in details are demonstrated in Appendices (A-E).

The scope of this work was carried out within the European MIcrowave and TErahertz PHOtonic (MITEPHO) project [cf. Appendix E]. The results obtained and presented in this thesis have been published in the international peer-reviewed journal citation reports (JCRs) [41-47], the newsroom and feature articles [48, 49], and the invited international conference presentations [35, 36, 50-53].

Chapter 2:   Broadband Terahertz Time Domain Spectroscopy

2.1 Introduction

In this chapter, the broadband THz radiation techniques will be reviewed. The basic concepts surrounding the generation of broadband THZ signals from the ultrashort pulsed optical excitation through the photoconductive antenna (PCA) technique will be studied. It will be shown how the properties of such ultrashort trained pulses generated from a femtosecond laser can accelerate the electron and holes effect on a micrometer gap, and consequently the THz signals are emitted and detected by the PCAs. The generated THz pulse has a width of 1-2 ps. To fully understand the process of fs optical pulses to THz signals, it is essential to identify the sampling steps of waves by adding an optical delay stage.

Considering this, the sections of this chapter will deal with the generation of broadband THz signals for carrying out noncontact and nondestructive measurements at frequency range of 0.1-2 THz. Other key components of the used THz time-domain spectroscopy (THz-TDS) set-up will be explained in order to generate and detect the THz signals using the PCAs and the scanning technique. The objective of this review not only serves to introduce the mechanisms required to build up a classical THz-TDS, but will also be applied to transfer the THz time-domain signals into the frequency domain for further signal processing using a delay stage and Fourier transform method.

It will be demonstrated that the optical and electrical properties of sample can be extracted from the differential signal method. This will be applied later for the complex system for the references and the samples taken in this study in Chapters 4-6. As an example, the thick

reference quartz substrate optical properties, mainly the complex refractive index, will be shown. A complementary analysis of the thickness influence of material and Fabry-Perot (FP) effects in the differential transmission mode of both thin (e.g., CNT) and thick (e.g., quartz) samples will be provided in Appendix B.

2.2 THz Broadband Radiation

Present THz systems are restricted by the lack of accessibility to the high power and the low cost frequency radiation. THz can be generated with different techniques [54] that have their own advantages and disadvantages for spectroscopic studies. These techniques are synchrotron radiation from a storage ring [55], free-electron lasers [56], quantum cascade lasers [57], quantum dot lasers [58], dual-mode distributed feedback (DFB) lasers [59], ultrafast mode-locked optical lasers by using either non-linear optical materials or photoconductive semiconductors switches [60], and Fourier transforms infrared spectroscopy (FTIR) [61] which has really high bandwidth. In the electromagnetic spectrum, FTIR spectroscopy enables the characterization the materials from THz frequencies upto the infrared gap [62].

The main disadvantage of this technique is spectral resolution limitation and also the loss of phase information. In addition, FTIR measures the power absorption coefficient of materials directly. The main restriction of FTIR is to derive a complicated numerical transformation process of the Kramers-Kronig relationship in order to obtain the refractive index [63]. High resolution measurements of THz-TDS can be obtained directly using coherent and tunable sources such as the backward wave oscillator or optically pumped THz lasers. However, the narrow range of these sources makes it difficult to obtain measurements at various frequency bands. This is especially problematic since many interesting properties can only be ascertained from the general behavior of the complex permittivity, conductivity, or refractive index over a wide spectral range. The next chapter will study how the Drude and non-Drude models can help us to extend the spectra in this limited frequency range.

Optical rectification (since 1970 [64]) and photoconductive switch (since 1975[65]) are two useful techniques to generate short THz pulses. The optical rectification is based on the inverse method of the conventional semiconductors (GaAs [66] and ZnTe [67]) properties of electro-optic crystals where the energy of the picosecond THz pulse directly comes from the laser pulse excitation. This technique provides wider bandwidth that might goes to 50 THz [68]. The main disadvantage of such system is low generated power of THz pulses.

The photoconductive technique is based on the Auston switch [65, 69] that generates and detects sub-ps THz pulses generated (or detected) via illumination from a femtosecond (fs) laser with an optical pulse duration of the order of fs. Fig. 2.1 shows the Auston switch, comprising of a semiconductor substrate and electric contacts with a gap of the order of micrometers. The train fs laser pulses illuminate this gap and the photogenerated carriers are speeded up by the bias field which makes current. The shorter dipole of photoconductive antenna (PCA) gives a shorter THz pulse width and thus broader bandwidth [70]. For example, a 50µm dipole PCA provides the broadest spectral band from 0.1 to 2 THz. Typical photoconductors is made of the low temperature grown GaAs (LTG-GaAs) and Indium phosphide (InP).
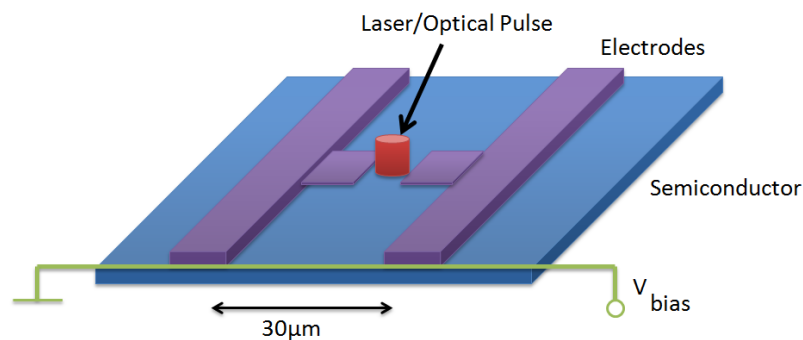
Figure 2.1: The general structure of Auston switch used in the PCA.

The PCA mechanism details will be explained in coming sections. In 1988, the PCA with a 10µm dipole was developed to be applied in a free-space THz spectrometer [71] and later, in 1989, the water vapor was tested as sample which analyzed via Fourier transform in the frequency range of 0.2 THz to 1.45 THz [72]. This system was called terahertz time-domain spectroscopy (THz-TDS) [73]. Since then THz-TDS has been applied to characterize different solid and semiconductor materials [8]. The THz-TDS is an absorption method

which can enable the precise, simple and exact complex permittivity compared to the far-infrared and microwave spectroscopy. The complex transmitted or reflected function of the THz pulse detected in the THz emitter gives details measurement about the electric field amplitude and phase. They can lead us to obtain the power absorption coefficient and refractive index simultaneously using the coherence radiation with duration pulse of 1-2 ps [74].

2.2.1 Ultrafast Femtosecond Laser

Numerous chemistry and physics studies like relaxation, vibrations, and rotations occur on a fast time spectroscopy than a continuous wave (CW) form. Hence it is essential to somehow gate the detection by increasing the SNR to quantify only a short time of the physical processes. Table 2.1 shows the available techniques to generate the short pulses laser with different lengths and repetition rates.

Table 2.1: Short laser pulses techniques with different length and repetition rates.

Technique	Pulse length	Repetition rate
Germanium laser with a beam chopper	µs	several kHz
Active Q switching	sub-µs	several MHz
Passive Q switching	ns-ps	GHz to sub-THz
Mode-locking (based on in-phase interference)	Ultra-short pulses (need superposition of enormous frequencies)	

The mode-locking laser can provide the ultra-short pulses (=2×cavity length/speed of light× number of modes). However, this needs enough number of axial modes and a constant phase relation. In this line, a multi-mode laser that operates as self mode-locking without needs to active switch technique can be a suitable broadband tool for generating ultra-short pulse on the order of fs.

The Ti: Sapphire laser is usually gained in the high bandwidth in the wavelength range of 700-1200nm (even more) which makes it suitable of mode-locking technique in order to generate fs pulses. The repetition rate of Ti: Sapphire laser is between MHz-GHz which

relies on the cavity length (several mm to several 100 cm) with laser pulse energy of the order of nJ. The high peak power of such a system permits studying the non-linear effect and the time-resolved experimental in different materials. The short fs pulse light can make a transient conductivity in the different PCA semiconductor based in the sub-THz and THz frequencies with pulse duration of a few ps.

In this thesis, in order to generate the frequency bandwidth of 0.1-2 THz, a home-made TH-TDS set-up has been built by a commercial fs Ti: Sapphire laser (Spectra-physics, Tsunami model) to perform the experiments. Fig. 2.2 shows a simple analysis of peak and average power of optical pulses with repetition of $f = 1/T$. The average power in a laser beam is the power delivered over a long period of time. It yields to calculate the power or energy of optical pulses. Assume the energy, E, contained in every pulse is constant.

The power is just the change time rate of the energy flow (energy per unit time). The average power is the rate of energy flow over one full period, $P_{ave} = \dfrac{E}{T} = Ef$. The peak power is rate of energy flow in every pulse, $P_{peak} = \dfrac{E}{\Delta t}$. The output of the laser system used in this study has a transform pulse width of <100 fs with a peak power of >500 kW (average >4.0 W) at a wavelength of 800 nm, with a pulse energy of ~50 nJ and a repetition rate of 80 MHz. The diameter of the pulse given by the manufacturer is ≈2mm.
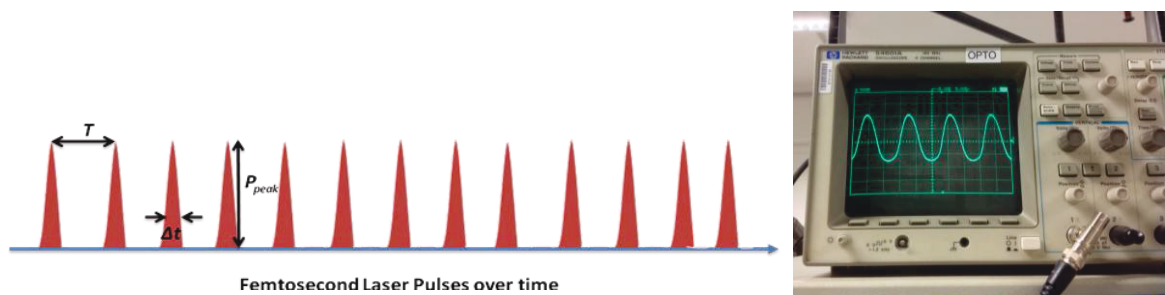
Figure 2.2: [Left] The schematic of the ultrafast train pulse. [Right] The experimental fs train pulses observed in the oscilloscope.

2.2.2 Photoconductive THz Antennae: Generation and Detection

There are different PCAs to generate and detect the THz signals due to variety in design, material, power and pulse duration. In this thesis, the universal broadband PCA fabricated by low temperature grown (LTG) GaAs has been used [75]. Fig. 2.3 shows the main principle of PCAs based on the photocarrier transport process [76]. The antenna is consisting of metallic coplanar transmission lines imprinted on a photoconductive substrate. In general, by illumination of the fs laser pulse, a sub-picosecond transient THz frequency can be generated from an antenna with the carrier lifetime on the order of the nanosecond [77]. In the generation of THz pulses the ultrafast laser pulse generates an electron-hole pairs which decreases the conductivity of antenna gap. The recombination rate of electrons and holes is determined by the recombination time, so-called the carrier lifetime.
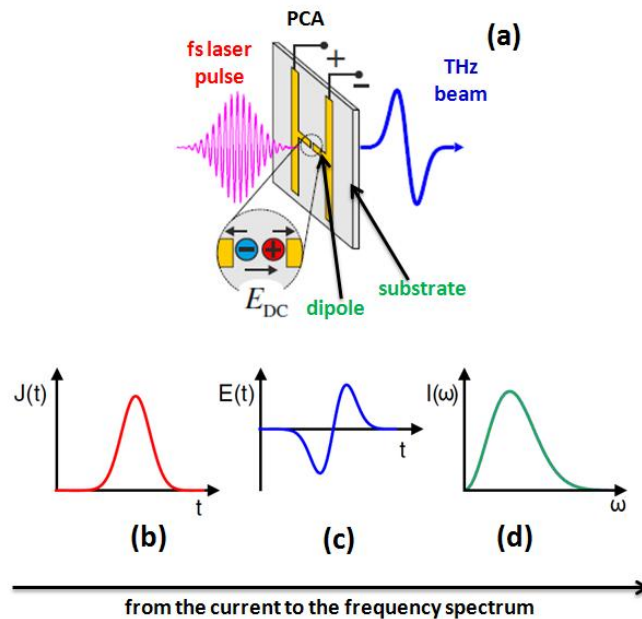
Figure 2.3: (a) The THz generation in the PCA using photocarrier transport process. (b) The time-dependent of generated photocurrent. (c) The THz field emission. (d) The broadband spectrum [76].

The energy excitation photon wavelength of laser has to be selected such as the energy of the photon is larger than the energy band-gap of the semiconductor applied with the charge carrier mobility of $\sim$200 cm^{2}V^{-1} s^{-1}. The connected bias voltage to the circuit accelerates the electrons and the holes, resulting in a short-time current. The photocurrent

carrier density in a PCA with the photocarrier density $n(t)$ and the photocarrier velocity $v(t)$ is defined by convolution between the pumped pulses power by laser $P(t)$ and the impulse response of PCA ($qn(t)v(t)$):

$$J(t) = P(t)*(qn(t)v(t)), \tag{2.1}$$

where q is the electron charge. The generated THz electric field at the far field is proportional to the photocurrent and linearly polarized along the direction of the DC electric field $E \propto \dfrac{dJ(t)}{dt}$ (several kV/cm), and hence after converting it into the frequency domain through a Fourier transform, the broadband spectrum $I(\omega)$ is appeared [78].

The THz pulse polarization is based on the Maxwell principle which is perpendicular to the bias electrodes of the micro-gap PCA. From the far-field point-of-view, the THz pulse propagates as a Gaussian beam that the distribution of beam can be found in the center at higher THz frequencies [79].

The THz radiation energy is linked more into the substrate rather the air [70]. Because of which a hyper hemispherical silicon lens is mounted on the substrate to accumulate the radiation. The eventual THz energy emitted from the antenna is 10~20% of the total radiation energy as there is reflection losses between the substrate-silicon lens and silicon lens-air interfaces [75, 80]. The detection process at the PCA receiver is practically vice versa of the generation process at the emitter. Fig. 2.4 shows the top and side views of PCAs connected to the silicon lenses. The THz pulse travels from the emitter to the receiver.

At the receiver PCA, the μm-gap is continuously excited by a sequence of fs optical probe pulses. In this case, the electrodes are attached to a lock-in amplifier (LIA) to measure the current. In the nonexistence of the emitted THz pulse incident on the receiver, the free carriers induced by fs pulses recombine without creating a current flow between coplanar transmission lines. However, the incoming radiated THz electric field accelerates the photocarrier which is proportional to the incident THz radiation and detected by the LIA. Hence the whole THz pulse can be mapped out by adding an optical delay line on the pump beam path.
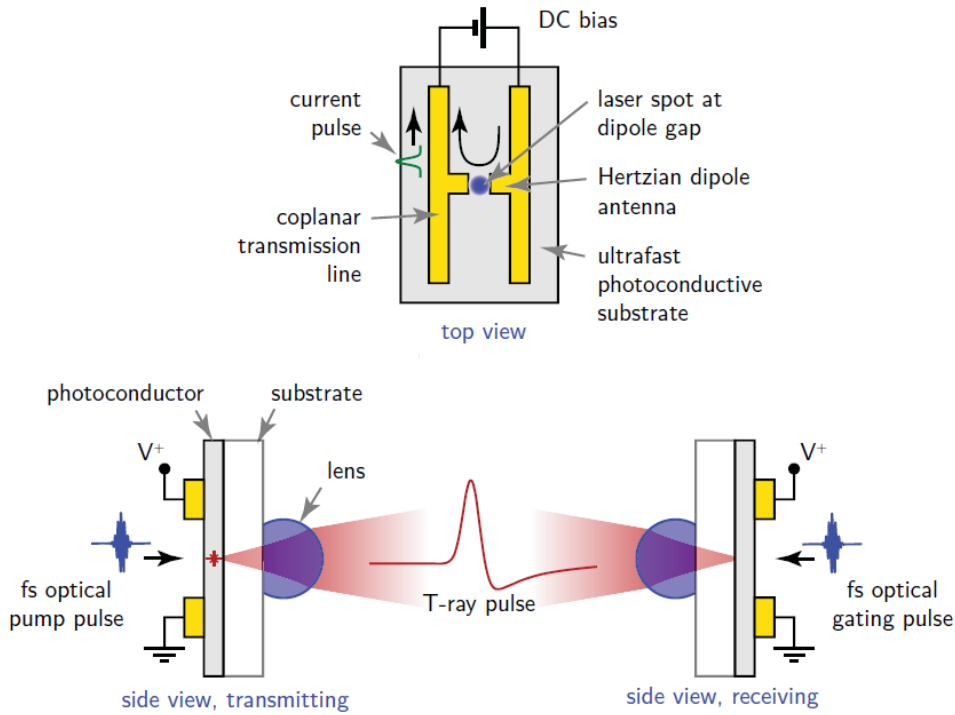
Figure 2.4: The top and side views of emitter and receiver PCAs [78].

In a general term, the average photocurrent at receiver for a relative time delay, τ, can be stated by the convolution of the transient conductance, σ(t) and the incident THz beam, E(t) in the photoconductor as follows [81, 82]:

$$J_r \propto \int E(t)\sigma(t-\tau)dt, \qquad (2.2)$$

2.2.3 Chopper and Lock-in Amplifier

Using a beam splitter (BS), the initial beam laser is divided into two beam-paths (pump and probe) with same phase and half of original intensity of initial fs laser. The pump and probe beams go to the emitter and detector THz antenna, respectively. A chopper (CH) is put in the pump beam-path to generate a better reference signal. The CH blocks the signal as close to the end of the train pulse as possible and takes off the noise that occurs after the chopped signal [cf. Fig. 2.5]. The narrower bandwidth of the light pulse gives the higher SNR which decreases the Johnson-Nyquist noise effect as well.
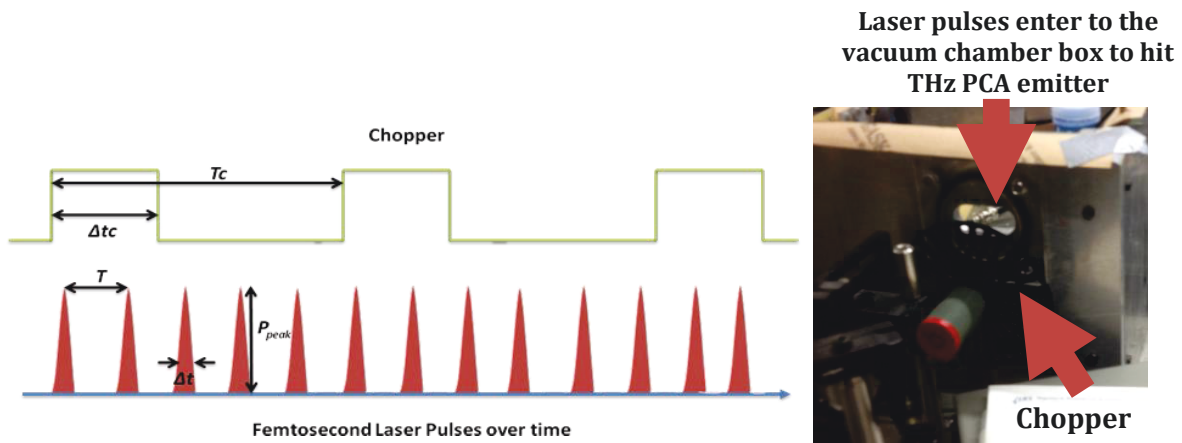
Figure 2.5: [Left] The ultrafast train pulse and the generic timing for the Chopper. [Right] The chopper in THz-TDS system in the pump beam path located before the PCA emitter in the vacuum chamber box.

With increasing the CH frequency, the accuracy of the signal measurements increase as there are more samples for each time interval. In other words, this enables for shorter data acquisition time that the time-constant for the LIA can be decreased and maintained approximately the same SNR. A LIA is applied to measure and extract signals hidden in a noisy environment. LIA is also to supply high-resolution measurements of pure signals as it can be included signals over a large order of magnitude and frequencies. The CH operates in combination with a LIA to make a reference signal. They are connected to an acquisition system to measure signals. The time-constant uses a mean value for each time-interval of the measurements to filter out some of the noise. The SNR can be improved by increasing and the sensitivity the time-constant (ms ~ a few seconds) [83]. Fig. 2.6 shows the front panel of the LIA in the THz-TDS experimental set-up.
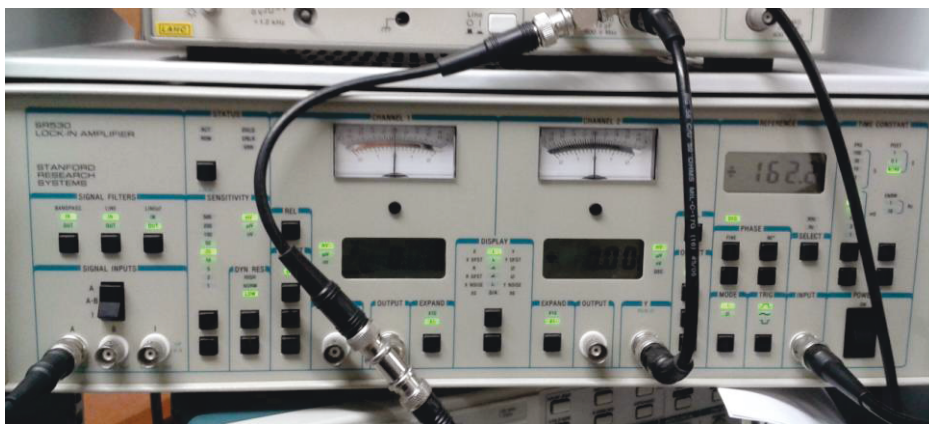
Figure 2.6: The lock-in amplifier front panel display.

2.2.4 Lens and Parabolic Mirrors

As explained in the above section about the PCA technology, the hyper-hemispherical Si lenses [cf. Fig. 2.7] are mounted on the back of the emitter for coupling the energy transient pulse into free space, and also mounted to the back of the detector to couple the incoming THz beam into the receiver. To focus the beam energy on a spot, the outgoing THz at emitter needs to be collimated at the trainmaster antenna and focused onto the sample under study, and then the THz transmitted signal through sample should be re-collimated upon the receiver antenna.
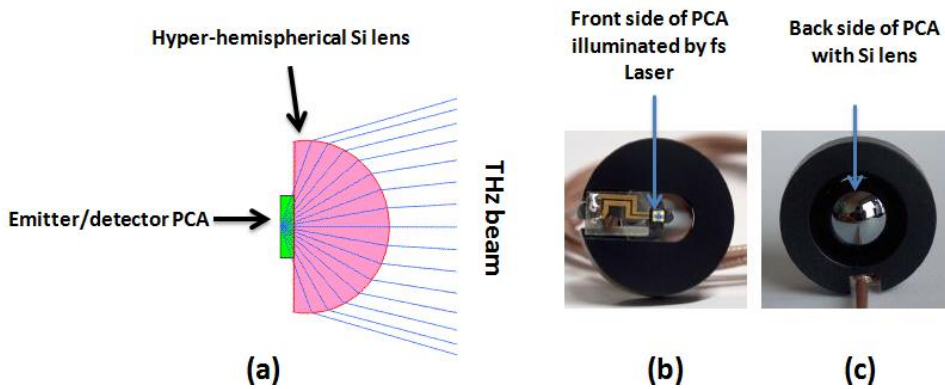
Figure 2.7: (a) The side view of the hyper-hemispherical Si lens function at PCA emitter or detector. (b) The front side of PCA illuminated by fs laser pulse. (c) The back side of PCA with Si lens.

Off-axis parabolic mirrors (P) with focal length f are used to guide the THz pulse from the emitter, through a sample onto the detector. The mirrors are arranged as follows: ***f-2f-2f-2f-f***, where $f = \dfrac{D^2}{16d}$ with the depth of parabolic mirror of d, and diameter of the parabolic mirror of D. Fig. 2.8 shows that the intense of THz electric field is higher at middle of a confocal system (green area). As it is a Gaussian shape, the diameters of THz beam beings narrow at higher frequencies. For example, at frequency of 3 THz, the diameter of beam is between 0.5-1 mm. Thus the focal point is the best place in where the sample under test can be located, which the THz emission focuses through the sample before being collimated again in the detector.
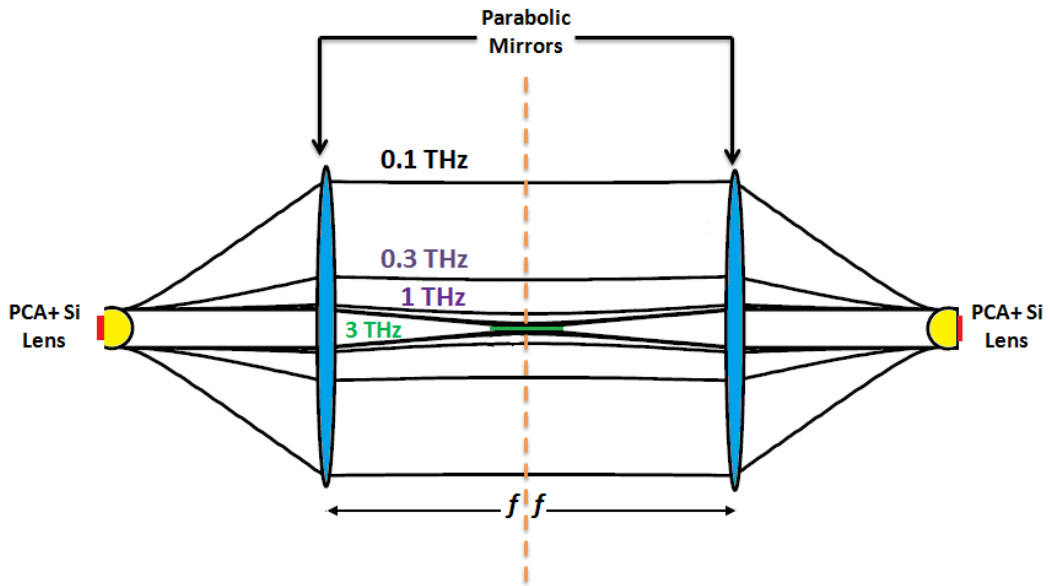
Figure 2.8: The beam focus point for various THz frequencies between two mirrors.

Fig. 2.9 shows the final THz pulse domain of air reference detected at the receiver with three important specifications: amplitude, width (1~2 ps) and center of wave. The THz beam diameter of THz emission is reported to be in range of 0.5mm~2mm [37, 84].
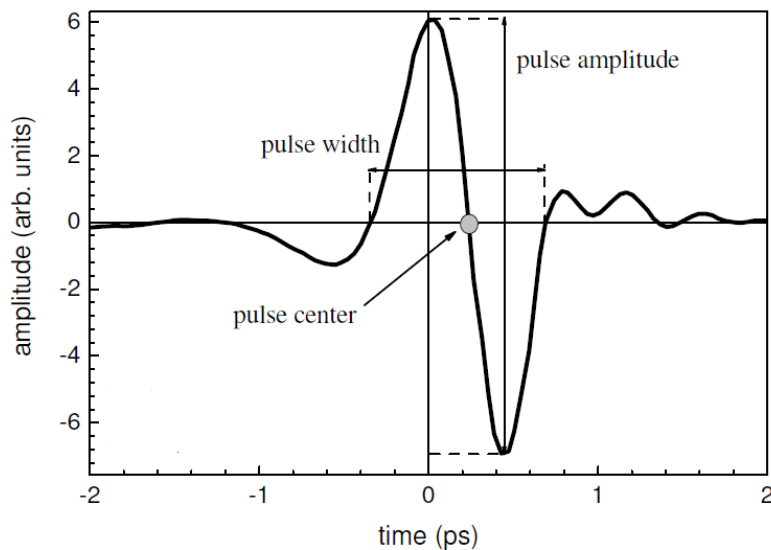
Figure 2.9: The THz pulse shape in time-domain [85].

2.2.5 THz-TDS Experimental Set-up

All aforementioned electronic, electrical and optical components yield to build the home-made THz-TDS set-up to measure the THz signal of the samples taken in this thesis. Fig. 2.10 shows a general configuration of the utilized THz-TDS in this study. In order to eliminate and remove the water vapor effects on the THz beam, the THz system needs to mount in an airtight or dry nitrogen atmosphere. The details of used sensor to control the water line absorption will be discussed in Chapter 4. In Fig. 2.10, the red and blue lines are the optical path and the THz wave, respectively.

The THz temporal signals are collected using an acquisition software and then are transferred into the Matlab and Origin platform for further process. For each measurement, the time windows of 30-75 ps are considered which take 1-3 minutes of scanning.
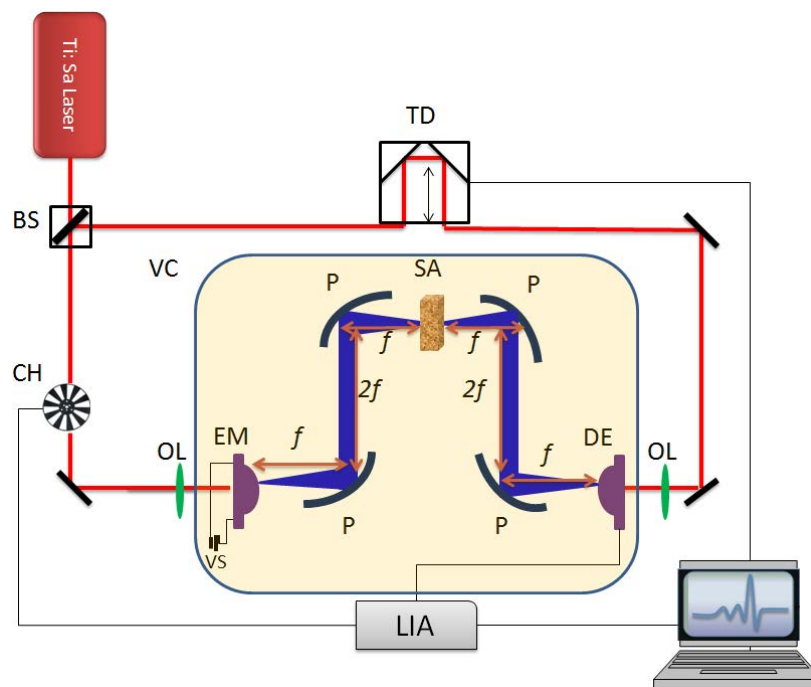
Figure 2.10: The THz-TDS schematic used in this study (BS: beam splitter; TD: mechanical time delay; CH: chopper; N2A: dry nitrogen atmosphere; P: parabolic mirror; SA: sample; OL: optical lens; EM: emitter; DE: detector; SL: silicon lens; VS: voltage supply; LIA: lock-in amplifier).

2.3 THz Scanning and Sampling

2.3.1 Delay Stage

To delay the excitation THz pulse with respect to the received pulse at the PCA detector, a delay distance of 0.3 mm corresponds to a time of 1 fs can be considered. The output signal of the detector is proportional to the magnitude and the sign of the THz pulse in every certain moment of time. Thus the variation of the time delay (TD) between pump and probe optical pulses can trace the whole time profile of the THz pulse. The TD mechanically can controlled by acquisition delay step of several hundred nanometers [75]. Fig. 2.11 shows that how this delay is translated into the THz pulse shape from the exciting fs laser pulses over the time. The sampling principle is by shifting the delay stages in discrete spatial steps Δx corresponding to the discrete temporal steps (c is the speed of light in vacuum):

$$\Delta t = \frac{2\Delta x}{c} \tag{2.3}$$
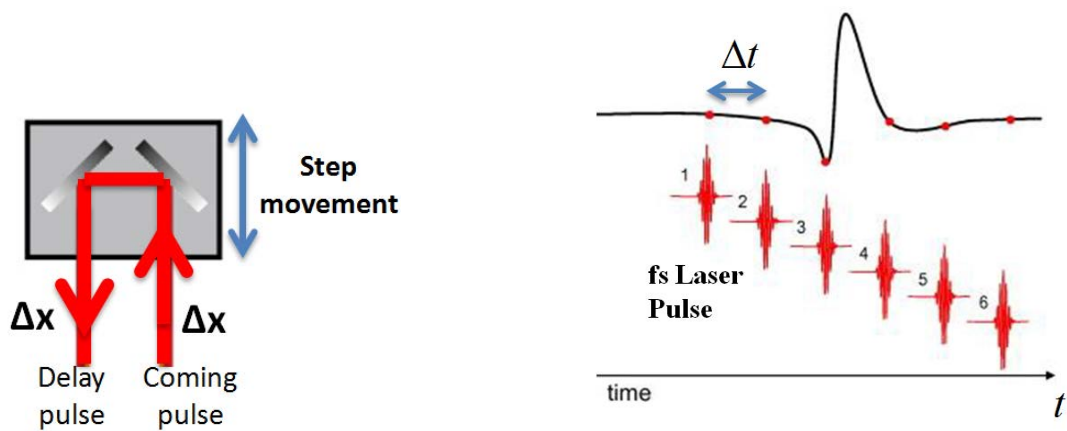
Figure 2.11: [Left] The optical delay stage function. [Right] The fs laser pulses and time vector in THz-TDS sampling to get temporal waves.

2.3.2 Time Process at Detector

Fig. 2.12 shows the photoconductive detection sampling THz waveform process, where a THz beam is propagating from the emitter and it is not yet arrived to the receiver [60]. The electric field measurement is determined by the relative arrival times of the optical and

THz pulse. Fig. 2.12 (a) demonstrates the optical pulse that arrives before the THz pulse in detector. In this state, as the bias voltage is zero, there is no current through the PCA receiver ($t_a < 0$). Figs. 2.12 (b-c) come later with the delaying arrival of the optical pulse to coincide the THz pulse. The time axis is determined by the delay between the laser pulse that generates the THz pulse and the pulse that gates the THz antenna. In $t_b = 0^-$ and $t_c = 0^+$, the THz electric field $E_{THz} > 0$ which is proportional the measured time current flow average. The time resolved measurement of the THz pulse electric field is thus made by changing the delay between the optical gating pulse and generating pulse. The final measured current maps out the THz field in time as shown in Fig. 2.12 (d).

Therefore, at each position one sample point of the delay stage of signal $E(t)$ is recorded in time-domain with time window of $t = n\Delta t$ ($n = 1, 2, 3..., N$). To obtain the frequency spectrum of this emitted electric field, the obtained signal in the time-domain is transformed into the frequency domain $E(\omega = 2\pi f)$ with amplitude $A(\omega)$ and phase $\varphi(\omega)$ using the Fourier transform method:

$$E(\omega) = \frac{1}{2\pi} \int_{-\infty}^{+\infty} E(t) e^{-i\omega t} dt = A(\omega) e^{i\varphi(\omega)} . \qquad (2.4)$$

To increase the frequency resolution in obtained spectrum, the zero padding can be applied. The obtained spectrum from the Fourier transform technique gives the discrete values of the difference frequency as:

$$\Delta f = \frac{1}{N\Delta t}. \qquad (2.5)$$

This presents that by increasing the sampling point number (N) the spectrum frequency resolution can be increased.
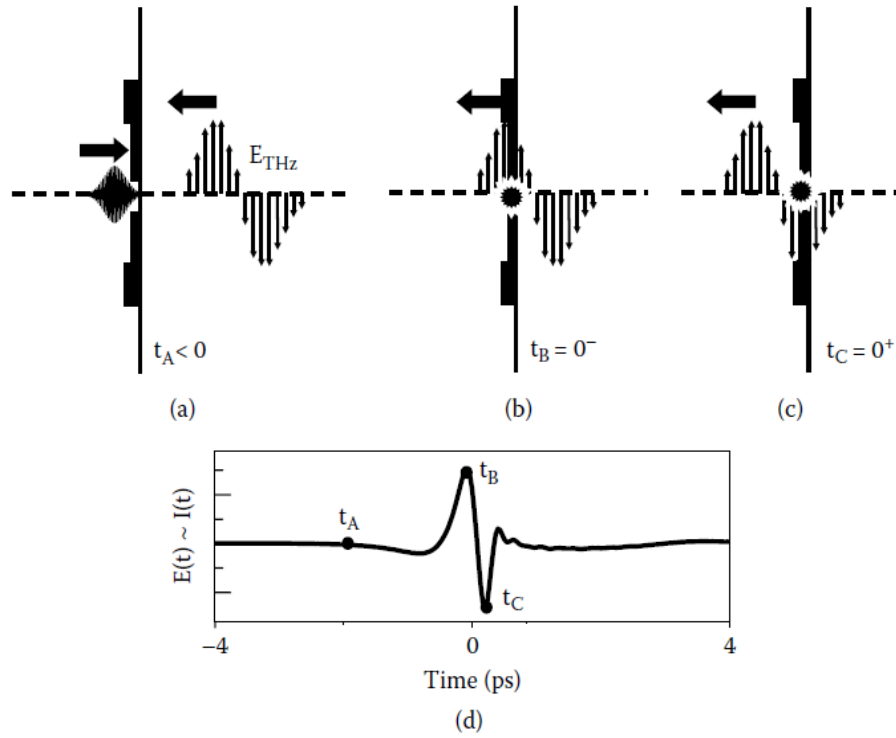
Figure 2.12: The PCA detection process and sampling (a) before and (b-c) after the incident pulse is (d) mapped out within the THz time domain [60].

2.3.3 Fourier transform Sampling for THz Waves

The generated THz wave from an emitter antenna can be considered as an electromagnetic sinusoidal wave with amplitude *A* in the time-domain in z direction as follows:

$$E(t) = A\cos(kz \pm \omega t). \qquad (2.6)$$

There is a continuity of THz wave in the time-domain which consists of *N* samples by step time size of *dt*. Then the whole duration of a wave is:

$$t = Ndt, \qquad (2.7)$$

where $dt = 2dx/c$ for a delay line with the scanning length of *dx* (usually in μm size), and the speed of light in vacuum of *c*. Relation (2.6) can be rewritten as follows:

$$E(N\Delta t) = A\cos(kz \pm \omega N\Delta t), \qquad (2.8)$$

where $E_n = E(n\Delta t)$ for $n = 1, 2, 3, 4, \ldots, N$. Practically, N is power of 2 (for example $N = 2^{10} = 1024$). $\varphi = (kz \pm \omega N\Delta t)$ is the phase and $\omega = 2\pi / f$ is singular frequency. Fig. 2.13 shows an example of the detected THz signal at the receiver antenna for a reference signal and a sample signal in the time-domain.
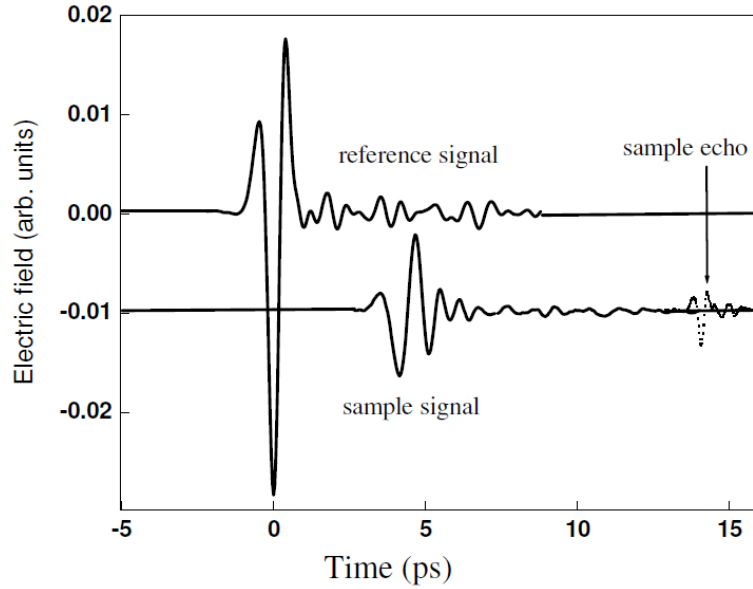
Figure 2.13: The reference and sample THz signal examples shape in the time domain [85].

In order to transform the detected THz wave from the time-domain into the frequency domain using the Fourier technique presented in (2.4). Because of the Euler's formula:

$$e^{-i\omega t} = \cos(\omega t) + i\sin(\omega t), \tag{2.9}$$

(2.4) relation can be extended in the real and imaginary parts of the THz electric wave as follows:

$$E(\omega) = \frac{1}{2\pi} \int_{-\infty}^{+\infty} E(t)\cos(\omega t)\, dt + \frac{1}{2\pi} \int_{-\infty}^{+\infty} E(t)i\sin(\omega t)\, dt = A(\omega)\cos(\omega) + iA(\omega)\sin(\omega). \tag{2.10}$$

Fig. 2.14 shows the transformed amplitude and phase for the sample and reference signals in the frequency-domain obtained in Fig. 2.13.
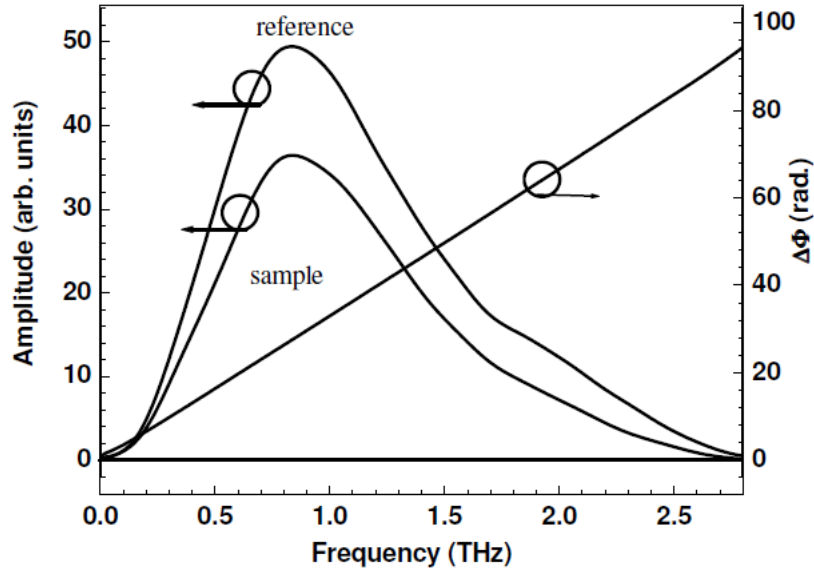
Figure 2.14: The amplitude and phase of the THz time domain signals in Fig. 2.13 transformed into the frequency domain [85].

The frequency sample rate (*f*) and frequency step or frequency resolution (*df*) are defined as follows:

$$f = \frac{1}{dt},$$

(2.11)

$$df = \frac{f}{N} = \frac{1}{dt.N} = \frac{1}{t}.$$

(2.12)

The frequency resolution directly depends on whole duration of signal *t*. By inserting (2.3) in (2.11), the relationship between frequency sample rate and the scanning length of optical delay can be defined as:

$$f = \frac{c}{2dx}.$$

(2.13)

Fig. 2.15 (a) shows a real-time example of measurement in the lab done within this thesis in which the detector takes the THz signal by acquisition system at the receiver antenna for a transmitted signal through the sample and its reference in the time-domain. All data from the acquisition system are processed in the coded platform for further signal processing. Fig. 2.15 (b) shows the transformed THz signals in the frequency domain of achieved

signals in Fig. 2.16 (a). The transformed singles in the frequency-domain is completed after finishing the measured THz signals in the time-domain with calculating phase difference as a function of frequency.
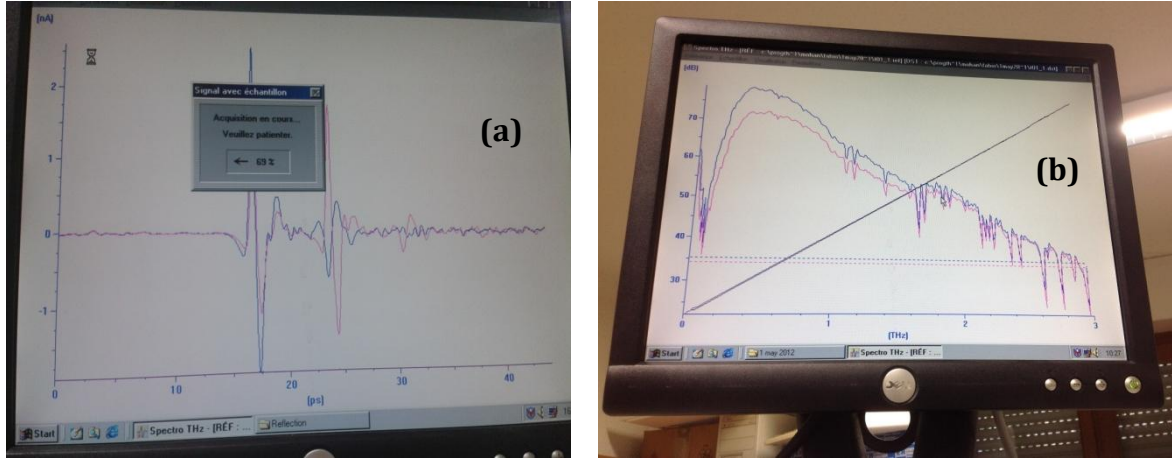
Figure 2.15: (a) The time trace of the THz pluses in the lab from the THz-TDS measurements of the sample and its reference. (b) The amplitude and phase difference of the complex THz electric fields for the sample and its reference signals.

2.3.4 Signal-to-Noise Ratio of THz-TDS

The absolute boundary of the THz-TDS set-up is essentially limited by the dynamics (DR) measurement or signal-to-noise ratio (SNR) performances defined by [86, 87]:

$$SNR(\omega) = \frac{S_{THz}(\omega)}{SD(\omega)},$$ (2.14)

$$DR = \frac{S_{THz}(\omega)}{S_{min}(\omega)},$$ (2.15)

where S_{THz} is the absolute THz amplitude, and SD is the standard deviation of signal originated from noise, and S_{min} is the minimum measurable THz signal [86]. Fig. 2.16 shows the dynamic range of the reference THz signal with a SNR of 300 at around 400 GHz obtained from the THz-TDS set-up taken under this study [75]. The results shows a broad band THz signals (0.1-2 THz) with an extracted linear phase which will be discussed in Chapter 4.
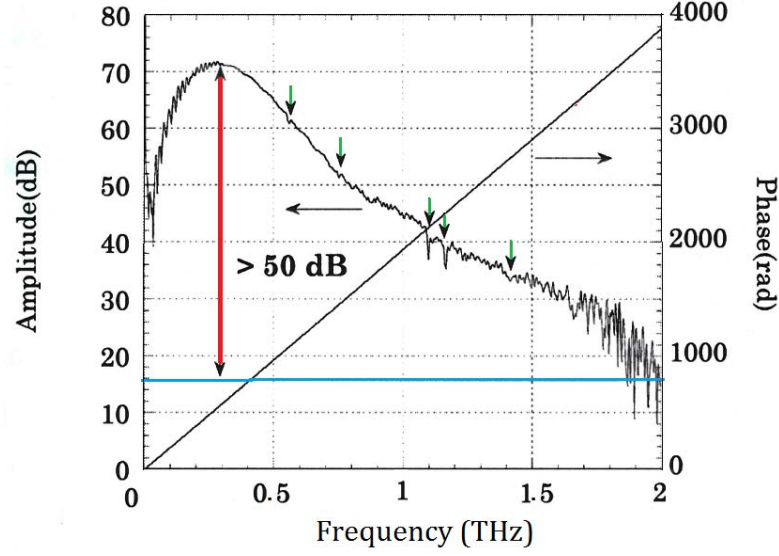
Figure 2.16: The dynamic range of THz-TDS set-up with a linear phase used in this study. The blue line is noise floor. The red line shows the absolute value of maximum dynamic range, and the green line shows the water line absorptions.

2.4   Reference Substrate Optical Properties

The importance of substrate transparency in the THz measurements has been studied in Appendix B. To find the intrinsic optical and electrical properties of the thin film materials, the quartz was chosen as the substrate for all samples because of its high transparency in the THz regime. Since the deposition of the graphene-like thin films on the high permittivity gate insulator does not degrade the perfect high speed carrier transport of samples, deposition of such high conductance thin films has been made on the top of quartz bar [36].

In the generated THz in from the PCA can be considered as parallel throughout the samples. A classical extracting technique has been employed to calculate both the refractive index and the absorption coefficient of the bar substrate using a similar approach explained in Ref. [88]. The complex refractive index of the substrate with thickness of D is extracted based on the measured transmission signals by:

$$T_{c,S}\left(\omega,\tilde{n}_s\right) \approx T_{m,S}\left(\omega,\tilde{n}_s\right),$$

(2.16)

and the reflected ones from:

$$R_{c,S}\left(\omega,\tilde{n}_s\right) \approx R_{m,S}\left(\omega,\tilde{n}_s\right),$$
(2.17)

by taking the experimental modulus and phase. The subscripts m and c designate the experimental measurements, determined from $E_{S,T}/E_{Air}$ or $E_{S,R}/E_{Air}$, and the calculated ones respectively for transmitted and reflected THz signals. To carry out the transmission and reflection THz measurements of the reference substrate, two main signals are considered. The first signal is the reference air space, and the second one is signal transmitted (reflected) through (from) the reference substrate surrounded with air. Fig. 2.17 shows the main principle of THz-TDS measurement for the thick substrate:

1- $E_0(\omega)$ is the incident,

2- $E_T(\omega)$ is the transmitted,

3- $E_R(\omega)$ is the reflected.
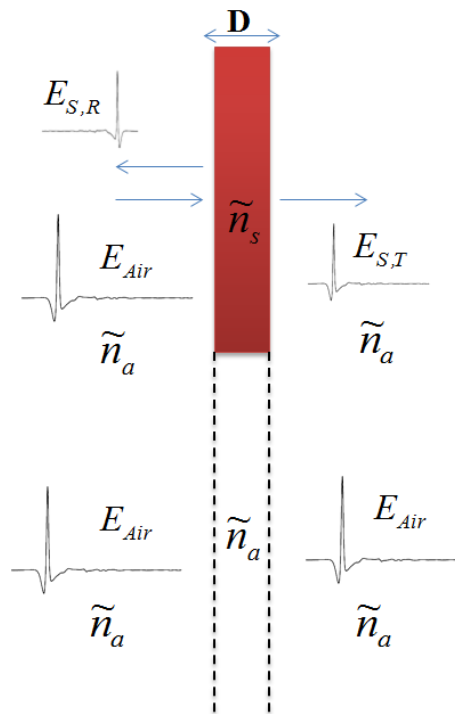
Figure 2.17: The schematic of THz-TDS transmission and reflection measurements for the reference substrate with thickness of D parallel face to the THz electric field.

To find the complex refractive index of the sample ($\tilde{n}_s = n_s + ik_s$) from the transmission and reflection measurements, (2.16) and (2.17) are solved, respectively:

$$T_{m,S}(\omega)e^{i\varphi_{T,m,S}(\omega)} \approx \frac{4\tilde{n}_s 1}{(\tilde{n}_s + 1)^2} e^{-i[(\tilde{n}_s-1)\omega D/v]} , \qquad (2.18)$$

$$R_{m,S}(\omega)e^{i\varphi_{R,m,S}(\omega)} \approx \frac{\tilde{n}_s - 1}{\tilde{n}_s + 1} . \qquad (2.19)$$

The subscripts m and c designate the experimental measurement, determined from $E_{S,T}$ /E_{Air} or $E_{S,R}$ /E_{Air} , and the calculated one respectively for transmitted and reflected THz signals, where $\tilde{n}_a = n_a + ik_a$ is the air refractive index ($n_a \approx 1$ and $k_a \approx 0$). Details are explained in Appendix B. Since the bar substrate is enough thick, the backward and forward reflections and transmissions are eliminated inside the sample. Then the real and imaginary frequency-dependent functions for the transmission measurements from (2.18) are calculated by (approximation of $0.9 \leq \dfrac{4\tilde{n}_s \tilde{n}_a}{(\tilde{n}_s + \tilde{n}_a)^2} \leq 1$):

$$n_s \approx \frac{c}{\omega D}\varphi_{T,m,S} + 1, \qquad (2.20)$$

$$k_s(\omega) \approx \frac{c}{\omega D}T_{m,S}. \qquad (2.21)$$

In the same approach and from (2.19) the frequency-dependent of sample refractive index complex functions can be calculated from the reflection measurements by:

$$n_s \approx \frac{1-R_m^2}{1-R_m \cos\varphi_{R,m,S} + R_m^2}, \qquad (2.22)$$

$$k_s \approx \frac{2R_m \sin\varphi_{R,m,S}}{1-R_m \cos\varphi_{R,m,S} + R_m^2}. \qquad (2.23)$$

Fig. 2.18 shows the extracted complex refractive index of the quartz substrate. The real one is equal to 1.95 over the whole THz range of interest, as determined from the air reference

and transmitted sample electric fields. The real and imaginary parts of refractive index function obtained from reflection measurements, determined from the air reference and reflected sample electric fields, are also plotted. Even if noisier as expected because of the weaker sensitivity of extraction from the reflection THz-TDS data, the information obtained from both transmission and reflection records are in good agreement. The available THz power decreases sharply and falls below the noise level at lower frequencies.
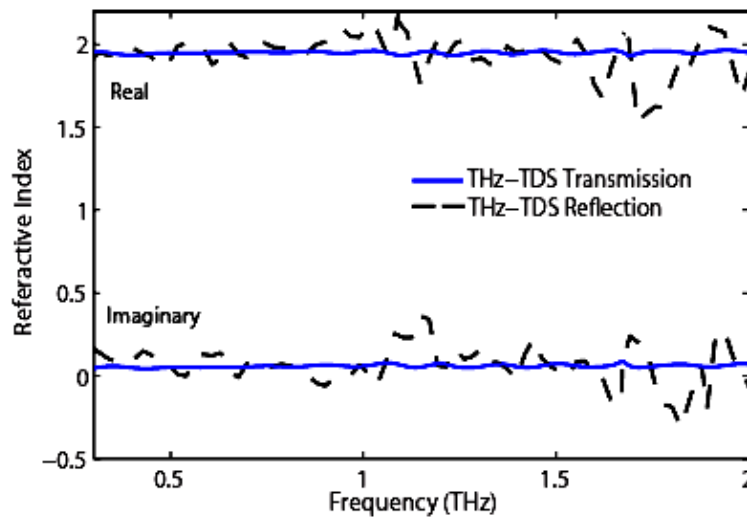
Figure 2.18: The complex refractive index of fused quartz as a function of frequency (0.3-2 THz) using THz TDS transmission and reflection.

The quartz-based were chosen as the transparent substrates at THz regime for all materials samples taken in this thesis with a real refractive index of 1.73 [cf. Fig. 2.19 (a)] and 1.95 [cf. Fig. 2.19 (b)]. The frequency-dependent power absorption ($a(\omega) = 2\omega \dfrac{k_s(\omega)}{c}$) values for both quartz-based substrates are low, but increases continuously with frequency to reach, respectively, 6 cm^{-1} [cf. Fig. 2.19 (a)] [51] and 8 cm^{-1} [cf. Fig. 2.19 (b)] at 2 THz [50]. So, the corresponding extinction, i.e. the imaginary part of the refractive index, remains very small ($\approx$0.01 at 2 THz). Fig. 2.19 (a) presents that both the relatively high value of the index of refraction and the increase of absorption with frequency demonstrate that the substrate material is not a pure fused quartz as indicated by the supplier, but certainly a silicate glass with a low doping concentration. This value can be neglected. The real and imaginary parts of refractive index function of the bars indicate they are the quartz and fused quartz by comparing previous reports [62]. Since they have almost the same level of THz power

absorptions, throughout this thesis, the terms 'quartz' will be used for all substrate materials.
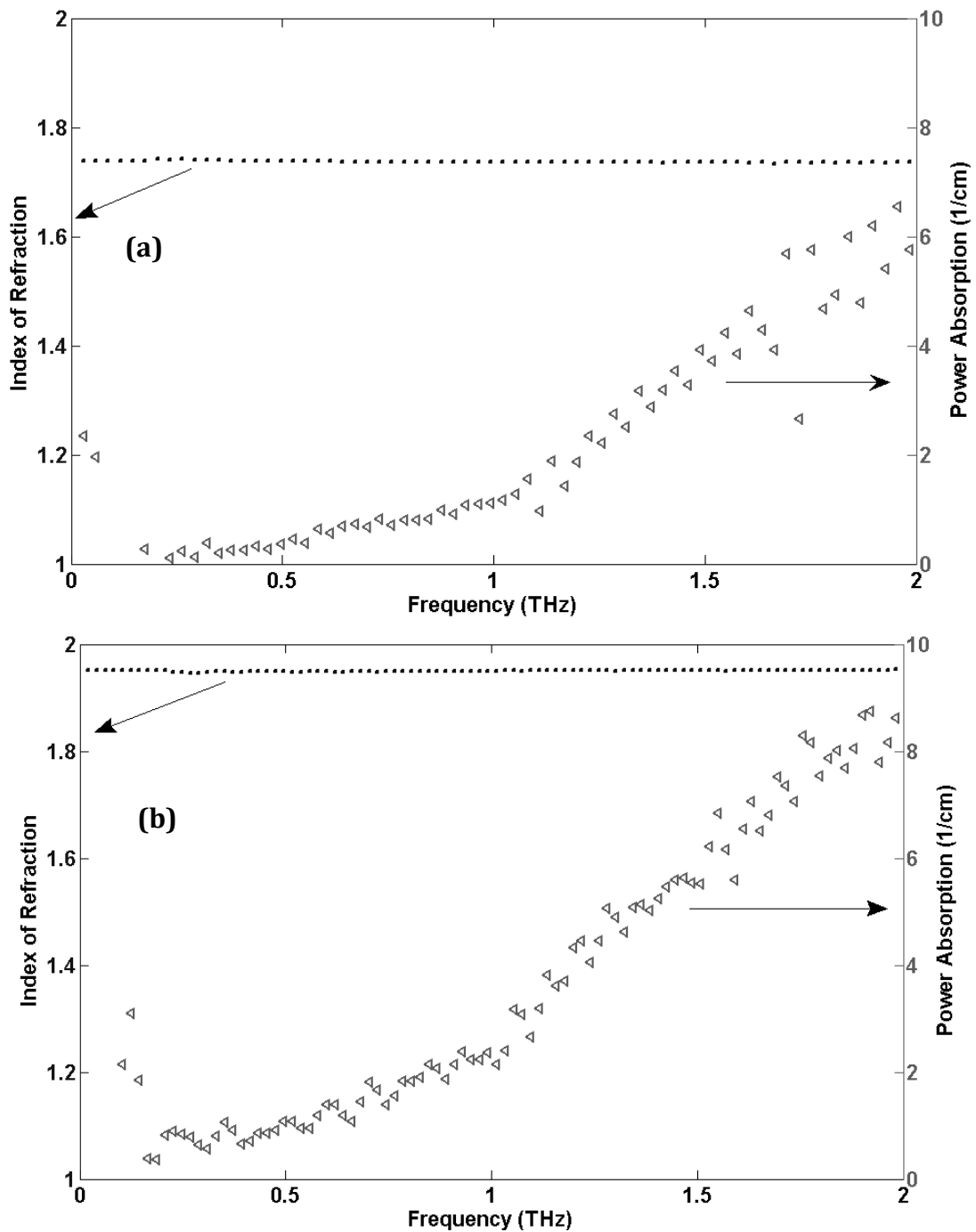
Figure 2.19: The obtained power absorption and the refractive index of (a) quartz, and (b) fused-quartz reference substrates using THz-TDS measurements.

2.5 Conclusions

In this chapter the key concepts related to the THz generation and detection signals have been presented. This review has begun with a description of the THz broadband radiation using ultrafast femtosecond laser and its history. It has been shown here that the photoconductive THz antennae are principally governed by photo-generation carries techniques in the semiconductors.

A review of the optoelectronic THz-TDS measurement concepts employed in this research work have been presented by introducing different components of set-up and their functions such as fs laser, PCA, chopper, lock-in amplifier, and parabolic mirrors. This has been followed by the THz scanning and samplings temporal signals at the PCA detector using an optical delay stage and time process in different steps. This obtained temporal THz wave has been transformed into the frequency domain using Fourier technique which allows studying the coherent complex electric field, obtaining the phase and the amplitude values simultaneously.

A review of theory of THz extraction the optical and electrical parameters of the thick quartz samples has been explained by taking experimental modulus and phase equal to the theory modulus and phase in the transmission and the reflection THz-TDS measurements. The used differential THz transmission of this extraction procedure has provided a clear understanding of the multiple reflections of incident wave (or Fabry-Perot effect) inside the thin film and thick substrate samples and studying the thickness influences on the absorption and refractive index values. It has been explained in Appendix B.

Chapter 3: THz Wave Interaction with Solid Sates and Graphene-Like Materials

3.1 Introduction

This chapter will be brought together the key concepts of the electric field interaction with the solid-sates material, mainly semiconductor and semimetals, along with the optical and electrical properties of such samples, to study the THz parameters. This chapter will deal with the study of semiconductor materials by studying the energy gaps in the THz frequencies using the Maxwell principle. The sections will start by fundamental of the EM wave interaction with the semiconductors to study three absorption, stimulated emission, and spontaneous emission phenomenal. Details will provide the inter- and intra-transitions.

The THz electric field provides sufficient energy around the Fermi level and also intra-transition to characterize the electrical and optical properties of semiconductors. To gain more inside into the conductivity and absorption of material, a theoretical analysis based on the Drude model will be presented to study the plasma and collision time of the semiconductor sample. The Drude model will define the electrical and optical parameters in functions of the most important semiconductor physical properties.

In addition, this chapter will deal with the study of the absorption and conductivity transitions of graphene using Drude based models. Compared to the recent works, this thesis will use the Drude model modified by addressing the Smith theory to take into account non-random scattering of free carriers and also impurity of samples to better adjust the experimental data with the fitted curves for THz characterization of graphene-like samples. The CNTs' physical structure made from graphene will be investigated to study the electrical conductivity responses of such thin films using effective medium theory and hybrid Drude-Lorentz models to consider the Drude response (free electrons

contributions) and Lorentz oscillation (sum of oscillation of bound electrons to calculate the relative permittivity of the nanotubes).

3.2 Nano Semiconductor Devices and Moving to Graphene-Like Materials

The solid-state materials can be categorized into three groups: 1) insulators, 2) semiconductors, and 3) conductors. The range of electrical conductivities and the corresponding resistivity is shown in Fig. 3.1 [89]. The fused quartz has very low conductivity and silver shows high conductivity. Semiconductors, for example silicon (Si), have been intensively interested because the energy band-gaps located between the insulators and those of conductors. This feature allows them to be sensitive to different phenomenal such as temperature, frequency, wave illumination, current and EM field for different optic and electronic devices.
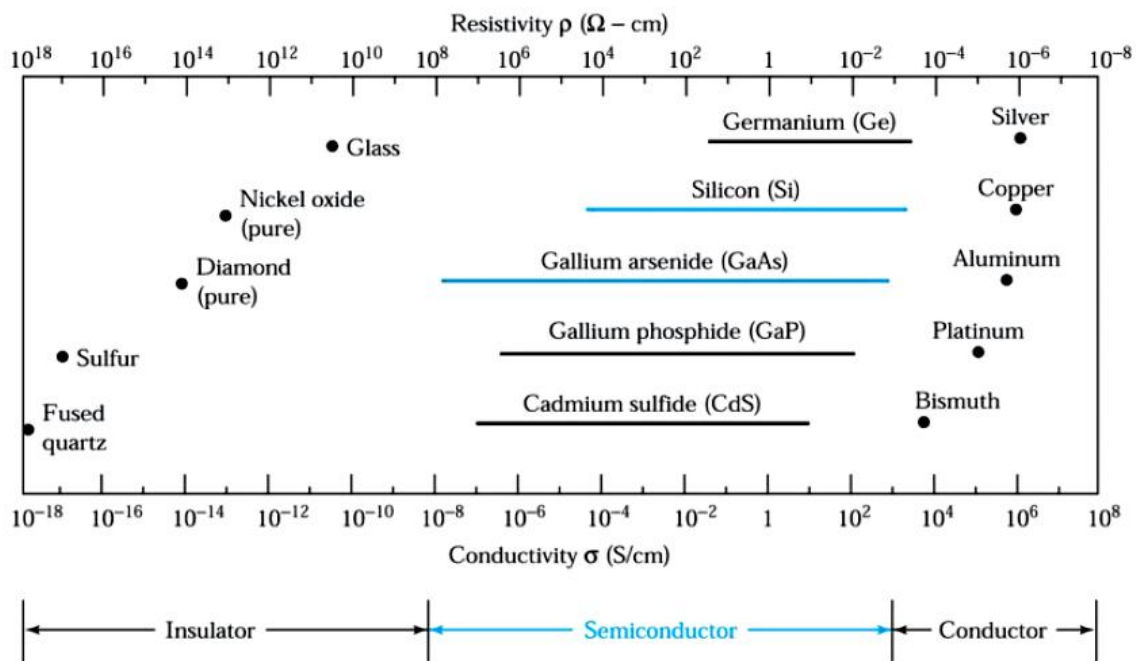
Figure 3.1: The conductivity and resistivity range of insulators, semiconductors and conductors [89].

The fulfillment of Gordon Moore's prediction is followed by a continuous growth in the switching speed of electronic devices using semiconductors by reducing size [90]. The

Moore's law has been affected by the potential advances in silicon technology. The broad lifetime of Moore's law and a well evolution of nanoscale semiconductor electronics are demanded in coming years. The present electronics devices are made from the semiconductors. For example, Si metal oxide semiconductor field effect transistors (MOSFETs) with sub 100-nm gates are in mass production, and they are in a roadmap of sub 20-nm in the next 10 years [91].

Researchers are struggling to develop and design the fast semiconductor based devices using Si and GaAs, which are also smaller than those currently available in the market. However, it has seen limited in the switching speed, essentially due to the high power utilization penalty related to pushing silicon-based transistors to greater speeds. Indium tin oxide (ITO) is considered as an alternative candidates for transparent electrodes (with sheet conductance between 10Ω and 100Ω at optical transmittances of 85%-90%) [92]. Because of the scarceness of indium, ITO is becoming more expensive. New graphene-like materials that are transparent, conductor, and flexible have major advantages over brittle ITO coatings and its cost [93].

Graphene, a single layer of carbon atoms arranged in a hexagonal crystal lattice, has recently appeared as a promising candidate not only for facilitating transistor downscaling but also to increase switching speeds. They are considered as alternative materials to semiconductors and ITO for flexible transparent conductive films since they have unique electrical, optical and mechanical properties [41, 94-101]. Graphene-based materials mobility, stability and compatibility with classical Si technologies lead us to the quick development of optoelectronic devices on photonic platform, such as transistor photodetectors, light-emitting diode (LED) and high quantum capacitors [102].

One dimensional (1D) CNTs[1] and two dimensional (2D) graphene forms find applications in microelectronics, biotechnology and even in energy storage and environment. Their chemical and dimensional compatibility with proteins and DNA has enabled them to be of high interest to use as parts of biosensors [93, 103]. The carbon nanostructures have been

---

[1] Carbon nanotubes (CNT) are cylinders made of rolled up graphene sheets.

introduced in numerous electronic devices, such as field-effect transistors [104], super-capacitors [18] or as conductive flexible adhesives [105].

The CNTs may be single walled if the tubes consist of just one sheet of graphene or multi-walled if there exists more than one sheet of graphene. The single walled carbon nanotubes (SWCNTs) are either semiconducting or metallic. Diameter of a SWCNT is typically around 0.8 to 2nm and that of a multi walled carbon nanotube (MWCNT) are 20 to 50 nm although it can go beyond 100 nm. They are believed to be much stronger than steel, can conduct electricity as efficient as copper at the same time behaving as semiconductors. Nanotubes are perfect systems for studying transport of electrons in one dimension and also holds commercial potential as transistors, sensors and nanoscale wires [106, 107].

In spite of the higher value of conductance in SWCNT film in comparison to MWCNT film, they are expensive to produce. Two significant advantages of MWCNTs are higher mechanical strength and broken voltage which are applicable for microwave and terahertz devices. Researchers are more interested to use MWCNTs for fabrication of excellent nanocomposites with improving electrical properties for highly flexible and low cost devices [20]. Having such a highly conductance material and particularly by formation of polymer composites enables us to apply it for the recent and state-of-the-art thin devices such as the field-effect and transistors [17, 108].

The road history of graphene-like device has been begun since 1947. Wallace demonstrated the band structure and predict energy gap of a hexagonal 2D lattice single layer of carbon atoms i.e., graphene [109]. In next 20 years, as shown in Fig. 3.2 , Boehm et al. produced single graphene layers by the reduction of graphite oxide [110] followed by observation of single-layer graphene on metal by May [111]. This process was continued by producing graphene using the thermal decomposition of silicon carbide (SiC) by Van Bommel [112]. In Boehm's study in 1994, graphene was introduced for single carbon layers of the graphitic structure [113].
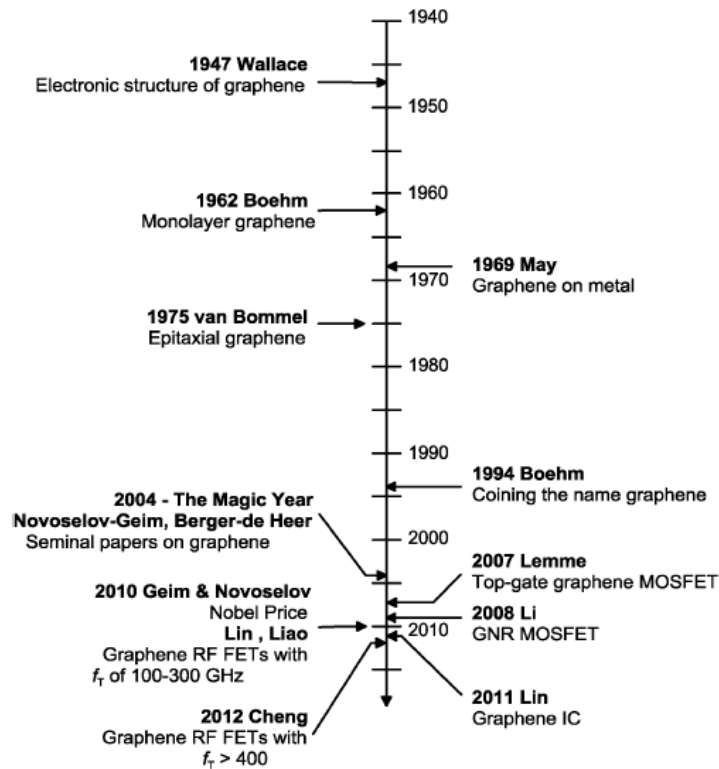
Figure 3.2: The graphene road map and its recent applications in optoelectronic devices [102].

This roadmap explores that the graphene-like materials have been widely recognized as the perfect option for next generation of the ultrafast high performance transistors and optoelectronic applications for the III–V compounds in the radio frequency (RF) devices. Although the key challenge is that all usual semiconductors possess a sizeable band-gap (e.g., Si 1.1 eV and GaAs 1.4 eV), which is zero for natural graphene and the missing gap has influences for the operation of graphene devices [102].

The first report graphene based MOSFET appeared in 2007 [114]. Following that, magically attentions have been under taken to apply such devices in high frequency systems. Within 3 years, graphene MOSFETs reported to operate at 100 GHZ [115, 116]. In 2012, this frequency range has been extended to 400 GHz [117].

3.3 Electronic Band Structure of Graphene

The band gap in materials is an energy range where no electrons can exist. Fig. 3.3 shows the band structures and energy gaps of insulator (Fermi level in middle of the energy band gap), semiconductor (Fermi level in middle of the energy band gap), metal (Fermi level in the overlap of valance and conduction bands), and graphene (Fermi level in the Dirac point) based devices. The energy gap is a major determining factor in all materials' properties. Large band gaps are insulators, small band gaps are semiconductors and materials without a band gap are conductors. The Fermi level can be changed by n/p-doping of the materials.

Carbons in the solid phase are in three allotropic forms: graphite, diamond, and buckminsterfullerene [118, 119]. But graphene is none of these. Graphene is a monolayer of carbon atoms packed into a two dimensional honeycomb crystal structure. It combines the nanometrics size and high electrical conductivity, 10-100 times faster than Si, for a wide range of technology. Graphene has a vanishingly small gap at what is called the Dirac point [102]. Details are described in Appendix C.
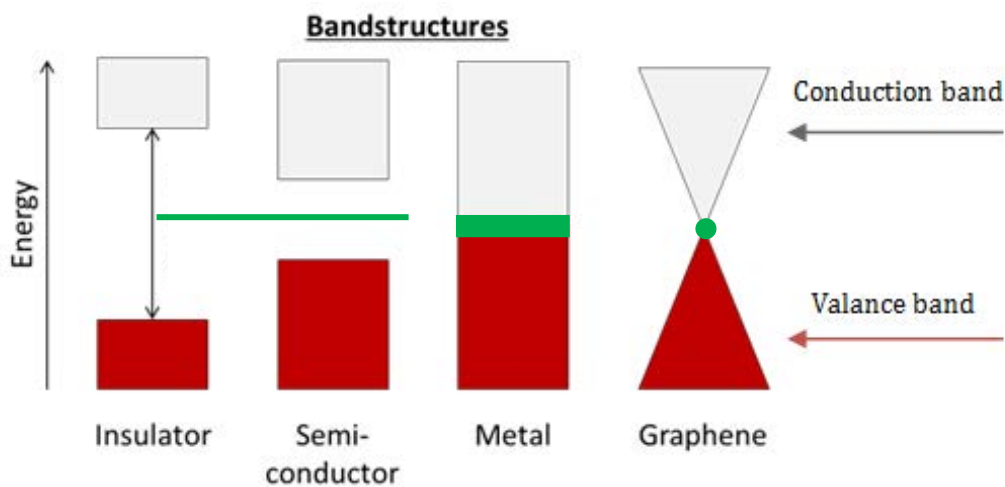
Figure 3.3: The band structures and energy gaps of insulator, semiconductor, metal and graphene. The green colors show the Fermi level areas in different materials.

3.4 THz Electric Field Interaction with Graphene and Electron Transition

In accordance with the classical Maxwell's explanation, an electromagnetic wave [cf. Fig. 3.4] sinusoidally oscillates and comprises electric and magnetic fields which are commonly perpendicular to each other. These fields are also perpendicular to the direction of propagation with wavelength of $\lambda = c / f$, which is the distance between two consecutive peaks in an electromagnetic with amplitude of A. The frequency $f = 1 / t$ is the number of λ repeating event per unit time (t) and has the the international system of units of hertz (Hz). In the case of light wave propagation, $c \approx 3 \times 10^8 m / s$ [120].

An electric field wave is the sum of a series of monochromatic waves via Fourier transform. The interaction between wave and material can also be presented as the sum of material interacts with the series of monochromatic waves. The incident of energy wave with semiconductors and metallic makes the transitions between electron states in the partially filled band –intraband transitions – together with transitions between different bands – interband transitions – are responsible for the electrodynamics [121].
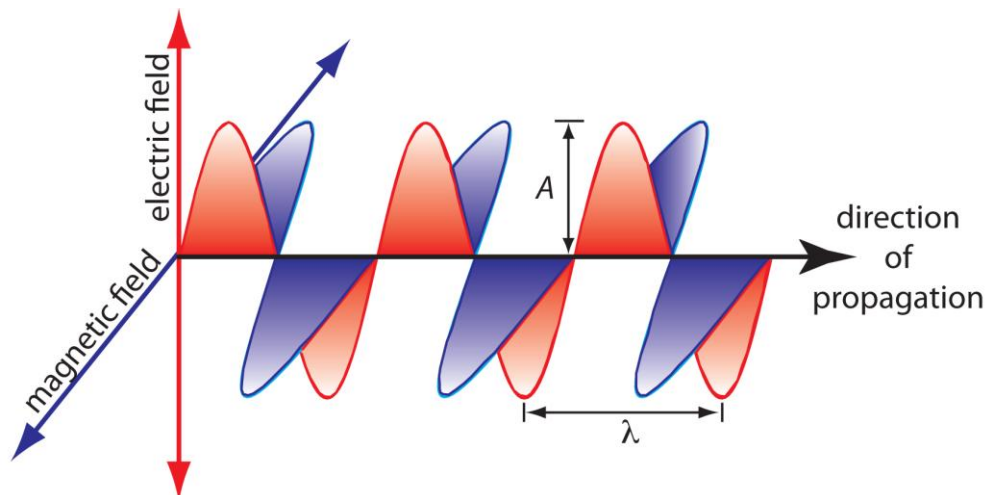
Figure 3.4: Electromagnetic wave propagation with wavelength of λ and amplitude A perpendicular to the direction of propagation.

According to the quantum theory, the stationary quantum states of a single electron are presented with a time-independent Schrödinger relation [122]:

$$H_0(r)Z_n(r) = E_n Z_n(r), \tag{3.1}$$

where H_0 is the Hamiltonian, E_n is the energy eigenvalues, and Z_n is the energy eigenstates. The Hamiltonian is the summation of the kinetic and potential energies. If the electron is confined to a limited gap by the potential, the energy levels turn into discrete. We consider an electromagnetic wave $E(t)$ which travels in time t interacting with the electron. When the dipole approximation is assumed, the Hamiltonian of the electric dipole interaction is written as:

$$H_I(t) = -\mathrm{P}.E(t), \tag{3.2}$$

where $\mathrm{P} = -er$ is the electric dipole moment. Then relation (3.1) can be rewritten as a time-dependent Schrödinger relation of the electron as:

$$i\hbar \frac{\partial}{\partial t} Z_n(r,t) = [H_0 + H_1(t)]Z_n(r,t), \tag{3.3}$$

where $\hbar$ is the reduced Planck constant (or Dirac constant). The electron response to the applied $E(t) = E_\omega e^{-i\omega t} + c$ field, with the radiation frequency of ω and the complex conjugate of c, is resonant with the ΔE energy eigenstates, $\hbar \omega = \Delta E$. As shown in Fig. 3.5, from the quantum mechanical point-of-view, three phenomena near the resonances are:

a) *Absorption*: the electron in the lower energy level is excited to the higher energy level by absorbing an incident photon,

b) *Stimulated emission*: the energy transition is from the higher to the lower level. The emitted photon is in-phase with the incident photon, which is the original process driving the coherent radiation,

c) *Spontaneous emission*: thanks to the relaxation of the electron from the higher energy level to the lower energy level without any external perturbation a photon is emitted.
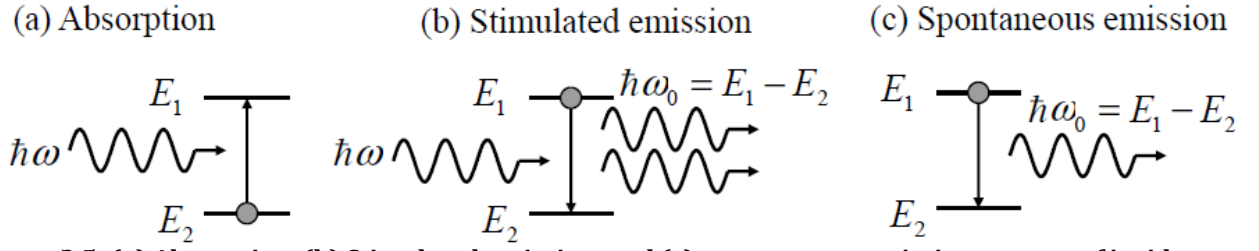
Figure 3.5: (a) Absorption, (b) Stimulated emission, and (c) spontaneous emission process of incident wave of with radiation frequency of ω_0 [122].

3.4.1 THz Characterization in Semiconductors and Semimetals

The main aim to characterize the electrical and optical properties of semiconductors is their energy band-gaps, addressing to the difference of photon energy between the highest level of valence band (E_2) and the lowest level of conduction band (E_1). The electronic band structure of a direct band-gap and an intrinsic three dimensional (3D) semiconductor [cf. Fig. 3.6] can be expressed by parabolic conduction and the valence energies bands in the electron m_e^* and the hole m_h^* effective masses approximation [122]:

$$E_1(k) = \Delta E + \frac{(\hbar k)^2}{2m_e^*},$$ (3.4)

$$E_2(k) = \frac{(\hbar k)^2}{2m_h^*},$$ (3.5)

where k is the wave-vector and thus $\hbar k$ is the momentum.
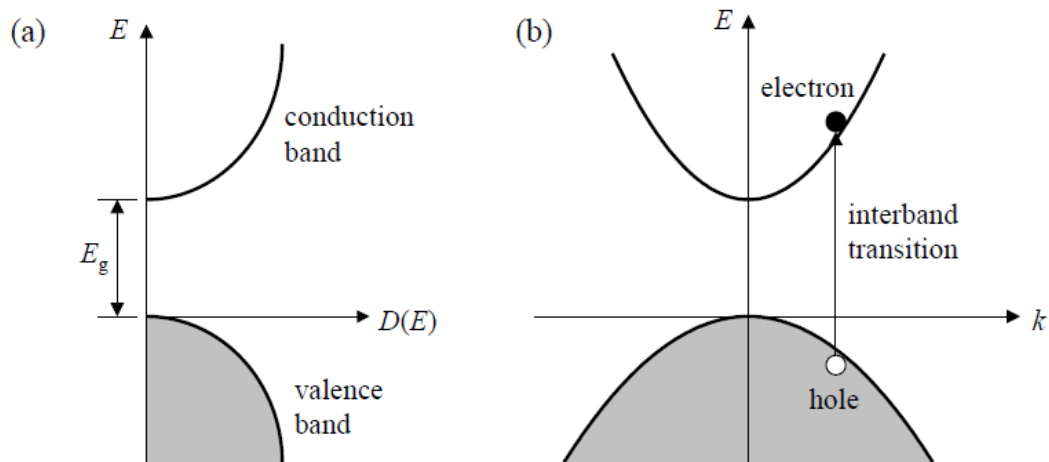
Figure 3.6: The conduction and valence bands of a direct band-gap semiconductor considering the effective mass approximation with (a) Density of states and (b) the parabolic band energies as a functions of the momentum [122].

As earlier explained, there is a discrete energy gap in semiconductors between the conduction and valence bands. But, the studies of transition energy levels within a band are continuous for bulk material needs to low excitation energy. Fig. 3.7 shows the corresponding photon energy to THz frequencies, 0.1-10 THz [4], which increase with increasing the frequency. The interaction of THz radiation with matter provides a vital low-energy probe of the electronic nature of a system close to its equilibrium state.
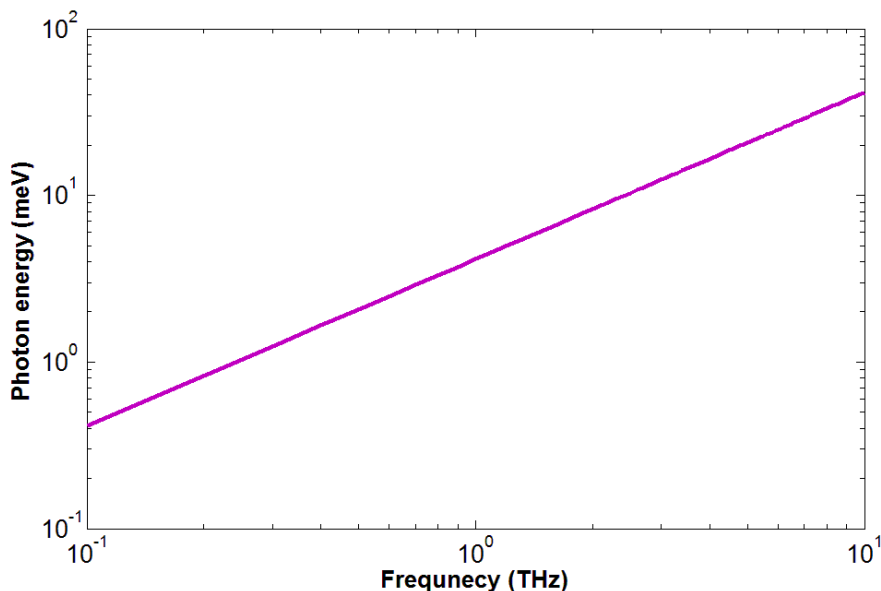
Figure 3.7: The equivalent photon energy of the THz bandwidth gap as a function of frequency.

There are several evidence of THz excitations interest such as Rydberg transitions in atoms [123, 124] or among impurity states in semiconductors [125], phonon resonance in crystals [126], rotation vibration transitions in molecules [127], and large-amplitude movements in biological samples [128]. But, one of the key interest of THz excitation interest is to study the absorb transitions within an energy band (intraband transition) [129-131]. It is because the band-gap energy of typical semiconductors is larger than the THz photon energy. Fig. 3.8 shows a general schematic diagram of the resonances of the refractive index and absorption coefficient of a hypothetical solid between microwave and optic spectral region. The strong absorption value is observed at infrared, visible and ultraviolet regimes. In addition, the 1st resonances are happen at several THz frequencies which allow us to investigate the dynamic carries without needs to excite the sample.
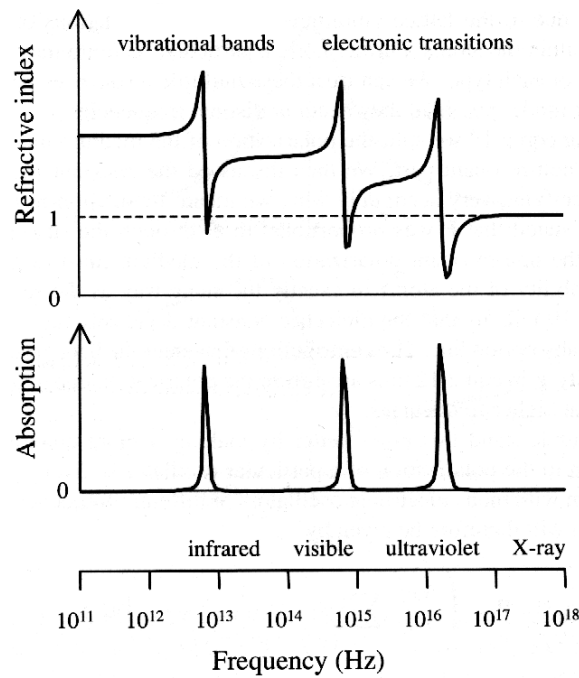
Figure 3.8: The frequency dependence of refractive index and power absorption coefficient of a hypothetical solid [132].

3.4.2 THz Characterization in Graphene- Materials

Appendix C presents the importance details of graphene and CNT structure. Fig. 3.9 shows the full band structure (the valance and conduction bands) of graphene and magnification around the vertex of the Dirac cone, so-called Dirac point. By absorbing a phonon an electron is excited from the lower cone to the upper cone [133].
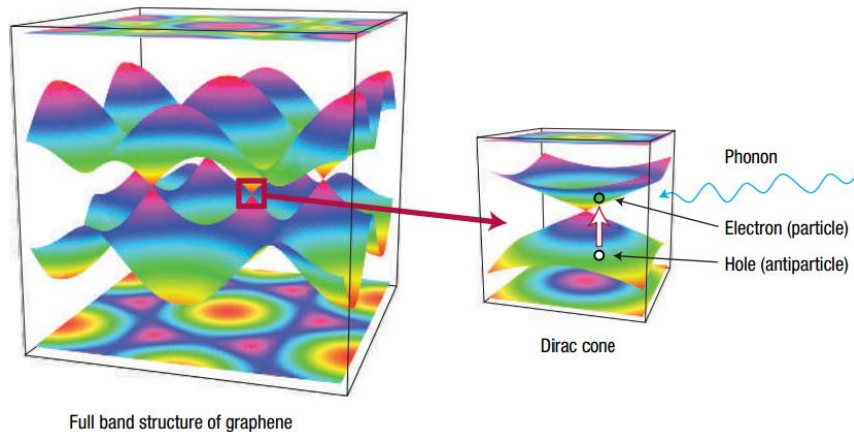
Figure 3.9: The full band structure of graphene and Dirac point in its energy gap [133].

For graphene made by chemical vapor deposition (CVD) process, the initial doping is on the order of 10^{12} cm^{-2}. It approximately corresponds to a Fermi level energy of 100meV. Metals have abundance of free charges. But, graphene is a semimetal that free electron can be induced using chemical doping or electrical gating with straightforwardness because of its two-dimensional nature. Perfect metal plasmons have application range is in the visible part of the spectrum. In contrast, graphene plasmonics operate at infrared and terahertz ranges. For example, the high sensitivity of the graphene surface plasmons can be used in the environment sensor capabilities. The free carriers in graphene can reach around 0.001~0.01 per atom (considerably smaller than of metals; 1 per atom), or doping concentration of 10^{12} ~10^{13} cm^2. This feature of the two-dimensional and semimetallic nature of graphene enables the electrical tunability applications. To improve the conductivity of graphene films, the carrier concentration of the carbon layer must be adjusted by shifting the Fermi level of graphene's zero-gap band structure away from the Dirac point. Fig. 3.10 shows the dispersion relation for graphene can be tuned (the Fermi level away from the Dirac point) for the optoelectronic applications by transferring electrons (or holes) [134]. This shift can be induced by chemical doping [135] or a metal

contact [136]. For example, silver nanowires (AgNWs) are flexible materials with excellent electrical conductivity [137-139]. Recently, the new AgNW-graphene transparent conducting hybrid films have been intensively investigated in view of the developing of DNA sensor [140], biological [141] and optoelectronic devices [142]. A comprehensive knowledge of the electrical conduction in GRP and AgNW-GRP hybrid films, as well as a precise measurement of their optical and electrical parameters, is compulsory for designing optimized electronic components.

Figs. 3.11 (a-b) shows characteristic absorption spectrum of n doped graphene with different optical transition processes involved in inter and intra bands. A Drude THz peak response appears because of intraband free carriers' absorption (state 1). A minimal absorption (consequently minimal optical conductivity) in the mid-infrared frequencies is due to Pauli blocking (state 2). In the frequency range of near-infrared to visible, absorption is attributable to direct interband transitions which are almost constant (state 3).
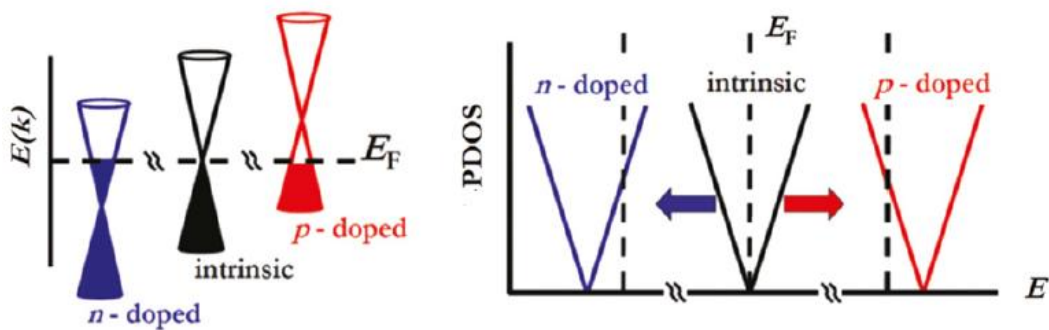
Figure 3.10: The Fermi level shifting from the Dirac point of intrinsic graphene to use in the optoelectronic applications. PDOS is projected density of states for graphene [134].
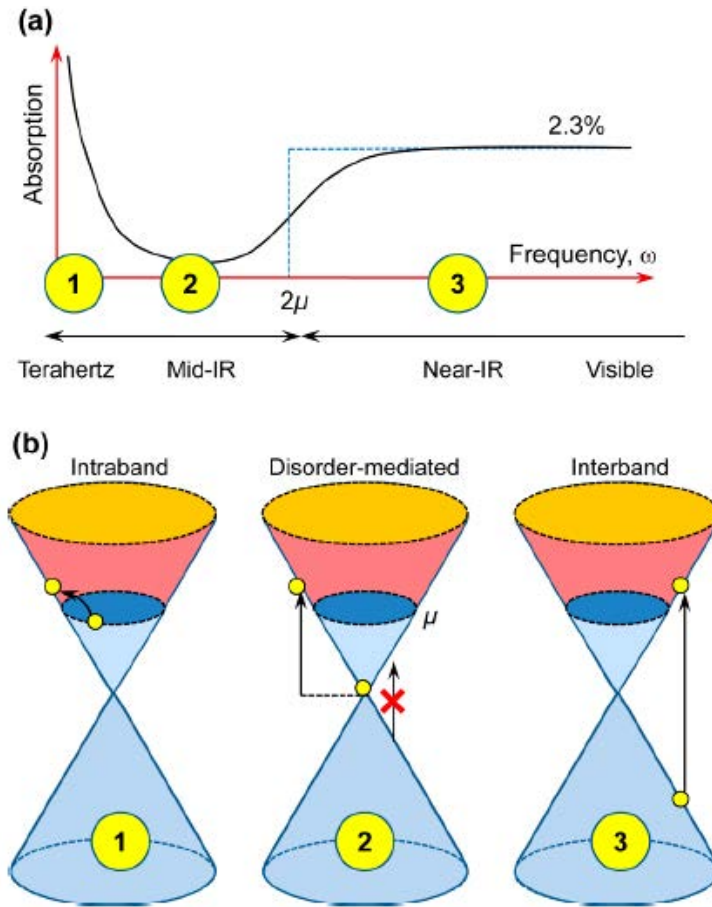
Figure 3.11: (a) absorbance behavior of doped graphene in different range of frequencies. (b) The various optical transition states: at frequency ω smaller than the thermal energy, absorption transitions happen via intraband processes. At finite ω < 2 μ, disorder is key in imparting the momentum for the optical transition. A transition occurs around ω ≈ 2μ, where direct interband processes lead to a universal 2.3% absorption [143].

3.5 THz Dynamic Models of Nano-Semiconductors

Each THz monochromatic wave and its induced polarization are simple harmonic oscillations, with formations of $E(t) = E_0 e^{-i\omega t}$ (with the phase of ωt and the amplitude of E_0). The characteristic time of a wave at 1 THz (~4.1 meV) is 1ps. As shown in Fig. 3.12, the amplitude and the phase of THz electric field change after interacting with a semiconductor. For example, a semiconductor electron diffusivity of ~25cm^{2}s^{-1} gives us a nanometrics scale of diffusion length during one period (1ps). Because of which, THz spectroscopy enables us to study the semiconductor materials, even if at a nanometrics scale.
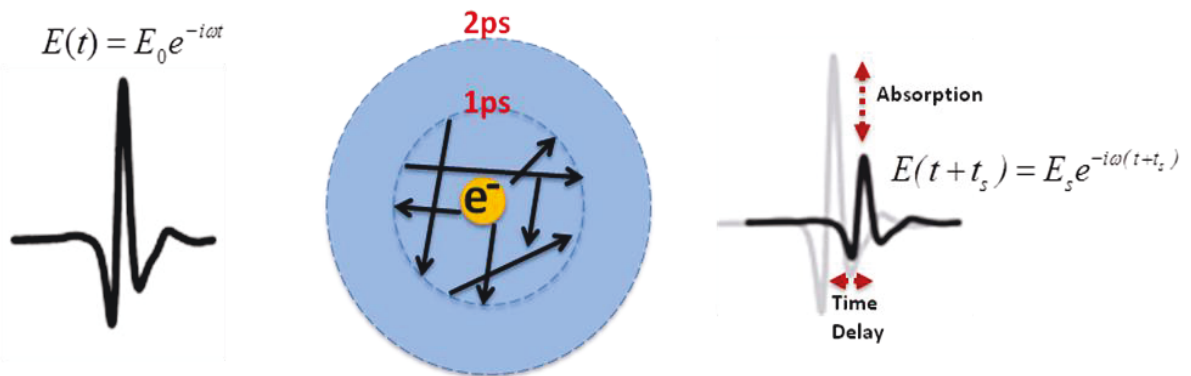
Figure 3.12: The principle of a THz wave interacted with a semiconductor.

The complex permittivity responses of semiconductors can be described using Drude behaviors with $\Gamma = 1/\tau$. This is the coherent decay factor of the electrons in the matter with plasma frequency $f_p = \omega_p / 2\pi$. The THz spectroscopy studies the photocarrier dynamics in semiconductors as a great of interest because of unique capability to determine fundamental physical processes and optoelectronic applications such as an ultrahigh speed modulation device operated at the sub-THz and THz frequencies.

3.5.1 Drude THz Responses of Semiconductors and Semimetals

The electrical conductivity and the physical characterization in a solid can be derived from the THz electronic transitions. The key element is to find the dielectric constant[1] in relation to free carriers. Such free carriers contribution in semiconductors/metals can be studied by a simple Drude conductivity model. The conductivity model is based on the classical equations of motion of an electron in an electric field, and gives the simplest theory of the optical constants.

The propagated fields will be modified after the interaction with matter i.e., the material parameters and properties. The propagation of EM radiation in interaction with homogeneous media changes the amplitude and phase of electric fields. This aims us to

---

[1] The dielectric constant is the ratio of the permittivity of a substance to the permittivity of free space.

understand the physical properties of materials. The comparison between propagate EM fields and passed waves can characterize the electrical conductivity and the optical dispersions of semiconductors and metals.

The theoretical description of the dynamic phenomena of THz wave in interaction with semiconductor is based on Maxwell's equations in their solutions for time-varying of electric fields. An electric field can be created by a presence of a charged particle such as electron or proton. Thus, the Maxwell's equations in THz can be presented due to the time dependent solution of the equations leading to electric wave propagation:

$$m^* \frac{d^2x}{dt^2} + \frac{m^*}{\tau}\frac{dx}{dt} - qE(t) = 0 ,$$ (3.6)

where $E(t)$ is the electric field as a function of time with spatial x, m^* is effective the carrier mass, and τ is the collision time with the charge of the carrier $q \approx 1.6 \times 10^{-19} \text{coulombs}$. The electric field induces polarization (P) of the matter created by carrier displacement:

$$P = (\varepsilon - \varepsilon_\infty)\varepsilon_0 = Nqx ,$$ (3.7)

where N is the free carrier density, ε_∞ is the high frequency relative permittivity, ε is the relative permittivity of the matter at high frequency of the interaction electromagnetic field, and $\varepsilon_0 \approx 8.85 \times 10^{-12}$ is the permittivity in vacuum. From (3.6) can be rewritten as an expression of the polarization of matter in (3.7):

$$\frac{d^2P}{dt^2} + \frac{1}{\tau}\frac{dP}{dt} - \frac{Nq^2}{m^*}E(t) = 0 .$$ (3.8)

Each monochromatic wave and its induced polarization are simple harmonic oscillations, with formations of:

$$E(t) = E_0 e^{-i\omega t} ,$$ (3.9)

$$P = \chi\varepsilon_0 E_0 e^{-i\omega t} .$$ (3.10)

From the above relations, (3.8) can be rewritten as:

$$\chi(\omega^2 + i\frac{\omega}{\tau}) + \frac{Nq^2}{\varepsilon_0 m^*} = 0,\tag{3.11}$$

where χ is the electric susceptibility of matter that can be derived from $\varepsilon = \varepsilon_\infty + \chi$. Therefore, the complex permittivity ($\widetilde{\varepsilon} = \varepsilon_1 + i\varepsilon_2$) of the materials as a function of frequency (i.e., Drude model) is explained by:

$$\widetilde{\varepsilon}(\omega) = \varepsilon_\infty - \frac{\varepsilon_\infty \omega_p^2}{i\omega^2 \Gamma} = \varepsilon_\infty [1 - \frac{\omega_p^2}{\omega^2 + \Gamma^2} + i\frac{\omega_p^2 \Gamma}{\omega(\omega^2 + \Gamma^2)}],\tag{3.12}$$

where $\Gamma = \frac{1}{\tau} = \frac{Nq^2}{m^*\sigma_{dc}}$ is the coherent decay factor of the electrons in the matter, so-called damping rate. The plasma frequency appears where ε_1 becomes zero which defines as [cf. Fig. 3.14]:

$$\omega_p^2 = \frac{Nq^2}{m^*\varepsilon_\infty\varepsilon_0} = \frac{4\pi Nq^2}{m^*\Gamma}.\tag{3.13}$$

It can be seen that the plasma frequency of the matter is proportional to the square root of the free-carrier density which is various in different semiconductors and metals. The effective electron mass m^* (where $m_0 \approx 9.1\times10^{-31}Kg$ is the electron rest mass), the electron the carrier consideration N, the plasma frequency $\omega_p/2\pi$ and the collision time τ for various semiconductors and metals are presented in Table 3.1.

Table 3.1: Effective electron mass, electron carrier consideration, plasma frequency and collision time for various materials.

Material	m^*	N (cm⁻³)	$\omega_p/2\pi$ (THz)	τ (fs)
Germanium (Ge) [62]	$0.12m_0$	2.4×10^{13}	0.127	265
n-doped Silicon (Si) [144]	$0.26m_0$	4×10^{14}	0.35	294.7
p-doped Silicon (Si) [144]	$0.26m_0$	9.2×10^{14}	0.448	154.5
n-doped Gallium arsenide (GaAs) [145, 146]	$0.067m_0$	1.41×10^{18}	41.2	69.2
Gold (Au)[147]	$0.99m_0$	5.91×10^{22}	2080	18

As studied in (3.13), the plasma frequency is generally proportional to effective electron mass and carrier consideration [cf. Table 3.1]. Semiconductors have less plasma frequency in THz compared to metal ones. Also, the relaxation or the collision time is faster in metal. For example, an intrinsic silicon sample shows a plasma frequency oscillation ω_p at less than 0.01 THz for the free electron density on the order of 10^{10} cm^{-1} [4]. Fig. 3.13 shows the real (solid-line ε_1) and imaginary (dashed-line ε_2) parts of permittivity as functions of doping density and frequency for n-type silicon ($\varepsilon_\infty = 11.7$) calculated from (3.13).
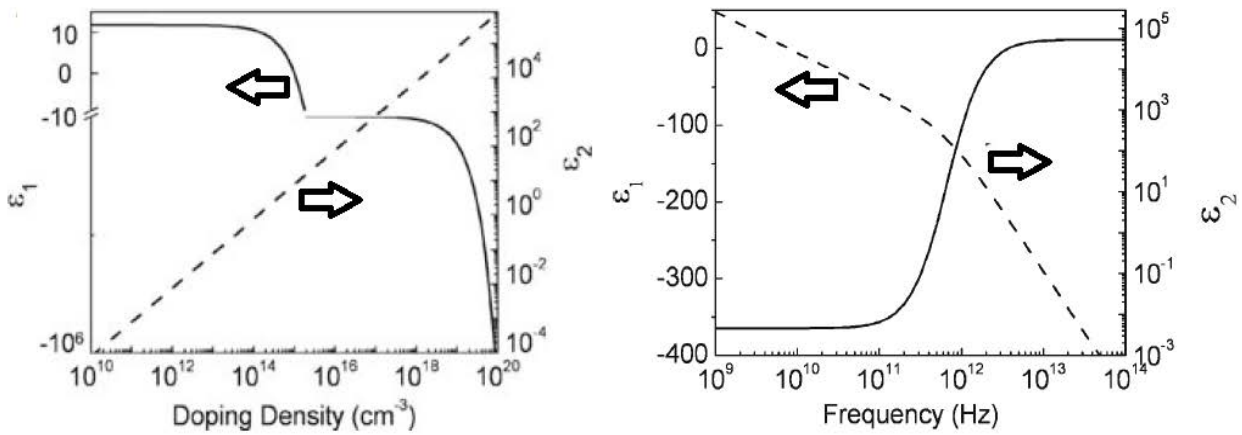
Figure 3.13: [Left] Complex permittivity for n-type silicon as a function of density at 1 THz, and [Right] Complex Permittivity for n-type silicon as a function of frequency at doping density of 10^{16} cm^{-3}[4].

In an ideal case in which $\varepsilon_\infty \approx 1$, the complex permittivity in (3.12) can be express in the real and imaginary parts as

$$\varepsilon_1 = 1 - \frac{\omega_p^2}{\omega^2 + \Gamma^2},$$
(3.14)

$$\varepsilon_2 = \frac{\omega_p^2 \Gamma}{\omega(\omega^2 + \Gamma^2)}.$$
(3.15)

Fig. 3.14 presents the general spectral dependence of the real and imaginary parts of complex permittivity for the semiconductors and semi-metals described by Drude model [148].
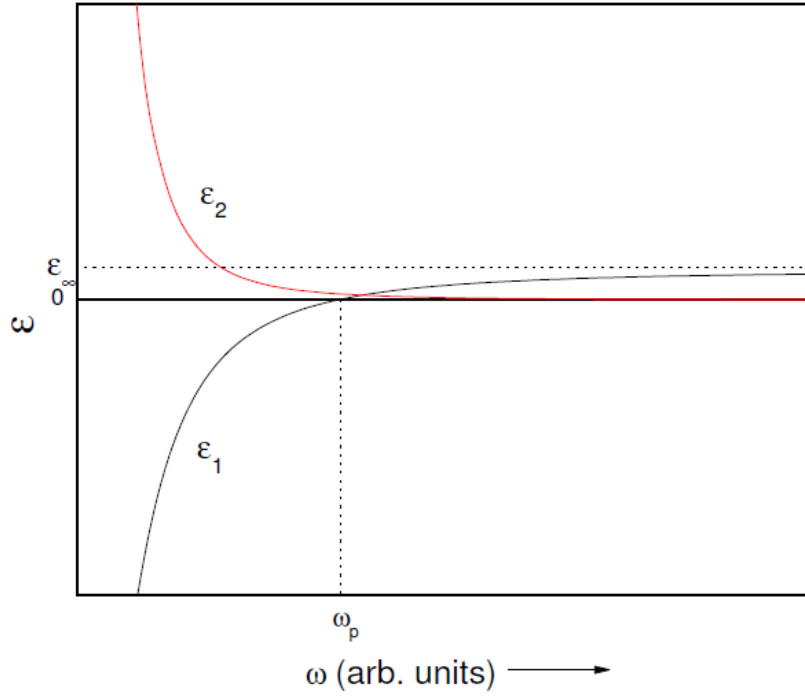
Figure 3.14: The real and imaginary parts of permittivity function in the Drude model [148].

The semiconductors carrier response (density, mobility, effective mass, etc.) is affected by THz wave's interaction. These responses allow characterizing the THz electrical conductivity, mainly for high speed semiconductor devices, as their operation frequencies is at several GHz reaches even to the sub-THz and THz gaps. Thus, the THz spectroscopy can be applied to evaluate the THz responses of semiconductor based materials or devices. The complex Drude and permittivity has the following relationship [4]:

$$\tilde{\varepsilon} = \varepsilon_1 + i\varepsilon_2 = \varepsilon_\infty + i\frac{\tilde{\sigma}}{\omega\varepsilon_0}. \tag{3.16}$$

Inserting (3.14) and (3.15) in (3.16) gives us the real and imaginary part of the complex conductivity explained as:

$$\sigma_{real} = \frac{\omega\varepsilon_2(\omega)}{4\pi}, \tag{3.17}$$

$$\sigma_{img} = \frac{\omega(1-\varepsilon_1(\omega))}{4\pi}, \tag{3.18}$$

According to the frequency range there are three different regions of the Drude responses at THz ranges [121]:

A) Hagen-Rubens regimes: where ω<<1/τ,

B) Relaxation regime: where 1/τ<< ω<< ω$_\rho$,

C) Transparent regime: where ω$_\rho$ <<ω,

Fig. 3.15 describes these three regions and the frequency-dependent relationship between the complex permittivity and conductivity of Drude response for a semiconductor sample [149] with the relaxation rate of $\Gamma = 1/\tau \approx 0.5$ THz and the plasma frequency $\omega_p \approx 30$ THz.
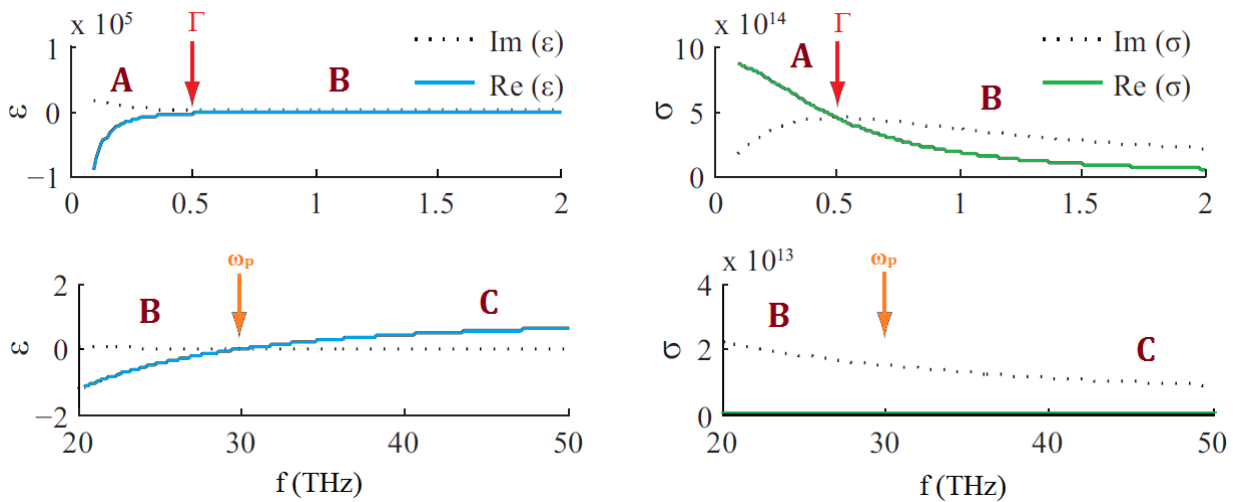
Figure 3.15: Different Drude behavior of the complex permittivity and conduct function in the regions A, B, and C at low and high THz frequencies [149].

The imaginary part of the permittivity of samples is in turn proportional to the real part of conductivity $(\sigma_{real} = 2\varepsilon_0 \omega n_s k_s = \omega\varepsilon_0\varepsilon_{imag})$. The sheet conductivity $(\sigma_s = \sigma_{real}d)$, where d is the thickness of film and ε_{imag} is the imaginary part of effective relative permittivity, can provide a direct evaluation of the metallic content in thin film as outcomes of complex THz transmission. The transmission is a frequency-dependent function of conductivity through the first interface with the vacuum impedance.

In a metallic behavior at the THz frequency ranges, a transition of several orders of magnitude in the value of sheet resistance $(=1/\sigma_s)$ happens which decreases with increasing of thickness. Fig. 3.16 is obtained by the noncontact THz measurement and the Drude electrical conductivity analysis for three different metals: Titanium (Ti), Nickel-chromium (NiCr), and Gold (Au). The large value of sheet resistance is similar to an electrically insulating dielectric material. At much thicker size, the sheet resistance decreases which is characteristic of perfect metallic behaviors [150].
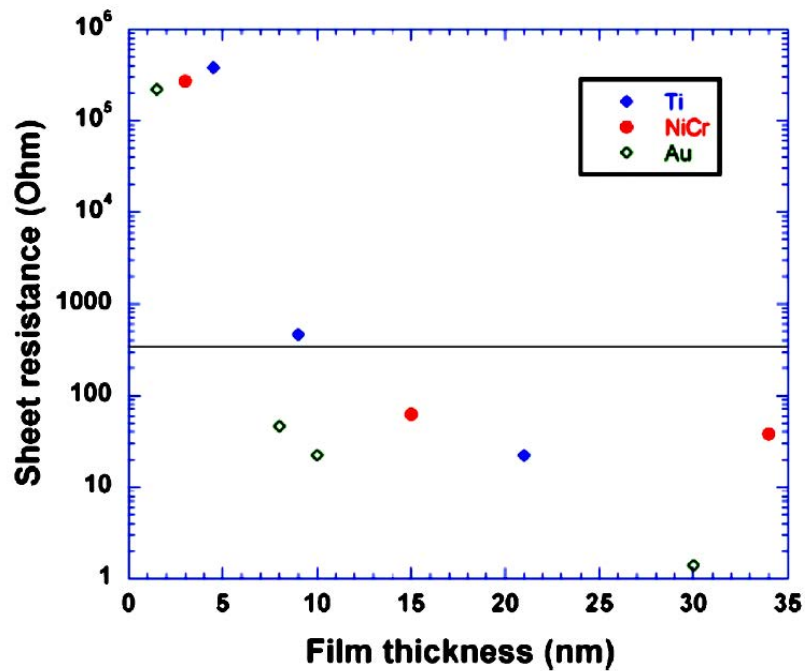
Figure 3.16: The sheet resistance of thin metal films with different thicknesses at THz regime. The solid line is the free space impedance (377 Ω) [150].

3.5.2 Drude-Smith THz Responses of Graphene

In an ideal case, the constant transmittance (*T*) of monolayer graphene, with a constant optical conductivity ($\sigma_0 = e^2 / 4\hbar$), across the visible range can be explained by:

$$T = (1 + \frac{\sigma_0}{2c\varepsilon_0}) \approx 1 - \pi\alpha , \qquad (3.19)$$

where *c* is the speed of light in vacuum, ε_0 is the permittivity of free space. The absorption is $\pi\alpha \approx 2.3\%$ ($\alpha = e^2 / 4\hbar\pi\varepsilon_0 c$). Fig. 3.17 shows the real part of the optical conductivity in graphene versus frequency in the THz scale. At low frequencies, thus low photon energies, the graphene optical conductivity is mainly determined by intraband transitions, while at high frequencies, the contribution of interband transitions becomes dominant. The dependence of optical conductivity with Fermi level, thus tunability, is high in the THz ranges and reduces to zero for the visible range.
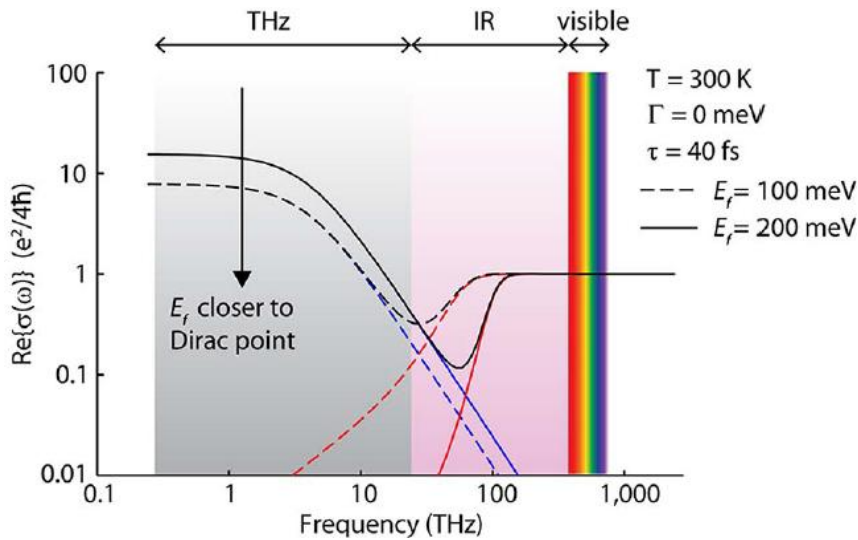
Figure 3.17: The contribution from total (black), the contribution from intraband transitions (blue), and the contribution from interband transitions (red) where in the THz range, the contribution from interband transitions to the optical conductivity becomes negligible [19].

For the Drude-like form of the semiconductors/metals in the THz regime, the general Drude expression considering the DC conductivity, σ_{dc}, can be explained as:

$$\tilde{\sigma} = \frac{\sigma_{dc}}{1-i\omega\tau} = \frac{ne^2\tau / m^*}{1-i\omega\tau} \, , \tag{3.20}$$

where e is the electron charge, m^* is the effective mass of charge carriers, and τ is the average collision time. The real and imaginary parts of complex THz Drude conductivity are explained, respectively, as

$$\sigma_{real} = \frac{\sigma_{dc}}{1+\omega^2\tau^2} = \frac{ne^2\tau / m^*}{1+\omega^2\tau^2} \, , \tag{3.21}$$

$$\sigma_{img} = \frac{\sigma_{dc}}{1+\omega^2\tau^2}\omega\tau = \frac{ne^2\tau / m^*}{1+\omega^2\tau^2}\omega\tau \, . \tag{3.22}$$

As earlier explained, compared to the visible range, the Fermi energy of graphene is usually much larger than the photon energy in the THz frequency. In other words, in the THz range, the absorption through intraband transitions dominates the one related to interband transitions [19], and thus intraband absorption influences mainly the THz conductivity. Therefore, from now on, because of the Pauli block, the interband excitation is usually negligible in the THz case; this study considers the intraband interaction when building the model for the THz frequency range.

A graphene film is a homogeneous conducting material. The plasma frequency and carrier density have a nonlinear dependency, because of the conical dispersion of the energy with momentum. As the conductivity of such materials with charge carrier localization is disorder [151, 152], the nano-scale conductivity needs to explain with a collision fraction of electron velocity.

The THz conductivity of graphene films has been fitted using the Drude model [153]. However, in this thesis, the Drude model is modified by Smith theory [154], so-called Drude-Smith (DS), to take into account non-random scattering of free carriers and also impurity of samples which allow ones to better adjust the experimental data with the modeled curves. This is not only for pristine graphene made by the CVD process but also for hybrid graphene thin films. The DS model enables to incorporate the phenomenon of carrier back-scattering into the Drude model. The DS was developed to express the

conductive behavior of disordered materials, which may not be perfectly illustrated by the Drude response. Such disorder materials (e.g., organic polymers [149], nano-crystalline system [155], silver nano-wires [139], actual metal materials like gold [156]) have a peak at non-zero of real conductivity with a negative imaginary conductivity at low THz frequencies.

The DS model is made under the statement in which an electron has a velocity memory (or persistence of velocity) from previous collisions in scattering event. This velocity can be described by the Poisson distribution [154]. If an electron experiences m collisions in the time interval (0, t), the distribution probability is explained as follows:

$$p_m(0,t) = \left(\frac{t}{\tau}\right)^m \frac{\exp\left(\frac{-t}{\tau}\right)}{m!}.$$
(3.23)

Taking into account this electron with a unit impulse of electric field applied at t=0, the current $j(t)$ decays exponentially to equilibrium with a relaxation time of τ and conductivity explained in (3.20). Smith explained this static distribution of the impulse current response function, with the fraction of carrier momentum c_m retained after m^{th} ($m > 0$) scattering collision, as follows:

$$j(t)/j(0) = \exp(\frac{-t}{\tau}) \left[1 + \sum_{m=1}^{\infty} \frac{c_m \left(\frac{t}{\tau}\right)^m}{m!} \right],$$
(3.24)

where $j(t)/j(0) = \exp(\frac{-t}{\tau})$ is the probability of zero collision or the exponential decay of initial current to its equilibrium value of zero. In the classical Drude model, a charge carrier does not have a velocity memory or a scattering event, and therefore $c_m = 0$. Fig. 3.18 shows the impulse current response function based on the probability of zero collision for the 1st collision, m=1. The Drude model shows an exponential decay behavior that the current falls uniformly to zero. In contrast, DS model has negative c-values, which the current falls to

negative rapidly before relaxing to zero. In this case, the charge carriers reverse their movement orientation because of the back-scattering.
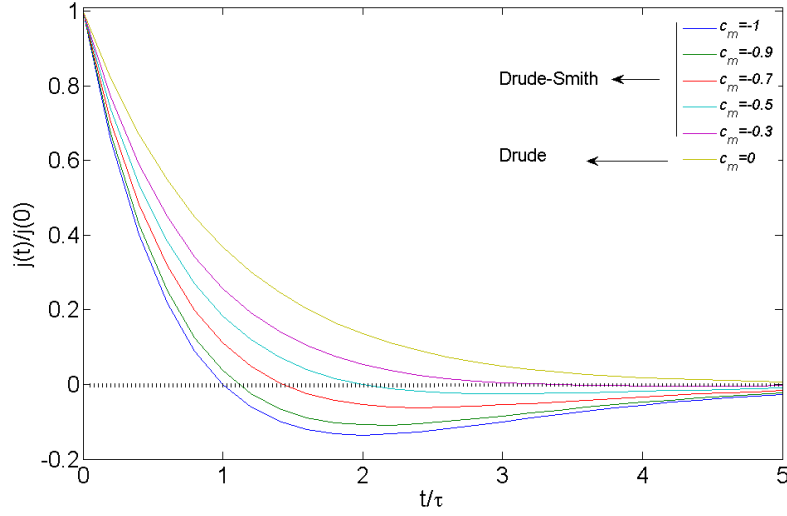
Figure 3.18: The impulse current response function based on the probability of zero collision (m=1).

The Fourier transformation of (3.24) gives the complex conductivity frequency-dependent, considering the memory velocity. In this model the non-random scattering of the free carriers is taken into account and the expression of the complex DS conductivity can be expressed by:

$$\tilde{\sigma} = \frac{\tilde{\sigma}_f}{d} = \frac{\sigma_{dc}}{1 - i\omega\tau}\left(1 + \sum_{m=1}^{\infty}\frac{c_m}{(1 - i\omega\tau)^m}\right), \tag{3.25}$$

where d is the thickness of the film. The coefficient c_m is the fraction of the electron original velocity that is retained after the mth collision. If we consider m=1, the real and imaginary parts of complex conductivity in (3.25) can be expressed, respectively, as

$$\sigma_{real} = \frac{\sigma_{dc}}{(1 + \omega^2\tau^2)^2}\left(1 + \omega^2\tau^2 + c(1 - \omega^2\tau^2)\right), \tag{3.26}$$

$$\sigma_{img} = \frac{\omega\tau\sigma_{dc}}{(1 + \omega^2\tau^2)^2}\left(1 + \omega^2\tau^2 + 2c\right), \tag{3.27}$$

If $c_m = 0$, the carrier momentum is totally randomized (Drude model). If $c_m = -1$, the free carrier is completely backscattered [147]. Fig. 3.19 shows the normalized real (solid lines) and imaginary (dashed lines) parts of a bulk gold conductivity considering *m=1,* where

value of c_1 =0 and -1≤c_1<0 demonstrate Drude and DS responses of the sample, respectively [156]. For -1≤c_1<0, a suppression of the complex conductivity takes place for low THz frequencies. In this case, the imaginary parts move to negative for -1≤c_1<-0.5. The negative imaginary is because of a capacitive response, steady with an instinctive behavior of disordered conductor materials. The DC conductivity is near zero around c_1=-1, showing an insulator-like response same as a Lorentz-oscillator shape.
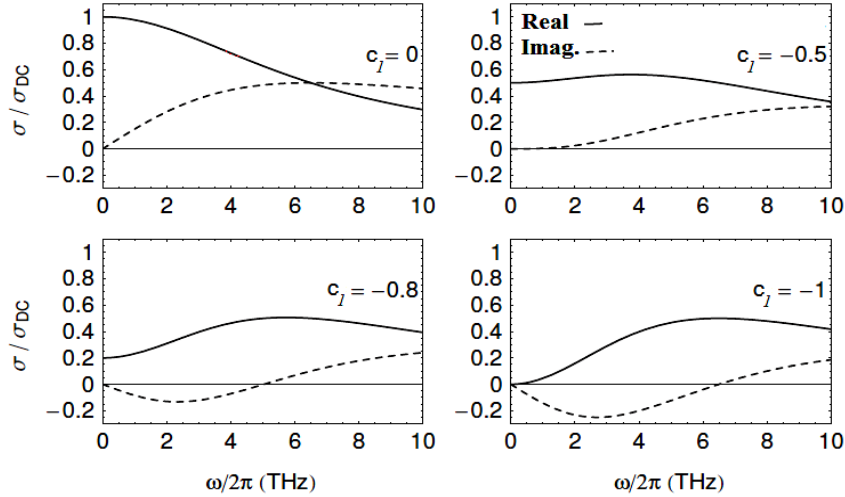
Figure 3.19: The normalized THz complex conductivity responses of bulk gold using the Drude (c_1 =0) and DS (-1≤c_1<0) models [156].

3.5.3 Drude-Lorentizan THz Responses of CNT

A CNT film contains metallic and semiconductor carbon nanotubes. The boundary condition of those conducting CNTs depend on how the graphene sheet are rolled into [157, 158]. To describe the relative permittivity of CNT thin film, a hybrid Drude-Lorentz (DL) model can be used in THz regime. In this model, a Drude component considers free electrons contributions and a Lorentz component is sum of oscillation of bound electrons. The relative permittivity of film is calculated taking the relative permittivity of the nanotubes constituent from DL model and fused-quartz as the host medium [37, 147].

To find the electron transport parameters, plasma frequency and conductance parameters, a precise extraction of THz frequency-dependent complex relative permittivity is demanded. We cannot really consider the films as bulk materials since it consists of

random nonaligned tubes. The 0.1-2 THz wavelength (photon energy of 0.4-8.2 meV) is larger than the tubes size. From the THz electromagnetic point-of-view, such a composite material can be treated as an effective medium From an electromagnetic point-of-view, such a film can be treated as an effective medium with a complex permittivity function $\tilde{\varepsilon}_{eff} = \varepsilon_{\infty} + i\tilde{\sigma} / \omega\varepsilon_0$ [159]. Fig. 3.20 shows the nanotubes with complex relative permittivity ε_{tube} deposited on the dielectric insulator with complex relative permittivity ε_i. A collection of aligned and nonaligned CNTs which are electrically polarizable nanoparticles, are transparent in the axial direction or they are opaque in the transverse plane of electromagnetic field in microwave and infrared frequency regimes [160, 161].
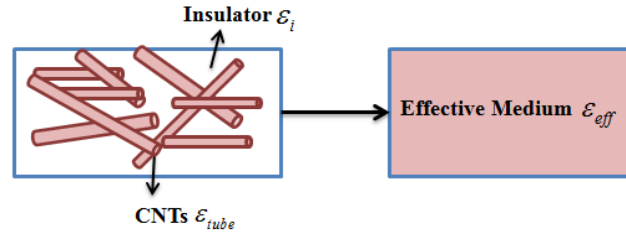
Figure 3.20: The effective medium model of CNTs deposited in an insulator.

The polarization-dependent THz time domain spectroscopy of aligned CNTs shows strong anisotropy at low and high frequencies [162]. In contrast, the tubes in this work are not aligned. The electrodynamic response of such composite material (e.g., carbon nanotubes and surrounded insulator) can be solved by Maxwell-Garnet (M-G) theory which can be assumed as one application of the general Clausis-Mossotti model [159]:

$$mz(\omega) = \frac{(\varepsilon_{eff}(\omega) - \varepsilon_i)\varepsilon_0}{N\varepsilon_{eff}(\omega) + (1 - N)\varepsilon_i}, \tag{3.28}$$

where ε_0 is the dielectric constant, $z(\omega)$ is the complex polarisability, g is geometrical factor, f is filling fraction. The relation between the terahertz electric field (E) at any point inside the carbon nanotubes and its polarization (P) can be written as

$$P = Ez(\omega) = \frac{(\varepsilon_{,m}(\omega) - \varepsilon_i)\varepsilon_0}{N\varepsilon_m(\omega) + (1 - N)\varepsilon_i} gE. \tag{3.29}$$

An isotropic behavior in the interaction with THz electromagnetic field can be observed and then the whole CNT sample responses with complex effective relative permittivity $\varepsilon_{eff} = \varepsilon_{real} + i\varepsilon_{imag}$ using M-G theory can be considered:

$$\varepsilon_{eff}(\omega) = \varepsilon_i \frac{[g + f(1-g)]\varepsilon_m(\omega) + [(1-g)(1-f)]\varepsilon_i}{g\varepsilon_m(\omega)(1-f) + (fg + 1 - g)\varepsilon_i}, \qquad (3.30)$$

where ε_m is the effective permittivity constant of CNTs network composed of tubes behaving as metals and semiconductors. Filling factor (f) represents the parts of unit volume filled by particles dispersed over the substrate. The resonance frequency moves to higher frequencies by decreasing the filling factor $(0 \le f \le 1)$. If the filling factor is near to 1, the CNTs behave like metals. Geometrical factor (g) depends on the form of the tubes and by shifting the geometrical factor $(0 \le g \le 1)$, the resonance frequency peak moves from zero to higher frequencies.

The imaginary part of effective permittivity is directly related to absorption of the CNT film that shows a Drude-like tail at low frequencies because of the small concentration of free carriers. The low frequency phonon modes, with major contribution to electrical conductivity and carrier scattering, and a broad resonance center of CNT films are mainly governed in the THz frequency regime [163]. The Drude model alone cannot be fitted at high frequencies to extract conductivity parameters [164, 165]. The high frequency-dependent complex relative permittivity of the vibrational modes for CNTs can be calculated by Lorentz model [166]. Hence, a combined Drude-Lorentz (DL) model can be used to study the excitations of the itinerant charge carriers, the excitations of localized carriers, and the interband transitions of the tubes at low and high THz frequencies. The classical Drude model is described for the metallic response of the conducting CNTs. The interband transitions normally evaluated by fitting optical parameters in Drude model, respond at the low and high frequencies [121]. The Lorentz model is to account for the bound electron contribution to the permittivity. Free electron scattering and vibration modes of bonded electrons are important key points as they contribute to the electrical losses. The resulting hybrid DL model is giving by:

$$\varepsilon_m(\omega) = \varepsilon_c - \frac{\omega_p^2}{\omega^2 + i\Gamma\omega} + \sum_j \frac{\omega_{p.j}^2}{(\omega_j^2 - \omega) - i\Gamma_j\omega} , \tag{3.31}$$

where ε_c is the frequency-independent relative permittivity of the CNTs network. ω_p is the plasma frequency, Γ is the damping rate, ω_j is the phonon frequency, Γ_j is the spectral width, and $\omega_{p.j}$ is the oscillator strength of the Lorentz oscillator j. Filling and geometrical factors are directly calculated using fitting DL model in THz measurement of complex effective relative permittivity. The Drude behavior around the plasma frequency has been already demonstrated in previous section in this chapter [cf. Fig. 3.14]. Fig. 3.21 shows a general picture of the Lorentz oscillation of complex permittivity (ω_0 is considered as a simple harmonic frequency) of a free-electron metal [148].
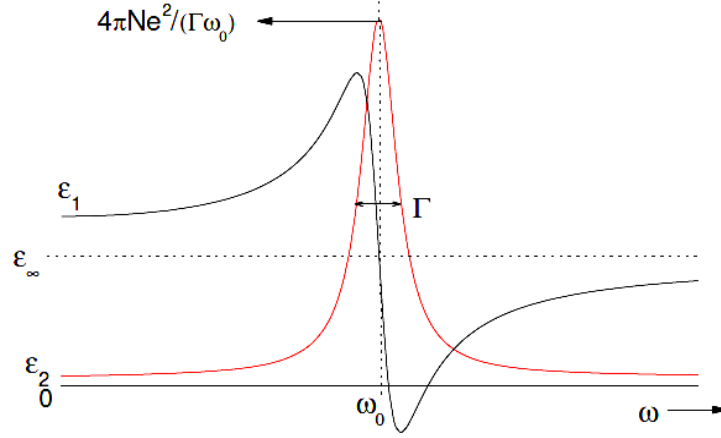
Figure 3.21: The real and imaginary parts of permittivity function in the Lorentz model.

The hybrid DL model describes an excellent correlation with the experimental measured complex permittivity of many metals like materials. Table 3.2 demonstrates the DL model parameters for Cu and Au as good metals with high values of plasma frequency. Mostly, there are several resonances like molecular vibration and interband electron transition.

Table 3.2: The DL model parameters of Cu and Au.

Metal	ε_∞	$\omega_p/2\pi$ (THz)	$\Gamma/2\pi$ (THz)	τ (fs)	$\omega_{p.j}/2\pi$ (THz)	$\omega_j/2\pi$ (THz)	$\Gamma_j/2\pi$ (THz)
Copper (Cu)[167, 168]	6.34	2195.4	16.7	9.53	674.34	2.62	151.04
Gold (Au) [167, 169]	7.7	2242.6	0.001	16E4	720.02	2.105	131.94

3.6 Conclusions

Reviews of the electron transition and energy band concept regarding the THz wave interaction with the nano-scale semiconductors in this research work have been presented. This has been followed by details regarding the Drude responses of semiconductors at THz regimes, which extract the optical and electrical parameters of the semiconductors and the metals from the permittivity complex functions as function of frequency. The frequency-dependent THz conductivity gave the details of plasma frequency and decay rate considering three regimes: i) Hagen-Rubens, ii) B) Relaxation, and iii) Transparent.

In this chapter the importance of electrical conductivity parameters have been investigated for the graphene and CNTs devices that are currently finding applications in the optoelectronics industry as they prove high mobility compared the classical nanoscale semiconductor components. These features yield us to apply the graphene-like sample for different optic and electronic devices to operate at the sub-THz and THz frequencies.

It has been demonstrated the electronic band engineering of graphene that has a vanishingly small gap at the Dirac point, where the Fermi level energy and charge carriers shows a linear dispersion in comparison with the parabolic dispersion of semiconductors. A Drude THz peak response has appeared because of intraband free carriers' absorption. The phenomenon associated at low THz frequencies (or low photon energies) of the graphene conductivity is mainly determined by intraband transitions. The dependence of optical conductivity with Fermi level, thus tunability, is high in the THz ranges and reduces to zero for the visible range. The optical and electrical parameters of the CNTs' samples have been studied using effective medium theory with combination of free electrons contributions and oscillation of bound electrons to calculate the relative permittivity of the nanotubes deposited on the top of substrate.

Chapter 4: Experimental THz Signal Measurements on the Electrical and Optical Characterization of CNTs and Graphene Thin Films

4.1 Introduction

Through this thesis the advantages of using noncontact and nondestructive THz-TDS technique to characterize the semiconductor and semimetallic CNTs and graphene-like materials have been studied. The preliminary analysis of THz signals was investigated for the thick samples in Chapter 2. This chapter describes the experimental results and measurement THz signals of the CNTs and graphene samples explained in Chapter 3 and Appendices C-D. This chapter demonstrates the THz transmission and reflection THz-TDS set-up and also the measured temporal signals of the samples mentioned in Appendix D. The steps of THz measurements are followed by the experimental signals in both time and frequency domains, which here have been divided into three different sections.

The first set of results is based on the THz transmission signal measurements for the micrometrics SWCNT and MWCNT samples. The second set of results is from the THz transmission signals of the nanometrics MWCNT and the graphene samples. Finally, and in accordance with the objectives laid out for the transmission and reflection experimental schemes, the third measurement includes the THz transmission and the THz reflection signals of nanometrics MWCNT, graphene and hybrid silver nano-wire graphene samples. This chapter will also show the air and the reference substrate signals, where all CNT and graphene samples deposited over the transparent quartz substrates with thicknesses of several hundred and a few thousand micrometers.

The final THz signal analysis in the third measurement will emphasize on the advantages and disadvantages of reflection measurements of such high absorber and conductance samples. Using these THz-TDS measurements, all amplitude and phase information can be extracted directly from the spectra. The principle of getting the unwrapped phase from the measurement signal will be presented. They will need to be corrected and being start from zero frequencies as there is not enough SNR at the low THz frequencies.

4.2   Samples Design to Carry out THz Measurements

To design and fabricate the carbon nanostructure samples before carrying out the THz measurements, this work started to study the fundamentals of physics beyond the deposition and geometrics of the samples. The first and important key element is the transparency of substrate while THz wave illuminate sample (mainly in transmission mode). Table B.3 in Appendix B demonstrates the different studies of THz characterization for semiconductor samples at 1 THz. As the lowest attenuation and the minimum influence of the electrical conductivity can be found in the quartz bar, the objective of the experimental presented in this thesis has been focused on deposition of the thin films on top of such a bar with a thickness of order of μm and mm.

The second point is the size of the thin films. To get rid of the diffraction effect, the samples (both thin film and substrate) have been fabricated with a size larger than the THz beam (<1 mm). It is important to note that all THz measurements have been carried out under the assumption of thin films homogeneity in surface. Fig. 4.1 presents the general schematic of a stack sample in the three-layer optical system that THz wave transmitted/ reflected to/ from.

To fulfill the objective of this study, the THz-TDS was measured for various graphene and carbon nanostructure samples with different specifications, fabrication process and also geometries, provided by the external partners after characterizations at Universidad Carlos III de Madrid within the MITEPHO Project [cf. Appendix E]. Appendix D presents the samples in the details of fabrication process and physical characterizations (Raman spectroscopy, atomic and microscopic images, etc.).
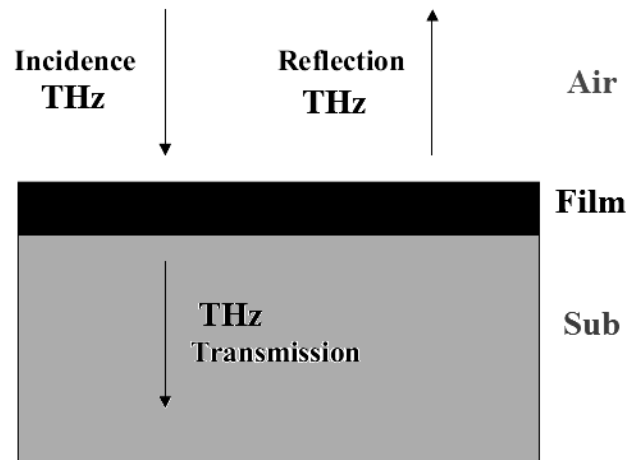
Figure 4.1: The general schematic of the three-layer (air, film and transparent substrate) optical system for the transmission and reflection THz measurements.

4.3   THz-TDS Signal Measurements

4.3.1   Transmission Mode

As earlier explained in Chapter 2, the THz-TDS experimental scheme has been designed based on the femtosecond (fs) pulses of infrared radiation (from a mode-locked Ti: Sapphire laser with a central wavelength of 800nm) to generate and detect single-cycle pulses of radiation. The optoelectronic THz-TDS configuration is consisted of a beam splitter, optical time delay stage, and THz antennae. The generated fs laser beam is split into two optical pulses, pumped and probe. The pumped and probe beams respectively go to the THz emitter and THz receiver antennae using lenses. The two optical paths from beam splitter to emitter and receiver have the same length, as the receiver antenna is gated synchronously with an excitation of the transmitter. Fig. 4.2 (a) shows a general schematic of THz-TDS in the transmission mode.

4.3.2   Reflection Mode

One challenge is the thickness or shape of substrates used in comparison with one another. Uncertainty values between the reference substrates and the substrate covered with film

can influence phase and amplitude of transmitted THz signals, which makes a variation in the extracted complex reflective index of thin films. To overcome this issue, the temporal THz beam reflected by the samples has been also measured at a normal incidence. Fig. 4.2 (b) shows a picture of THz-TDS set up in the reflection mode.

The main drawbacks of reflection THz-TDS mode is associated with the error caused by an even small misalignment of sample (ΔL), positing of reference mirror and the beam shape which is not completely parallel of the sample under test (angle of incidence not exactly equal to 0°). These uncertainties will effect on the achieved optical and electrical properties of materials. The error of achieved standard deviation can be minimized in experimental by performing several measurements of sample in THz-TDS. In this study, for each sample, multiple numbers of reflection measurements are performed and good repeatability of the measured spectra is observed. The measurement is repeated several times to find the average amplitude and phase of THz waveforms.
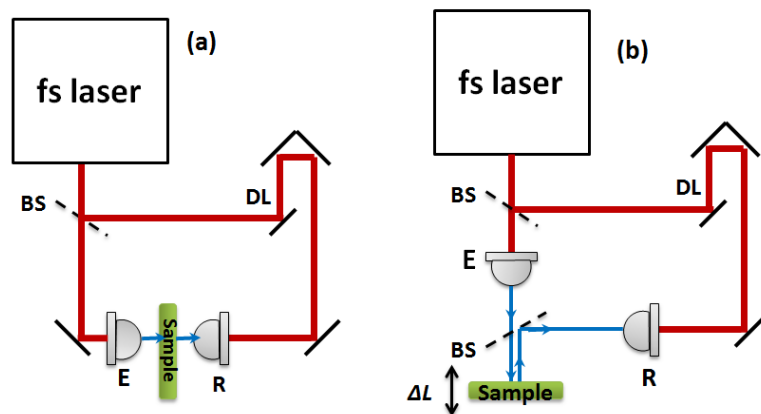
Figure 4.2: (a) The transmission, and (b) the reflection THz-TDS set up in normal incidence configuration (fs= femtosecond, DL=delay line, BS= beam splitter, E=THz Emitter, and R=THz receiver). The red and blue lines are optic and THz signals, respectively.

4.3.3 Sample Holders and Sample Location

After setting up the sample on a holder [cf. Fig. 4.3] with a hole of 2~5 mm, the sample holder is located exactly between the emitter and receiver THz antennae. The parabolic mirrors with focal length f are used to guide the THz pulse with output power on the range of mW from the emitter, through the sample onto the detector. The distance between two

parabolic mirrors is *2f*. The sample exactly is located on the focal point of these mirrors with distance of *f* of each mirror which makes the THz emission focus through the sample before being collimated again. Fig 4.4 presents the configuration of mirrors and PCA antennae inside the box of vacuum chamber for both transmission and reflections modes.

Figure 4.3: [Left] the sample holder with whole of 5 mm. [Right] the sample holder aligning and setting up in THz-TDS set up.
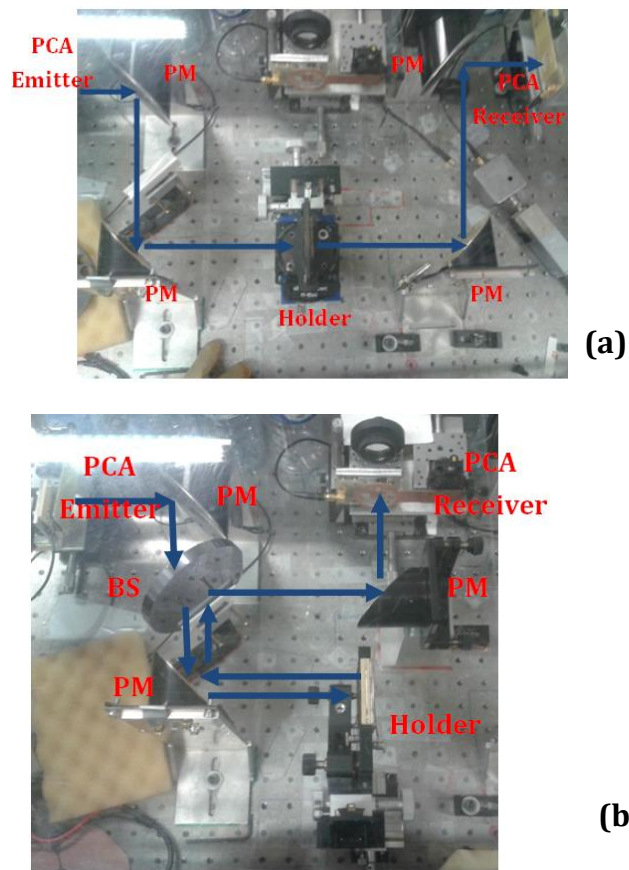
Figure 4.4: (a) The transmission, and (b) the reflection parabolic mirrors and PCA antennae configurations at a normal incidence of THz beam (PM= parabolic mirrors, BS= beam splitter). The blue arrows shows THz signal path. The configurations are placed inside the box of vacuum chamber.

4.3.4 THz Measurements Steps

There are generally six main steps in the THz-TDS measurements:

1) Switching on the pulsed laser (checking the power of the fs laser, whether it is pulsing or not),

2) Aligning the optical and electrical components (mainly mirrors, holders and antenna positions) to get suitable forms of the time domain signal and the spectrum in frequency domain,

3) Preparing the vacuum chamber (to minimize the water line absorption influences in the measured temporal signals and their THz spectra),

4) Measuring the THz air space signal (without putting any sample between emitter and receiver) as the 1st reference signal,

5) Measuring the THz signal of substrate as the 2nd reference,

6) Measuring the THz signal of the film deposited on top of substrate.

In this study, all transmission and reflection measurements for the samples have been performed at room temperature. The samples are located at the waist of the THz beam: at any frequency of the available THz signal, the Rayleigh length of the beam is much larger than the bare or covered substrate, therefore the sample can be considered as illuminated at normal incidence by a plane wave. THz pulses are measured in the time-domain by varying the time-delay between the THz and the optical pulse by an optical delay stage.

4.3.5 Control Waterlines Absorption

The water vapor shows strong absorption lines in the THz frequency bands. The water content and relative humidity of the environment would therefore significantly influences on the THz frequency spectra at certain frequencies. All experimental THz measurements have been performed inside a dry vacuum box to reduce the water absorptions to minimum values [cf. Fig. 4.5]. The relative humidity percentage was checked concerning a

sensor voltage. During this study, it was reduced to a min 9% and a max 13% during all presented temporal signal measurements for all samples.

Figure 4.5: [Left] the THz-TDS set up in vacuum chamber. [Right] The sensor voltage to control relative humidity % in the set up (it has been optimized in 9~13 % corresponding 1~2 V).

4.4   THz-TDS transmission and Reflection Measurement of Samples

In this section the THz signals in time and frequency domains will be demonstrated based on the availability of spectroscopy equipments to carry out the transmission and reflection measurements at different schedule and objectives of the project. Here the presented experimental results have been divided into three different subsections.

4.4.1   THz Transmission Signals of Micrometrics SWCNT and MWCNT Samples

The SWCNT and MWCNT thin films with thickness 1.09 μm and 1.2 μm have been fabricated on face of the fused-quartz substrates [cf. Appendix D.1]. The tubes randomly and horizontally distributed on top of the bar substrate.

When the thin films, made from different types of carbon nanotubes, are exposed to electromagnetic radiation in the range of 0.1–2THz, the optical and electrical properties of carbon nanostructures are revealed as a response [41, 48]. The samples are located at the waist of the THz beam that can be considered as an almost perfect Gaussian beam. The beam waist is very much smaller than the sample surface 2.5×2.5 cm^2 and no diaphragm is

needed to resize the THz beam to the sample size. Moreover, the Rayleigh length of the THz beam is much longer than the sample thickness throughout the whole THz experimental frequency range [51]. Therefore, the samples are illuminated by plane THz waves. The waveforms are recorded over a 35-ps time-window, leading to a spectral resolution of 28 GHz. The measurements of temporal waveforms are performed as shown in Fig. 4.6. The first measurement recorded is the reference signal without sample in between THz emitter and detector antennas. The second measurement is recorded with the reference quartz substrate in the THz-TDS set-up, and the third with the quartz substrate covered by the CNT film. For each sample the measurement is repeated four times to find the average amplitude of each THz waveform. The Fourier transform is applied to map the THz spectra [cf. Fig. 4.7].
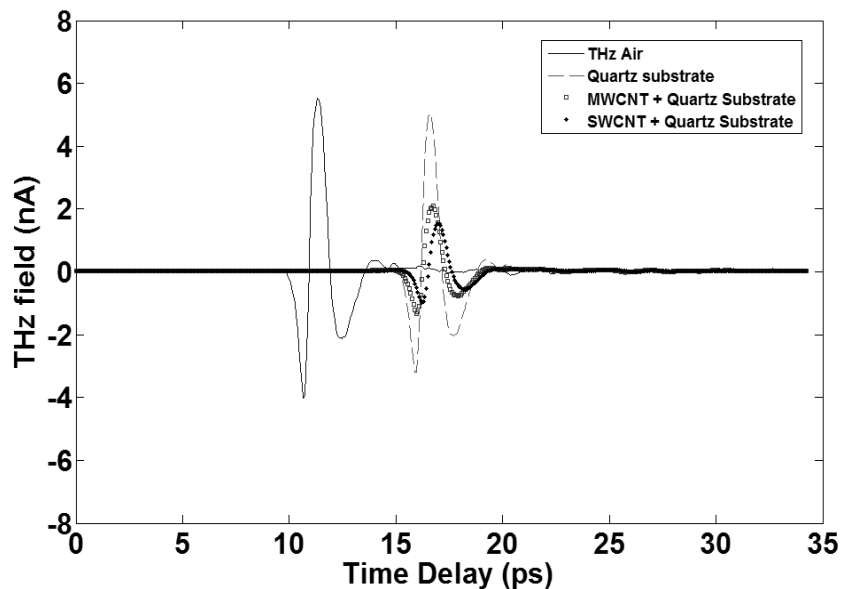
Figure 4.6: The THz temporal signals of the free space, the reference quartz substrate, and the MWCNT and the SWCNT samples using THz-TDS transmission mode.
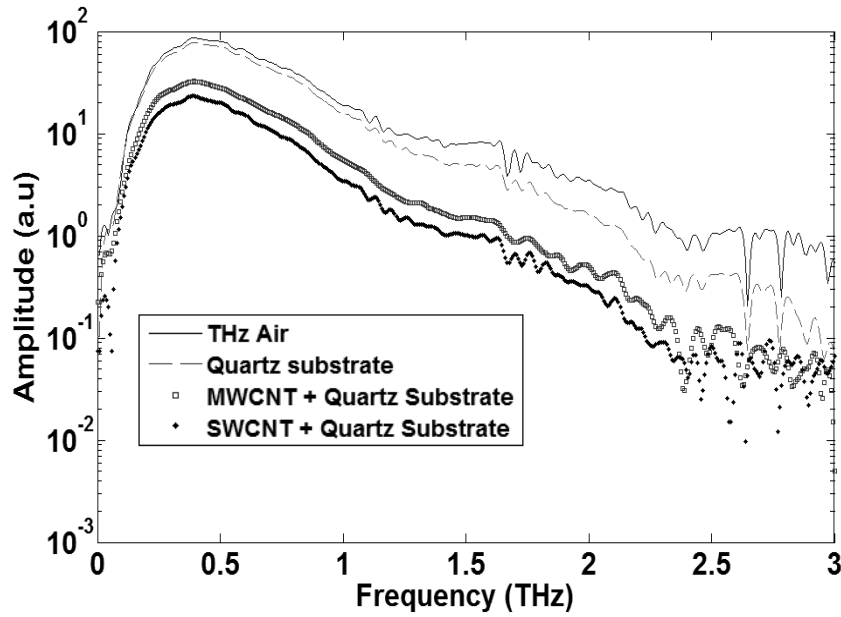
Figure 4.7: The THz spectrum for the free space, the reference quartz substrate, and the MWCNT and the SWCNT samples with time window of 30ps using THz-TDS transmission mode.

Fig. 4.8 presents the transmitted (sample/reference) THz module of the different studied samples as determined from the experimental data. The SWCNT has a lower transparency rather the MWCNT as expected in Figs. 4.6 and 4.7. The transmission curves show that with increasing the frequency, the transparency of the samples decrease due to absorption phenomena.
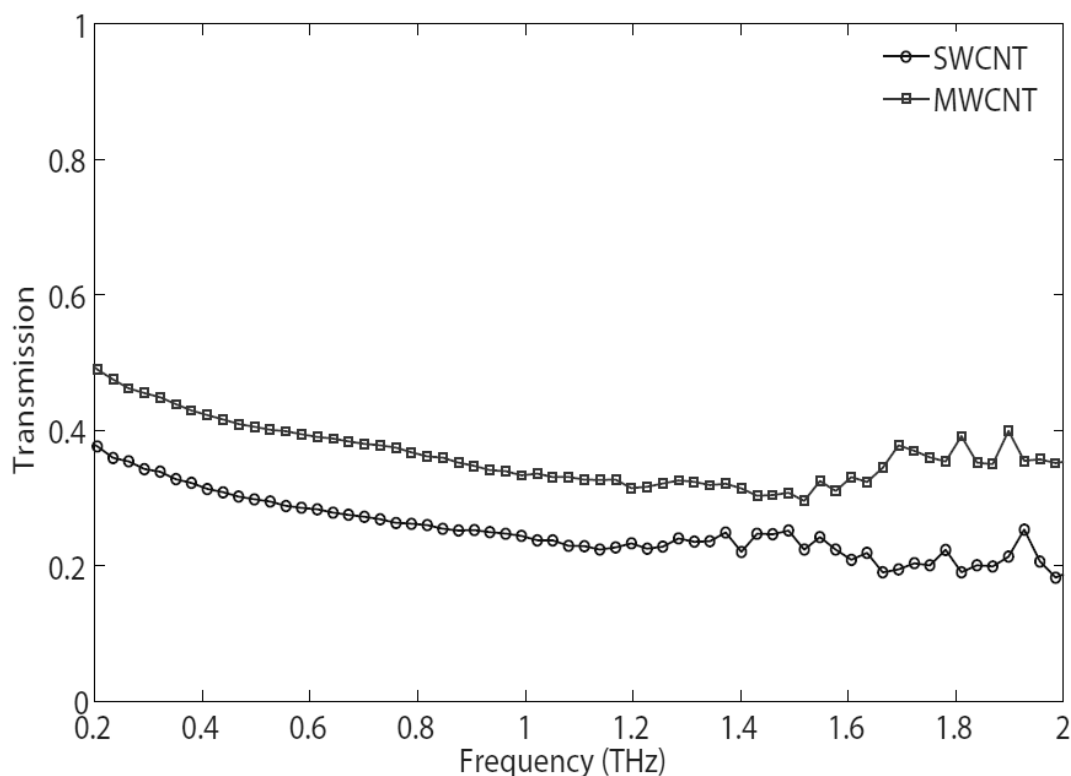
Figure 4.8: The THz pulses transmitted (sample/reference) through the SWCNT and MWCNT samples over frequency range of 0.2-2THz.

Furthermore, the vertically aligned MWCNT arrays deposited on a quartz with tube site density of 10^{10} -10^{11} nanotubes/cm^2 (distance between two adjacent CNTs ∼ 200-300 nm) have been tried to measure in this thesis.

As with increasing length of tubes in the CNTs structure, the conductivity increases [170] and also due to the high consideration and the vertical deposition of MWCNTs, the total THz waves were absorbed. Because of which, the THz signals could not pass through the samples. Then there was no any signal at the detector. Due to these reasons, there was no further characterization of such array samples.

4.4.2   THz Transmission Signals of Nanometrics MWCNT and Graphene Samples

In this experiment, two different graphene-like samples have been tested. The MWCNT film thickness of two samples, namely MWCNT1 and MWCNT2 [cf. Figs. 4.9 (a) and (b)], is 162 and 193 nm respectively [cf. Appendix D.2]. The films have a diameter of 18 mm, while the quartz substrate is a 25×25 mm² square. The monolayer graphene (MG) film thickness of our two samples, namely MG1 and MG2 [cf. Figs. 4.9 (c) and (d)], is a one-atom thick layer (~0.34 nm) deposit on over quartz substrates (15×15×0.5 mm³) [cf. Appendix D.3].
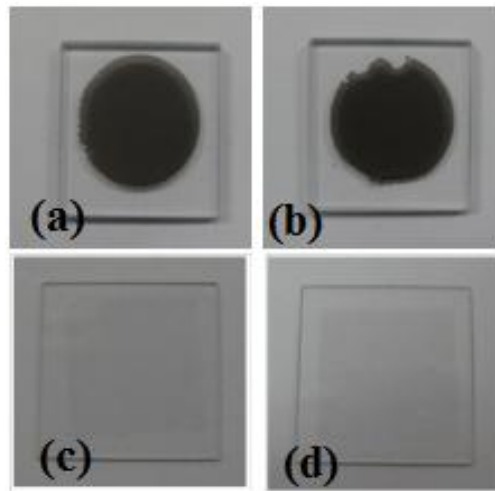
Figure 4.9: (a-b) The MWCNT films with thicknesses of 162 and 193. (c-d) The MG film with a one-atom thick layer (0.34nm) deposited over the quartz substrate.

The waveforms are recorded over a 35-ps time window, leading to a spectral resolution of 28 GHz. Each waveform has been recorded several times, in order to check the experimental reproducibility and to minimize the noise by averaging the records. The THz spectrum of the averaged waveforms is obtained through a numerical Fourier transform for the MWCNT [cf. Fig. 4.10 (a)] and the MG [cf. Fig. 4.10 (b)] samples over frequency range of 0.1-2 THz. To simplify the extraction of the film parameters, an appropriate time-windowing of the substrate and sample waveforms rejects the echoes resulting from rebounds in the substrate [42, 50, 52].
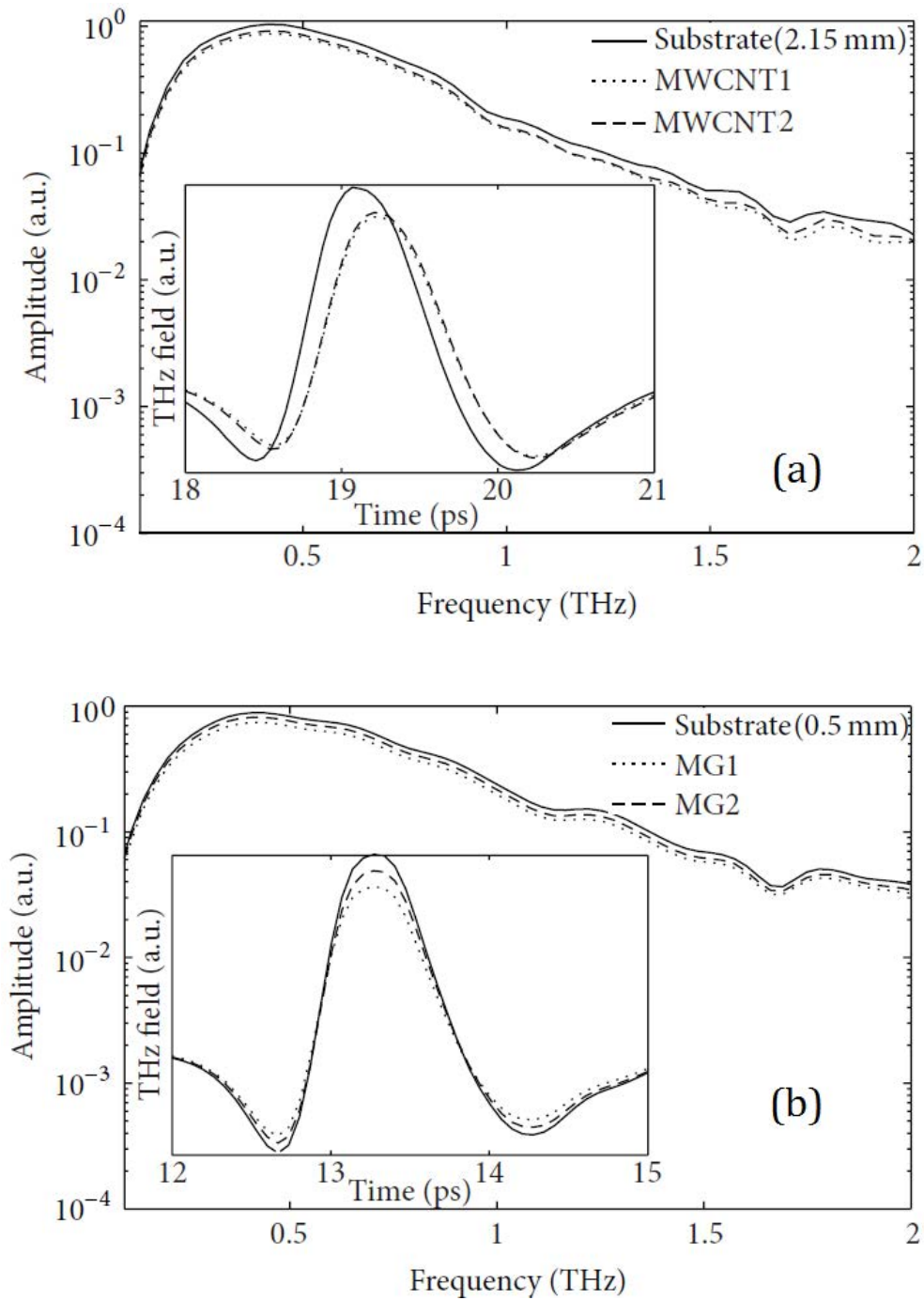
Figure 4.10: The THz spectra obtained for (a) the MWCNT samples and (b) the MG samples. Insets show the corresponding temporal signal achieved.

Fig. 4.11 presents the transmission spectra of the different studied samples as determined from the experimental data. All samples show almost a steady state transmission line up to

1.5 THz. However, afterwards there are fluctuations due to the insufficient THz power. MG2 and MWCNT2 are respectively the most (~94%) and least (~81%) transparent samples.
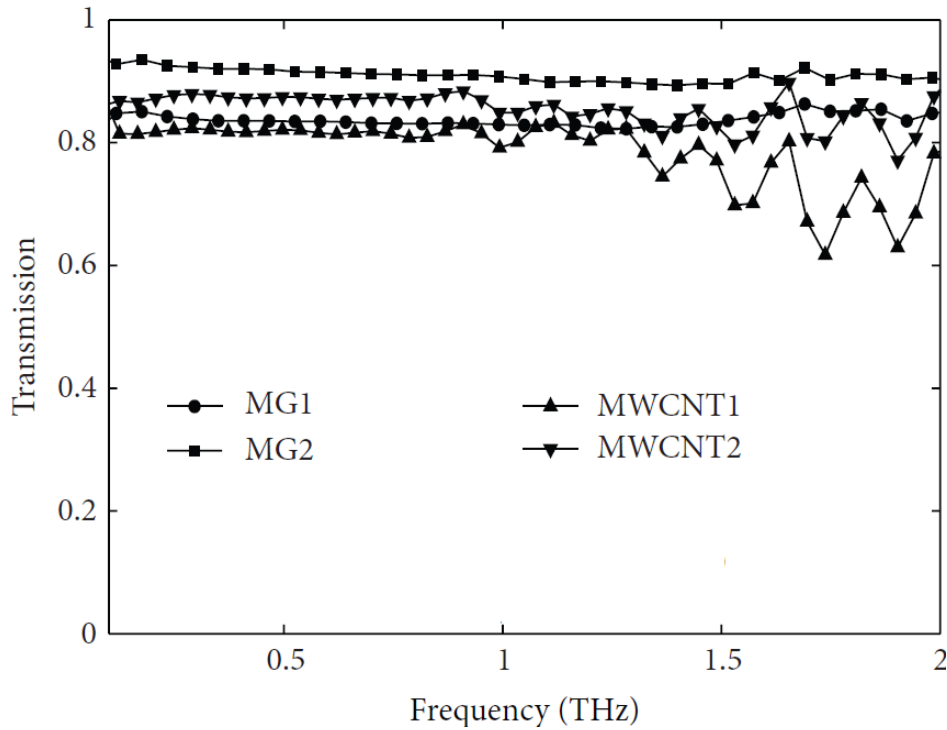
Figure 4.11: The THz pulses transmitted (sample/reference) through the MWCNT and MG samples over the frequency range of 0.2-2THz.

4.4.3 THz Transmission and Reflection Signals of Nanometrics MWCNT, GRP and AgNW-GRP Samples

In this experiment, both transmission and reflection THz measurements have been carried out for three different samples:

i) The MWCNTs film (193nm thick) was transferred onto fused quartz substrates with thickness of 2.15mm [cf. Appendix D.2].

ii) The mono-layer (~0.34 nm) pristine graphene (GRP) was grown CVD transferred onto the fused quartz substrate with thickness of 0.5 mm [cf. Appendix D.5].

iii) The silver nanowire-graphene hybrid (AgNW-GRP) film was deposited over fused-quartz with thickness of 0.5mm using CVD process. The average thickness of the AgNW-

GRP hybrid film was measured by atomic force microscopy (AFM) technique [cf. Appendix D.5].

To measure the complex THz transmitted function (amplitude and phase), as carried out for the former samples, three steps were performed for each sample: one without sample, one with a bare substrate, and finally one with thin film deposited over substrate. The waveforms were recorded over a 20-ps time-window, leading to a spectral resolution of 50 GHz. Each waveform was recorded several times, in order to check the experimental reproducibility and to minimize the noise by averaging the records. Fig. 4.12 shows the measured temporal THz signals. E_{Air} is the air-incident beam. The subscripts F and S are for film and reference substrate.
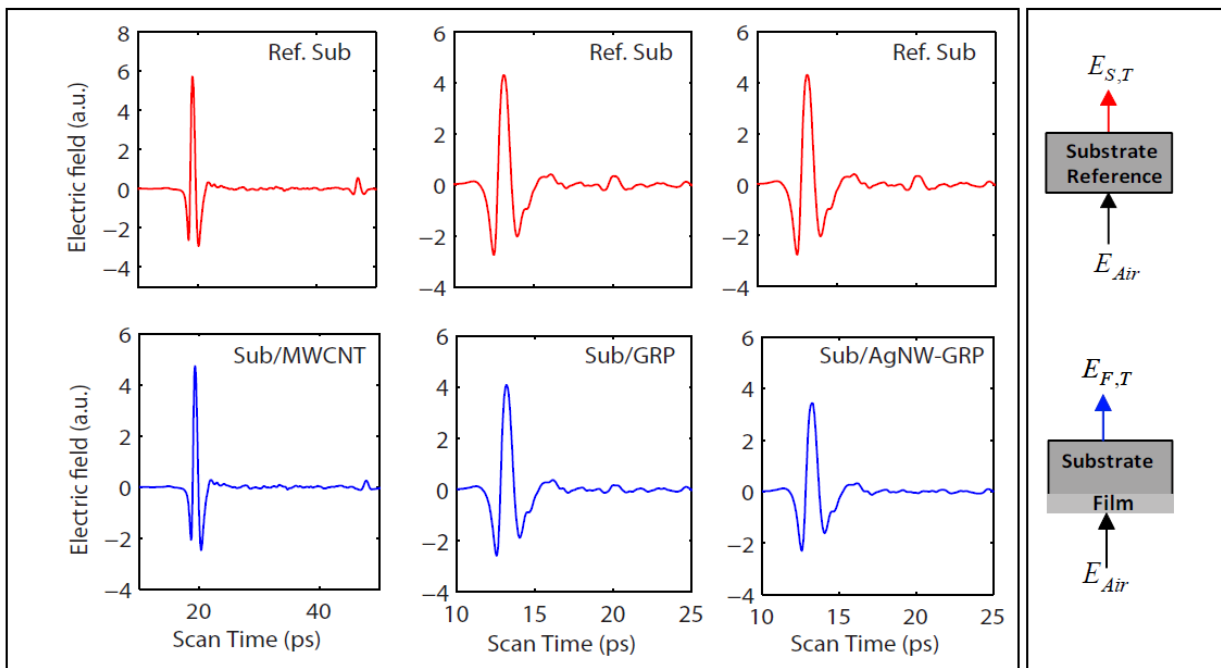
Figure 4.12: [Left] The performed THz-TDS transmission measurements to obtain the temporal signals for three MWCNT, GRP and AgNW-GRP sample and their reference substrates. [Right] The schematic of measurements for the reference substrate and substrate covered with nanostructured films.

In case of the reference substrate in Fig. 4.12, since the MWCNT's substrate is thicker (2.15 mm), the second echo (~50 ps) is much far from the main echo compared to the reference substrates of GRP and AgNW-GRP ones (~20 ps) with thickness of 0.5 mm. The amplitude of second echoes of the samples decrease (MWCNT at ~50 ps) or disappears (GRP and

AgNW-GRP at~20 ps) compared to the uncoated reference substrates, due to antireflection coating of high conductance thin films [171]. Figs. 4.13-14 demonstrate the smooth and normalized spectra of the MWCNT, the GRP and the AgNW GRP samples with their air and substrate references signals are obtained using the Fourier transform method discussed in Chapter 2. The transmission spectra of three different studied samples obtained from the differential complex experimental data ($T_{sample}/T_{ref-substrate}$). Fig. 4.15 shows the transmission module of all samples: the GRP (~ 90 %), the AgNW-GRP (~ 76 %), and the MWCNT (~85 %) films. The spectra show an almost constant transmission value up to 1.5 THz. For higher frequencies, there are some fluctuations due to the insufficient THz power.
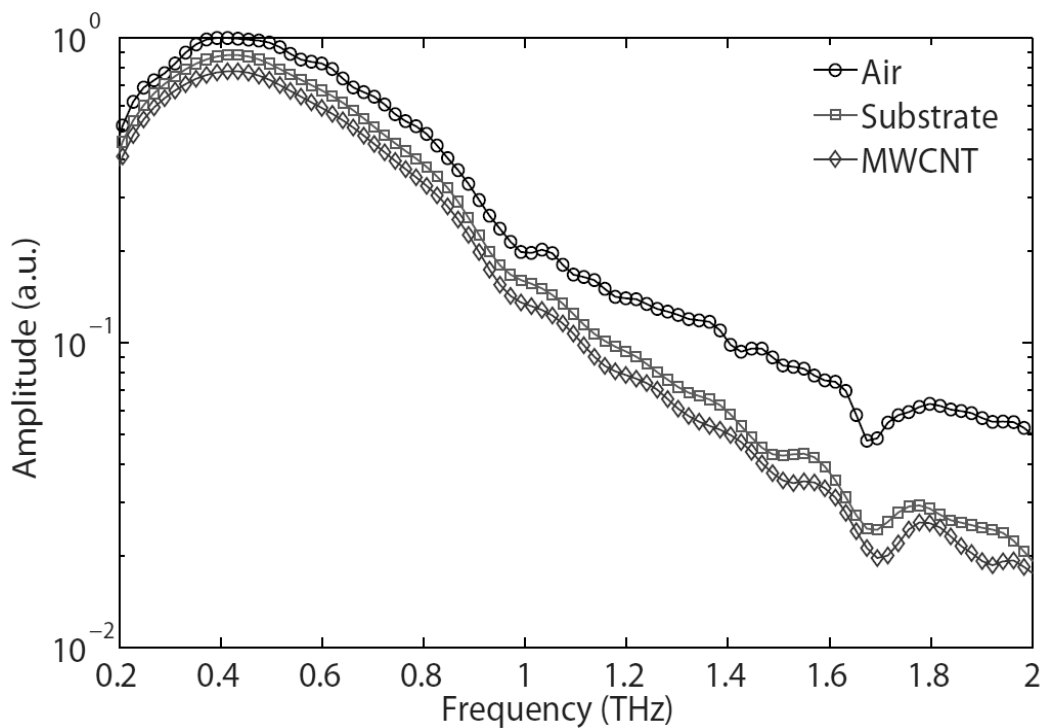
Figure 4.13: The THz transmission spectra of air reference, substrate reference and MWCNT sample.
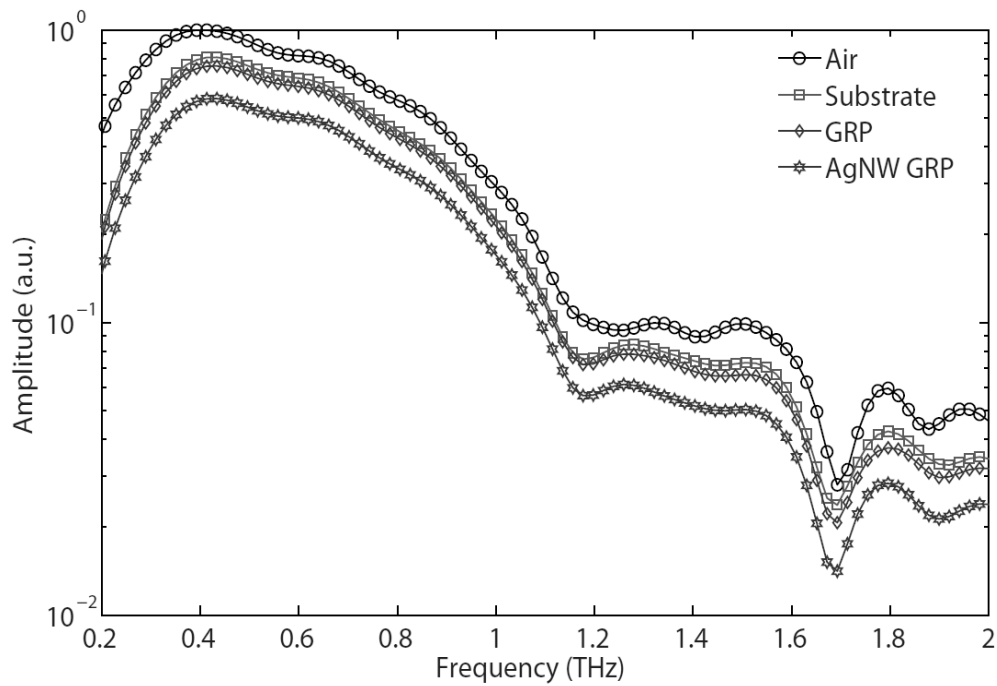
Figure 4.14: The THz transmission spectra of air reference, substrate reference, GRP sample, and AgNW GRP sample.
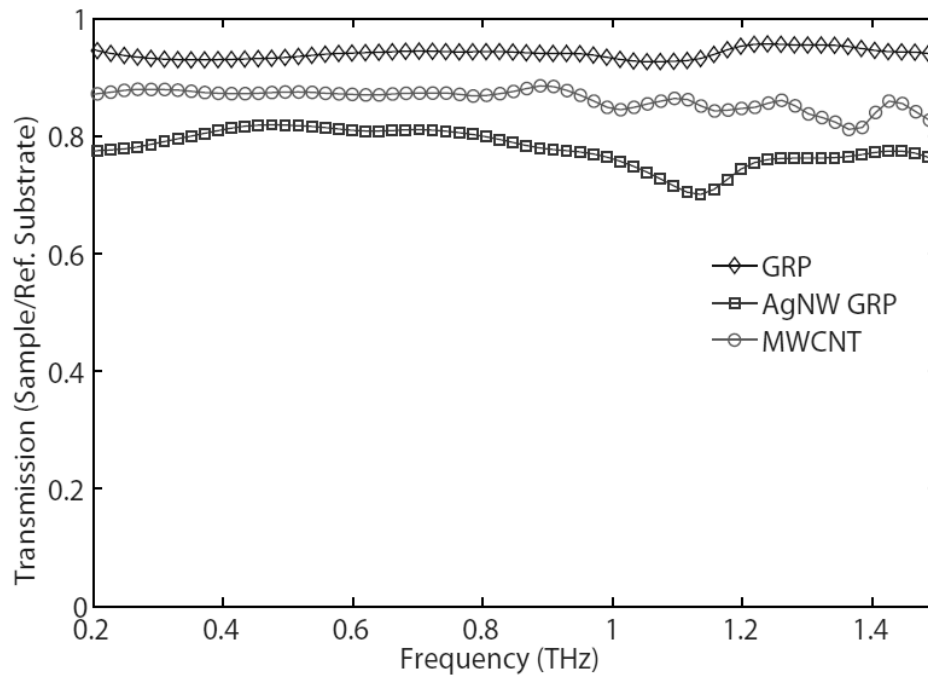
Figure 4.15: The THz transmittance (sample/reference) of MWCNT, GRP, and AgNW GRP samples over frequency range of 0.2-1.5THz.

The temporal THz beam reflected by the samples at a normal incidence was also measured. As shown in Fig. 4.16, the signal reflected $E_{S,R}$ by the bare side of the sample measured at the first step, and then the covered side of the sample. The sample up-side-down has been put and the reflected signal $E_{F,R}$ has been recorded. In all samples, only the first reflected pulse or main echo was saved [43].

The main drawbacks of reflection THz-TDS is associated with the error caused by small misalignments (ΔL) of the sample, positioning of the reference mirror and the beam shape (which may not be completely parallel to the sample under test i.e., angle of incidence not equal to 0°). These uncertainties modify the achieved optical properties (refractive index and absorption) and so-achieved electrical conductivity of materials. In this study, for each sample, the measurement was repeated several times to find the average amplitude and phase of THz waveforms. In Fig. 4.16, it can be seen that there is a bit variation in size between the reference substrate of MWCNT (dash green lines) and bare side of the sample (red line) which is not appeared for the GRP and the AgNW-GRP samples.
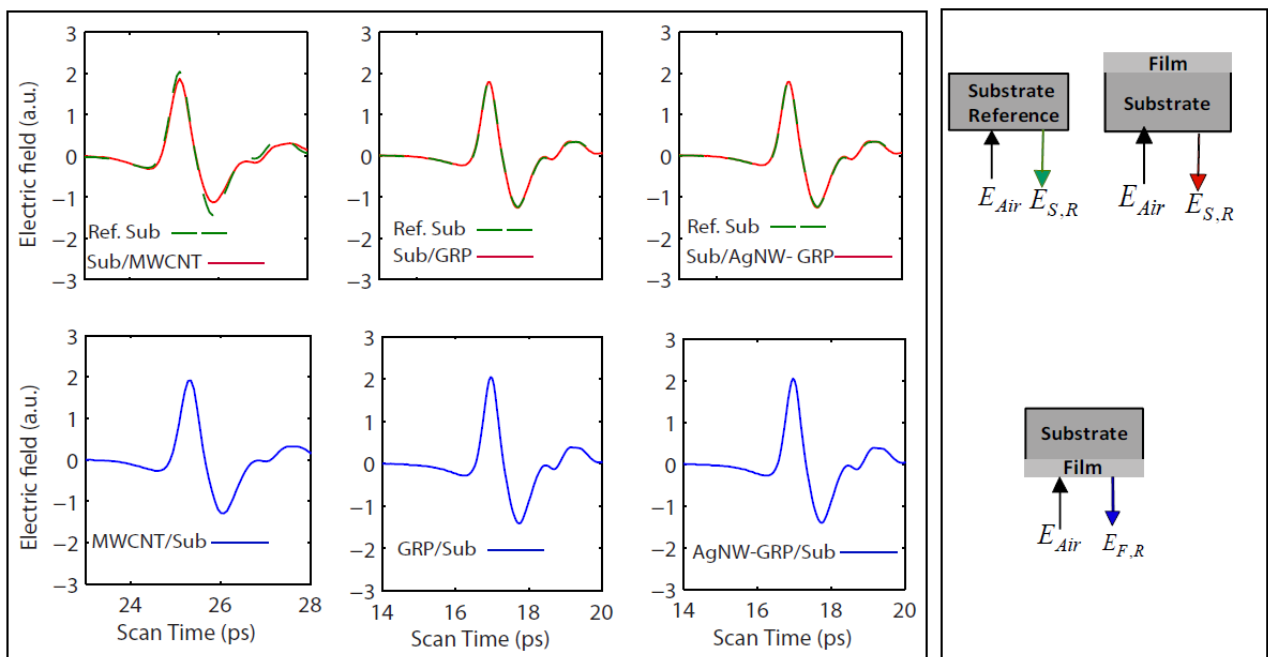
Figure 4.16: [Left] The performed THz-TDS reflection measurements to obtain the temporal signals for three MWCNT, GRP and AgNW-GRP samples and their reference substrates. [Right] The schematic of measurements for the reference substrate and substrate covered with nanostructured films.

Figs. 4.17-19 show the normalized spectra of MWCNT, GRP and AgNW-GRP samples with their air and substrate references signals obtained from the Fourier transform method explained in Chapter 2. The results show the back-side of sample (substrate not covered with the film) has very similar spectra as the reference substrate give. A bit difference can be explained because of uncertainty values (lack of sameness or uniformity) reflected from the surface of the bar.

The reflection spectra of three different samples are calculated from the differential complex experimental data ($R_{sample-film-side}/R_{ref-substrate}$ or $R_{sample-film-side}/R_{sample-substrate-side}$). Fig. 4.20 shows the reflection module of all samples: the GRP (~ 1.2), the AgNW-GRP (~ 1.65), and the MWCNT (~ 1.3) films. The spectra show fluctuated values due to the insufficient THz power and also the weaker sensitivity of extraction from the reflection phase and amplitude data because of imperfect alignment of the samples.
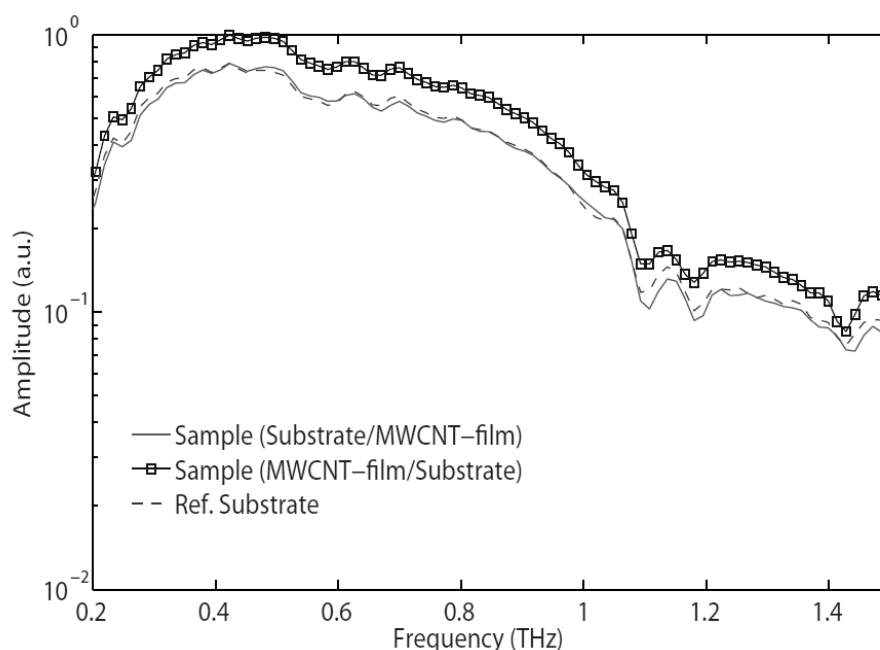
Figure 4.17: The THz reflection spectra of substrate reference and both sides of MWCNT sample.
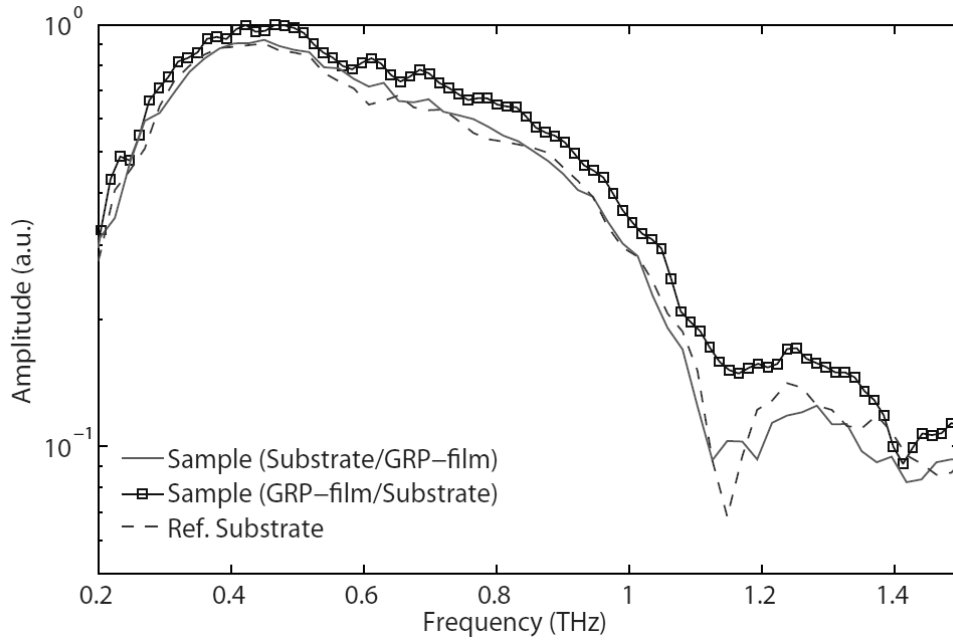
Figure 4.18: The THz reflection spectra of the substrate reference and both sides of GRP sample.
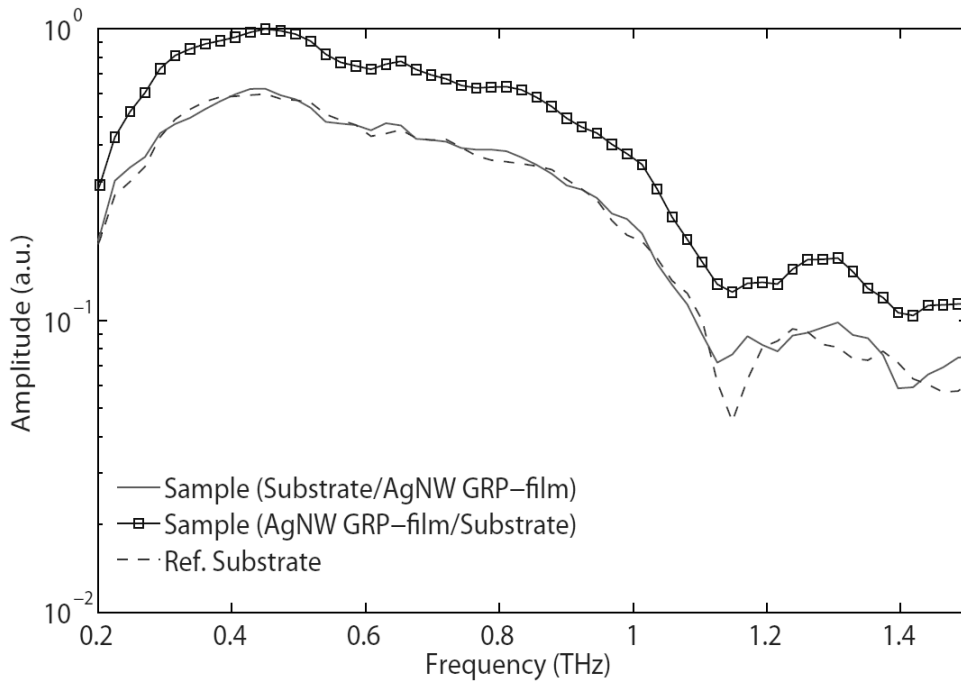
Figure 4.19: The THz reflection spectra of substrate reference and both sides of AgNW GRP sample.
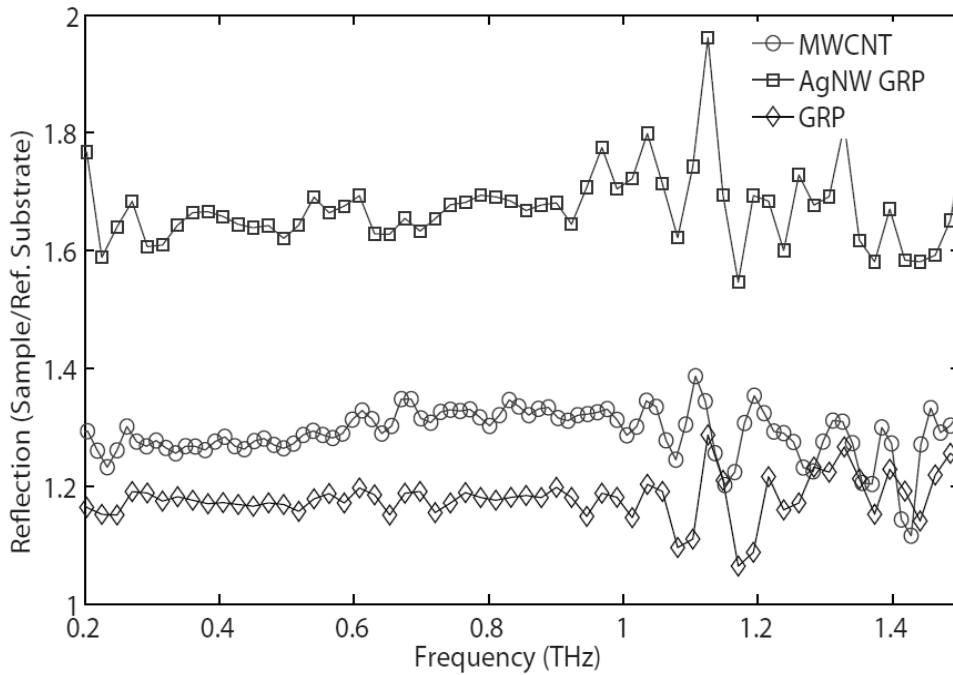
Figure 4.20: The THz reflection module (sample/reference) of MWCNT, GRP and AgNW GRP samples over frequency range of 0.2-1.5THz.

4.4.4 Unwrapped Phase and Phase Correction

All THz transmission and reflection temporal signals with proper time windows, considering the main echoes, mapped into the frequency domain through Fourier transform method that gives the phase of the signal with tolerance of π. Figs. 4.21 (a) and 4.22 (a) show the original phase angles of the graphene sample, in radians, for the transmission and reflection complex signals, where the angles are located between $\pm\pi$. The angle functions for the both transmission and reflection signals are calculated in the Matlab platform based on the below definitions:

Angle for transmission signal= imag [log(complex transmission signal)],

Angle for reflection signal= imag [log(complex reflection signal)].

Following that, the phase of signal is unwrapped. This corrects the radian phase angles by adding multiples of ±2π once absolute jumps between successive values are equal or greater than to the default jump tolerance of π radians. A jump tolerance less than π has the same consequence as a tolerance of π. For a tolerance less than π, if a jump is greater than the tolerance but less than π, adding ±2π would result in a jump larger than the existing one. Figs. 4.21 (b) and 4.22 (b) show the unwrapped transmission and reflection phases excreted from Figs. 4.21(a) and 4.22 (a), respectively. In Fig. 4.22 (b) the slop is not totally a straight line (indicated by arrows) compared to the presented phase in Fig. 4.21 (b) which behaves almost like a straight line. This may explain the sensitivity of the phase measurements in reflection mode rather the transmission ones.

It should be noted that there is not signal (or existing the high level of noise compared to the signal one) at low frequencies in THz-TDS measurements, thus it is normal practice to linearly extrapolate up to the first relevant phase value at $\omega=0$. Figs. 4.21 (c) and 4.22 (c) show the extrapolated phases which start from zero frequency considering the natural behavior in Figs. 4.21 (b) and 4.22 (b) at high frequencies. In other words, the phase slope is calculated at frequency range of 0.3-0.4 THz and the phase value are extrapolated based on this slop from 0 THz up to 0.3 THz. Finally, all values from 0.4 THz up to 1.6 THz are moved to according to the calculated line distance between the original phase at 0.3 THz and the extrapolated one at 0.3 THz.
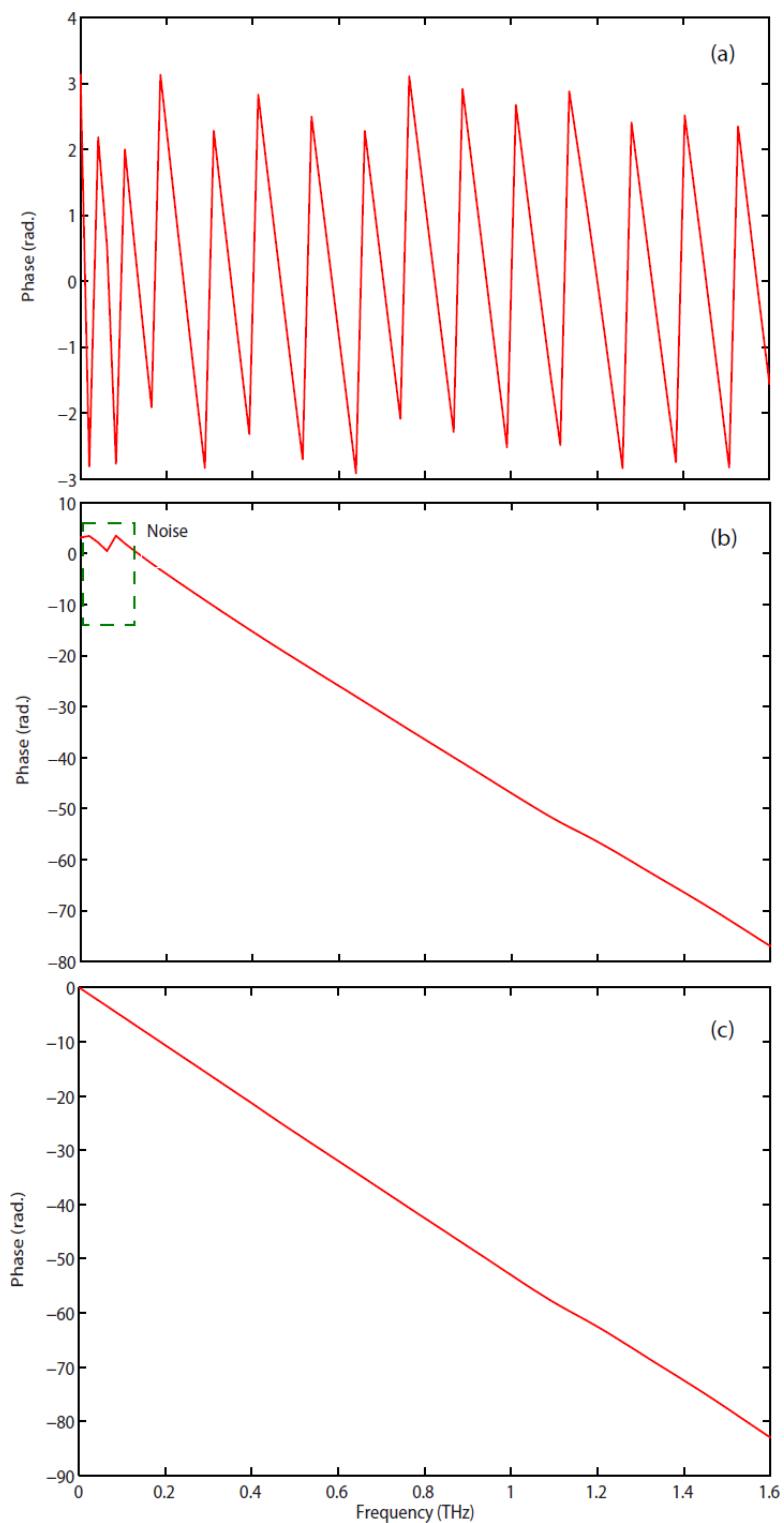
Figure 4.21: (a) The original phase, (b) the unwrapped phase, and (c) the corrected unwrapped phase at low frequency extracted from transmission THz measurement (0-1.6 THz) of mono-layer graphene sample.
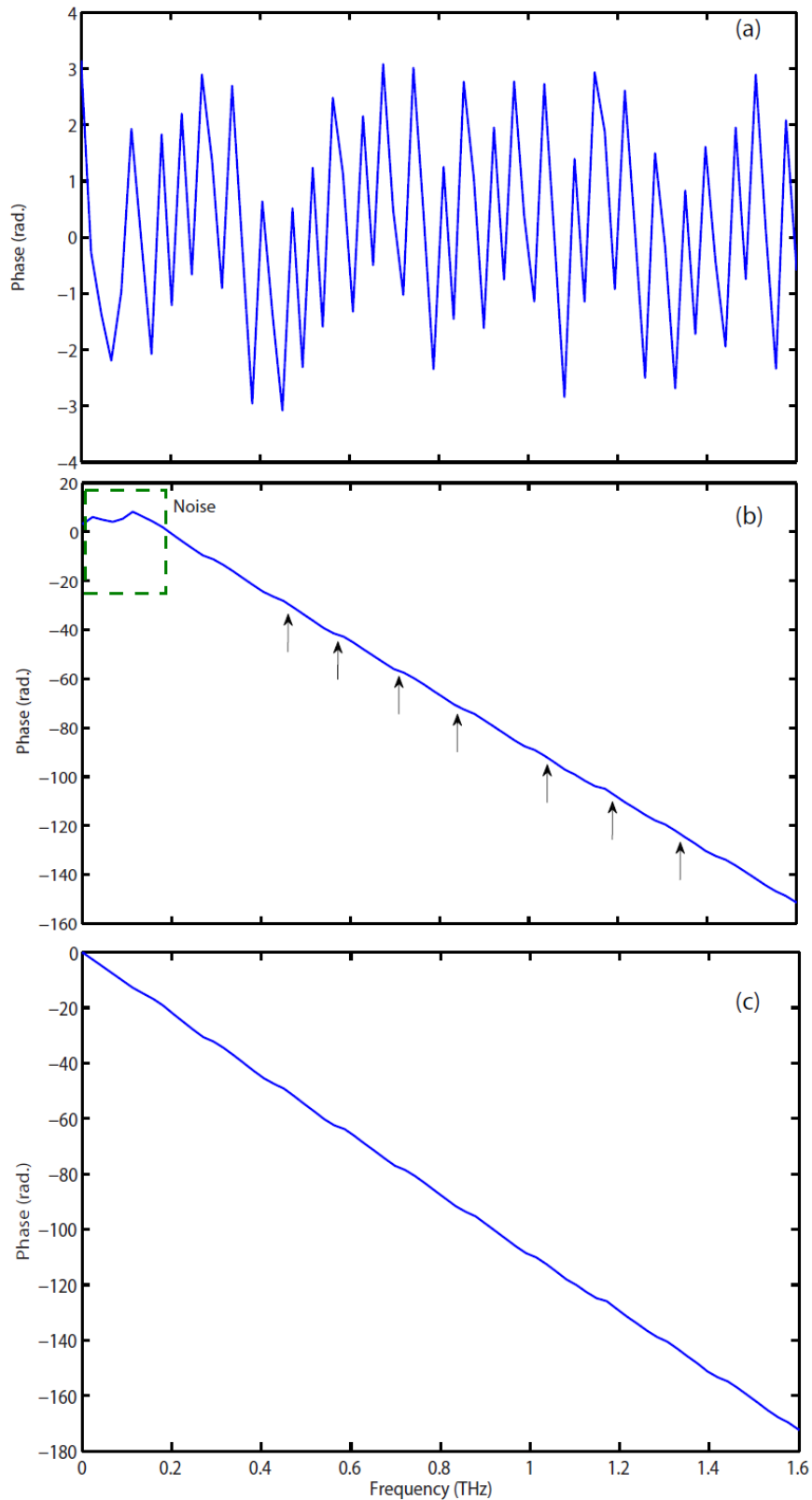
Figure 4.22: (a) The original phase, (b) the unwrapped phase, and (c) the corrected unwrapped phase at low frequency extracted from reflection THz measurement (0-1.6 THz) of mono-layer graphene sample.

4.5 Conclusions

In this chapter a comprehensive presentation of the transmission and the reflection THz-TDS techniques to measure the module and phase of temporal signals of the graphene and the CNT thin film deposited on a quartz bar has been studied. The experimental scheme designed for the measurement procedures have been described and have involved THz signal generation of 0.1-2 THz. The schemes have incorporated a parallel collimated THz transmission and/or the reflections setups, under the same experimental conditions, and were used to measure the air reference, the reference substrate, and the sample, allowing a comparative analysis of all the results obtained.

Three sets of experimental tests have been devised to measure the THz temporal signals, complex functions consisted of the amplitude and the phase information, under the control waterlines absorption using a vacuum chamber. The experimental findings presented in this chapter were seen to be good approaches to study the transmitted and the reflected spectra for the different graphene and CNT thin films based on their physics and geometries. The results presented have led to present results in Chapter 5. These analyses have motivated further investigation to determine the electrical and optical parameters of the high conductance graphene-based materials. The results from this spectroscopic analysis at the AC (frequency-dependent absorption, refractive index and electrical conductivity), the DC levels will be presented in the following Chapters 5-6.

Chapter 5: Experimental Analysis on the THz-TDS Optical and Electrical Parameters of the Micro/Nanometrics Graphene-Like Films

5.1 Introduction

The features of THz-TDS as a noncontact technique to quantify the electrical and optical properties of the thick and thin semiconductor samples have been established in Chapter 2. The reliability of this technique has been confirmed by means of a comparative analysis of the complex refractive index of the reference quartz substrate obtained from the measured THz signals in both transmission and reflection modes. The presented results in this chapter deals with the THz optical and electrical parameters of the micro and nanometrics CNT and graphene films in Chapter 3 measured in Chapter 4.

In this chapter, the set of experimental results of the high conductance thin CNT and graphene films from the THz-TDS transmission measurements will be presented in the frequency range of 0.1-2 THz. Using this information and the presented conductivity models in Chapter 3, a comparative analysis of the Drude and non-Drude responses from the THz measurements schemes will be shown to be in close agreement, demonstrating the scope of THz conductivity models for the AC characterization of the conductance CNT and graphene samples. In accordance with the objectives laid out for this experimental analysis, the Drude and non-Drude models will be studied the AC electrical conductivity of 1D and 2D carbon nanostructures which identify the physical understanding of the samples beyond their optical and electrical parameters.

Finally, throughout this thesis, the achieved results from continuous wave vector network analyzer, with great spectral resolution and a good dynamic range in the sub-THz

frequency regime (60-70 dB around 500 GHz), will be taken to compare them with the obtained THz-TDS results for the thick quartz substrate and thin graphene-like films in the frequency of 200 GHz-500 GHz.

5.2 THz Characterization of SWCNT and MWCNT Films [41, 48, 50]

In this study, the SWCNT and MWCNT thin films with thickness of 1.09 μm and 1.2 μm have been fabricated on face of the fused quartz substrates [cf. Appendix D.1]. The extraction of the electrical and optical properties has been performed from the differential transmission THz-TDS measurements. As already explained, three different temporal waveform measurements have been performed (reference Air, reference substrate and sample). The first measurement has been recorded a reference signal without a sample in between the THz emitter and detector antennas. The second has been measured with the reference quartz substrate in the THz-TDS set up, and the third with the quartz substrate covered by the CNT film. Four times in the THz measurements for each sample have been done to find the average electric field of each THz waveform.

The real conductivity of the CNT samples [cf. Fig. 5.1 (e)] is obtained from the real [cf. Fig. 5.1 (a)] and imaginary [cf. Fig. 5.1 (b)] parts of complex refractive index. Also, the imaginary part of the permittivity of films [cf. Fig. 5.1 (d)] is in turn proportional to the real part of electrical conductivity ($\sigma_{real} = 2\varepsilon_0 \omega nk = \omega \varepsilon_0 \varepsilon_{imag}$). To find the phonon and electron parameters of the CNT samples, the measurement data have been fitted with the presented DL theoretical curves in Chapter 3. The extracted DL conductance parameters in Fig. 5.1 are in the THz regime as reported for the SWCNT [164] and the MWCNT [37] thin films. The power absorption coefficient $\alpha = 2\omega k / c$, where c is the speed of light in vacuum, is shown in Fig. 5.1 (c).
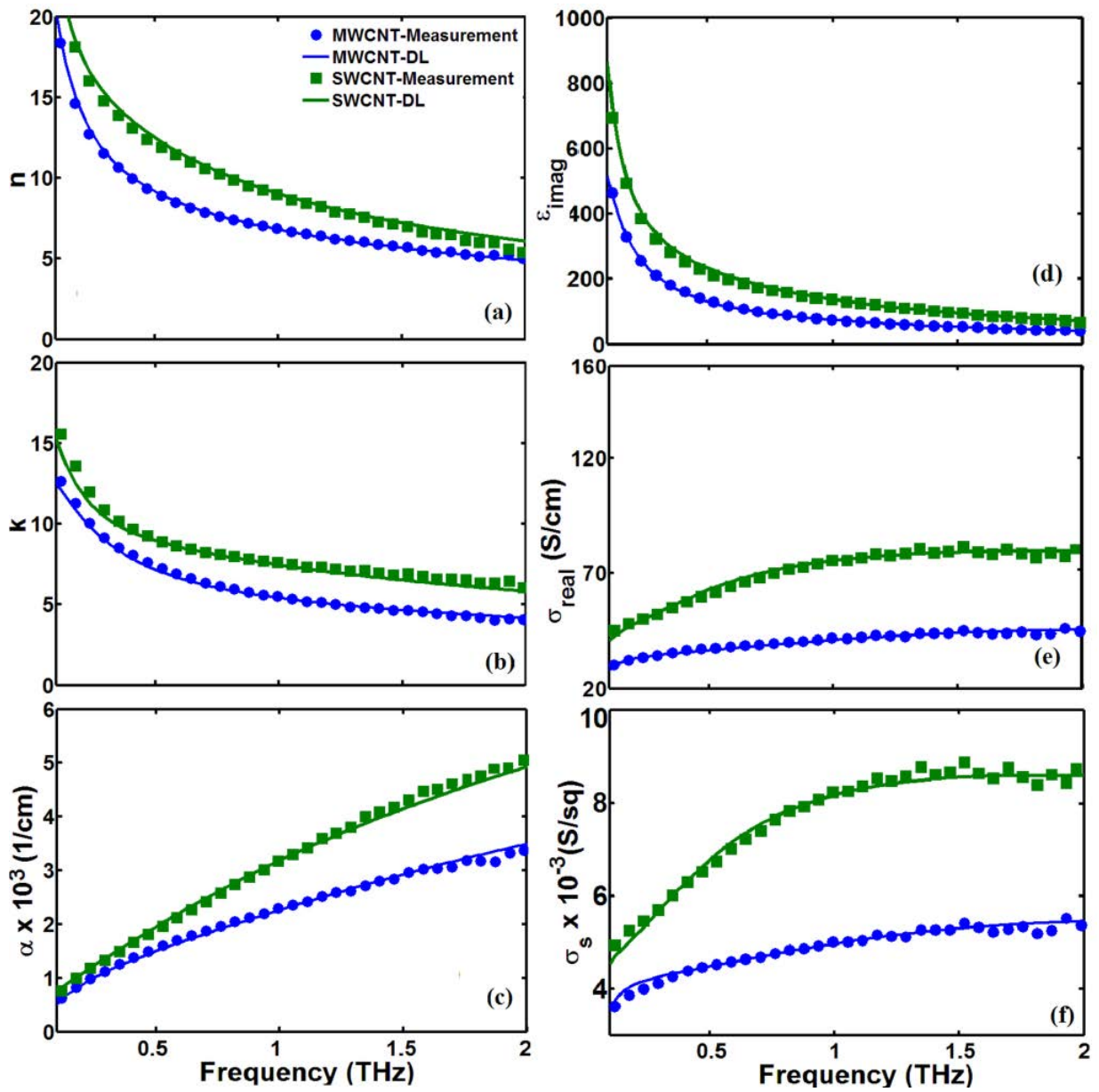
Figure 5.1: (a) The real and (b) the imaginary parts of refractive index, (c) the power absorption, (d) the imaginary part of effective permittivity, (e) the real part of conductivity, and (f) the surface conductivity of SWCNT and MWCNT thin films as functions of frequency. The points and continuous lines are measurement and theoretical results, respectively.

5.2.1 THz Drude-Lorentz Responses of SWCNT and MWCNT [41]

The frequency response curves for both the refractive index and the absorption in Fig. 5.1 are those of a metallic layer with a plasma frequency at different THz frequencies. The measurement data and the theoretical DL results confirmed that the power absorption coefficient of the SWCNT thin film is higher. This can be attributed to the larger length and diameter of MWCNTs compared with SWCNTs as well as contribution of the carrier density to which the power absorption coefficient is proportional to. Table 5.1 illustrates the best fit parameters of the experimental data by the DL model which is plotted in Fig. 5.1 as continuous lines.

Table 5.1: The best fit parameters used in DL curves for SWCNT and MWCNT thin films.

Film	ε_∞	$\omega_p/2\pi$ (THz)	$\Gamma/2\pi$ (THz)	τ(fs)	$\omega_{p,j}/2\pi$ (THz)	$\omega_j/2\pi$ (THz)	$\Gamma_j/2\pi$ (THz)	g	f
SWCNT	8.9	30	10.2	15.6	23.65	2.16	9.5	0.2	0.998
MWCNT	7.6	22.4	7.8	20.4	25.4	5.19	23.3	0.15	0.995

The average effective electron mass and electron carrier consideration of CNT samples are located between doped semiconductors (e.g., n-doped silicon) and perfect metals (e.g., Au). This is due to the behavior of CNTs depending on physical structure and varying chiral vector indices of tubes. CNT samples have higher plasma frequency compared to semiconductor ($\omega_p/2\pi \approx 0.35$ THz for n-doped silicon) [144] and lower compared to metals ($\omega_p/2\pi \approx 2080$ THz for Au)[147]. The free electron wave function is perturbed leading to some scattering effect at the crossing junction. This collision time is between 15fs and 21fs, corresponding to the order of magnitude for semimetals. The filling factor is about 1 that proves metallic behavior with geometrical factors 0.2 and 0.15, respectively, for the SWCNTs and MWCNTs [159]. As the plasma frequency is proportional to the square root of carrier density, SWCNTs have higher carrier density. The higher damping rate in SWCNTs indicates large number of electrons available in a bonded regime and also the larger bounding of graphitic order.

Furthermore, the surface conductivity ($\sigma_s = \sigma_{real} d = 2\varepsilon_0 \omega n k d = \omega \varepsilon_0 \varepsilon_{imag} d$), where d is the thickness of film and ε_{imag} is the imaginary part of effective relative permittivity, can provide a direct evaluation of the metallic content in thin film as outcomes of complex THz transmission. The transmission is a frequency-dependent function of conductivity through the first interface with the vacuum impedance. In addition to studies given in recent report [172], the surface conductivity frequency-dependent function of carbon nanostructures has been extended from 700 GHz up to 2 THz [cf. Fig. 5.1 (f)]. Table E.1 has presented that the cross-sectional diameter and length of the tubes are in the range of nanometers and microns, respectively. Using Eq. (3.30) in Eq. (3.31), the effective permittivity or dielectric constant has been obtained. It has a frequency limitation about 20 THz. Beyond this frequency, the value of effective permittivity may not be precise since the effective medium theory is not applicable.

5.2.2 *Optical Absorption and Electrical Conductivity Peaks of SWCNT and MWCNT from THz Characterization [41]*

As mentioned previously, it is difficult to find the exact values of THz conductivity in measurement results for the frequency range higher than 1.7 THz because of insufficient THz power in the experimental set-up. However, by extending the obtained DL curves to higher frequencies of absorption, the broadening optical density (or absorbance) peaks are appeared at 7 THz for SWCNT and 5.7 THz for MWCNT [cf. Fig. 5.2 (a)] thin films. The optical density peaks of different composite SWCNTs increase at high THz frequencies by decreasing the length of tubes using Fourier transform infrared spectroscopy at room temperature [173, 174]. Increase in the optical density peaks in this experiment can be explained due to the decrease (2-3 times) in the average length of tubes in comparison to the reported far-infrared absorption of pristine and doped SWCNT composites (peak at ∼ 3 THz) [175]. The THz conductivity peaks are at 2 THz and 2.6 THz , respectively for SWCNT and MWCNT [cf. Fig. 5.2 (b)] thin films as the graphite phonon resonance is located in the THz regime, mainly from 1meV to more than 10meV [176]. The conductivity of SWCNTs and MWCNTs indeed depend on the crystallinity of the graphitic layers and the number of

surface defects in the carbon nanostructures [177]. The obtained theoretical THz conductivity peak of SWCNT samples in this study is lower than recent report [174] as a result of the interband transition in small-gap CNTs [33]. Then the frequency of optical conductivity peak depends on the average diameter of tubes [178].
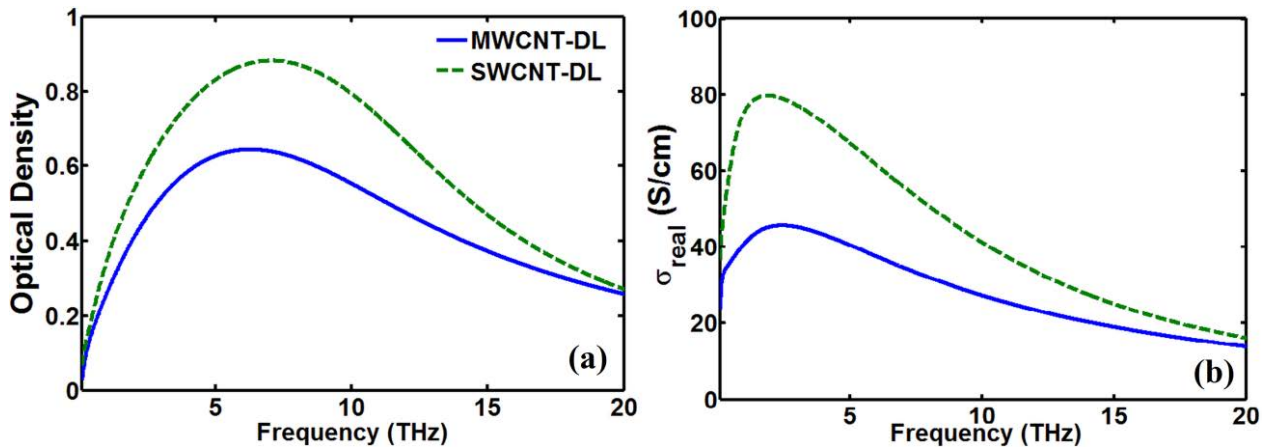
Figure 5.2: The THz peaks of (a) optical density and (b) electrical conductivity of SWCNT and MWCNT thin films at high frequency based on the DL model.

5.3 AC Electrical Conductivity of Carbon Nanostructure (1D) and Graphene (2D) Samples

In this study, the real and imaginary parts of complex electrical conductivity of two different sets of carbon nanostructure, the MWCNT and the mono-layer graphene (MG), are extracted from the differential transmission THz-TDS measurements:

i) **1D carbon nanostructure**: The MWCNTs films were transferred on fused-quartz substrates. The MWCNT film thickness of two samples, namely MWCNT1 and MWCNT2, is 162 and 193 nm respectively. Typically, the films have a diameter of 18 mm, while the fused-quartz substrate is a 25×25 mm^2 square [cf. Appendix D.2].

ii) **2D carbon nanostructure:** The MG film thickness of two samples, namely MG1 and MG2, is a one-atom thick layer deposit on over quartz substrates with size of 15×15×0.5 mm^3 [cf. Appendix D.3].

5.3.1 AC Conductivity Measurements and Non-Drude Responses of 1D and 2D Graphene Samples [42, 50]

One atomic single-layer of graphene film shows a very clear THz response which reduces 15~20% the power of a transmitted THz pulse. Moreover, the THz probing beam particularly has small energy excitation energy. These combinations will find to study the carrier dynamic characterization of 1D and 2D graphene-like materials. The THz-TDS does not only allow for the characterization of charge carriers of graphene in stabilize conditions, but it is also particularly appropriated for non-equilibrium measurements from time-resolved THz spectroscopy where an optical pulse can be applied to make charge carriers and the subsequent evolution of charge carriers can be monitored in femtosecond scale for imaging gas molecular adsorption and desorption sensing applications [179, 180]. The complex permittivity function of the thin films, to which is related the real refractive index and absorption of the electromagnetic wave are extracted in the same method as explained in the previous section.

Fig. 5.3 (a) depicts the THz real conductivity of the films: it monotonically increases with increasing frequency for both MWCNT samples. Fig. 5.3 (b) shows the imaginary part of the electrical conductivity, which decreases with increasing frequency. Then, the conductivity does not follow the simple Drude model and it is needed to consider the Lorentzian contribution at high frequencies. The fits of the experimental data are plotted as lines in Fig. 5.3. One can notice the excellent agreement between measured and calculated conductivities, in both cases of real and imaginary parts. The so-achieved plasma frequency is $f_p = \omega_p / 2\pi \approx 45$ THz, corresponding to an equivalent-bulk density of carriers of 2-4×10^{19} cm^{-3}. Thus, this plasma frequency of MWCNT films is much higher than the one in semiconductors, and smaller than in metals with a scattering time ($\tau \approx$ 10 fs) of the order of metallic materials. In regular semiconductors, f_p is proportional to the square root of carrier density and inversely proportional to the effective mass of the carriers. The Lorentz resonance frequency is around 4 and 6 THz respectively for MWCNT1 and MWCNT2.
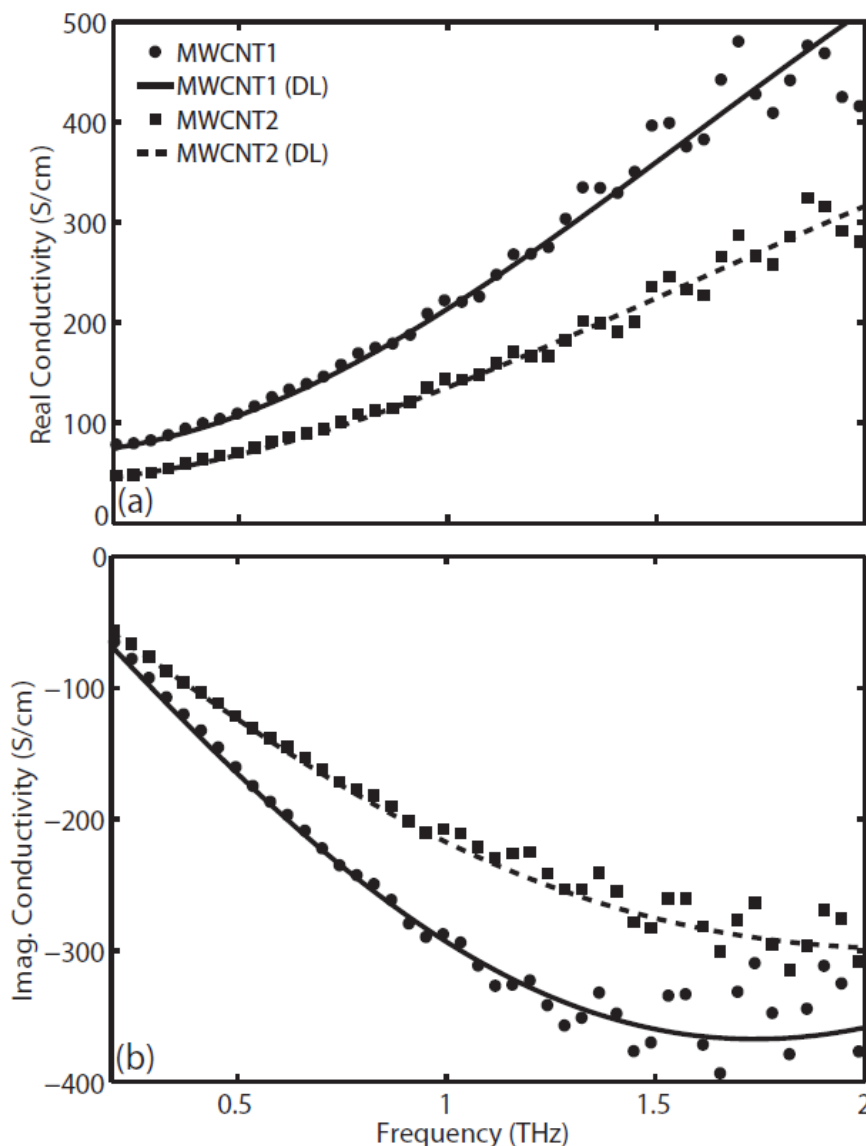
Figure 5.3: (a) The real and (b) the imaginary parts of measured (markers) and fitted DL model (lines) results of electrical conductivity for MWCNT samples.

The plasma frequency and carrier density of MG have a nonlinear dependency, because of the conical dispersion. As discussed already in Chapter 3, the two processes involved in optical absorption in graphene are: carrier intraband transitions and interband transitions [181]. The intraband transition conductivity in the THz range dominates the interband transition conductivity [19]. The measured intraband conductivity is 30 times larger than the interband [182]. Because of this, the conductivity by the intraband free-carrier response in sub-THz analysis is only considered.

Figs. 5.4 (a) and (b) display the THz conductivity of the MG samples. MG1 real conductivity is twice the one of MG2, while its imaginary part is much higher. The values of conductivity are known to be sensitive to the thickness of the MG films [151]. This difference in conductivity behavior of the studied MG samples could come from the slight variation in the transfer during the CVD synthesis process. Also, MG2 shows a non-Drude response because of its smaller area than MG1, which explains why the conductivity shows an oscillator at higher frequencies. As a result of large scattering rates, the studied spectral range is below the Drude roll-off frequency. For the MG1 sample, both real and imaginary parts of conductivity increase with increasing frequency, which is well fitted by a Drude-like form ($c_m = 0$, $f_p \approx 571\,\text{THz}$ and τ = 34 fs) of the frequency-dependent conductivity [153]. For the MG2 sample, however, the negative imaginary part of THz conductivity decreases with increasing frequency. As shown in Chapter 3, it cannot be explained by a simple Drude model, but it is well described by the Drude-Smith (DS) theory with m=1 and $c_1 = -0.6$. The large negative value of c_1 indicates that the electrons are affected by backward scattering as a result of the structural disorder effects in graphene [151]. As for MG1 sample, the plasma frequency $f_p \approx 492\,\text{THz}$ is in the visible range while the collision value (τ = 53 fs) is comparable to the ones of metals.
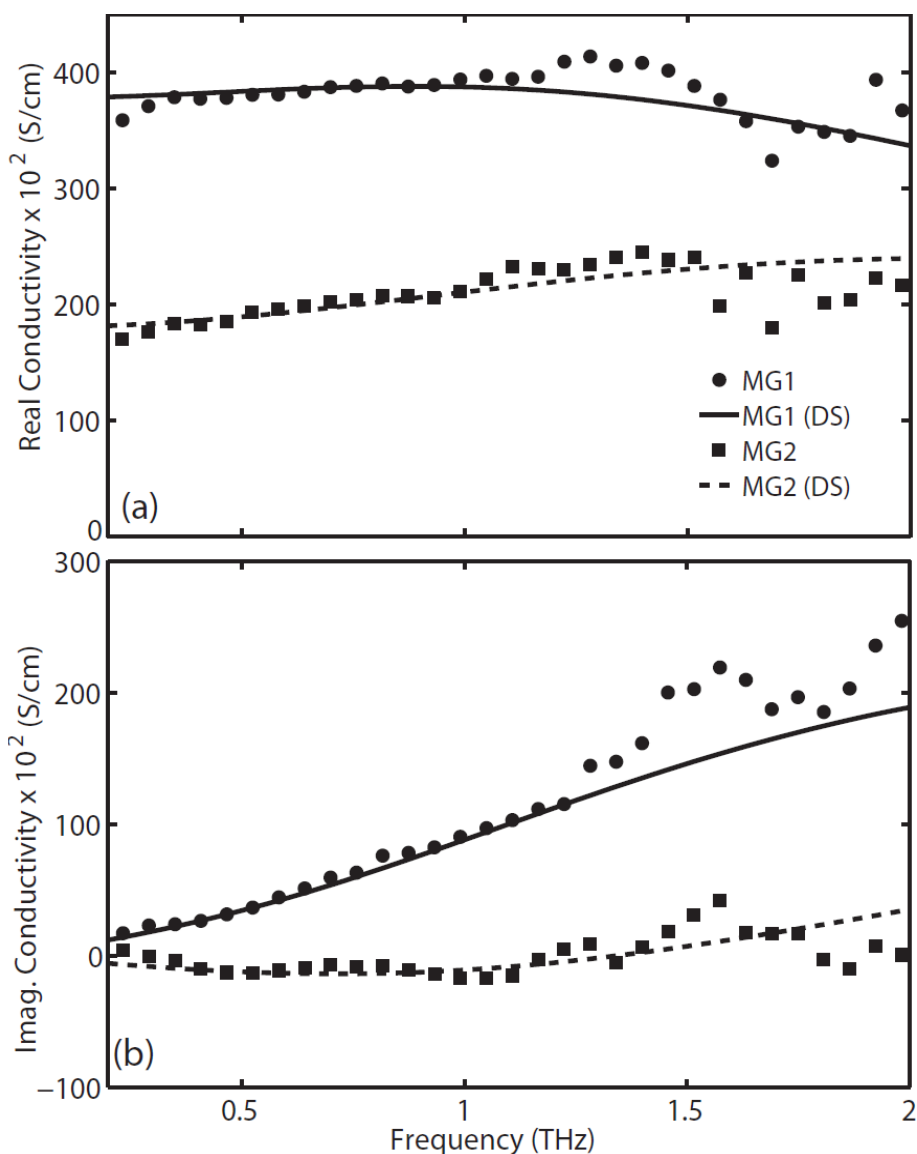
Figure 5.4: (a) The real and (b) the imaginary parts of measured (markers) and fitted DS model (lines) results of electrical conductivity for the MG samples.

5.3.2 AC Sub-THz Characterization of MWCNT and Graphene Thin Films Using Pulsed THz-TDS and CW VNA Techniques [45-47, 49]

One of the main challenges it can be faced while coming down to the lowest frequencies using the THz-TDS is the decrease of SNR due to a drop in THz power. Vector network analyzer (VNA) offers a great spectral resolution and a good dynamic range in the sub-THz frequency regime (60-70 dB around 500 GHz). The advantages of continuous wave (CW)

characterization using VNA over pulsed THz-TDS are higher spectral resolution and huge dynamic range in the sub-THz frequencies (60-70 dB around 500 GHz) [183]. For above 500 GHz, pulsed THz-TDS offers better spectral resolution and dynamic range. The electrical properties, such as conductivity, can be easily derived from the measured optical constants at THz frequencies [8, 184].

As a complementary sub-THz measurements in this thesis, the MWCNT thin films [cf. Appendix D.2], and an industrial based mono-layer graphene deposited over a fused quartz substrate [cf. Appendix D.4] have been also characterized in the 220-325GHz (WR3.4) and 325-500GHz (WR2.2) using a broadband frequency-domain technique by a VNA setup. The measurements are carried out in free space. Thanks to the VNA, all the scattering parameters are measured simultaneously, from which the effective material parameters are extracted using the Nicholson-Ross-Weir (NRW) method. The full details to extract the electrical conductivity of the thin films are studied in the recent reports in Refs. [45, 46].

In the same approach as TDS, the first is to obtain the refractive index of the reference quartz for both non-covered and covered samples that has a refractive index ∼ 1.95. The extinction coefficient or imaginary part of complex refractive index of the substrate is nearly zero in the frequency range of 325-500 GHz [cf. Fig. 5.5]. In CW results, the measurements are not averaged as curves fluctuations are due to FP residual effects, which cannot be suppressed with averaging. The parameters of the thin film have been extracted. The refractive index, absorption coefficient and conductivity are calculated from the obtained permittivity.
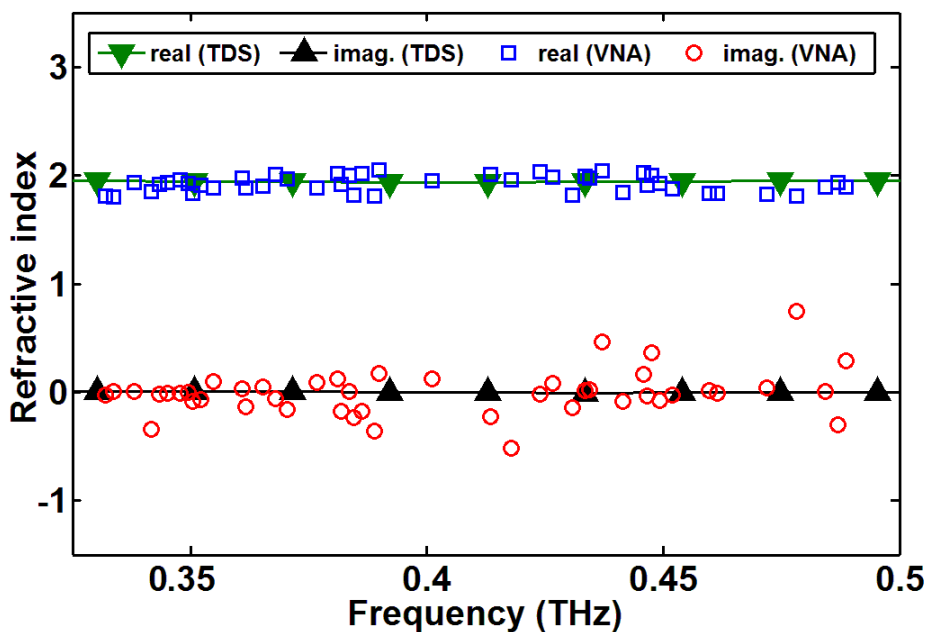
Figure 5.5: The complex refractive index of fused quartz as a function of frequency for both (i) THz TDS (ii) CW-VNA methods.

In order to obtain the parameters of the thin film alone [185], the effect of substrate have been eliminated and extracted the complex refractive index of the thin films. Figs. 5.6 (a) and (b) present the refractive index and conductivity of the MWCNT thin film samples respectively. It can be seen from the figures that the optical and electrical values of reference substrate and MWCNT thin films [cf. Fig. 5.6] obtained using NRW method are close to the ones achieved by THz-TDS. Differences between both could be due to residual oscillations in the VNA data and possible misalignments of the sample.
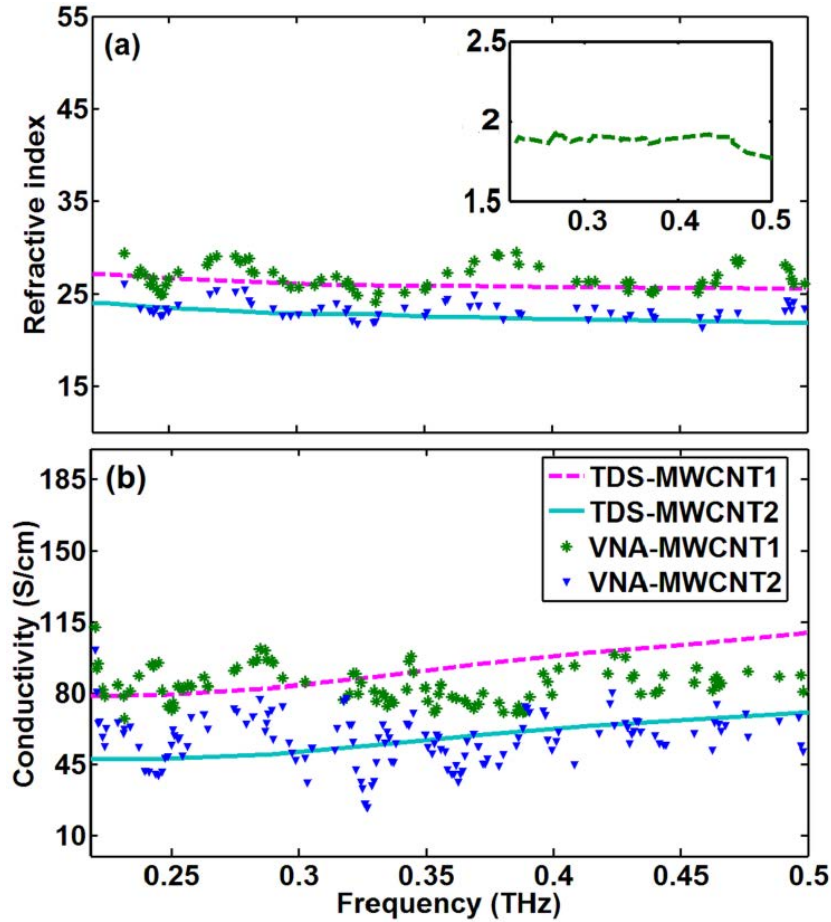
Figure 5.6: (a) The refractive index and (b) the conductivity of MWCNT1 and MWCNT2 extracted using the NRW method (markers) and the THz-TDS (lines). The refractive index of quartz substrate extracted using NRW method is given inset of (a).

The thickness of a single layer of graphene is very small compared to the thickness of the substrate which has a lower attenuation at sub-THz frequencies. Because of this, in TDS analysis, the multiple-reflections happening inside the MG sample are taken into account. The values of conductivity in TDS measurement are sensitive to the thickness difference between the MG and reference substrate. CW-VNA method offers a higher spectral resolution and a good dynamic range. The obtained results using TDS analysis and NRW method are consistent with respect to each other. Fig. 5.7 (a) shows the frequency-dependent refractive index obtained for MG sample. The high absorption of electromagnetic wave passing through the sample, shown in Fig. 5.7 (b), is in turn proportional to the carrier density of MG. Fig. 5.7 (c) shows the conductivity obtained for the MG sample using THz-TDS and CW- VNA techniques.
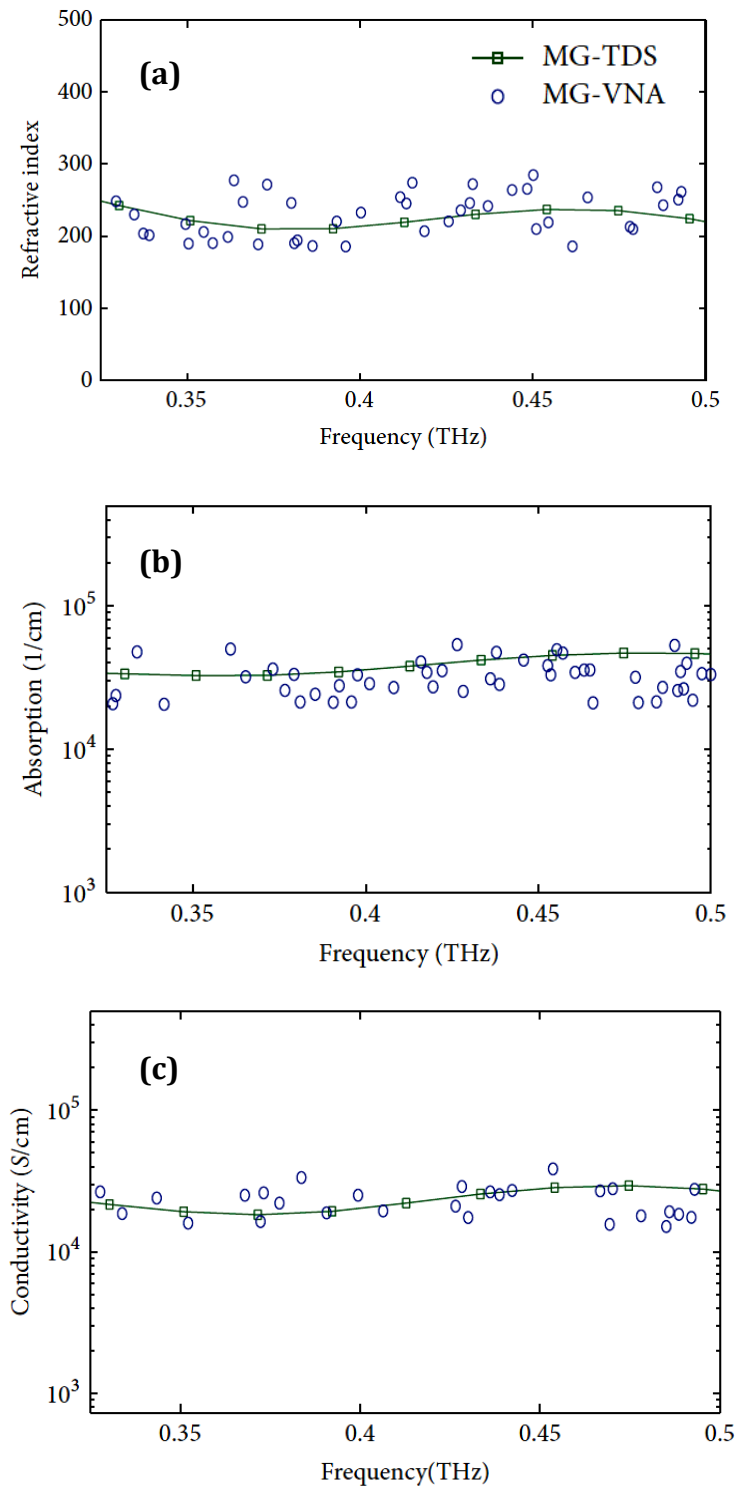
Figure 5.7: The obtained (a) real refractive index, (b) power absorption and (c) electrical conductivity of MG using the THz-TDS and the CW NRW techniques.

5.4   Conclusions

In this chapter a set of the THz-TDS results of the electrical and optical frequency-dependent properties of the CNT and the graphene thin films have been presented. The experimental scheme designed for this procedure, described in Chapter 2, has involved at AC level with a broad frequency range of 0.2-2 THz. The scheme has incorporated parallel collimated THz setups in Chapter 4, under a similar experimental procedure, a reference substrate was used as a reference, allowing a comparative analysis of all the results obtained by applying the differential method in Appendix B.

These experimental analyses have been motivated by the success of the measured transmission and reflection spectra presented in Chapters 3 and 4. Preliminary results of the SWCNT and MWCNT thin films have been performed using the THz-TDS differential transmission technique and the reference substrate measurement in Chapter 2. Agreement is observed between both measurement results and the theoretical Drude and non-Drude curves.

The conductivity is higher in the SWCNTs compared to the MWCNT ones due to the increased number of free-electron density, regions of graphitic order and higher mobile carriers with high filling factor. From the theoretical models, the optical density peaks and the THz conductivity peaks have been observed at 3 THz for the CNT samples. The graphene electrical conductivities have been well described by Drude and non-Drude models. The backward scattering occurring in the free electron movement may be explained by the structural disorder of the graphene film Drude-Smith response

Using THz-TDS measurement, the surface boundary condition has been considered of the CNT/graphene thin samples between transparent fused quartz substrate and air to precisely achieve the complex refractive index and the AC electrical conductivity of single-layer graphene. These results have been compared with achieved results from CW-VNA free space measurements using NRW considering the advantages of using a good dynamic range in sub-THz frequencies (60-70 dB around 500 GHz).

Chapter 6: DC Conductivity and Carrier Responses of Graphene Nanostructures from THz Characterization

6.1 Introduction

Because of the dielectric properties of substrate and the Fabry-Perot effect within thin films, measuring the electrical and optical properties of films deposited over substrate at AC and DC level are more challengeable in comparison to bulk one using noncontact THz-TDS. There is difficulty in deposition and integration of fragile CNT and graphene samples to the optoelectronic devices may prevent a multiple measurement procedure and/or subsequent use of the tested devices. Chapter 6 is motivated by the success of the optical and the electrical analysis presented in Chapter 5.

To find the electrical and optical properties of the graphene-like thin films, this chapter deals with the extract frequency-dependent data from the conductance films coated on the thick substrate from the transmission and reflection THz-TDS measurements by demonstrating an equivalent circuit. This will enable presenting the Fresnel equations considering the sheet conductivity as well as the complex refractive index of samples.

As explained in Chapter 4, the samples taken under this study have the stack structure, which the CNT or graphene thin films are on top of the bar substrate, then they can be applied to the optoelectronic applications. For the graphene samples, a modification of Drude model was explained in details in Chapter 3. It expressed the back scattering time due to collision influences because of impurity and large scale of CVD grown in fabrication process. In addition, the semiconductor and metallic CNTs' physical structure made from

graphene layer(s) can be provided to study the electrical conductivity responses of such thin films from the effective medium theory and hybrid Drude-Lorentz models.

Measuring the DC conductivity of very thin and fragile graphene-like films is rather difficult because of the electrical contact issue. This Chapter will deal that the comparative Drude and non-Drude theoretical models from the transmission and reflection THz-TDS measurements will highlight one of the major advantages of using THz conductivity model not only to extract the DC conductivity but also to study the high carrier mobility responses of samples without using any contact element or post-process pattering. These achievements will be validated and discussed with the recent state-of-the-art contact measurement results in order to be applied for the new optoelectronic devices to operate at the sub-THz and THz frequencies.

6.2 DC Conductivity of Graphene-Like Samples [42, 50, 53]

In Appendix B, the differential THz-TDS method was applied to analysis and study the absorption and dispersion properties of the MWCNT thin films (with thicknesses on the order of nm) without using the complex iteration for extracting THz transmission data. The complex refractive index was derived to find the real part and extinction coefficient which give us the precise dispersion and absorption of MWCNT thin films. However, the THz-TDS set up do not offer enough SNR to determine the precise conductivity at low frequencies (typically below 200 GHz), because the efficiency of their dipole-like THz antennae vanishes when reaching the DC regime.

This is obvious that by decreasing the time windowing in Fourier analysis the THz spectra will be smoother. But, the significant data and information are missed in the THz signals by reducing the time window especially once the edge of time window is close to the THz temporal signals. Furthermore, there are inconsistent values of the THz signal in the low frequencies. Those ripples are because of the sampling time which is very small and not enough to recover the equivalent low frequencies below 0.2 THz. This thesis studied two approaches to derive the DC conductivity for such high conductance samples: i) extrapolation using polynomial function, and ii) Drude/non-Drude responses using plasma frequency and collision time.

6.2.1 DC Extraction Using Extrapolation Functions

In this experiment, two uniform MWCNT thin films with homogenous surface and thicknesses of 193 nm (MWCNT1) and 162 nm (MWCNT2) have been studied [cf. Appendix D.2]. Figs. 6.1 (a) and (b) show the THz signals before and after using the extrapolation approach by fitting a polynomial function in the frequency domain to find more precise and smooth information at lower THz frequencies. The rest ripple effect at higher frequencies can be cause of noise in system and the absorption lines of atmospheric water vapour (e.g., around 1.7 THz).

From the relation between the complex permittivity function and the complex refractive index $\tilde{\varepsilon} = \varepsilon_1 + i\varepsilon_2 = \tilde{n}_f^2 = (n+ik)^2$, the real part of refractive index and excitation coefficient (or imaginary part of refractive index) can be extracted. The real part of frequency-dependent refractive index of two MWCNT thin films is presented in Fig. 6.2 (a). Furthermore, the power absorption coefficient (α) of MWCNT thin films as a function of frequency can be expressed in terms of the extinction coefficient (k), $\alpha = 2k\omega / c$ [cf. Fig. 6.2 (b)]. As mentioned in Chapter 5, the refractive index decreases with increasing frequency in the THz regime. While the power absorption coefficients significantly increase at the higher frequencies.
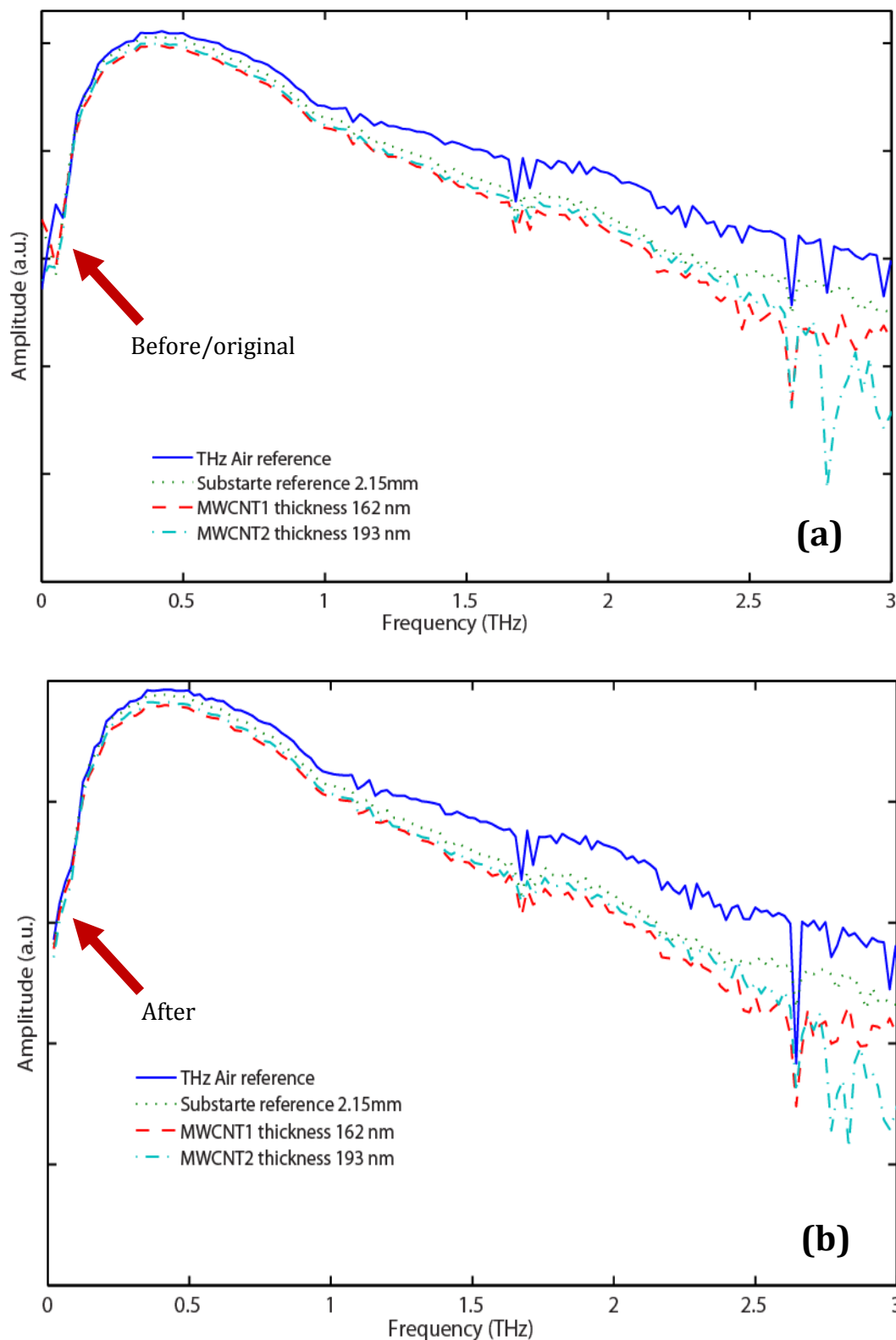
Figure 6.1: The THz spectrum of free space, the references substrate, and the MWCNT samples in time-window of 35ps (a) before and (b) after the extrapolation of data at the low frequencies using a polynomial function.
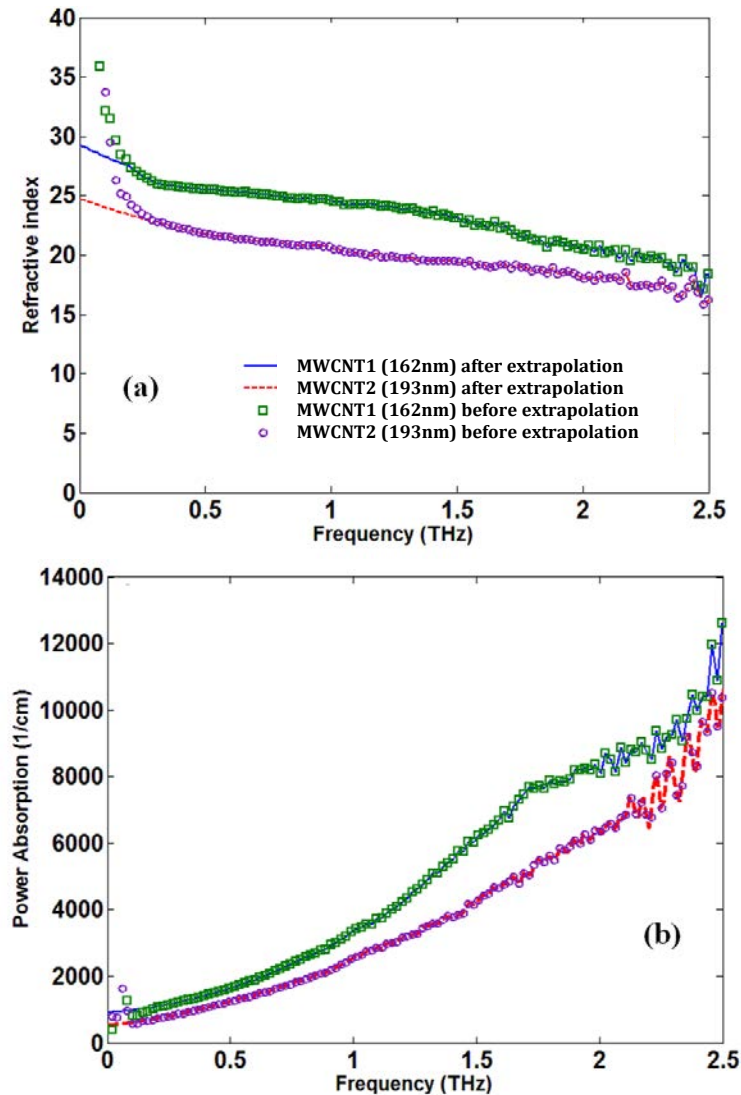
Figure 6.2: The frequency-dependent refractive index (a) and power absorption (b) of the MWCNT thin films with thicknesses of 162 nm and 193 nm considering a time-window of 35ps.

By taking into account that the refractive index of air n_1 and the complex permittivity (or dielectric constant) function which is equal to the complex refractive index square, the electrical conductivity as a function of frequency for the MWCNT thin films in the frequency range of 0-2.5 THz are illustrated in Fig. 6.3. Since there were the inconsistence values of electrical conductivity at low frequency, the extrapolation with polynomial functions have been applied to find the DC conductivity and compare them with the classical electrical conductivity measurement using the four-point probe method [186] with a current source (Keithley 6221) and a nanovoltmeter (Keithely 2182A). The average DC conductivities for

MWCNT1 and MWCNT2 have been demonstrated in Table 6.1 are 70.6 S/cm and 66.6 S/cm, respectively. The achieved conductivity using the extrapolation technique in the THz -TDS analysis at zero frequency respectively are about 74 S/cm and 37 S/cm for both MWCNT1 and MWCNT2.
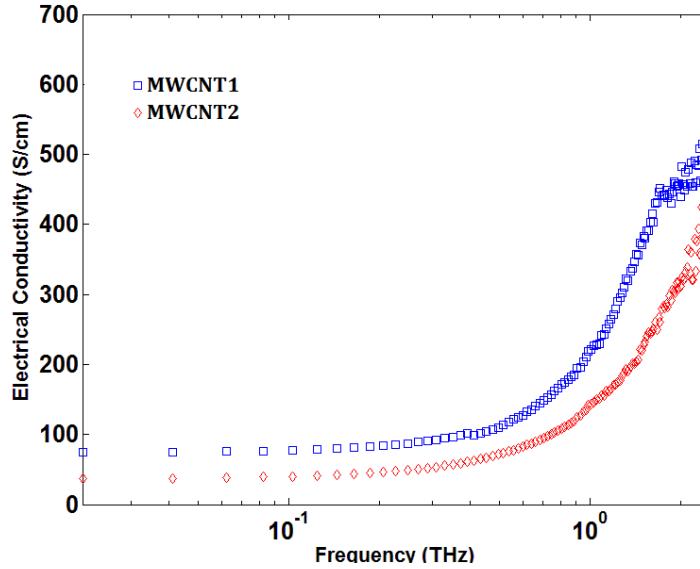
Figure 6.3: The frequency-dependent THz conductivity of the MWCNT thin films with thicknesses of 162 nm (MWCNT1) and 193nm (MWCNT2).

Table 6.1: The electrical conductivity of MWCNT1 and MWCNT2 measured by the four-point probe and the noncontact THz-TDS Extrapolation Methods.

Sample	Four-point probe method (S/cm)	Noncontact THz-TDS Extrapolation Method (S/cm)
MWCNT1	70.6	74
MWCNT2	66.6	37

6.2.2 DC Extraction from Plasma Frequency and collision time

To get close results with the probe-in line DC measurement, this work have presented more precise DC results using free contact THz-TDS method, by having accurate details of samples (e.g., geometry) and also physical understanding of the MWCNT and the MG properties from the Drude and non-Dude models studied in Chapters 3 and 5. This allows obtaining much accurate results of 74 S/cm and 37 S/cm for MWCNT1 and MWCNT2.

The high level of electrical properties inside the samples can be ascribed to relevant of the carrier density. Furthermore, the damping rate is proportional to the free-electron density. Then the higher damping rate indicates the large numbers of the electrons are available in a bonded regime. The high density of free-electron gives the possibility to make highly conductive nano-composite films. These electrical parameters can be extrapolated from the conductivity by fitting the spectra over the whole THz range, which minimizes the effect of noise or of discrepancies at some given frequencies. The DC conductivity of the films is simply deduced from the permittivity constant at frequency $\omega = 0$, using the fitted plasma frequency and collision time $(\sigma_{dc} = \omega_p^2 \tau \varepsilon_0)$ in the Drude, DL and DS models studied in Chapter 5. The so-obtained values are given in the third column of Table 6.2.

To validate our method, the DC electrical conductivity of the presented MWCNT and MG [cf. Appendices D.2 and D.3] films was measured with a classical 4-probe technique [20], using a Keithley 6221 current source and a Keithley 2182A nanovoltmeter. Even though the 4-probe technique is always difficult to implement when dealing with thin films (the probes may mechanically damage the film at the contact location), the measured DC conductivity [column 2 of Table 6.2] is very close to the average values deduced from THz-TDS measurements and conductivity models [column 3 of Table 6.2]. There is only one disagreement related to sample MG2. It could arise from the not perfect fit of the conductivity curve at lower frequency [cf. Fig. 5.4], and especially of the imaginary part of the conductivity, which is too small to be determined with a great precision.

Table 6.2: The DC conductivity values obtained using 4-probe technique and determined from THz Drude models.

Sample	4-probe Conductivity (S/cm)	THz-Drude Conductivity (S/cm)
MWCNT1	70.6	70.7
MWCNT2	66.6	66.7
MG1	3.46×10^4	3.5×10^4
MG2	6.96×10^3	2.1×10^4

The investigation in this thesis shows that the difference between the extrapolated DC conductivity from the noncontact THz measurements and the ones from contact measurement can be attributed to 1) the environmental effects as the residual impurity charges can simply be influenced by the ambient conditions such as temperature and humanity [17, 187], 2) the slight variation in thickness of graphene layers deposited on bare [42, 43], 3) difficultly to implement of probe contact measurement when it deals with thin films where the probes may mechanically damage the film at the contact location [42, 43], 4) micrometer-scale using contact probes conductance measurement in DC compared to noncontact AC nanoscopic transport probed by THz conductivity measurement [188].

6.3 Fresnel Equations to Extract Direct Conductivity of Nanometrics Graphene-like Samples [43]

Incident of THz waves with a bilayer optic system, consisting of a thin film deposited on a substrate, cause multi reflections and transmissions because of inequality refractive index at interfaces of layers, so-called Fabry-Perot (FP) behavior. In case of high conductance thin film deposited over on the substrate, the Maxwell EM boundary conditions have been applied at this interface (air and substrate layers). To simplify this complex behavior in main reflection and transmission fields, an equivalent transmission line circuit has been developed in this thesis [cf. Fig. 6.4]. In this case, the THz E-fields transmitted and reflected from the high conductance thin film can be describe by the characteristic impedance.
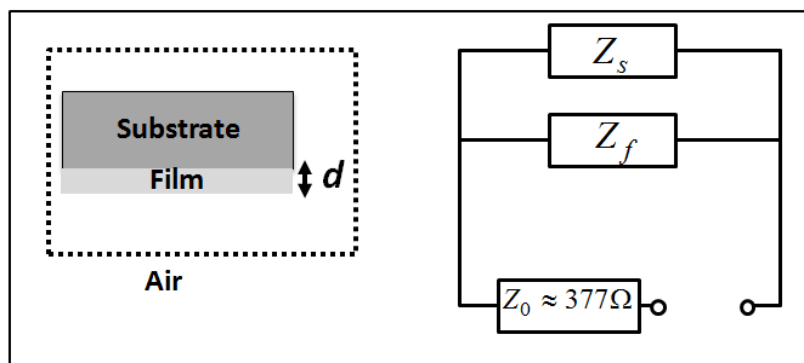
Figure 6.4: The wave reflected from surface of the thin film can be proposed in an equivalent circuit with the impedances for air (Z_0), film (Z_f) and substrate (Z_s).

In such a circuit, each layer of sample x has equivalent impedance $Z_x = Z_0 / \tilde{n}_x$, where the free space impedance is $Z_0 \approx 377 \, \Omega$. The medium x has a complex refractive index $\tilde{n}_x = n_x + ik_x$ which is equal to the square root of complex permittivity of medium $\sqrt{\tilde{\varepsilon}_x}$. x is the air and the substrate. Since the thickness of conducting layer film is much smaller than the skin depth of the incident THz wave, the current density can be uniform throughout the material corresponding to a surface current. Then the impedance of highly conductance thin film can be rewritten $Z_f \approx E/J \approx 1/\tilde{\sigma}_f$ [156], where E is the incident electrical field and J is the surface current in thin film with the sheet conductivity of $\tilde{\sigma}_f$. By knowing that in the equivalent circuit the time dependent field gets partially transmitted and reflected, we can write the transmission and reflection coefficients of surface of conductance film at the interface between the source Z_0 and the load $(Z_L = \dfrac{Z_s Z_f}{Z_s + Z_f})$:

$$t_{Film}\left(\omega, \tilde{\sigma}_f\right) = 2/(n_1 + n_2 + Z_0 \tilde{\sigma}_f) \quad \text{and} \quad r_{Film}\left(\omega, \tilde{\sigma}_f\right) = (n_1 - n_2 - Z_0 \tilde{\sigma}_f)/(n_1 + n_2 + Z_0 \tilde{\sigma}_f) \quad ,$$

respectively. The complex transmission and reflection of sample (film/substrate), whose amplitude and phase are respectively ρ and φ, writes:

$$\tilde{T}_{Film} = \rho_T \, e^{-j\varphi_T} = \frac{E_{F,T}}{E_{S,T}} \approx \left(1 + Z_0 \frac{\tilde{\sigma}_T}{1 + n_s}\right)^{-1}, \tag{6.1}$$

$$\tilde{R}_{Film} = \rho_R \, e^{-j\varphi_R} = \frac{E_{F,R}}{E_{S,R}} \approx \frac{1 - Z_0 \dfrac{\tilde{\sigma}_R}{1 - n_s}}{1 + Z_0 \dfrac{\tilde{\sigma}_R}{1 + n_s}}. \tag{6.2}$$

The real and imaginary parts of the sheet conductivity can be easily obtained from (6.1):

$$\sigma_{r,T} = \frac{1 + n_s}{Z_0}\left(\frac{\cos \varphi_T}{\rho_T} - 1\right), \tag{6.3}$$

$$\sigma_{i,T} = \frac{1 + n_s}{Z_0} \frac{\sin \varphi_T}{\rho_T}. \tag{6.4}$$

As in the transmission case, the film conductivity is deduced from the measured coefficient (6.2):

$$\sigma_{r,R} = \frac{1}{Z_0} \frac{1 + n_s - 2n_s \rho_R \cos \varphi_R - (1 - n_s)\rho_R^2}{\dfrac{1 + n_s}{1 - n_s} + 2\rho_R \cos \varphi_R + \dfrac{1 - n_s}{1 + n_s}\rho_R^2}, \tag{6.5}$$

$$\sigma_{i,R} = -\frac{2}{Z_0} \frac{\rho_R \sin \varphi_R}{\dfrac{1 + n_s}{1 - n_s} + 2\rho_R \cos \varphi_R + \dfrac{1 - n_s}{1 + n_s}\rho_R^2}. \tag{6.6}$$

6.3.1 Electrical conductivity and Optical properties

In this study, the electrical conductivity of three graphene-like samples is extracted from both reflection and transmission THz-TDS measurements:

i) **1D carbon nanostructure**: The MWCNTs film was transferred onto fused quartz substrates. The MWCNT Films is of thickness 193 nm. The thickness of the fused quartz substrate is 2.15mm [cf. Appendix D.2].

ii) **2D carbon nanostructure**: the mono-layer pristine graphene (GRP) was grown CVD transferred onto the fused quartz substrate with thickness of 0.5 mm substrate is 2.15mm [cf. Appendix D.5].

iii) **Hybrid 2D graphene and 1D nano wires**: The silver nanowire-graphene hybrid (AgNW-GRP) films were deposited over fused-quartz with thickness of 0.5mm using CVD process. The thickness of the AgNW-GRP hybrid films was measured by atomic force microscopy (AFM), and the average value was used to calculate the conductivity [cf. Appendix D.5].

By inserting the achieved refractive index of substrate in the prior sections, the conductivity values from the transmission and reflection modes have been extracted using equations (6.3)-(6.6). The conductivity function can provide a direct evaluation of the metallic behavior in these thin films. For example in case of GRP sample, the real and imaginary values of conductivity can be extracted [cf. Fig. 6.5]. The experimental data are well fitted with the DS model, in which $c_m = 0$, i.e. the conductivity behaves as a Drude-like one. As the corresponding plasma frequency ($f_p = 583$ THz) lies in the visible range, both real and imaginary parts of the THz sheet conductivity of GPR are almost constant.

Even if noisier as expected because of the weaker sensitivity of extraction from reflection THz-TDS data, the obtained values from both transmission and reflection records are in good agreement at high frequencies, validating the values obtained in transmission and thus the right substrate thickness value need to input in the calculation.
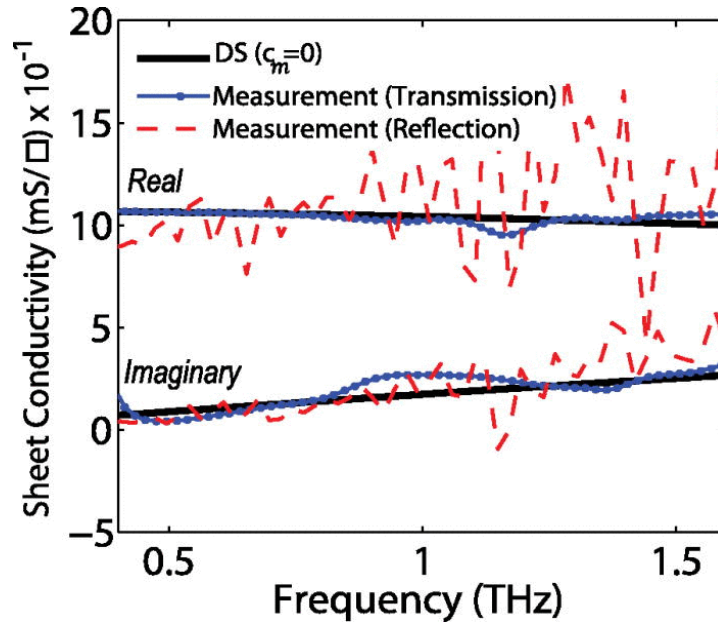
Figure 6.5: The real and imaginary parts of the sheet conductivity of GRP films versus frequency as determined from the THz-TDS measurements (doted and dashed) and fitting curves (lines).

Consequently, the refractive index and power absorption of these films can be derived from the complex surface conductivity. Figs. 6.6-8 present the refractive index, the power absorption, and the sheet conductivity of thin MWCNT, GRP and AgNW-GRP films using THz-TDS reflection and transmission measurements in the frequency range of (0.2-1.6THz). The THz conductivity of the MWCNT and the AgNW-GRP thin films monotonically increases with increasing frequency. However, it is almost constant for the GRP. The power absorption increases with increasing frequency for all samples where the GRP shows much higher absorbance compared to others. The frequency response curves for both refractive index and absorption are those of a metallic layer with a plasma frequency at different THz frequencies.
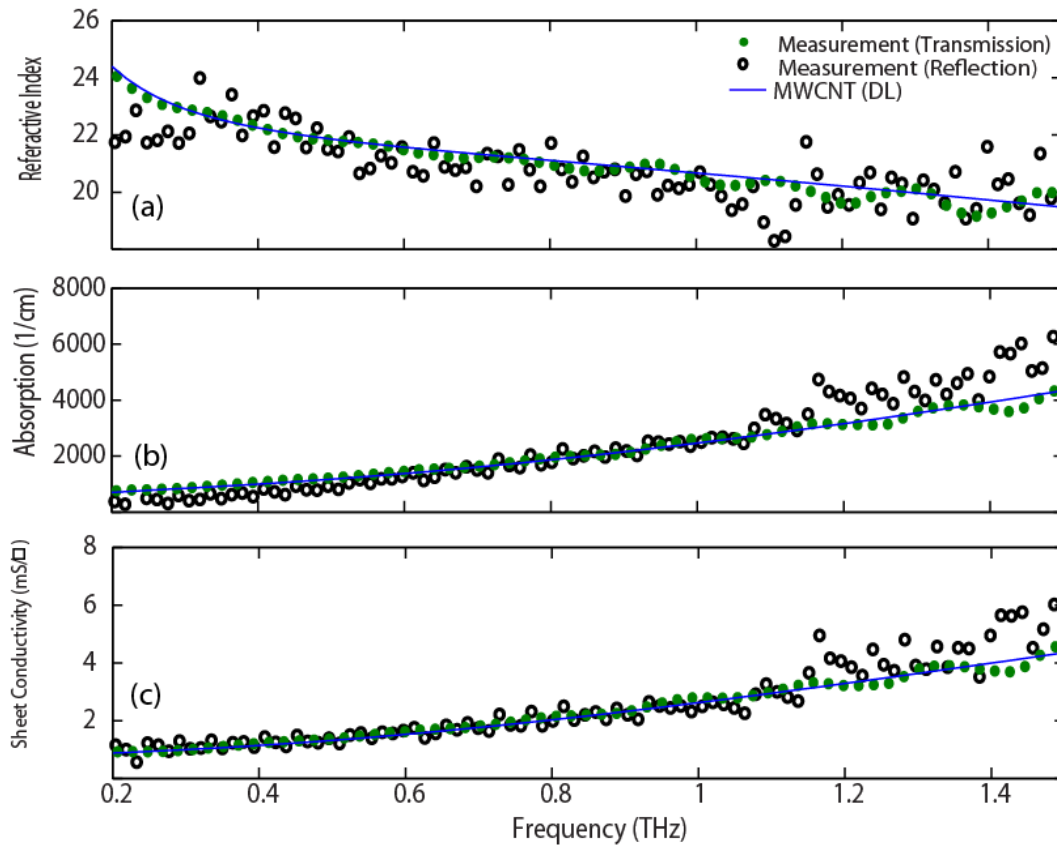
Figure 6.6: The frequency-dependent (a) refractive index, (b) power absorption, and (c) sheet conductivity of MWCNT sample from the transmission and reflection measurements (dots) which are in a good agreement with the theoretical Drude-Lorentz (DL) model (lines).
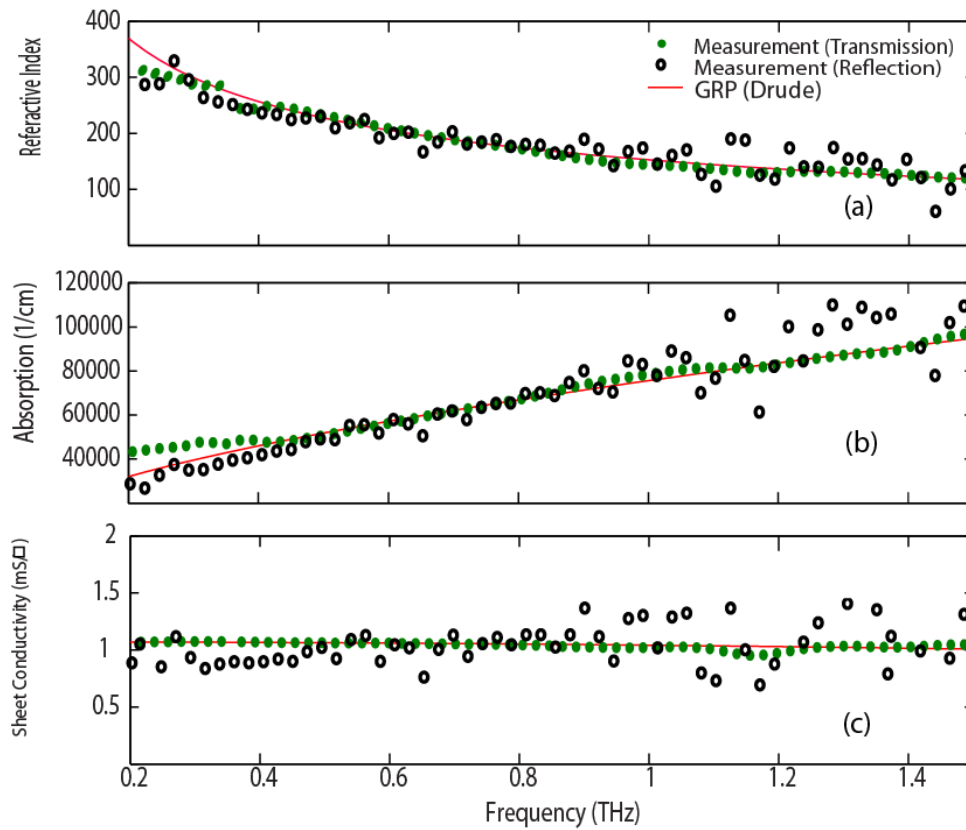
Figure 6.7: The frequency-dependent (a) refractive index, (b) power absorption, and (c) sheet conductivity of GRP sample from the transmission and reflection measurements (dots) which are in a good agreement with the theoretical Drude model (lines).
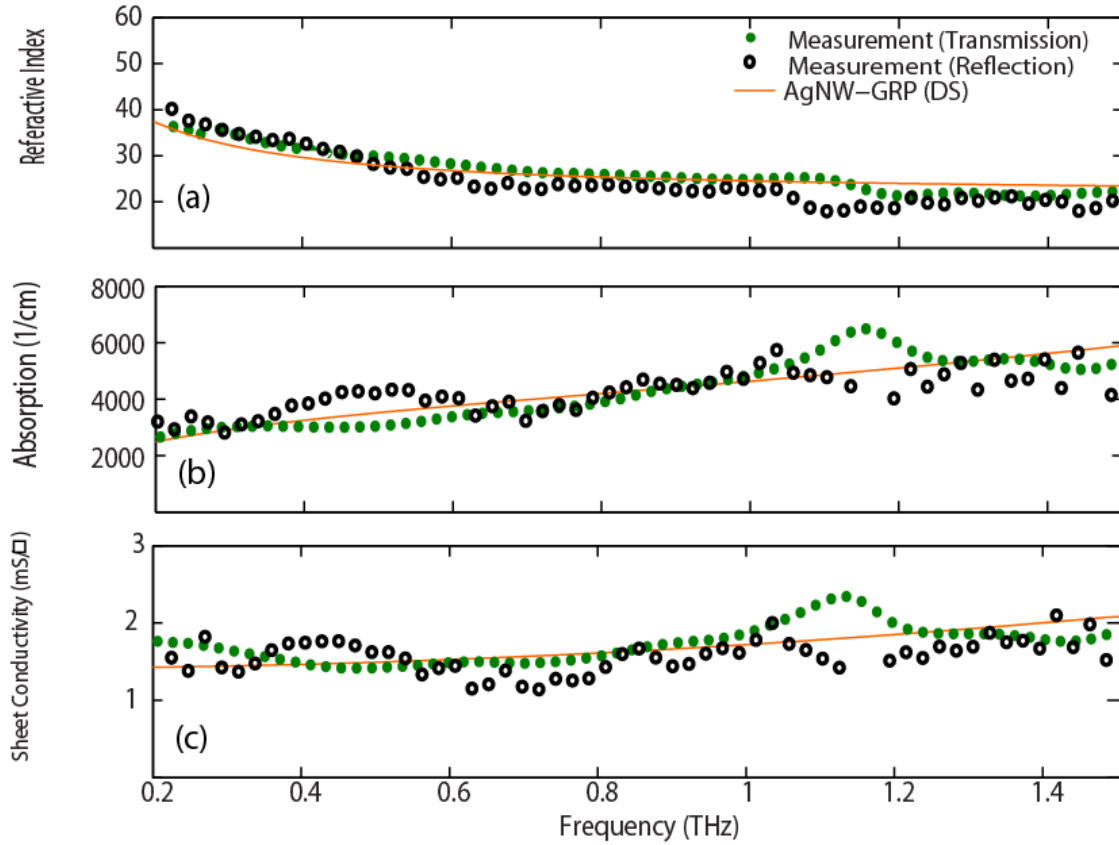
**Figure 6.8: The frequency-dependent (a) refractive index, (b) power absorption, and (c) sheet
conductivity of AgNW-GRP sample from the transmission and reflection measurements (dots) which
are in a good agreement with the theoretical Drude-Smith (DS) model (lines).**

The conductivity in the AgNW-GRP is more complex than in the GRP. In this thesis, two
different AgNW-GRP films have been effectively tested. The conductivity in such hybrid
films is strongly dependent on polarization and on the different orientations of the
nanowires inside the films [189]. The THz conductivity is dominated by the contribution of
the micro-structured nanowires oriented along the THz electric field. Indeed, the lengths of
the wires are comparable to the THz wavelength and thus the wires can be resonantly
excited by the incoming THz field. On the other hand, due to their nanometer-scale
diameter, the wires are insensitive to a THz E-field perpendicular to them. Figs. 6.9 (a) and
(c) depict the real part of conductivity as functions of frequency and thickness of thin films.

It should be noted that the thickness of the film is not constant and exhibits peaks at given
locations, due to the nanowires. Thus, Figs. 6.9 (a) and (c) are plotted versus the average

value of the film thickness. These experimental plots show a capacitive behavior due to electron scattering effects in the junctions of AgNW networks. The complex sheet conductivity of the films, deduced from Figs. 6.9 (a) and (c), is given in Figs. 6.9 (b) and (d). As the imaginary part of THz sheet conductivity decreases while increasing frequency, the conductivity model cannot be explained by a simple Drude response, but it is well fitted by the DS model.
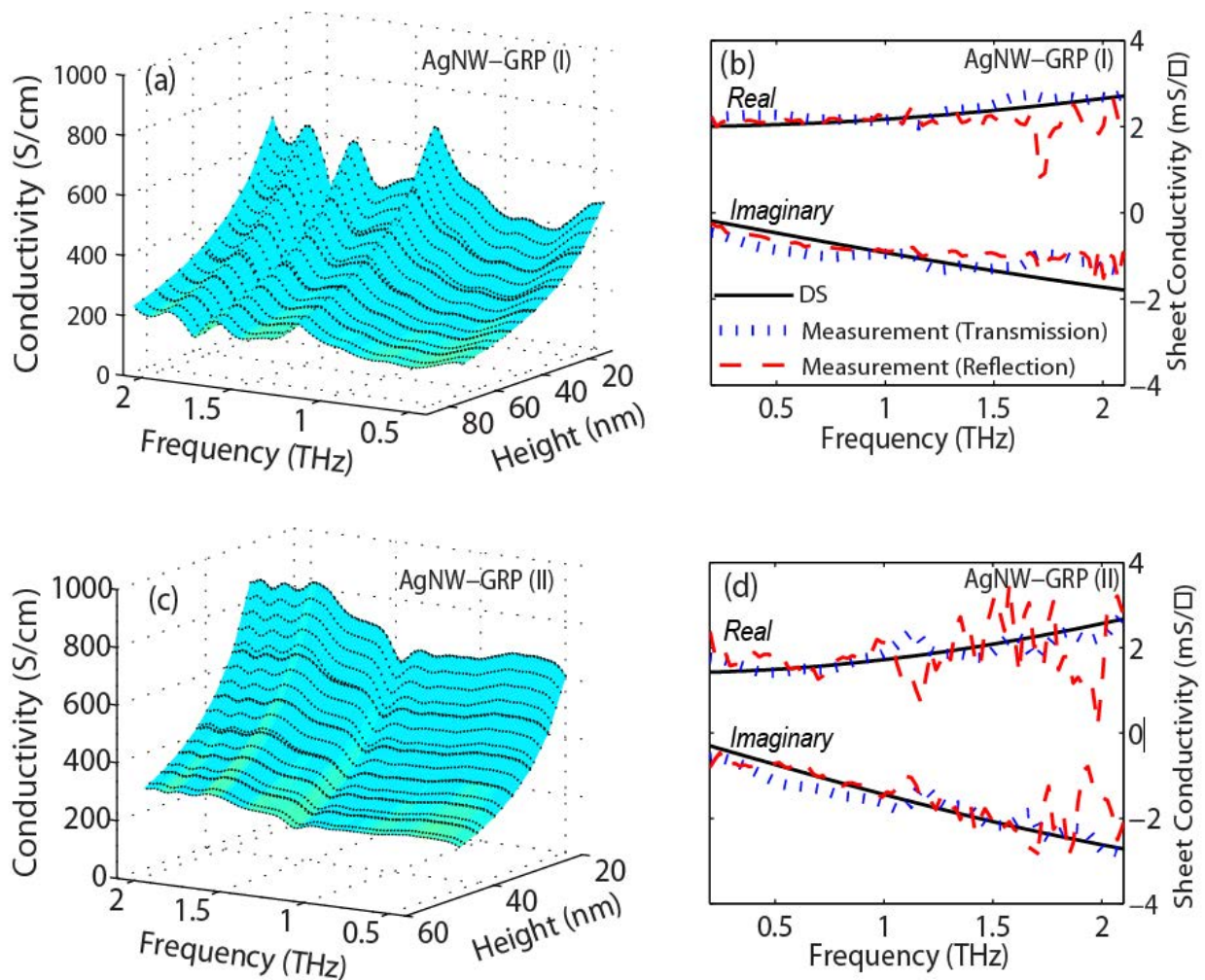
Figure 6.9: (a) and (c) The real conductivity of AgNW-GRP hybrid films as function of frequency and thickness determined from the transmission THz-TDS. (b) and (d) The real and imaginary parts of the sheet conductivity of AgNW-GRP hybrid films versus frequency. Dotted lines: transmission data; dashed lines: reflection data (marker lines); continuous lines: fitted curves calculated with the average film thickness.

6.3.2 DC and Peak of Electrical conductivity

Table 6.3 gives the parameters of the fits (plasma frequency f_p, scattering time τ and c_m coefficient) for the GRP and the two AgNW-GRP hybrid films. The scattering time τ is comparable to the one of noble metals and the plasma frequency is much higher than the exciting THz frequency. In the thinner film AgNW-GRP (I), the scattering time is slightly shorter than in the thicker AgNW-GRP (II), resulting in a larger sheet resistance. This could be due to a difference of filling fractions of AgNWs or/and to the contribution of scattering at the film surfaces. c_1 is close to -1 in AgNW-GRP, which means that most of the electrons are backscattered during a collision. These collisions certainly occur at the surface of the nanowires as the carrier mean-free path is of the order of the nanowires diameter [139]. The quite small sheet conductivity in the AgNW films, as compared to the AgNW-GRP, is due to a smaller charge carrier density in AgNW films.

To validate the results, the sheet resistance ρ ($=1/d\sigma_{dc}$) of the hybrid films was measured with a classical 4-point-probe technique, using a Keithley 6221 current source and a Keithley 2182A nanovoltmeter. Even though the 4-point probe technique is always difficult to implement when dealing with thin films (the probes may mechanically damage the film at the contact location), the measured ρ (column 5 of Table 6.3) is very close to the average values deduced from THz-TDS conductivity models (column 6 of Table 6.3).

Table 6.3: The THz fitting parameters used in the DS model (fp: plasma frequency, τ: scattering time, ρ: sheet resistance). The sheet resistance measured using 4-point probe contact method is also provided for comparison.

Sample	f_p (THz)	τ (fs)	c_1	*4-probe* ρ (Ω/□)	*DS Model* ρ (Ω/□)
GRP	583	26	0 (Drude)	1055	944
AgNW-GRP (I)	232	16	-0.92	56	56
AgNW -GRP (II)	294	14	-0.87	75	65

As the conductivity DS model is validated by comparison with experimental data in the THz range, the optical sheet conductivity of the AgNW-GRP hybrid films have been computed up to the UV domain, i.e. from 0.1 to 10^3 THz. A clear maximum of conductivity appears in

between 9 and 11 THz [cf. Fig. 6.10] which is in the same range as silicon nanoparticles film [147, 155], and 2-3 times higher than GaAs and ITO thin films [147, 190]. The peak originates in the resonant behavior of the Drude and DS models, through the term $(1 - i\omega\tau)$.

The peak conductivity is about 20 times larger than for GRP at 10 THz. Even around 1 THz, i.e. in the non-resonant regime, the sheet conductivity of the AgNW-GRP films (60-70 Ω/□) is comparable with the one of ITO (∼80 Ω/□), making these films a good flexible conductive material for replacing indium tin oxide in many electronic applications.
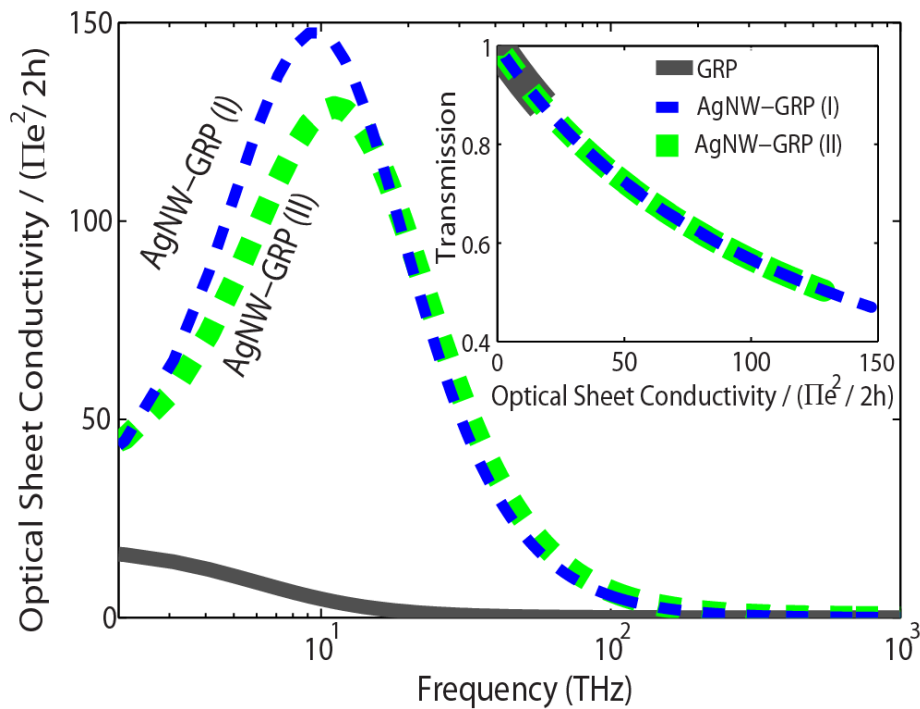
Figure 6.10: The sheet conductivity of GRP and AgNW-GRP hybrid films versus frequency calculated using the Drude and Drude Smith models. The sheet conductivity is normalized by the fine-structure constant ($\pi e^2/2h$). Inset shows the calculated THz transmission of the samples as a function of the normalized sheet conductivity.

6.4   High Mobility and Dynamic Carrier Characterization of Graphene-Like Samples [44]

In this study, multiple numbers of transmission and reflection measurements for different samples have been performed in order to find a good consistency of the experimental and theoretical results. From now on, this chapter follows the carrier dynamic response of different prior CNT (under the assumption of effective and homogeneous medium in DL model) and graphene (Drude and DS responses) samples by accessing to the obtained THz conductivity results in the present and previous chapters:

- SWCNT (1.09 μm) and MWCNT (1.2 μm)-details explained in Appendix D.1.

- MWCNT1 (162 nm) and MWCNT2 (193 nm)-details in Appendix D.2.

- MG1 (mono-layer graphene1) and MG2 (mono-layer graphene 2)-details explained in Appendix D.3.

- GRP (mono-layer pristine graphene) and AgNW-GRP (silver nanowire-graphene hybrid)-details explained in Appendix D.5.

6.4.1 Mobility and Dynamic Carrier Responses

The average effective electron mass and electron carrier consideration of graphene-like samples are located between semiconductors and perfect metals with higher plasma frequency compared to semiconductor ($f_p \approx 0.5$ THz for n-doped silicon)[144] and lower compared to metals ($f_p \approx 2000$ THz for Au)[147] [cf. column 5 of Table 6.4] . This collision time is on the order of magnitude for semimetals at room temperature [cf. column 6 of Table 6.4].

Table 6.4: The extracted σ: surface conductivity, fp: Plasma frequency and τ: scattering or collision time response of 1D and 2D graphene-like samples (d is the thickness of films).

Film	Appendix	d (nm)	σ (S/□)	fₚ (THz)	τ (fs)
SWCNT	D.1	1090	5.5E-03	30	16
MWCNT	D.1	1200	4.2E-03	22	20
MWCNT1	D.2	162	1E-03	45	12
MWCNT2	D.2	193	4.1E-03	55	10
MG1	D.3	~0.34	1.3E-03	571	34
MG2	D.3	~0.34	1.5E-03	492	53
GRP	D.5	~0.34	1E-03	538	26
AgNW GRP1	D.5	59	1.8E-02	232	16
AgNW GRP2	D.5	38	1.6E-02	294	14

Near the Dirac point, the group velocity v_f for carrier in metallic graphene-like materials is around $0.85 \sim 1.1 \times 10^6 \, m/s$ [29]. This yields to find the mean free path as:

$$L = v_f \tau .$$

(6.7)

This value is on the order of 25-55 nm for the 1D nanostructure graphene samples and 10-20 nm for the 2D ones [cf. column 2 of Table 6.5]. The difference value of mean free path for the mono-layer graphene samples can be explained by residual impurity charges in the fabrication process. Here, we assume that the electron and hole mobilities are of the same order of magnitude with complete ionization. Under the statement that carrier transport is dominated by long-range charged impurity scattering, the carrier density of samples related to the achieved sheet conductivity and scattering time can be derived by:

$$n = \sigma_{dc}{}^2 \pi \hbar^2 / (\tau e^2 v_f)^2 ,$$

(6.8)

being *e* the electronic charge. The results are presented in column 3 of Table 6.5.

Table 6.5: The extracted L: time mean free path, and n: carrier density responses of 1D and 2D graphene-like samples.

Film	L (nm)	n (cm^{-2})×10^{12}
SWCNT	16	6.2E+02
MWCNT	20	2.3E+02
MWCNT1	12	4.8E+01
MWCNT2	10	9.9E+01
MG1	34	7.8E+00
MG2	53	4.4E+00
GRP	26	8.6E+00
AgNW GRP1	16	6.5E+03
AgNW GRP2	14	7E+03

The latest results using the THz Drude model shows that the conductivity of graphene is constant and is temperature-dependent at a low carrier density. However, it has a nonlinear relation with the total carrier density ($\sigma \propto \sqrt{n}$) at high carrier concentrations where the Fermi level energy is not near the charge neutrality point [17]. The relationship between carrier mobility and carrier density can be derived from the scattering time within the regime of long-range scattering as:

$$\mu = ev_f\tau / \hbar\sqrt{n\pi}.$$ (6.9)

As a general trend, for the graphene and CNT samples like other conventional semiconductors, the mobility is inseparably connected to the band gap and carrier density. It increases with decreasing band gap and/or carrier density. The carrier mobility in column 2 of Table 6.6 is comparable with GaAs 2D electron gas and 10-500 times higher than silicon based devices at room temperature [191]. As studied in the Drude and non-Drude responses in steady-state condition, the electron effective mass is proportional to the inverse of mobility. So, it is calculated from:

$$m^* \approx e\tau / \mu.$$ (6.10)

The demonstrated results in column 3 of Table 6.6 can be verified with the reported contact measurements [29, 192]. The carrier density near the Dirac point is related to the quantum capacitance. It is calculated by:

$$C_Q \approx (\sqrt{n+n_g}\,2e^2)/(\hbar v_f \sqrt{\pi}). \tag{6.11}$$

This value is symmetric with respect to the Dirac point. The presented quantum capacitance of all samples in column 4 of Table 6.6 is calculated when $n_g = 0$ (potential is equal to zero, thus C_Q is limited only to n). The results for MG1, MG2 and GRP are in very good agreement with the contact quantum capacitance measurement for the graphene sample [193]. Moreover, the Ag NWs in hybrid AgNW-GRP films increases C_Q up to $200\mu F/cm^2$.

Table 6.6: The extracted μ: carrier mobility, m*/m₀: electron effective mass, and C_Q: quantum capacitance responses of 1D and 2D graphene-like samples.

Film	μ (cm²/V s)	m*/m₀	C_Q (μF/ cm²)
SWCNT	55	5.1E-01	69
MWCNT	112	3.1E-01	42
MWCNT1	124	1.4E-01	19
MWCNT2	86	2E-01	27
MG1	1033	5.8E-02	8
MG2	2169	4.3E-02	6
GRP	758	6E-02	8
AgNW GRP1	17	1.7E+00	237
AgNW GRP2	14	1.7E+00	230

The energy in the Fermi level can be derived from carrier density $E_f = v_f \hbar \sqrt{n\pi}$, where the carrier density nonlinearity increases with an increase of the external potential, for example the gate voltage in a graphene field–effect transistor. As it was expected, the E_f of AgNW GRP is much higher than other sample and shows a metallic behavior in a further Fermi velocity of 1.4× 10⁶ [139]. The E_f for MG1, MG2 and GRP is in the range of 300-400 meV which is in a good agreement with the CVD graphene measured by the Hall-effect

method [194]. THz conductance gives a nanoscale characteristic length in contrast to micro-scale contact probe measurements of carrier transport by:

$$L_c = (D_c / \omega)^{1/2}. \tag{6.12}$$

This length is 1-2 times is shorter for CNT and AgNW GRP samples compared to the graphene films (as electrically continuous sheets) [188]. It may be because of inhomogeneous and discrete surfaces of the films for randomly and horizontally distributed wires and tubes. The reflected spatial nanometrics THz conductance measurement is under the hypothesis of diffusive coefficient [cf. column 2 of Table 6.7] with time $t_c = L_c / D_c$ (~sub-ps) in transport regime, which is expressed by:

$$D_c = E_f \mu / 2e. \tag{6.13}$$

The characteristic length scale around 1 THz and 0.2 THz are demonstrated in columns 3 and 4 of Table 6.7. This length can be considered as the distance which a charge carrier travels within one-half time of an oscillating electric field. This will consequently change the conductivity response at different frequencies corresponding to a probing length.

Table 6.7: The extracted D_c: diffusive coefficient, and L_c: characteristic length around 0.2 and 1 THz of 1D and 2D graphene-like samples.

Film	D_c (cm²/s)	L_c (nm) at 0.2 THz	L_c (nm) at 1 THz
SWCNT	80	78	35
MWCNT	105	90	41
MWCNT1	60	67	31
MWCNT2	50	62	28
MG1	170	113	51
MG2	265	142	64
GRP	130	99	45
AgNW GRP1	90	83	38
AgNW GRP2	70	73	33

6.4.2   Graphene-Like Sample THz Characterization for the new Optoelectronics

Fig. 6.11 extends the characteristic length in the frequency range of up to 100 THz of all samples taken in this study. It maps the theoretical and contact experimental projected intrinsic Sub-THz and THz cut-off frequency of the graphene and CNTs based device in the previous reports (such as transistors and photodetectors) with different channel lengths. Table 6.8 shows instances of Fig. 6.11 for the 1D and 2D graphene-like films applied to the devices in comparison with noncontact THz-TDS measurement to predict the cut-off frequencies of the sample before fabricating whole devices. The cut-off frequency of devices designed from the graphene and CNTs films increase as the characteristic length of the channel decreases. In a wider perspective, there is a dependency between diffusion coefficient time in the samples and the cut-off THz frequency which increases with decreasing the channel length. For clarity, it can be noted that the fabrication process, deposition, the level of impurity in graphene, the gate and substrate materials are the main reasons for the different cut-off frequencies for the same length of channel. The application of this study proves that there is a direct relation between the nanometric characteristic length and channel length for graphene-based devices in sub-THz and THz ranges.
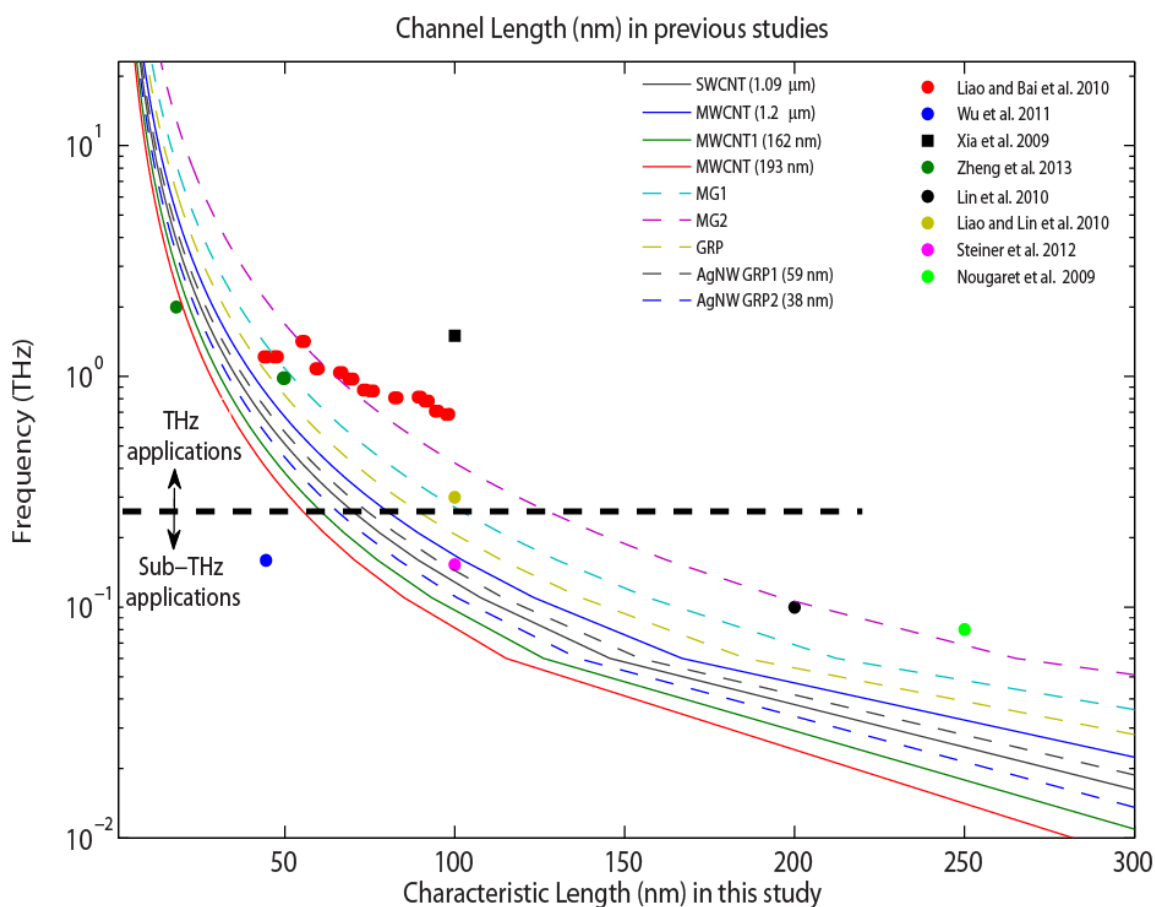
Figure 6.11: The achieved frequency for different characteristic lengths in this study for graphene-like samples (lines) in comparison with the projected cut-off frequencies for different graphene and CNT channel lengths in previous studies (dots: Liao and Bai et al. [195], Liao and Lin et al.[116], Wu et al. [196], Xia et al. [197], Steiner et al. [198], Zheng et al.[199], Lin ea al. [115], and Nougaret et al.[200]).

Table 6.8: The detailed examples of prediction for the cut-off frequencies of 1D and 2D graphene-like optoelectronic devices in Fig. 6.11 that can be obtained by deriving the characteristic length of noncontact transmission/reflection THz-TDS measurements without requirement for post process pattering.

Graphene-Like Films	Noncontact transmission/reflection THz-TDS measurements		Contact measurements in optoelectronic devices		Ref.
	Sub-THz/THz Characteristic length (nm)	Frequency (THz)	Channel length (nm)	Cut-off Frequency (THz)	
1D	99	0.16	100	0.15	[198]
	212~265	0.06	250	0.08	[200]
2D	55	1.35	55	1.4	[195]
	66	0.96	67	1	
	48	1.21	50	1.2	
	49	0.9	50	1	[199]

6.5   Conclusions

This chapter has dealt that the comparative Drude and non-Drude theoretical models from the transmission and reflection THz-TDS measurements give one of the major advantages of using THz conductivity model not only to extract the DC conductivity but also to study the high carrier mobility responses of samples without using any contact element or post-process pattering. These achievements have been validated and discussed with the recent state-of-the-art contact measurement results in order to be applied for the new optoelectronic devices to operate at the sub-THz and THz frequencies.

The difference between the extrapolated DC conductivity from the noncontact THz measurements and the ones from contact measurement was because of ambient conditions such as temperature, variation in thickness of graphene layers, implementation of probe contact measurement, and micrometer-scale using contact probes conductance measurement in DC compared to noncontact transport probed by THz conductivity measurement.

The noncontact THz-TDS has presented a directly conductivity-dependent observation of the ultrafast dynamic responses (i.e., carrier density and high mobility) for the graphene-like samples without requirement for post process patterning. The THz characteristic length observed from diffusion time of carbon nanotube and graphene samples have revealed. This provides an advance study required to develop new optoelectronic devices to generate and detect THz frequencies. The results have showed that this frequency increases with the reduced length, as the length scales down to a few nm and reaches a few tens of THz.

Chapter 7: Conclusions

THz electromagnetic waves certainly push the border in science and technology (sensing, imagery, telecoms…) to higher performance. Thus high technology devices and systems are more and more compulsory. The THz-TDS is known for years to be a precise tool for noncontact characterization of samples like semiconductors/semimetals. The THz-TDS delivers the magnitude and phase of the THz waves transmitted or reflected by the samples, the complex permittivity of the sample material is obtained from THz-TDS data. In the case of conductive materials, the THz conductivity can be calculated from the complex permittivity.

The new optoelectronic devices request new materials and techniques, among which graphene and CNTs are promising due to their unique optical and electrical conductivity behavior. This study was a contribution to the effort of the new graphene and CNT devices characterization. Difficulty in deposition and integration of such fragile samples to the optoelectronic devices may prevent a multiple measurement procedure and/or subsequent use of the tested devices.

The new work in this study has presented that carriers transport, scattering and density characterization at and near the Dirac point, related to the quantum capacitance of the graphene-like materials, with Fermi level of 0.2~0.4 eV at room temperature, can be characterized by low photon energies of THz wavelengths (4.2 meV at 1 THz). By taking the advantages of coherency, large dynamic and simultaneously measuring of magnitude and phase of the noncontact THz-TDS, this thesis has used the transmission and reflection measurements to extract the frequency-dependent electrical and optical properties of high conductance graphene nanostructure samples deposited on top of the substrates in the frequency range of 0.1-2 THz.

The DC conductivity could not be directly determined, as the available THz power decreases sharply and falls below the noise level at lower frequencies. Also, the results showed that the electrical and optical frequency-dependent parameters were rather noisy due to thickness of thin films compared to the thick substrates and also the limited sensitivity of the THz-TDS set-up over 1.5 THz. Because of a great interest which relies a wide range of electronic device applications and minimum effect of water line absorptions in the frequency range of 225-500 GHz, the results have been compared to the frequency range of by CW technique, taking the advantages of characterization using a VNA with the high spectral resolution and good dynamic range in the mid-frequency range (60-70 dB around 500 GHz). The results showed a good agreement between the THz-TDS and THz CW data.

As a new work and for the first time, this thesis also has extended this spectra range at low and higher frequencies to study the key electrical and optical parameters of the graphene-like and CNT thin films using theoretical Drude and non-Drude conductivity models. These results were validated with the experimental measurements. This allows applying such unique characterization for the new optoelectronic devices from zero-frequency (i.e., so-achieved DC) upto several THz frequencies without using any contact tools in these frangible samples. In the THz gap, the graphene conductivity is mainly determined by intraband transitions. Therefore, the dependence of conductivity with Fermi level is high in the THz ranges and reduces to zero for the visible range. The electrical conductivity of graphene films with zero band-gap was almost three orders of magnitude at DC level, and two orders of magnitude at THz frequencies, larger than the one of carbon nanotube films.

This extraction procedure was validated by the good agreement between the so-obtained DC conductivity and the one measured with a classical four-point probe in-line contact method. The difference between the extrapolated DC conductivity from the noncontact THz measurements and the ones from contact measurement can be attributed to the ambient conditions such as temperature, the slight variation in thickness of graphene layers, difficultly to implement of probe contact measurement when it deals with thin films where the probes may mechanically damage the film at the contact location, and micrometer-scale

using contact probes conductance measurement in DC compared to noncontact AC nanoscopic transport probed by THz conductivity measurement.

The results have shown that the CNT and graphene-like materials conductivity indeed depends on the crystallinity of the graphitic layers and the number of surface defects. The backward scattering occurring in the free electron movement may be explained by the structural disorder of the graphene film Drude response. It has been shown that the performance of integrating dielectrics of pristine graphene based devices can be reduced because of defects into the carbon lattice in the THz characterization of graphene-like materials.

The whole spectrum analysis gives us reliable information on the frequency-dependent complex refractive index, absorption and conductivity of the samples. The conductivity of the films was extracted from THz-TDS data using combined conductivity models in this frequency range. The agreement between measured and fitted values has been demonstrated in a good shape, even though the experimental values were slightly noisy for below 0.1 THz and for above 1.5 THz. The another novelty of this thesis was a comparative optical and electrical study of one-dimensional (1D) and two-dimensional (2D) graphene nanostructures using Drude and non-Drude (Drude-Lorentz and Drude-Smith) models to demonstrate the potential feature of broadband THz-TDS measurements to derive the AC and DC electrical conductivity as well as to extract the optical parameters and ultrafast mobility carrier transport parameters without the need for application of gating potentials or magnetic fields.

The combination of noncontact THz-TDS measurement and Drude/non-Drude models in this work not only extrapolated the DC values but also it presented a directly conductivity-dependent observation of the ultrafast dynamic responses (i.e., carrier density and high mobility) for the graphene-like samples without requirement for post process patterning. The THz characteristic length observed from diffusion time of carbon nanotube and graphene samples have revealed. This provides an advance study required to develop new optoelectronic devices to generate and detect THz frequencies. The new results of this study showed that this frequency increases with the reduced length, as the length scales down to a few nm and reaches a few tens of THz.

The achieved results in the presented work open up new lines of the THz spectroscopy application as a noncontact tool for the nanometrics material study in various industries such as fabrications of semiconductor devices. A noncontact THz-TDS is particularly promising to map the complex nanoscopic conductance materials with different number of layers. In a wider outlook, the application of this study can be extended to measure the conductivity values of stack of graphene layers for various structures on the optoelectronic devices. The THz-TDS reveals that electrical and carrier charge characterization of high conductance materials can be applied to semiconductors or polymer-based devices without need for post process patterning.

Another possible direction for our future research is to derive a more comprehensive experimental and theoretical model for the optical conductivity (finite band-gap, electron-electron interaction and excitations) of graphene and carbon based devices. It can be focused on the extinction of conductivity models to the visible band, for example, to study plasmon waves on the surface of graphene-like material. Using such features enable us to explore the possibilities of other applications such as photodetectors and optical modulators which highly depend on the understanding of both THz and visible frequency-dependent conductivity.

Last but not least, the future research line of graphene and CNT materials can be applied to the contrast agents in the biomedical applications for photoacoustic and thermoacoustic tomography, which is currently running in our lab in GOTL at UCIIIM in the OILTEBIA project funded by the European Union.

Appendices

Appendix A: THz Pulsed vs. Continuous Wave Spectroscopy

There are many techniques to generate and radiate the THz EM waves based on the applications and features such as power, tunability, limitation frequency range, and cost of systems. Table A.1 compares the different THz sources which are available commercially or in research grades.

Table A.1: List of available THz sources and their features for Spectroscopy (Ref: www.coherent.com).

Technology	Direct Laser				Laser-Enabled	Electronic	
	Optically Pumped	Quantum Cascade	Parametric Oscillator	Photomixer	Time-Domain System	Backward Wave Oscillator	Direct Multiplied Sources
Power (average)	Up to 1 W at specific frequencies	Several mW	10's nW	10 nW	~ 1 μW	mW	Up to μW
Frequency range	0.3-10 THz	2-10 THz	1-3 THz	0.3-10 THz	0.1-10 THz	0.1-1.5 THz	0.1-1.5 THz
Tunability	Discrete Lines**	10 GHz	1-3 THz	0.3-10 THz	Depend on resolution	20% of f_0	10-15 % of f_0
Wave form	Pulsed/CW	Pulsed/CW	Pulsed	CW	Pulsed	Pulsed/CW	CW

* can be converted to tunable output using a schottky-based sideband generator.

In Table A.1, there are two types of THz wave sources in different frequency operations and emission modes:

- Continuous wave (CW),
- Pulsed or time-domain.

As the THz CW systems operate at a single frequency and emission modulated up to GHz frequencies, they are narrowband and, usually, have a limited tunability with high spectral resolution in several MHz. Because of which, CW systems are useful in gas phase spectroscopy rather than solid or liquid phase. The CW detection can be done either in narrowband or broadband. Narrowband ones, usually, are sensitive to a specific frequency and with less noise that do not require modulation to realize high sensitivities. Broadband

detectors ones are sensitive to the broader frequency range and modulation that they need filtering to reduce the effects of background noise.

The pulsed THz radiation offers a higher bandwidth and permits very fast measurements - a spectrum can be acquired within milliseconds. The system operates based on the generation and detection of an electromagnetic transient that has duration of few picoseconds. The frequency resolution is limited to several GHz. The time-domain generations are the short pulse made of many frequencies that can be accessed with a Fourier transform of the pulse. The time-domain systems are suitable in spectroscopy and ultrafast phenomena studies in a broadband frequency range. In contrast, a CW system features a somewhat lower bandwidth and requires longer measurement times - acquiring a spectrum typically takes several minutes. Table A.2 summarizes the major differences between CW and time-domain systems.

Table A.2: Comparison between Continuous Wave and Pulsed THz spectroscopy systems features.

THz Spectroscopy	Frequency Gap	Specification
CW	100GHz-1.5 THz	-High resolution, -Narrowband, -No immediate spectra data, -High power available, -High sensitivity, -Available in active and passive configurations.
Time-Domain/Pulsed	100GHz-5THz	- Broad spectrum, - Coherent phase and amplitude information, -Thickness and depth information, -Available in active mode, - Lower resolution than CW.

Appendix B: THz Temporal Window and THz-TDS Extraction Data

B.1 Time Window

To study the window size of the main echo in the THz transmission analyze, the different time-domain window sizes of the spectra air, bar substrate and the substrate cover with μm CNT thin films were studied [53]. Fig. B.1 shows the measured THz spectra for the air reference, the substrate reference, and the CNT samples. The substrate thickness and CNT absorption change the phase and intensity of THz air field.
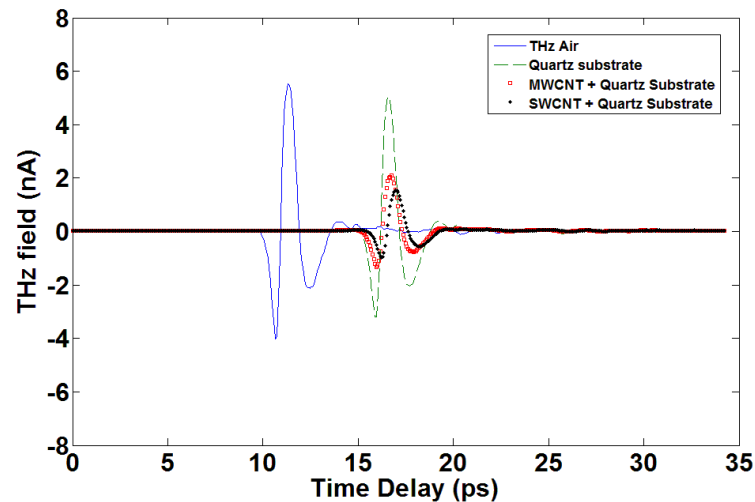
Figure B.1: The THz temporal signals of free space, quartz substrate, and MWCNTs and SWCNTs samples.

Fig. B.1 shows the THz temporal signals of 35ps with sampling number of 512 and time step of 67 fs for all measured samples. To transform these THz temporal signals into the frequency domain, the Fourier transform technique explained in Chapter 3 was applied with different time windows (20ps, 25ps and 30ps). The results in Fig. B.2 shows that by decreasing the window size in the time domain, the smoother THz spectrum in frequency domain can be observed. But, the important information such as absorption lines and phase details is missed in the THz signals by reducing the window. This is more distinct where the edge of time window is much closer as possible to the THz temporal echoes (i.e., of 20 ps).
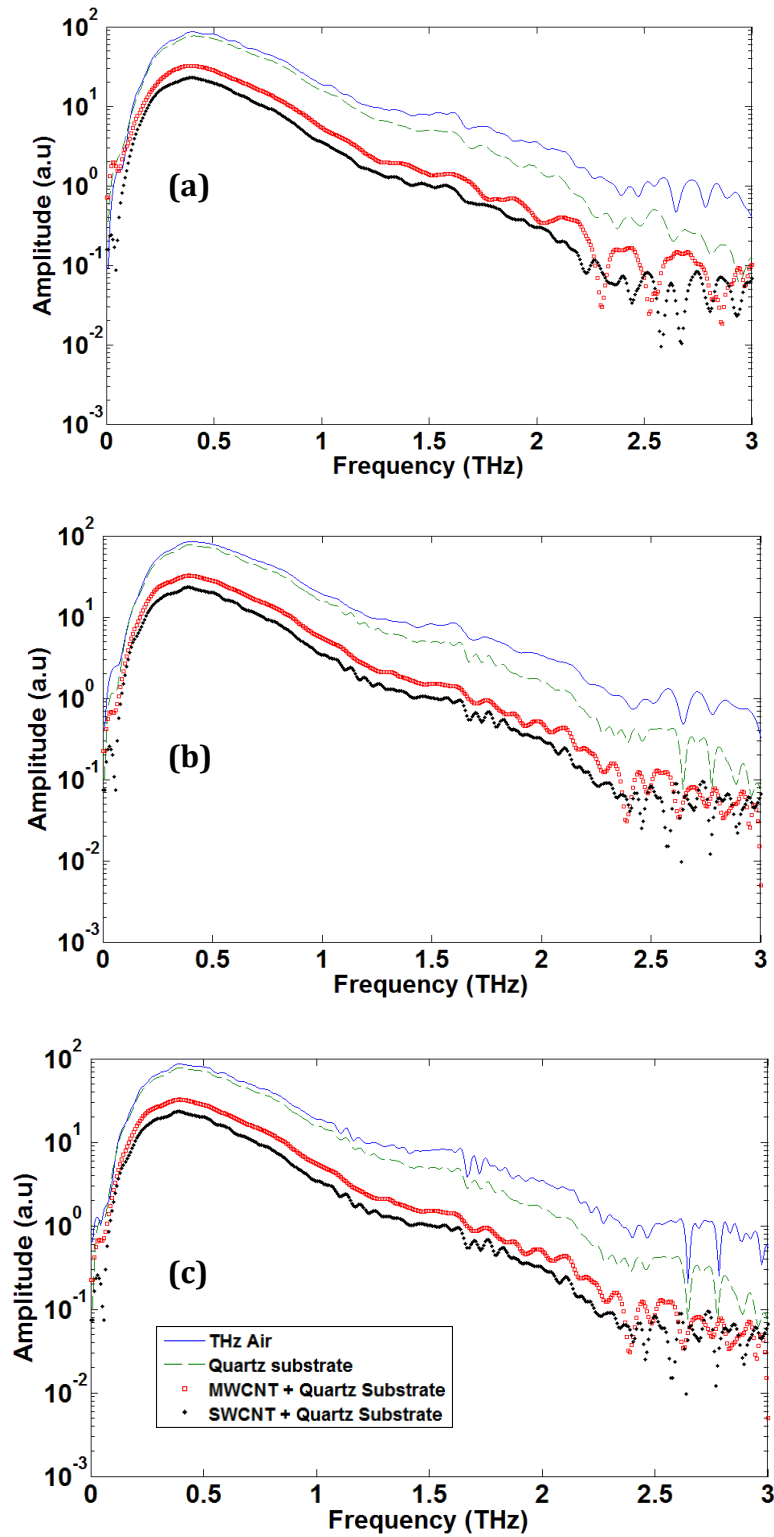
Figure B.2: The THz spectra for time windows of (a) 20ps, (b) 25ps and (c) 30ps.

Larger window sizes give us better frequency resolution, but have more variability in the high frequency range. A small window size averages out the low frequency information because each window gets de-trended. The approximately lowest frequencies (Δf) that can be resolved with the different window sizes (T) are calculated in Table B.1 according to the simple explanation of $\Delta f = 1/T$.

Table B.1: Different window sizes resolved different frequency resolutions.

Time window (ps)	Lowest frequency resolution (GHz)
20	50
25	40
30	33

B.2 Extraction Principle

The obtained THz fields in the frequency-domain are complex functions of amplitude and phase. In the basic THz-TDS analysis, two main waves need to be measured:

1- The input or reference signal $THz(\omega)_{input}$: there is no any sample between the emitter and receiver. This is the air reference signal.

2-The output signal $THz(\omega)_{output}$: the input signal is modified (in amplitude and phase) because of passing through the sample.

In a simple definition, the absorption (α) and dispersion (n_{real}) properties of sample (thickness of d) can be obtained as functions of frequency considering the above input and output THz signals by:

$$THz(\omega)_{output} = THz(\omega)_{input}\, e^{\left(-\frac{d\,\alpha(\omega)}{2}\right)} \times e^{\left(i\frac{2\pi}{\lambda}n_{real}(\omega)d\right)}.$$

(B.1)

Table B.2 shows the remarkable parameters that can derived from the THz-TDS analysis and the ratio between two $THz(\omega)_{output}$ and $THz(\omega)_{input}$ signals in (B.1).

Table B.2: The electrical and optical parameters can be achieved from the THz-TDS measurements.

Parameter	Symbol	Unit
Index of refraction (real part)	$n_{real}(\omega) = 1 + [\dfrac{\varphi_{output} - \varphi_{input}}{d\omega c^{-1}}]$	-
Complex Index of refraction	$(n = n_{real} + in_{img})$	-
Power absorption	$\alpha(\omega) = \dfrac{1}{d}\ln\dfrac{THz(\omega)_{output}}{THz(\omega)_{input}} = \dfrac{4\pi n_{img}}{\lambda}$	1/cm
Conductivity (real part)	$\sigma_{real}(\omega) = 2\omega\varepsilon_0 n_{real}(\omega)n_{img}(\omega)$ $= c\alpha(\omega)n_{real}(\omega)\varepsilon_0$	$1/\Omega.\,cm$
Surface Conductivity	$\sigma_s(\omega) = \sigma_{real}(\omega)d$	$1/\Omega.sq$

Fig. B.3 shows the temporal signals and spectra of the thick quartz sample and its air reference. All measurements were carried out with dry air in the THz-TDS box as explained in Chapter 4.
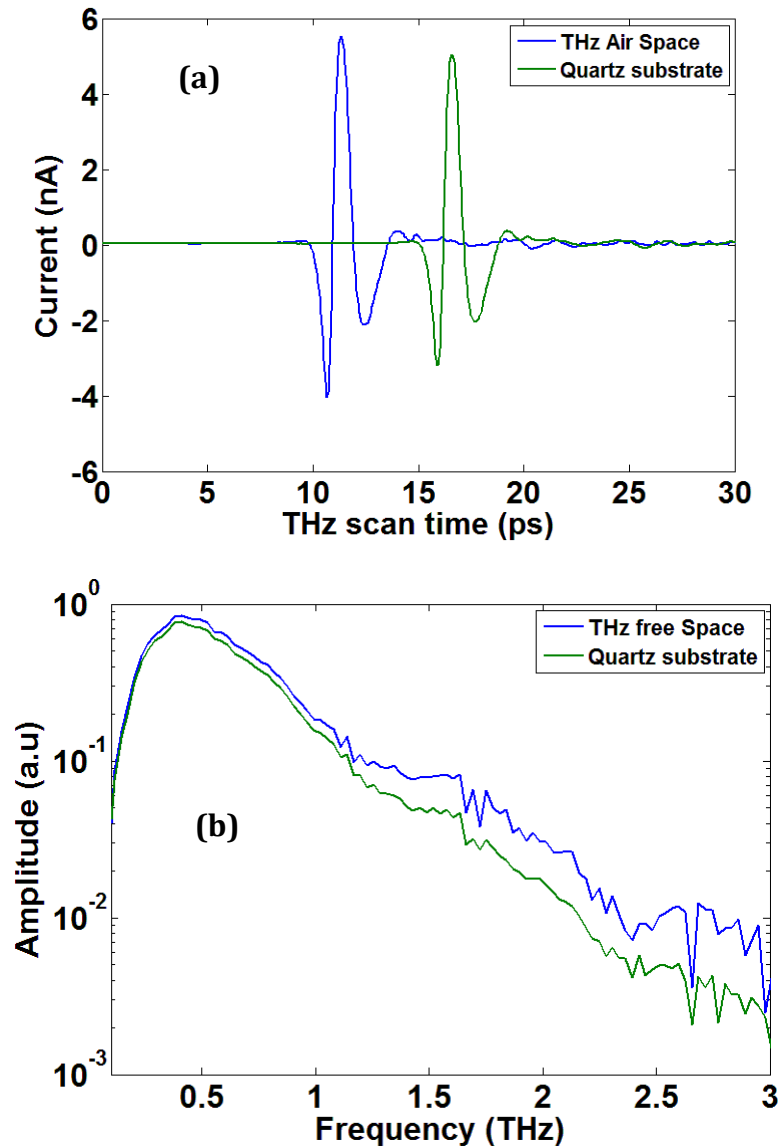
Figure B.3: The THz air and quartz substrate signals in (a) the time domain and (b) transformed spectra in the frequency domain using Fourier technique.

In a complete THz-TDS analysis, as demonstrated in Fig. B.4, there are three THz fields:

1- $E_0(\omega)$ is the incident field coming from THz emitter to the sample,

2- $E_a(\omega)$ is the air reference field after passing the air space with thickness of L,

3- $E_s(\omega)$ is the field passed through the sample with thickness of L.

In this case, there are two complex refractive indices:

1- $\tilde{n}_a = n_a + ik_a$ is related to the air reference ($n_a \approx 1$ and $k_a \approx 0$),

2- $\tilde{n}_s = n_s + ik_s$ is related to the sample.

These refractive indices give two propagation constants of different layers with thickness of L:

$$P_a(\omega, L) = e^{(\frac{-i\tilde{n}_a L}{c})},$$ (B.2)

$$P_s(\omega, L) = e^{(\frac{-i\tilde{n}_s L}{c})}.$$ (B.3)
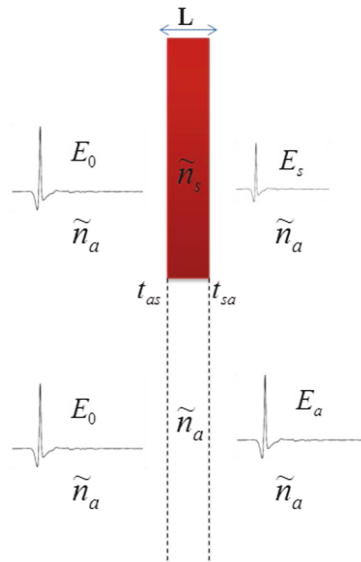
Figure B.4: The schematic of THz-TDS transmission experimental for the stand-alone sample (thickness of L) with parallel face to electric field.

For the complex transmission fields of the reference air and the sample, we can respectively write:

$$E_s(\omega) = E_0(\omega)t_{as}(\omega)P_s(\omega, L)t_{sa}(\omega)FP(\omega),$$ (B.4)

$$E_a(\omega) = E_0(\omega)P_a(\omega, L),$$ (B.5)

where $t_{as}(\omega) = \dfrac{2\tilde{n}_a(\omega)}{\tilde{n}_a(\omega) + \tilde{n}_s(\omega)}$ and $t_{sa}(\omega) = \dfrac{2\tilde{n}_s(\omega)}{\tilde{n}_a(\omega) + \tilde{n}_s(\omega)}$ are the Fresnel equations of the transmission coefficients of the air->sample and the sample->air. The backward and forward reflections in the sample, so-called Fabry-Perot (FP), can be defined as a series of the multi-reflections of the incident waves inside the sample:

$$FP(\omega) = \sum_{k=0}^{+\infty} \{r_{s,a}^2 \cdot p_{s,a}^2 (\omega, L)\}^k = \frac{1}{1 - (\dfrac{\tilde{n}_s - \tilde{n}_a}{\tilde{n}_s + \tilde{n}_a})^2 \cdot e^{[-2i\tilde{n}_s \omega L / c]}} . \tag{B.6}$$

The complex transmission coefficient of the sample can be achieved by recoding the ratio THz signal between the sample and the air reference:

$$T(\omega) = \frac{E_s(\omega)}{E_a(\omega)} = \frac{t_{as}(\omega) P_s(\omega, L) t_{sa}(\omega)}{P_a(\omega, L)} FP(\omega) , \tag{B.7}$$

$$T(\omega) = \frac{E_s(\omega)}{E_a(\omega)} \approx \frac{4\tilde{n}_s \tilde{n}_a}{(\tilde{n}_s + \tilde{n}_a)^2} \exp\left[-i(\tilde{n}_s - \tilde{n}_a)\omega L / c\right] FP(\omega) = A(\omega)e^{i\phi(\omega)}. \tag{B.8}$$

If the sample is thick, we can eliminate the FP effect inside the sample [88]. The simplified complex transmission in (B.8) can be rewritten as:

$$T(\omega) \approx \frac{4\tilde{n}_s \tilde{n}_a}{(\tilde{n}_s + \tilde{n}_a)^2} \exp\left[-i(\tilde{n}_s - \tilde{n}_a)\omega L / c\right]. \tag{B.9}$$

The next step is to extract the phase information ($\arg[T(\omega)]$) and obtain the absorption coefficient ($\ln[T(\omega)]$) of the sample from the complex transmission in (B.9) given by:

$$arg[T(\omega)] \approx arg[\frac{4\tilde{n}_s \tilde{n}_a}{(\tilde{n}_s + \tilde{n}_a)^2}] - (\tilde{n}_s - \tilde{n}_a)\frac{\omega L}{c} , \tag{B.10}$$

$$ln[T(\omega)] \approx ln[\frac{4\tilde{n}_s \tilde{n}_a}{(\tilde{n}_s + \tilde{n}_a)^2}] - k_s \frac{\omega L}{c} . \tag{B.11}$$

The above equations are fixed-point (or convergence) functions $\lim_{x \to C} f(x) = C$ [201]. To solve them and extract the real n_s and imaginary k_s part of refractive index at different THz frequencies, we can write:

$$n_s = f_1(n_s, k_s) \approx -\frac{c}{\omega L}(arg[T(\omega)] - arg[\frac{4\tilde{n}_s\tilde{n}_a}{(\tilde{n}_s + \tilde{n}_a)^2}]) + n_a, \qquad \text{(B.12)}$$

$$k_s = f_2(n_s, k_s) \approx -\frac{c}{\omega L}(ln[T(\omega)] - ln[\frac{4\tilde{n}_s\tilde{n}_a}{(\tilde{n}_s + \tilde{n}_a)^2}]). \qquad \text{(B.13)}$$

If the sample is transparent and $1 \le n_s \le 2$, we have following approximation:

$$0.9 \le \frac{4\tilde{n}_s\tilde{n}_a}{(\tilde{n}_s + \tilde{n}_a)^2} \le 1. \qquad \text{(B.14)}$$

So, Eq. (B.12) can be simplified to calculate the real part of complex refractive index of sample by:

$$n_s(\omega) \approx -\frac{c}{\omega L} arg[T(\omega)] + n_a, \qquad \text{(B.15)}$$

and the extinction coefficient or the imaginary part refractive index from (B.13) is:

$$k_s(\omega) \approx -\frac{c}{\omega L} ln[T(\omega)]. \qquad \text{(B.16)}$$

Finally, the frequency-dependent absorption coefficient of sample can be calculated from (B.16) by:

$$a(\omega) \approx 2\omega \frac{k_s(\omega)}{c} \qquad \text{(B.17)}$$

If the approximation condition in (B.14) cannot be made, the iteration numerical algorithm is applied in (B.8) to find the roots of function once the phase and amplitude of measurement are equal to the calculated ones. It has been programmed in the Matlab and Wolfarm Mathematica platforms by the author of this thesis and the algorithm shows very efficient (precision of 0.001) and quick response (less than 1 sec for a normal i5-based PC) by starting points of $n_s = 1$ and $k_s = 1$. The results show after a few iterations the roots of function can be found. Table B.3 shows the real refractive index and power absorption for the different doped semiconductors at 1 THz as reported in Refs. [145, 190, 202, 203].

The extracted complex reflective index for the THz signal will be demonstrated in the next section by studying the FP and thickness impact.

Table B.3: The refractive index and the power absorption of different semiconductor samples.

Samples	*Thick* (nm)	$\sim n_{s*}$	$\sim\alpha*$ (1/cm)
Silicon (n-type)[202]	29E+04	3.2	75
Silicon (p-type) [202]	20E+04	3.2	550
GaAs (n-type)[145]	90	9	5800
GaN (n-type)[203]	45E+2	4	1500
ITO[190]	345	30	30
Quartz	1750	1.7	1.1
Fused Quartz	2150	1.9	1.2

* The values are around 1 THz

B.3 Fabry Perot and Thickness Influences

In this study, a thick quartz sample is under test. In order to study the multi-reflection effect in the obtained results, the complex refractive index functions calculated in the THz frequencies with and without considering the FP. Fig. B.5 shows the real and imaginary parts of complex refractive index achieved from the previous section by extracting the THz transmission from (B.15) and (B.16). It is seen that the FP effect is higher at lower frequency and make fluctuation at the lower frequencies below 1 THz for both the real and imaginary parts of refractive index of sample. This effect is disappeared at the high THz frequencies.

To study the influence of the thickness of the sample (as a non-absorber material in THz regime) two different values of 1.75mm and 2.15mm have been considered. Fig. B.6 shows the refractive index and the power absorption of the sample with different thicknesses in calculation. The results indicate that the refractive index more relies on thickness compared to the power absorption for such THz transparent materials. It is because of a delay shift of the phase for the larger thickness. The power absorption is almost in the

same range for both thickness of 2.15 mm and 1.75 mm as quartz shows high transparency at THz range [62].
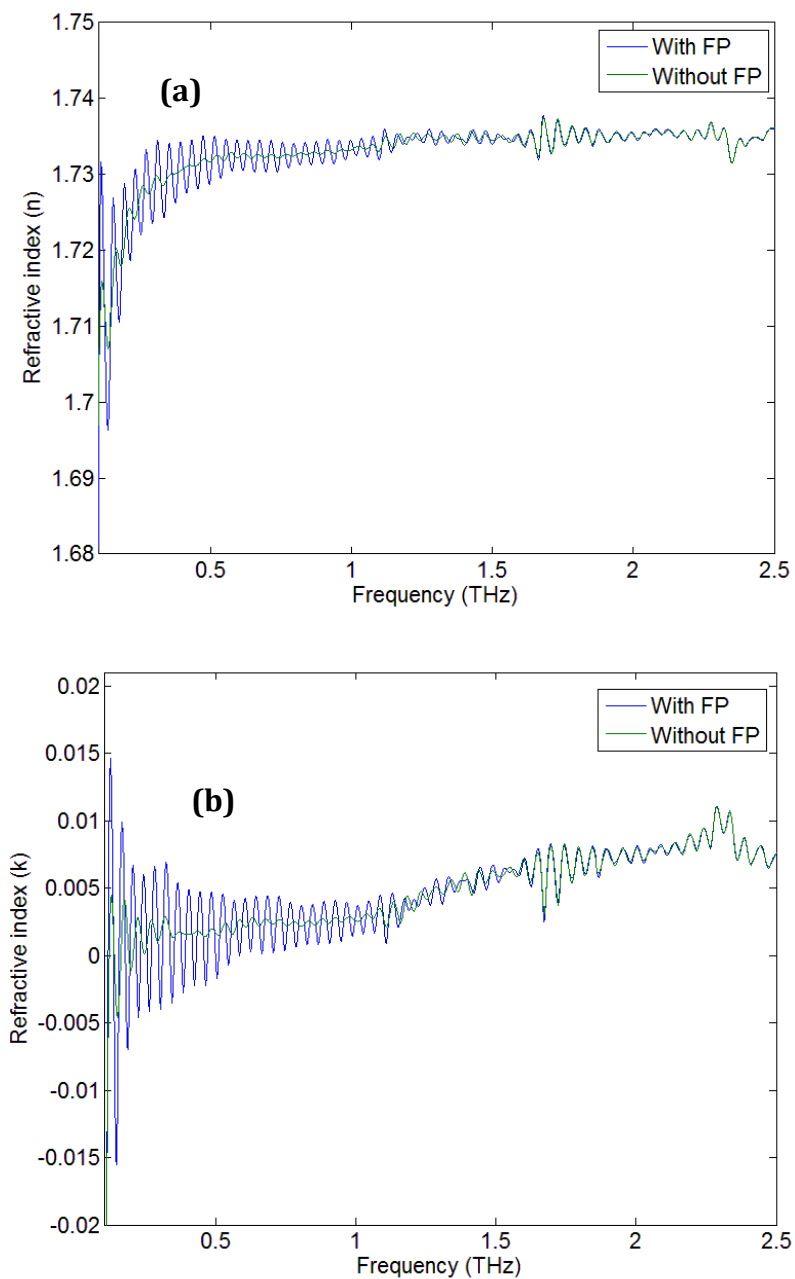
Figure B.5: The FP effect in (a) real and (b) imaginary parts of complex refractive index function of the quartz substrate.
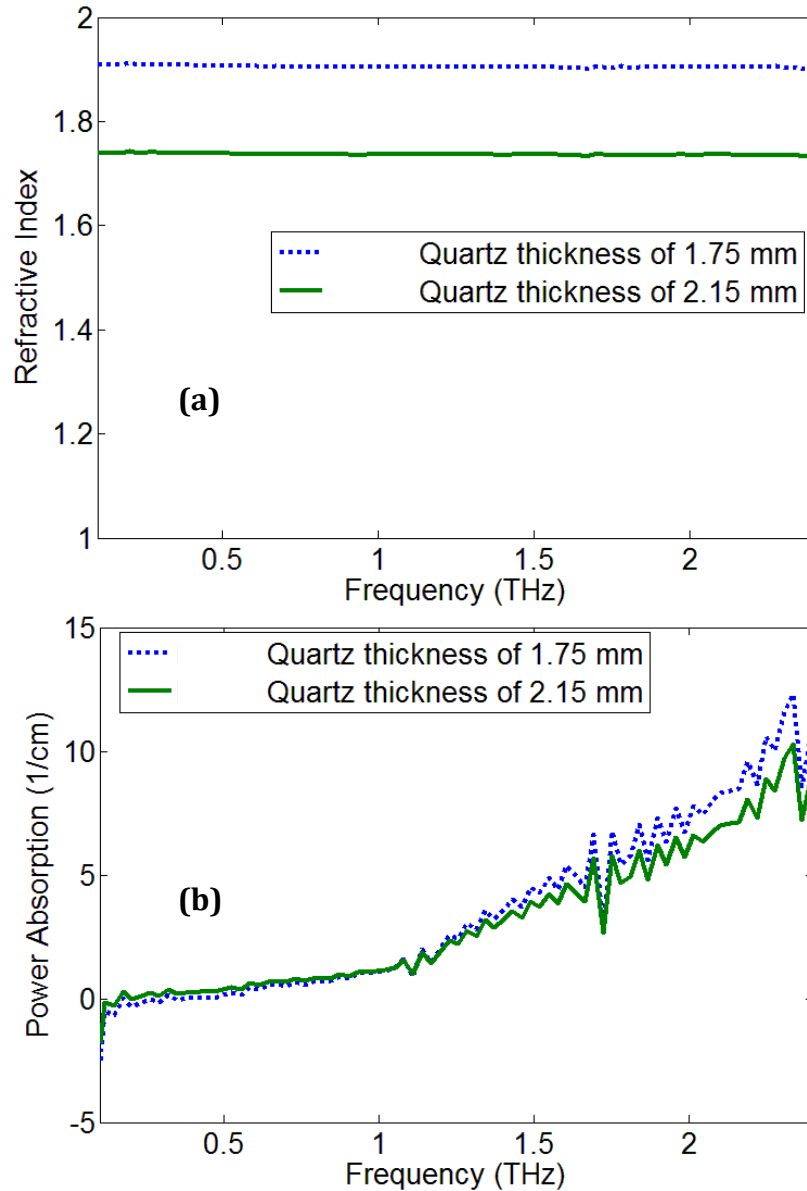
Figure B.6: Comparing the results of (a) refractive index and (b) power absorption coefficient for the quartz sample with changing its thickness in the calculation.

B.4 Preliminary Optical and Electrical Results of Micrometrics SWCNT and MWCNT Samples Using Differential Transmission THz-TDS Analysis

In this study, the SWCNT and MWCNT thin films with thickness 1.09 μm and 1.2 μm have been fabricated on face of the fused quartz substrates [cf. Appendix D.1]. The extraction of the electrical and optical properties has been performed from the differential transmission THz-TDS measurements [52]. Following the studied analysis for the reference substrate

earlier in this section, to obtain the complex refractive index of the CNT thin film in THz regime, a simple schematic with different three layers is designed [cf. Fig. B.7]. Compared to the reference substrate model, there is a new CNTs thin film layer with refractive index of $\tilde{n}_f = n_f + ik_f$ and thickness of d on top of the substrate.
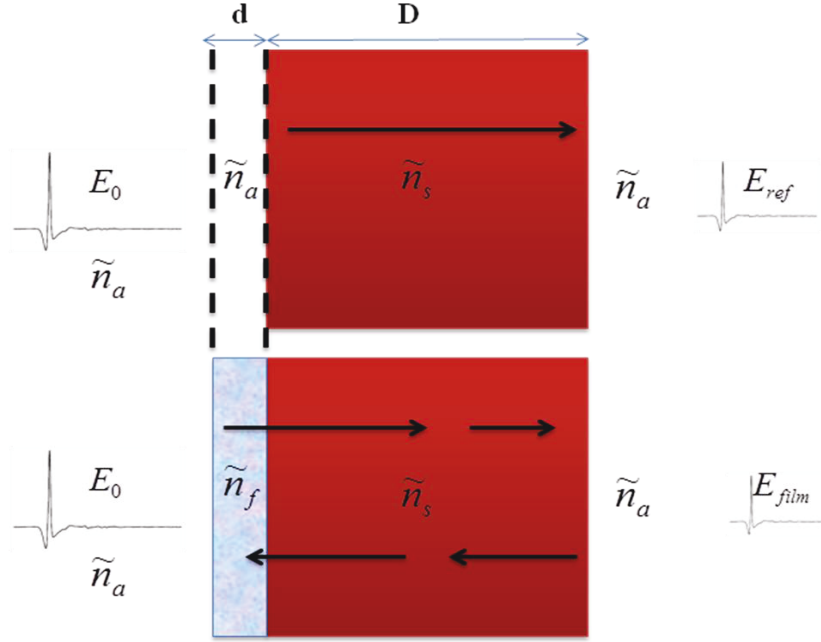
Figure B.7: The THz-TDS transmission experiment schematic by passing the signals through the thick reference substrate (with thickness D) and the CNTs thin-film (with thickness d).

In this schematic, as there are backward and forward reflections from the substrate to film the FP effect needs to be considered in the complex refractive index and power absorption, as follows:

$$E_f(\omega) = E_0 t_{12} t_{23} t_{31} \, exp(\frac{i\omega d\tilde{n}_f}{c}) exp(\frac{i\omega D\tilde{n}_s}{c}) FP(\omega)$$

$$= E_0 t_{12} t_{23} t_{31} \, exp(\frac{i\omega d\tilde{n}_f}{c}) exp(\frac{i\omega D\tilde{n}_s}{c}) \frac{1}{1 - r_{21} r_{23} \, exp(\frac{i2\omega d\tilde{n}_f}{c})}. \tag{B.18}$$

As earlier explained for the reference substrate, the transmitted THz electric field can be defined by:

$$E_{ref}(\omega) = t_{13}t_{31}\exp(\frac{i\omega\tilde{n}_a d}{c})\exp(\frac{i\omega D\tilde{n}_s}{c})E_0 . \tag{B.19}$$

The transmission and reflection Fresnel's coefficients respectively are $t_{ij} = \dfrac{2n_i}{n_i + nj}$ and

$r_{ij} = \dfrac{n_i - nj}{n_i + nj}$ as results of the electric field inside the sample after the parallel incident

angle THz beam to the sample. The differential THz field is explained by:

$$E_{diff}(\omega) = E_{film}(\omega) - E_{ref}(\omega) . \tag{B.20}$$

In the next step, the complex transmission coefficient of CNT thin film with amplitude A and phase φ is calculated by:

$$T(\omega) = \frac{E_{diff}(\omega)}{E_{ref}(\omega)} = [t_{12}t_{23}\exp(\frac{i\omega d\tilde{n}_f}{c})\frac{1}{t_{13}(1 - r_{21}r_{23}\exp(\frac{i2\omega d\tilde{n}_f}{c}))}] - 1 = A(\omega)e^{i\phi(\omega)} \tag{B.21}$$

.

Under the assumption $\left|\dfrac{\tilde{n}_f \omega d}{c}\right| << 1$ for high conductance samples, (B.21) can be simplified

($e^x \approx 1 + x$ if $x << 1$) and then the complex transmission coefficient is rewritten by:

$$T(\omega) = \frac{E_{diff}(\omega)}{E_{ref}(\omega)} \approx \frac{i\omega d}{c(n_1 + n_s)}[n_f^2 + n_1 n_s - n_1 - n_s] \approx A(\omega)e^{i\varphi(\omega)} . \tag{B.22}$$

The extracted real and imaginary parts of complex dielectric constant (or permittivity) $\tilde{\varepsilon} = \varepsilon_1 + i\varepsilon_2 = \tilde{n}_f^2$ from (B.22) are [cf. Fig. B.8]:

$$\varepsilon_1 \approx \frac{c}{\omega d}(n_a + n_s)A\sin(\varphi) - n_a n_s + n_a + n_s , \tag{B.23}$$

$$\varepsilon_2 \approx \frac{c}{\omega d}(n_a + n_s)A\cos(\varphi) . \tag{B.24}$$

Finally, the complex refractive index [cf. Fig. B.9] of the SWCNT and MWCNT films are calculated from (B.23) and (B.24):

$$n_f \approx \frac{1}{2}\sqrt{\left(\varepsilon_1 + \sqrt{\varepsilon_1^2 + \varepsilon_2^2}\right)}, \qquad \text{(B.25)}$$

$$k_f \approx \frac{\varepsilon_2}{2\sqrt{\left(\varepsilon_1 + \sqrt{\varepsilon_1^2 + \varepsilon_2^2}\right)}}. \qquad \text{(B.26)}$$
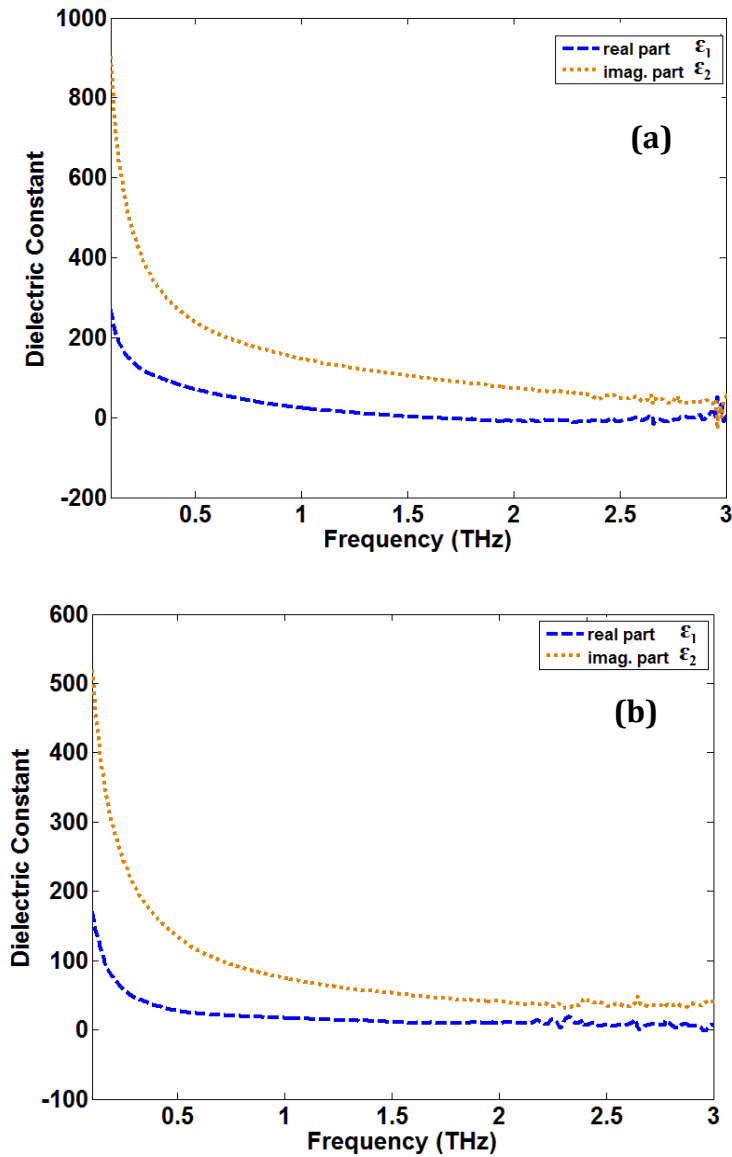
Figure B.8: The real and imaginary parts of dielectric constant of (a) SWCNT and (b) MWCNT thin films.
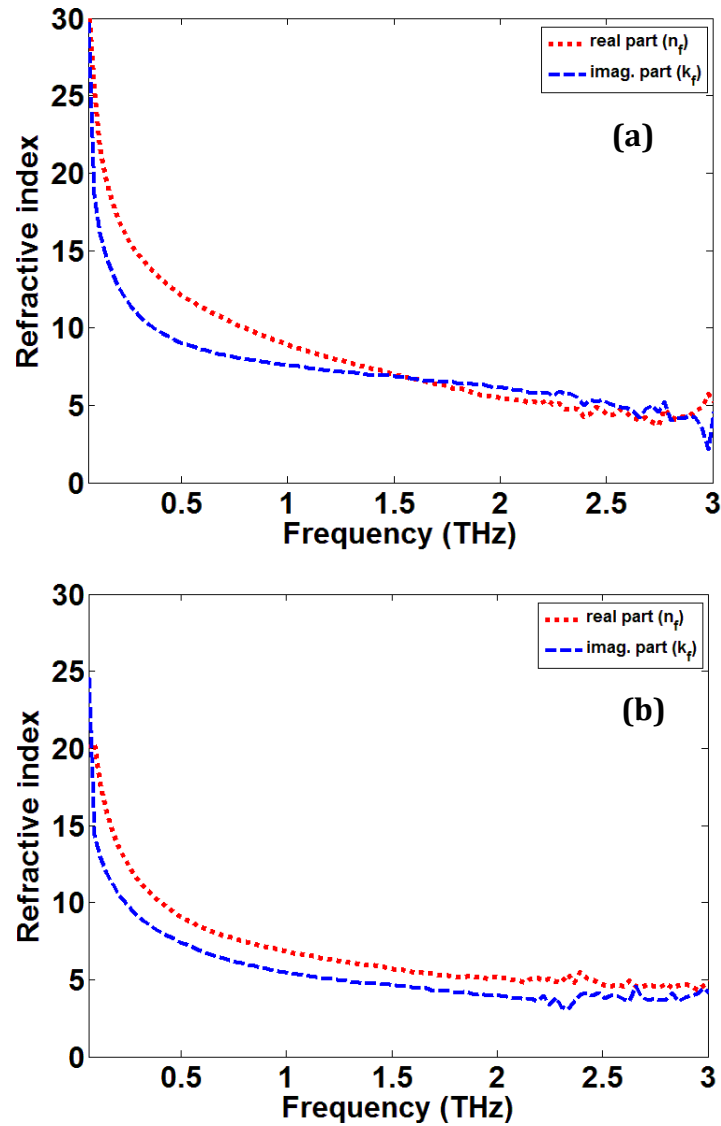
Figure B.9: The real and imaginary parts of refractive index of (a) SWCNT and (b) MWCNT thin films.

Tables B.4 and B.5 present the calculation details of the absorption (α), the complex refractive index (n) and the electrical conductivity (σ) as functions of frequency for the SWCNT and MWCNT samples using the above explained differential THz-TDS analysis.

Table B.4: The THz differential parameters of the SWCNT thin film (with thickness of 1.09 µm) deposited on top of a fused quartz substrate (with thickness of 2.15mm).

Pulse Frequency $\frac{\omega}{2\pi}$ (THz)	Reference Air			Reference Substrate			Thin-Film				
	E_0	n_a	$a = 2\omega\frac{k_a}{c}$ (1/cm)	E_s or E_{ref}	n_s	$a = 2\omega\frac{k_s}{c}$ (1/cm)	E_f	E_{diff}	n_f	$a = 2\omega\frac{k_f}{c}$ (1/cm)	$\sigma = 2c\varepsilon_0\omega n_f$ (s/cm)
0.46	-46-66i	1	0	19 +70i	1.73	0.32	20 +2i	-1-68i	12.11	1664	53.5
0.96	9+19i	1	0	12 + 12i	1.73	1.1	1-4i	-11-16i	9.09	3088	74.5
1.45	6- 4i	1	0	0.6 + 5i	1.73	3.55	0.1-1i	0.7-6i	7.15	4219	80.1
1.95	-3	1	0	0.4 + 1.5i	1.73	6.08	-0.3-0.2i	-0.7-1.7i	5.56	5106	75.4

Table B.5: The THz differential parameters of the MWCNT thin film (with thickness of 1.2 µm) deposited on top of a fused quartz substrate (with thickness of 2.15mm).
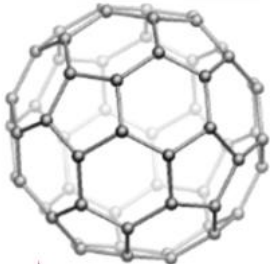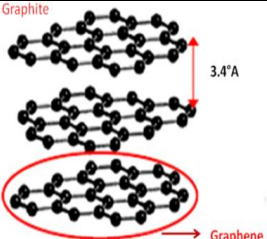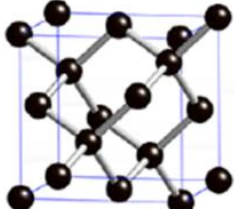
Pulse Frequency $\frac{\omega}{2\pi}$ (THz)	Reference Air			Reference Substrate			Thin-Film				
	E_0	n_a	$a = 2\omega\frac{k_a}{c}$ (1/cm)	E_s or E_{ref}	n_s	$a = 2\omega\frac{k_s}{c}$ (1/cm)	E_f	E_{diff}	n_f	$a = 2\omega\frac{k_f}{c}$ (1/cm)	$\sigma = 2c\varepsilon_0\omega n_f$ (s/cm)
0.46	-46-66i	1	0	19 +70i	1.73	0.32	16 + 24i	-3-46i	8.95	1617	38.4
0.96	9+19i	1	0	12 + 12i	1.73	1.1	5+ 2i	-7-10i	6.92	2245	41.2
1.45	6- 4i	1	0	0.6 + 5i	1.73	3.55	0.9+ 1.2i	0.3-3.8i	5.82	2861	44.2
1.95	-3	1	0	0.4 + 1.5i	1.73	6.08	0.3+0.3i	-0.1-1.2i	5.07	3261	43.9

Appendix C: Graphene and CNTs Physical Structure

C. 1 Graphene

Table C.1 shows the different carbon isomers of the carbon based material and their structures. For a carbon, there are 2s, 2px, 2py and 2pz valence orbitals. In graphene structure, three planers of 2s, 2px, 2py combine to three hybridized σ orbitals. The 2pz orbital does not couple with σ orbital for symmetry reasons. It is called π orbital [204]. Fig. C.1 shows the carbon inplanar σ and perpendicular π orbitals in a cell [205].

Table C.1: The different carbon isomers of the carbon based material [118, 119].

Carbon Material	Dimension	Hybrid	Density (g/cm³)	Bond Length (Å)	Material group/E_g	Structure
Fullerene	0-D	sp^2	1.7	1.4 (C=C)	Semiconductor /(~2 eV)	
Nanotubes	1-D	sp^2	1.2-2	1.42(C=C)	Semiconductor or Metal	
Graphite	2-D	sp^2	2.2	1.42(C=C)	Semi-metal	
Diamond	3-D	sp^3	3.5	1.54(C-C)	Insulator /(~5.5 eV)	
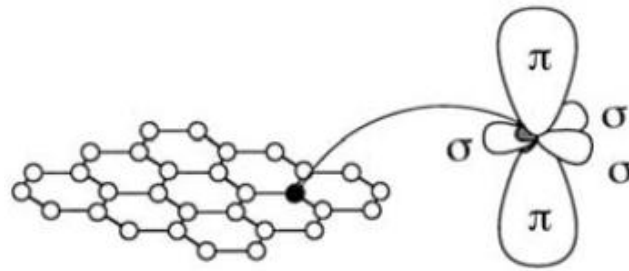
Figure C.1: The carbon valence σ and π orbitals [204].

The hexagonal graphene crystal structure is built in a triangular Bravais lattice shape with a two-atom structure within each unit cell. Fig. C.2 shows the first Brillouin zone of graphene band structure which is a hexagon with a unit cell of two atoms.

(a)   **(b)**
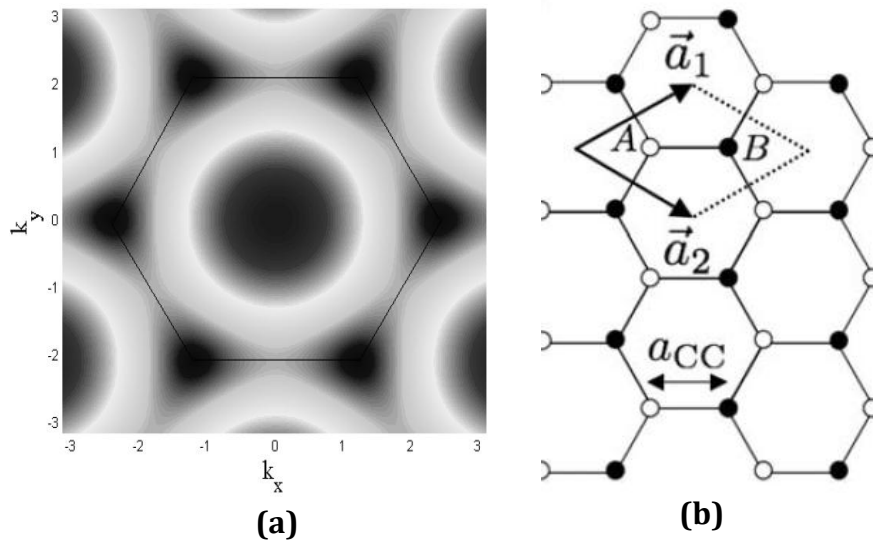
Figure C.2: (a) The first Brillouin zone of graphene layer where the solid line marks the boundary with different level of energy of the first Brillouin zone with a hexagon shape. (b) A unit cell of two atoms (A and B).

The first Brillouin zone is middle with three important points at center (Γ), corner (K) and middle of the edge (M or saddle) points of the zone [204, 206]. The map of Fig. C.2 is demonstrated in Fig. C.3 where the conduction and valance bands touch at corners of the hexagon, called the Dirac point (K points). The occupied (bonding) π and unoccupied (antibonding) π* bands do cross the K point. Fermi surface (E_f) then decreases to the six K points at the corners of the zone. Next to the Fermi energy π and π* bands have linear

dispersion[1] relation. Both electron and holes close the Fermi surface usually have quadratic dispersion relation and treat as free particles with effective mass $m^* \neq m_e$ [204].
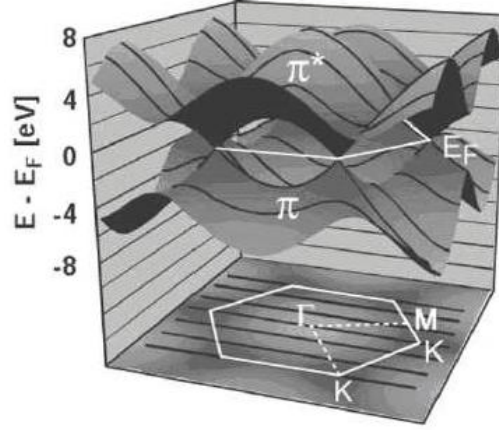
Figure C.3: The band structure of graphene and drawing of the possible optical transitions: six Dirac cones are shown in the vicinity (E-Ef=0).

The tight-binding analytical approximation expression presents good results near Fermi level for the dispersion relation and related eigenstates by focusing on π bands and only for nearest neighbor interactions [118]:

$$E_{2D}^{\pm}\left(k_x, k_y\right) = \pm V_n \sqrt{1 + 4\cos\left(\frac{\sqrt{3}k_x a}{2}\right)\cos\left(\frac{k_y a}{2}\right) + \cos^2\left(\frac{k_y a}{2}\right)}, \quad (C.1)$$

where V_n is the nearest neighbor C-C tight binding overlap energy (~3 eV) [207], k is the wave-vector in the hexagonal Brillouin zone, and $a = 1.42$ Å. E^+ and E^- correspond to the π^* and π energy bands, respectively. The high symmetry and energy values at points are $\Gamma = \left(0,0\right)$ with energy of $3V_n$, $K = \left(0, \frac{2\pi}{3a}\right)$ with energy of 0, and $M = \left(\frac{2\pi}{3a}, 0\right)$ with the energy of V_n. In case of an intrinsic graphene, we can say the Fermi level energy is around this Dirac point and charge carriers only experience a linear dispersion [208]. By expansion (C.1) in neighborhood of the K points, the low energy dispersion can be explained as:

---

[1] Linear dispersion is typical for massless Dirac fermions, i.e. particles with relativistic speed and no mass.

$$E_{2D}^{\pm}\left(\kappa\right)=\pm\hbar v_{f}\left|\kappa\right|, \tag{C.2}$$

where $\kappa=\left(k_{x},k_{y}\right)-K$ and $v_{f}=\dfrac{3aV_{n}}{2\hbar}\approx10^{6}$ is the Fermi velocity constant. This relation shows the linear nature of the electronic dispersion for small κ, equivalent to the electron energies close to the Fermi level. This characteristic infers that the carrier movement in graphene is similar to that of relativistic particles with minimum mass explained by Dirac's relativistic relation [209]. The difference with the conventional solid-state materials with the parabolic dispersion explained, by the Schrödinger in Chapter 3. This linear energy-momentum relationship occurs by intersecting the conduction and valence bands ($\kappa=0$ and $E_{g}\approx0$). The result of such a linear dispersion is a condensed matter property. Thus the charge carriers move with zero effective mass.

C.2 CNTs

Single-wall carbon nanotubes (SWCNTs) can be generally imagined as graphene sheet rolled at a certain "chiral" angle with respect to a plane perpendicular to the tube's long axis. The multi-walled carbon nanotubes (MWCNTs) is consisted of several concentric SWNTs, therefore, they have bigger diameters compared to the SWCNTs. Carbon nanotubes (CNTs) have been intensively interested because of their great physical, electrical, mechanical and optical properties [97]. Besides developing process of carbon nanotubes and controlling methods for the fabrication of tubes [210], CNTs are metals or semiconductors depending sensitively on their structures. They can be used to form metal–semiconductor, semiconductor–semiconductor or metal–metal junctions [119]. These junctions have great potential for applications since they are of nanoscale dimensions and are made entirely of a single chemical element. CNTs have the symmetric conduction and valence bands, which is advantageous for complementary electronics applications.

The conduction and valence bands of CNTs are symmetric, which is advantageous for complementary electronics applications. The conduction-band bottom and the valence-band top are at the same wave vector point, which enables optical emission. Fig. C.4

demonstrates the dispersion relation near (Kx and Ky wavevectors) the Fermi level[1] of semiconducting and metallic CNTs.
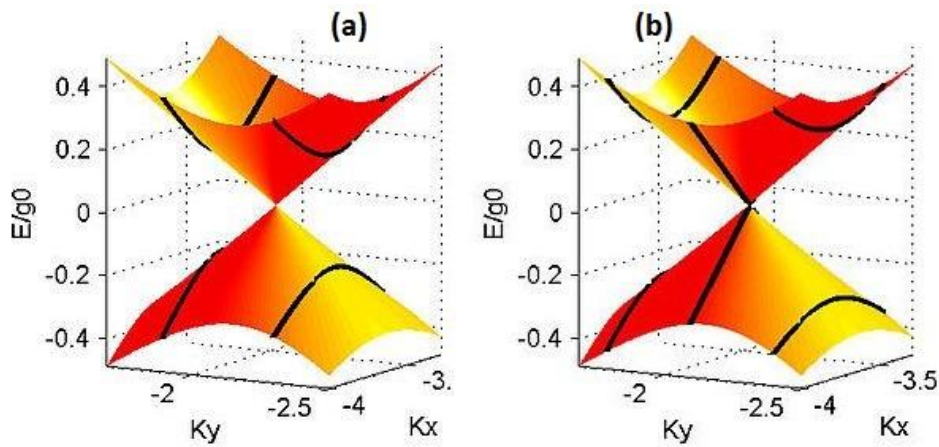
Figure C.4: The band structure and Fermi level dispersion of (a) semiconductor and (b) metallic CNTs.

The band gap energies increase with reduction nanotube diameter [211]. A pair of indices (n, m) is conveniently used instead to describe CNTs. In Fig. C.5, **C** is a (4, 2) vector: the sum of 4 unit vectors from the origin directly to the right, then 2 unit vectors at a 60° angle down and to the right. Besides this, the diameter of CNTs are obtained by $d = \dfrac{a}{\pi}\sqrt{n^2 + m^2 + nm} = \dfrac{L}{\pi}$. The vector magnitude is $a = a_1 = a_2 \approx 0.246nm$ and L is the length of vector **C**.

---

[1] Fermi energy is the maximum energy occupied by an electron at 0K
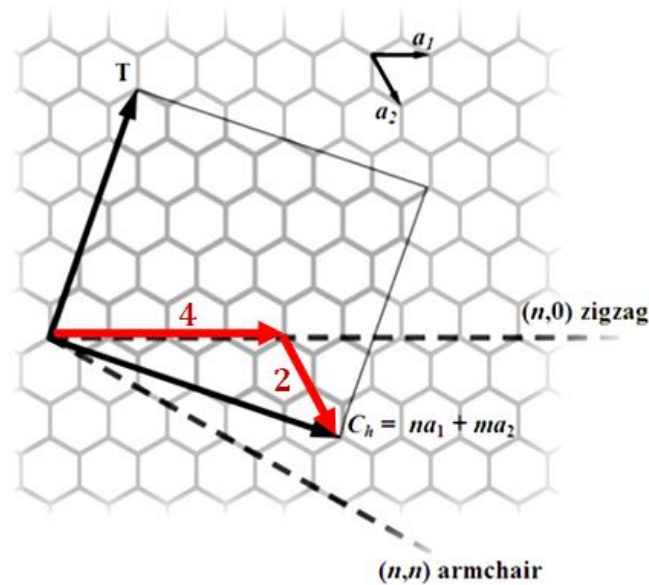
Figure C.5: Carbon nanotubes naming and vectors scheme.

The chiral angle is used to separate carbon nanotubes into three classes differentiated by their electronic properties [212]: armchair (n = m, θ = 30°), zig-zag (m = 0, n > 0, θ = 0°), and chiral (0 < |m| < n, 0 < θ < 30°).

If n=m, for example Fig. C.6 (c):

CNT has an armchair style with metallic properties (zero-band gap).

If n≠m for example Figs. C.6 (a-b):

2-1- If |m-n|= 3k (where k is an integer number and not zero) CNT has the zigzag or chiral style. CNT has semimetallic properties with tiny-band gap.

2-1- If |m-n|≠ 3k (where k is an integer number and not zero) CNT has the zigzag or chiral style. CNT has semiconductor properties with large-band gap.
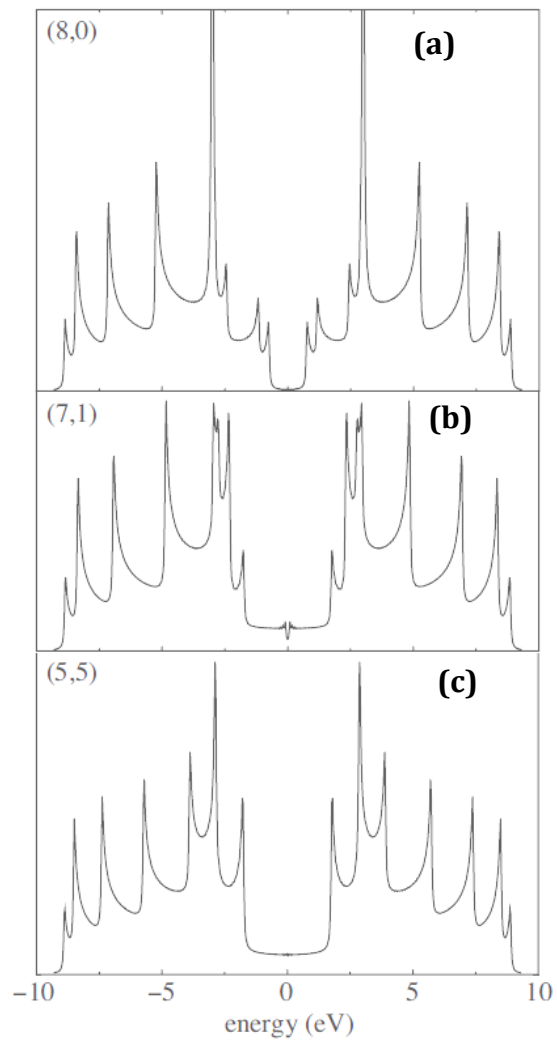
Figure C.6: The energy gap of SWCNTs while n≠m [119].

160

Appendix D: Graphene and CNT Samples

D.1 SWCNT and MWCNT Thin Films

The SWCNT and MWCNT thin films with thickness 1.09 µm and 1.2 µm were fabricated on face of the fused-quartz substrates [cf. Table D.1]. The carboxyl-functionalized of carbon nanotubes was performed and a stable suspension was formed in acetone at 1g/L. Then suspension was sprayed onto hot quartz substrate. The thickness was measured using scanning electron microscope (SEM). Once thickness was confirmed remaining samples were prepared following the above procedure. Fig. D.1 shows SEM image of CNTs sample and deposition over the quartz substrate.

Table D.1: The CNTs samples physical characterization.

Specification	SWCNT	MWCNT
Reference substrate	fused-quartz	fused-quartz
Substrate thickness	2.15 mm	2.15 mm
Size of device (LxW)	2.5cmx2.5cm	2.5cmx2.5cm
CNTs thin-film thickness	1.09 µm	1.2 µm
CNTs diameter	1.5nm	15nm
CNTs length	1-5 µm	15 µm
CNTs purity	>95%	>95%
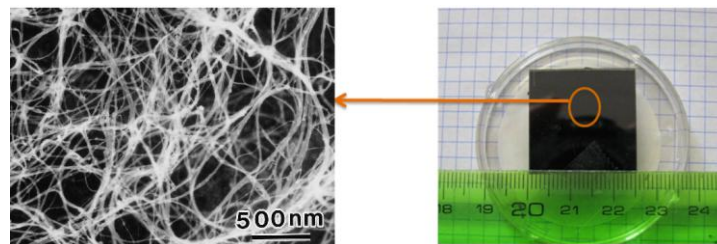
Figure D.1: The CNTs thin film deposited over the fused-quartz substrate (SEM image (left) and photography of the whole wafer (right)).

Fig. D.2 shows the atomic force microscopy (AFM) images of the MWCNT thin films deposited on a silicon substrate. Since the image was not taken right after the fabrication, dust or other external particles are present in the sample. A dust free part of the sample is shown on the left side of each figure, which clearly shows the non aligned tubes.
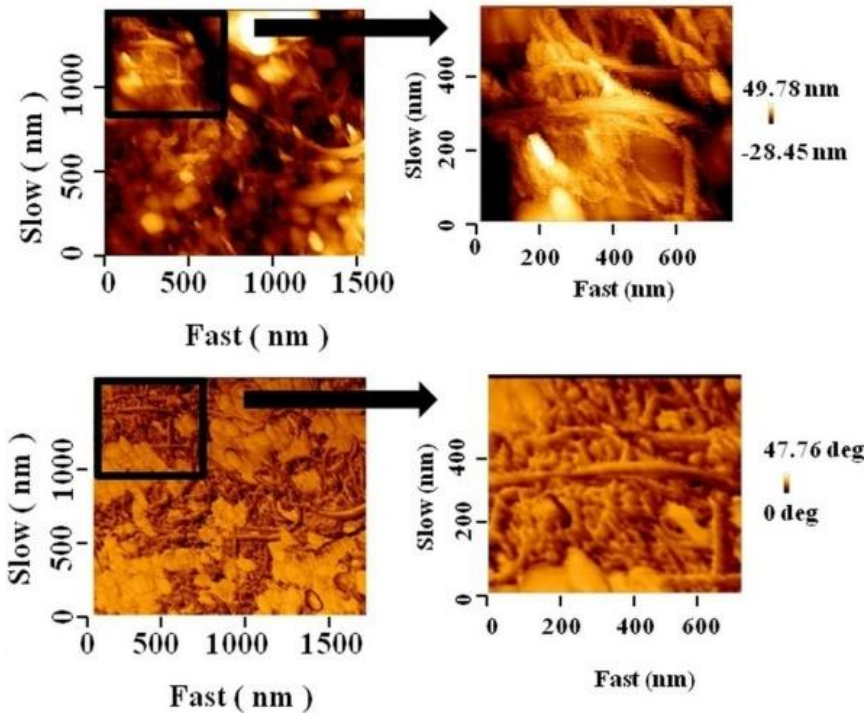
Figure D.2: The AFM images (height and phase) of the MWCNT thin film deposited on a silicon substrate

D.2 MWCNT1 and MWCNT2 Thin Films

The samples are made of a pure and homogenous thin films of MWNTs deposited over a quartz substrate. A nanotube suspension was prepared by mixing and ultrasonicating (380 W, 20 min) deionized water (10 ml), SDS (Sigma Aldrich, 71725, 0.1 g) and MWCNTs (Hanwha Nanotech, CMP-330F, 10 mg). The nanotube suspension was deposited on a filter paper (Whatman, Anodisc 25) by the vacuum filtration method. Then SDS surfactants were removed by rinsing with deionized water. Finally, the MWNTs films were transferred on quartz substrates. The MWCNT film thickness of our two samples, namely MWCNT1 and MWCNT2, is 162 and 193 nm respectively [cf. Fig. D.3]. The films have a diameter of 18 mm, while the quartz substrate is a 25×25 mm^2 square.

(a)   (b)
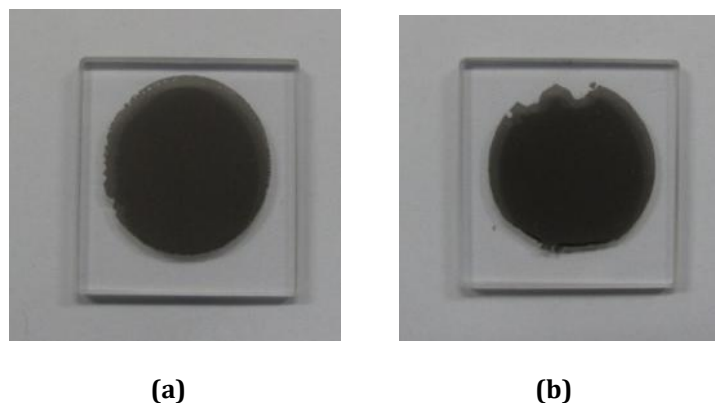
Figure D.3: The MWCNTs films with thicknesses of (a) 162.16nm and (b) 193.88nm deposited over the quartz substrate.

D.3 MG1 and MG2 Thin Films

MG films were fabricated as follows [26, 96]: Copper foils from Alfa Aesar (46986, 99.8%, thickness 25 µm) were used as catalytic substrates. They were heated to 1000 °C with H2 flow (3 sccm) and annealed at 1000 °C for 30 min. Then, graphene films were grown by a low pressure chemical vapor deposition (LPCVD) by introducing CH4 in the deposition chamber for 10 min (20 sccm). Specimens were lastly cooled rapidly to room temperature, without any gas flow. The synthesized MG films were transferred onto a fused quartz substrate (20×20×0.5 mm^3) by the wet transfer method. A thin layer of polymethyl methacrylate (PMMA) dissolved in chlorobenzene (Sigma-Aldrich 82265, 46 mg/mL) was put on top of MG, followed by a curing. Then, the copper substrate was etched in ammonium peroxydisulfate solution (Alfa Aesar 54106, ACS, 98.0 %, 0.1 M) for 3 hours. Finally, the PMMA/graphene film was transferred onto the fused quartz substrate, followed by removal of PMMA using acetone. The MG film thickness of our two samples, namely MG1 and MG2, is a one-atom thick layer deposit on over quartz substrates (15×15×0.5 mm^3).

D.4 MG Thin Film

The number of layers and the electronic structure of graphene sample can be explored in Raman spectrum [213]. The ratio intensities of G and 2D peaks can be changed as the number of graphene layers and also assessing the quality of sample [214]. Fig. D.4 shows the Raman spectra of transferred MG taken under this study with G (~1580 cm-1) and 2D

(~2680 cm-1) bands. The intensity of disorder-induced D band (~1,350cm-1) maybe because of edges and sub-domain boundaries in graphene consistent with MG as discussed in Ref. [215] with intensity ID/IG ratio ~ 0.2.
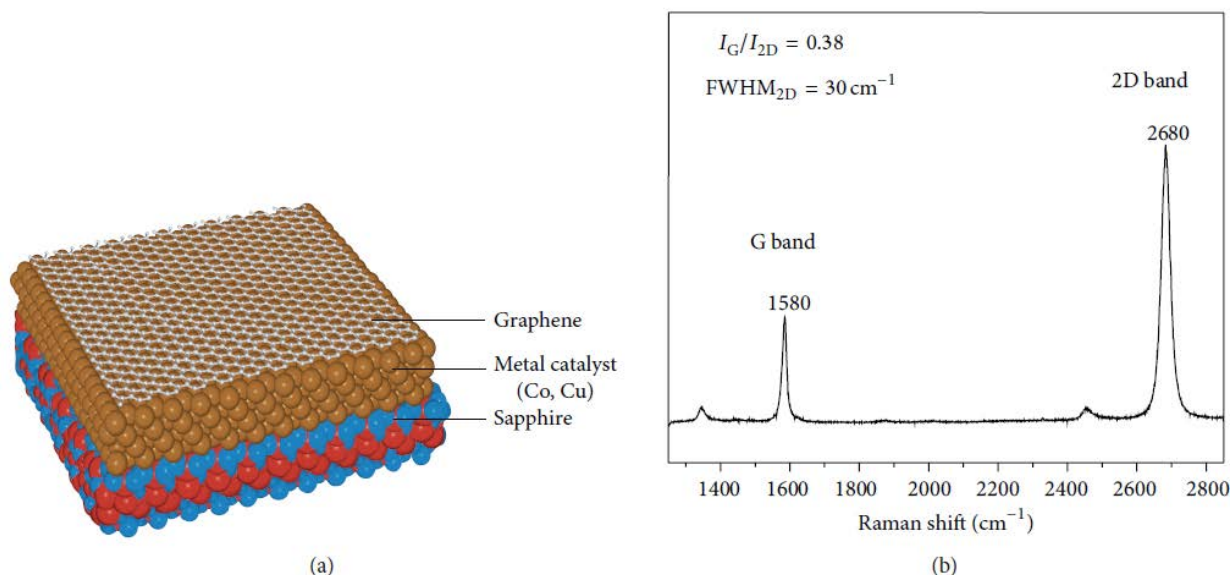
Figure D.4: (a) The model structure of transferred monolayer graphene. (b) The Raman spectra of transferred single layered graphene with G and 2D peaks [Meijo Nano Carbon Ltd.].

D.5 GRP and AgNW-GRP Hybrid Thin Films

GRP was grown on a raw copper foil (Nilaco, 99.96 %, and 100-µm thick) using chemical vapor deposition (CVD) with CH_4 and H_2 flow at 1000 ℃. A typical GRP synthesis procedure using CVD is provided elsewhere [216]. The synthesized GRP films were then transferred onto fused quartz substrates (20×20 mm², thickness 0.54 mm) following the wet transfer method published previously[214, 217, 218]. Firstly, polymethyl methacrylate (PMMA, from Sigma-Aldrich (46 mg/ml) dissolved in chlorobenzene was spin-coated on the GRP/Cu substrate followed by drying at room temperature. The GRP grown on the back side of the Cu substrate was removed by oxygen plasma. The Cu substrate was then etched by using Cu etchant (Transgene, CE-100) for 1 hour. The PMMA/GRP was washed by using deionized (DI) water for 1 hour followed by 0.5 M hydrogen chloride reatment to remove iron nanoparticle residues. The PMMA/GRP film was rinsed with DI water for 2 hours.

Finally, the PMMA/GRP was transferred onto the fused quartz substrate, and PMMA was removed using acetone for 5 min. For AgNW-GRP hybrid films, AgNWs dispersed in ethanol (Nanopyxis, 1.23 mg/ml) were spin-coated onto the fused quartz substrate at 1000 rpm for 60 s followed by a 6-h drying at room temperature. The average length and diameter of AgNWs were 25 µm and 35 nm, respectively. Finally, the CVD-synthesized GRP was transferred on top of spin-coated AgNWs using the same wet transfer method. The thickness d of the AgNW-GRP hybrid films was measured by atomic force microscopy (AFM), and the average value was used to calculate the conductivity [cf. Fig. D.5 (a)]. Two samples were characterized during this work AgNW-GRP (I) (d=59 nm) and AgNW-GRP (II) (d=38 nm). Fig. D.5 (b) shows the scanning electron microscope (SEM) image and energy dispersive X-ray (EDX) analysis of AgNW-GRP (I). The strong silicon and oxygen peaks came from the quartz substrate. Both carbon and silver peaks could be observed where AgNWs were on GRP (Spectrum 2) whereas only a carbon peak was present on the GRP surface without AgNW (Spectrum 1).
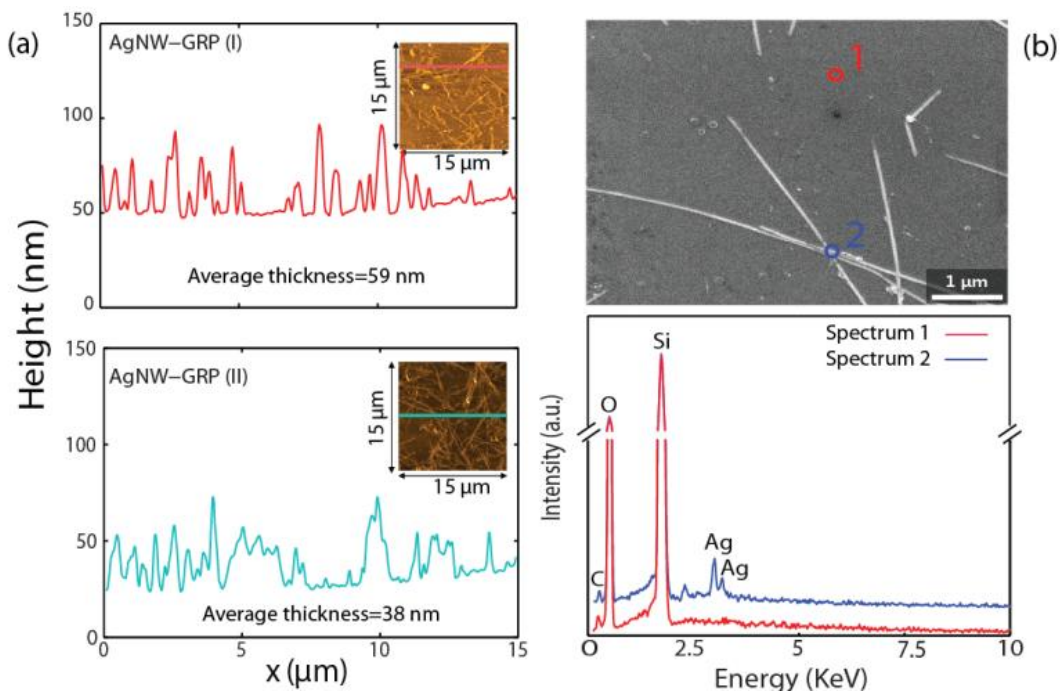
Figure D.5: The surface profiles of two AgNW-GRP hybrid films. AFM images are provided as inset. (b) The SEM image and EDX analysis of AgNW-GRP (I) (d=59 nm).

Appendix E: MITEPHO and Published Results

E.1 MITEPHO Project

MIcrowave and TErahertz PHOtonics (MITEPHO) was a project in techniques and integration for generation and applications under coordination of Universidad Carlos III de Madrid and Professor Horacio Lamela Rivera. MITEPHO was an Initial Training Network funded by the European Community's Seventh Framework Programme. Grant Agreement Number 238393. MITEPHO was seeking to train researchers to develop photonic sources for CW signal generation from microwave (μw) to terahertz (THz) frequencies. The main objective of the network was to establish a crossroad among the different technical domains that overlapped on this topic, gathering experts in the domains of photonic sources and detectors from physics and engineering backgrounds. The network consists of five University partners, two Research Laboratories and 4 Industrial partners from across Europe (01/01/2010-01/01/2014).

This thesis is supported by MITEPHO to develop THz spectroscopy in sensing, nanotechnology and biomedical applications. All material characterizations, THz-TDS study and signal processing analyzing were carried out in the Optoelectronics and Laser Technology Group (GOTL) at Universidad Carlos III de Madrid under Professor Horacio Lamela supervision.

http://www.uc3m.es/portal/page/portal/grupos_investigacion/optoelectronics/european_projects/mitepho

E.2 Journal Citation Reports

- S. Puthukodan, **E. Dadrasnia**, H. Lamela, G. Ducournau, and J.-F Lampin, *"Free Space Material Characterization of Carbon Nanotube Thin Films at Sub-Terahertz Frequencies",* to be submitted, 2015.

- **E. Dadrasnia,** and H. Lamela *"Terahertz conductivity characterization of nanostructured graphene-like films for optoelectronic applications*", Journal of Nanophotonic 9(1), 2015 [doi:10.1117/1.JNP.9.093598].

- **E. Dadrasnia**, F. Garet, D-.M. Lee, J.-L. Coutaz, S. Baik, and H. Lamela, *"Electrical Characterization of Silver Nanowire-Graphene Hybrid Films from THz Transmission and Reflection Measurements",* in Applied Physics Letters, 105(1), 011101, 2014 [doi: 10.1063/1.4889091].

- **E. Dadrasnia**, S. Puthukodan, Vinod V K T, H. Lamela, G. Ducournau, J.-F. Lam6pin, F. Garet, and J.-L. Coutaz, *"Sub-THz Characterisation of Monolayer Graphene"*, Journal of Spectroscopy, 2014(6), 2014 [doi: 10.1155/2014/601059].

- S. Puthukodan, **E. Dadrasnia**, Vinod V.K.T, H. Lamela, G. Ducournau , and J-.F Lampin , *"Study of Optical Properties of Carbon Nanotube Thin Films in Sub-Terahertz Frequency Regime",* Microwave and Optical Technology Letters 56(8), 1895-1898, 2014. [doi: 10.1002/mop.28477].

- **E. Dadrasnia**, H. Lamela, M. B. Kuppam, F. Garet, and J.-L. Coutaz, *"Determination of the DC electrical conductivity of multi-walled carbon nanotube films and graphene layers from non-contact time-domain terahertz measurements",* Advances in Condensed Matter Physics, vol. 2014, Article ID 370619, 6 pages, 2014. [doi:10.1155/2014/370619].

- S. Puthukodan, **E. Dadrasnia**, Vinod. V.K.T, H.K. Nguendon, H. Lamela, G. Ducournau, J.-F. Lampin, F. Garet, J.-L. Coutaz, D.-M. Lee, and S. Baik, *"Sub-THz Characterization of Multiwalled Carbon Nanotube Thin Films using a Vector Network Analyzer"*, Electronics Letters, vol. 50, no. 4, pp. 297–299, 2014, [doi: 10.1049/el.2013.4136].

- **E. Dadrasnia,** S. Puthukodan, and H. Lamela *"Terahertz electrical conductivity and optical characterization of composite nonaligned single- and multiwalled carbon nanotubes*", Journal of Nanophotonic 8(1), 083099, 2014; [doi: 10.1117/1.JNP.8.083099].

E.3 Invited Feature and Newsroom Articles

- S. Puthukodan, **E. Dadrasnia**, Vinod. V.K.T, H.K. Nguendon, H. Lamela, G. Ducournau, J.-F. Lampin, F. Garet, J.-L. Coutaz, D.-M. Lee, and S. Baik, *"inside view",* Electronics Letters, Volume 50, Issue 4, page 237, 2014, DOI: 10.1049/el.2014.0388.

- H. Lamela and **E. Dadrasnia**,*"Terahertz analysis reveals nanostructural dependence of carbon thin-film properties,"* in SPIE Newsroom, March 2012.

E.4 Conference Proceedings

➢ H. Lamela, **E. Dadrasnia**, D.-M. Lee, S. Baik, M. B. Kuppam, F. Garet and J.-L. Coutaz, "*Terahertz conductivity studies in carbon nanotube networks prepared by the vacuum filtration method*," in SPIE NanoScience+ Engineering, pp.84620C-84627 (2012)- <u>(Invited Talk).</u>

➢ **E. Dadrasnia** and H. Lamela, *"Studying and analyzing terahertz signals in carbon nanostructure composite thin-film,"* in SPIE NanoScience+ Engineering, pp. 84620E-84627(2012).

➢ **E. Dadrasnia**, H. Lamela, M.-B. Kuppam, F. Garet and J.-L. Coutaz, "*THz time-domain spectroscopy in different carbon nanotube thin films*," in SPIE OPTO, pp. 82610Y-82615 (2012).

➢ **E. Dadrasnia** and H. Lamela, *"Carbon nanostructures properties by terahertz time-domain spectroscopy analysis for nanoengineering applications,"* in SPIE Defense, Security, and Sensing, pp. 84010Q-84015 (2012).

➢ B. Gonzalez, H. Lamela, **E. Dadrasnia**, V. Sichkovskyi, K. Kozhuharov and J. Reithmaier, "*Temperature effects on the characterization of new quantum dot dual mode lasers for terahertz generation*," in SPIE OPTO,pp.82550C-82556 (2012).

➢ **E. Dadrasnia**, B. Gonzalez, H. Lamela, K. Kozhuharov, V. Sichkovskyi and J. Reithmaier,*"Thermally tunable DFB dual mode laser diode by an external platinum thin-film heater for THz generation,"* in SPIE OPTO,pp.825512-517 (2012).

➢ H. Lamela, **E. Dadrasnia**, F. Garet, M. B. Kuppam and J.-L. Coutaz,*"Carbon nanotube terahertz spectroscopy: study of absorption and dispersion properties of SWNT and MWNT,"* in SPIE NanoScience+ Engineering,pp.81010G-81017 (2011).

➢ **E. Dadrasnia** and H. Lamela, *"Optical and electrical characterization of carbon nanotubes by terahertz spectroscopy: comparison between modeling and experimental results,"* in SPIE NanoScience+ Engineering, pp. 80963P-80966 (2011) .

➢ **E. Dadrasnia** and H. Lamela, *"Nano-Graphene and Single-walled Carbon Nanotube Electrical and Optical Conductivity Properties by Terahertz Time-Domain Spectroscopy,"* in the 5th International Congress on Advanced Electromagnetic Materials in Microwaves and Optics- Metamaterials, pp. 722-724 (2011).

E.5 Workshop & Poster Contributions

➢ **E. Dadrasnia**, H. Lamela, M.B. Kuppam, F. Garet,J.-L. Coutaz, D.-M. Lee, and S. Baik "*Conductivity Measurement of MWCNT and Graphene Thin-films at DC and High Frequencies Using Noncontact Terahertz Time domain Spectroscopy*" in the MITEPHO Laboratory Platform, UCIIIM, Spain, Oct. 2013 (Presentation).

➢ **E. Dadrasnia** and H. Lamela, "*Film Noncontact Conductivity Measurements in Carbon Nanostructures at THz Frequencies*" in the 1st MITEPHO Industrial Workshop, THALES, France, Mar. 2013 (Poster Session).

➢ **E. Dadrasnia** and H. Lamela, "*Terahertz Time-Domain Spectroscopy to Study Free-contact DC Conductivity Measurement of CNTs Thin-Films*", the 1st MITEPHO Winter School, UDE, Germany, Dec. 2012 (Poster Session).

➢ **E. Dadrasnia** and H. Lamela, "*Terahertz Time-Domain Spectroscopy study and analysis of Optical and Electrical properties in Carbon Nanostructures*" in the 2nd MITEPHO Summer School, UCL, UK, Aug. 2012 (Poster Session).

➢ **E. Dadrasnia** and H. Lamela, "*Terahertz dielectric properties of carbon nanostructure films utilizing time-domain spectroscopy,*" in the 3rd International Topical Meeting on Optical Sensing and Artificial Vision, Saint Petersburg, Russia, May 2012 (Presentation).

➢ **E. Dadrasnia** and H. Lamela, "*Dual Mode DFB Laser THz Generation for Spectroscopy Applications,*" in the 1st MITEPHO Summer School, Areches-Beaufort, France, Sept. 2011 (Poster Session).

E.6 Conference Talks

➢ **E. Dadrasnia**, S. Puthukodan, H. Lamela Rivera, G. Ducournau, J.-F Lampin, M-B Kuppam, F. Garet, J.-L Coutaz*, "Comparisons between continuous wave and time-domain terahertz spectroscopy in carbon nanostructure",* in SPIE Defense, Security, and Sensing. Conference (2013)

➢ H. Lamela, S. Puthukodan, **E. Dadrasnia**, D-M Lee, S. Baik, G. Ducournau, J.-F Lampin, M-B Kuppam, F. Garet, J.-L Coutaz, "*Characteristic study of CNTs and graphene using terahertz time domain and continuous wave spectroscopy",* in SPIE NanoScience+ Engineering (2013)-**(Invited Talk)**

References

[1] J. C. Maxwell, "A dynamical theory of the electromagnetic field," *Phil. Trans. R. Soc. Lond.,* vol. 115, pp. 459-512, 1865.

[2] H. Hertz, *Electric Waves: Being Researches on the Propagation of Electric Action with Finite Velocity Through Space*: Dover Publications, 1893.

[3] M. Tonouchi, "Cutting-edge terahertz technology," *Nature Photon.,* vol. 1, pp. 97-105, 2007.

[4] X.-C. Zhang and J. Xu, *Introduction to THz wave photonics*. New York: Springer US, 2010.

[5] S. P. Mickan, K. S. Lee, T. M. Lu, J. Munch, D. Abbott and X. C. Zhang, "Double modulated differential THz-TDS for thin film dielectric characterization," *Microelectron J. ,* vol. 33, pp. 1033-1042, 2002.

[6] F. Shen and Y. B. Ying, "Applications of Terahertz Spectroscopy and Imaging Techniques in Food Safety Inspection," *Spectrosc. Spect. Anal.,* vol. 29, pp. 1445-1449, 2009.

[7] Y. Sun, M. Y. Sy, Y.-X. J. Wang, A. T. Ahuja, Y.-T. Zhang and E. Pickwell-Macpherson, "A promising diagnostic method: Terahertz pulsed imaging and spectroscopy," *World J. Radiol.,* vol. 3, pp. 55-65, 2011.

[8] M. Naftaly and R. E. Miles, "Terahertz time-domain spectroscopy for material characterization," *Proc. IEEE,* vol. 95, pp. 1658-1665, 2007.

[9] D. M. Mittleman, J. Cunningham, M. C. Nuss and M. Geva, "Noncontact semiconductor wafer characterization with the terahertz Hall effect," *Appl. Phys. Lett.,* vol. 71, pp. 16-18, 1997.

[10] T. Yasui, T. Yasuda, K. Sawanaka and T. Araki, "Terahertz paintmeter for noncontact monitoring of thickness and drying progress in paint film," *Appl. Optics,* vol. 44, pp. 6849-6856, 2005.

[11] J. Labaune, J. B. Jackson, S. Pages-Camagna, I. N. Duling, M. Menu and G. A. Mourou, "Papyrus imaging with terahertz time domain spectroscopy," *Appl. Phys. A-Mater. Sci. Process.,* vol. 100, pp. 607-612, 2010.

[12] E. Castro-Camus, M. Palomar and A. A. Covarrubias, "Leaf water dynamics of Arabidopsis thaliana monitored in-vivo using terahertz time-domain spectroscopy," *Sci Rep,* vol. 3, 2013.

[13] L. Duvillaret, F. Garet and J.-L. Coutaz, "Highly precise determination of optical constants and sample thickness in terahertz time-domain spectroscopy," *Appl. Opt.,* vol. 38, pp. 409-415, 1999.

[14] M. Bernier, F. Garet and J. Coutaz, "Precise determination of the refractive index of samples showing low transmission bands by THz time-domain spectroscopy," *IEEE Trans. Terahertz Sci. Technol.,* vol. 3, pp. 295-301, 2013.

[15] K. S. Novoselov, A. K. Geim, S. V. Morozov, D. Jiang, Y. Zhang, S. V. Dubonos, I. V. Grigorieva and A. A. Firsov, "Electric field effect in atomically thin carbon films," *Science,* vol. 306, pp. 666-669, 2004.

[16] K. S. Novoselov, D. Jiang, F. Schedin, T. J. Booth, V. V. Khotkevich, S. V. Morozov and A. K. Geim, "Two-dimensional atomic crystals," *Proceedings of the National Academy of Sciences of the United States of America,* vol. 102, pp. 10451-10453, 2005.

[17]   I. Maeng, S. Lim, S. J. Chae, Y. H. Lee, H. Choi and J.-H. Son, "Gate-controlled nonlinear conductivity of Dirac fermion in graphene field-effect transistors measured by terahertz time-domain spectroscopy," *Nano Lett.,* vol. 12, pp. 551-555, 2012.

[18]   D. Yu and L. Dai, "Self-assembled graphene/carbon nanotube hybrid films for supercapacitors," *J. Phys. Chem. Lett.,* vol. 1, pp. 467-470, 2009.

[19]   B. Sensale-Rodriguez, Y. Rusen, L. Lei, D. Jena and H. G. Xing, "Graphene for reconfigurable terahertz optoelectronics," *Proc. IEEE,* vol. 101, pp. 1705-1716, 2013.

[20]   K.-Y. Chun, Y. Oh, J. Rho, J.-H. Ahn, Y.-J. Kim, H. R. Choi and S. Baik, "Highly conductive, printable and stretchable composite films of carbon nanotubes and silver," *Nat. Nano,* vol. 5, pp. 853-857, 2010.

[21]   A. H. Castro Neto, F. Guinea, N. M. R. Peres, K. S. Novoselov and A. K. Geim, "The electronic properties of graphene," *Rev. Mod. Phys.,* vol. 81, p. 109, 2009.

[22]   K. F. Mak, M. Y. Sfeir, Y. Wu, C. H. Lui, J. A. Misewich and T. F. Heinz, "Measurement of the optical conductivity of graphene," *Phys. Rev. Lett.,* vol. 101, p. 196405, 2008.

[23]   H. Choi, F. Borondics, D. A. Siegel, S. Y. Zhou, M. C. Martin, A. Lanzara and R. A. Kaindl, "Broadband electromagnetic response and ultrafast dynamics of few-layer epitaxial graphene," *Appl. Phys. Lett.,* vol. 94, p. 172102, 2009.

[24]   V. Ryzhii, M. Ryzhii and T. Otsuji, "Negative dynamic conductivity of graphene with optical pumping," *J. Appl. Phys.,* vol. 101, p. 083114, 2007.

[25]   M. B. Klarskov, H. F. Dam, D. H. Petersen, T. M. Hansen, A. Löwenborg, T. J. Booth, M. S. Schmidt, R. Lin, P. F. Nielsen and P. Bøggild, "Fast and direct measurements of the electrical properties of graphene using micro four-point probes," *Nanotechnology,* vol. 22, p. 445702, 2011.

[26]   X. Li, Y. Zhu, W. Cai, M. Borysiak, B. Han, D. Chen, R. D. Piner, L. Colombo and R. S. Ruoff, "Transfer of large-area graphene films for high-performance transparent conductive electrodes," *Nano Lett.,* vol. 9, pp. 4359-4363, 2009.

[27]   G. Baumgartner, M. Carrard, L. Zuppiroli, W. Bacsa, W. A. de Heer and L. Forró, "Hall effect and magnetoresistance of carbon nanotube films," *Phys. Rev. B,* vol. 55, pp. 6704-6707, 1997.

[28]   J. L. Tedesco, B. L. VanMil, R. L. Myers-Ward, J. M. McCrate, S. A. Kitt, P. M. Campbell, G. G. Jernigan, J. C. Culbertson, C. R. Eddy and D. K. Gaskill, "Hall effect mobility of epitaxial graphene grown on silicon carbide," *Appl. Phys. Lett.,* vol. 95, p. 122102, 2009.

[29]   Y. Zhang, Y.-W. Tan, H. L. Stormer and P. Kim, "Experimental observation of the quantum Hall effect and Berry's phase in graphene," *Nature,* vol. 438, pp. 201-204, 2005.

[30]   W. Ziran, W. Lu, I. Zimmerman and X. Hao, "Microwave to terahertz characterization of carbon nanotube materials," in *The 11th IEEE Topical Meeting on Silicon Monolithic Integrated Circuits in RF Systems (SiRF)*, 2011.

[31]   O. Shaforost, K. Wang, M. Adabi, Z. Guo, L. Hao, J. Gallop and N. Klein, "Microwave characterization of large area graphene using a TE01δ dielectric resonator," in *International Kharkov Symposium on Millimeter and Submillimeter Waves (MSMW), Physics and Engineering of Microwaves*, 2013.

[32]   K. F. Mak, L. Ju, F. Wang and T. F. Heinz, "Optical spectroscopy of graphene: from the far infrared to the ultraviolet," *Solid State Commun.,* vol. 152, pp. 1341-1349, 2012.

[33]   A. Ugawa, A. G. Rinzler and D. B. Tanner, "Far-infrared gaps in single-wall carbon nanotubes," *Phys. Rev. B,* vol. 60, p. R11305, 1999.

[34]   N. Rouhi, S. Capdevila, D. Jain, K. Zand, Y. Wang, E. Brown, L. Jofre and P. Burke, "Terahertz graphene optics," *Nano Res.,* vol. 5, pp. 667-678, 2012.

[35]   E. Dadrasnia, H. Lamela, M. B. Kuppam, F. Garet and J. L. Coutaz, "THz time-domain spectroscopy in different carbon nanotube thin films," *Proc. SPIE in Terahertz Technology and Applications V, 82610Y,* vol. 8261-35, pp. 82610Y, 82610Y-5, 2012.

[36]   E. Dadrasnia and H. Lamela, "Optical and electrical characterization of carbon nanotubes by terahertz spectroscopy: comparison between modeling and experimental Results," in *Proc. SPIE in Plasmonics: Metallic Nanostructures and Their Optical Properties IX, 80963P*, 2011.

[37]   E. P. J. Parrott, J. A. Zeitler, J. McGregor, S. P. Oei, H. E. Unalan, W. I. Milne, J. P. Tessonnier, D. S. Su, R. Schlogl and L. F. Gladden, "The use of terahertz spectroscopy as a sensitive probe in discriminating the electronic Properties of structurally similar multi-walled carbon nanotubes," *Adv. Mater.,* vol. 21, p. 3953, 2009.

[38]   M. Inhee, K. Chul, O. Seung Jae, J. H. Son, A. Kay Hyeok and L. Young Hee, "Terahertz electrical and optical characteristics of double-walled carbon nanotubes and their comparison with single-walled carbon nanotubes," *Appl. Phys. Lett.,* vol. 90, p. 051914, 2007.

[39]   T. Kampfrath, K. von Volkmann, C. M. Aguirre, P. Desjardins, R. Martel, M. Krenz, C. Frischkorn, M. Wolf and L. Perfetti, "Mechanism of the far-infrared absorption of carbon-nanotube films," *Phys. Rev. Lett.,* vol. 101, p. 267403, 2008.

[40]   T.-I. Jeon, J.-H. Son, G. H. An and Y. H. Lee, "Characterization of carbon nanotubes by THz time-domain spectroscopy," *J. Kor. Phys. Soc.,* vol. 39, pp. S185-S188, 2001.

[41]   E. Dadrasnia, S. Puthukodan and H. Lamela, "Terahertz electrical conductivity and optical characterization of composite nonaligned single- and multiwalled carbon nanotubes," *J. Nanophotonics,* vol. 8, p. 083099, 2014.

[42]   E. Dadrasnia, H. Lamela, M.-B. Kuppam, F. Garet and J.-L. Coutaz, "Determination of the DC electrical conductivity of multi-walled carbon nanotube films and graphene layers from non-contact time-domain terahertz measurements," *Adv. Condens. Matter Phys.,* vol. 2014, 2014.

[43]   E. Dadrasnia, F. Garet, D. Lee, J.-L. Coutaz, S. Baik and H. Lamela, "Electrical characterization of silver nanowire-graphene hybrid films from terahertz transmission and reflection measurements," *Appl. Phys. Lett.,* vol. 105, p. 011101, 2014.

[44]   E. Dadrasnia and H. Lamela, "Terahertz conductivity characterization of nanostructured graphene-like films for optoelectronic applications," *J. Nanophotonics,* vol. 9, 2015.

[45]   S. Puthukodan, E. Dadrasnia, V. K. T. Vinod, H. K. Nguendon, H. Lamela, G. Ducournau, J.-F. Lampin, F. Garet, J.-L. Coutaz, D.-M. Lee, and S. Baik, "Sub-THz characterisation of multi-walled carbon nanotube thin films using vector network analyser," *Electron. Lett.,* vol. 50, pp. 297-299, 2014.

[46]   E. Dadrasnia, S. Puthukodan, V. V. K. Thalakkatukalathil, H. Lamela, G. Ducournau, J.-F. Lampin, F. Garet and J.-L. Coutaz, "Sub-THz characterisation of monolayer graphene," *J. Spectros.,* vol. 2014, p. 6, 2014.

[47] S. Puthukodan, E. Dadrasnia, V. K. T. Vinod, H. Lamela Rivera, G. Ducournau and J.-F. Lampin, "Optical properties of carbon nanotube thin films in subterahertz frequency regime," *Microw. Opt. Technol. Lett.,* vol. 56, pp. 1895-1898, 2014.

[48] H. Lamela and E. Dadrasnia, "Terahertz analysis reveals nanostructural dependence of carbon thin-film properties," *SPIE Newsroom,* 2012.

[49] S. Puthukodan, E. Dadrasnia, V. K. T. Vinod, H. K. Nguendon, H. Lamela, G. Ducournau, J.-F. Lampin, F. Garet, J.-L. Coutaz, D.-M. Lee, and S. Baik, "Inside view," *Electron. lett.,* vol. 50, pp. 237-237, 2014.

[50] H. Lamela, E. Dadrasnia, D.-M. Lee, S. Baik, M. B. Kuppam, F. Garet and J.-L. Coutaz, "Terahertz conductivity studies in carbon nanotube networks prepared by the vacuum filtration method," in *Proc. SPIE in Carbon Nanotubes, Graphene, and Associated Devices V, 84620C,* 2012.

[51] H. Lamela, E. Dadrasnia, F. Garet, M. B. Kuppam and J. L. Coutaz, "Carbon nanotube terahertz spectroscopy: study of absorption and dispersion properties of SWNT and MWNT," in *Proc. SPIE in Carbon Nanotubes, Graphene, and Associated Devices IV, 81010G,,* 2011.

[52] E. Dadrasnia and H. Lamela, "Studying and analyzing terahertz signals in carbon nanostructures thin-films," in *Proc. SPIE in Carbon Nanotubes, Graphene, and Associated Devices V, 84620E,* 2012.

[53] E. Dadrasnia and H. Lamela, "Carbon nanostructures properties by terahertz time-domain spectroscopy analysis for nanoengineering applications," in *Proc. SPIE 8401, in Independent Component Analyses, Compressive Sampling, Wavelets, Neural Net, Biosystems, and Nanoengineering X, 84010Q,* 2012.

[54] R. A. Lewis, "A review of terahertz sources," *J. Phys. D: Appl. Phys.,* vol. 47, p. 374001, 2014.

[55] F. Wang, D. Cheever, M. Farkhondeh, W. Franklin, E. Ihloff, J. van der Laan, B. McAllister, R. Milner, C. Tschalaer, D. Wang, D. F. Wang, A. Zolfaghari, T. Zwart, G. L. Carr, B. Podobedov, and F. Sannibale, "Coherent THz synchrotron radiation from a storage ring with high-frequency RF system," *Phys. Rev. Lett.,* vol. 96, p. 064801, 2006.

[56] G. L. Carr, M. C. Martin, W. R. McKinney, K. Jordan, G. R. Neil and G. P. Williams, "High-power terahertz radiation from relativistic electrons," *Nature,* vol. 420, pp. 153-156, 2002.

[57] S. Bartalini, L. Consolino, P. Cancio, P. De Natale, P. Bartolini, A. Taschin, M. De Pas, H. Beere, D. Ritchie, M. S. Vitiello, and R. Torre, "Frequency-Comb-Assisted terahertz quantum cascade laser spectroscopy," *Phys. Rev. X,* vol. 4, p. 021006, 2014.

[58] B. Gonzalez, H. Lamela, E. Dadrasnia, V. Sichkovskyi, K. Kozhuharov and J. P. Reithmaier, "Temperature effects on the characterization of new quantum dot dual mode lasers for terahertz generation," in *Proc. SPIE in Physics and Simulation of Optoelectronic Devices XX, 82550C,* 2012.

[59] E. Dadrasnia, B. Gonzalez, H. Lamela, K. Kozhuharov, V. Sichkovskyi and J. P. Reithmaier, "Thermally tunable DFB dual mode laser diode by an external platinum thin-film heater for THz generation," in *Proc. SPIE in Physics and Simulation of Optoelectronic Devices XX, 82550C,* 2012.

[60] S. L. Dexheimer, *Terahertz spectroscopy: principles and applications*: CRC Press, 2007.

[61] R. J. Bell, *Introductory Fourier Transform Spectroscopy*. New York: Academic, 1972.

[62] D. Grischkowsky, S. Keiding, M. v. Exter and C. Fattinger, "Far-infrared time-domain spectroscopy with terahertz beams of dielectrics and semiconductors," *J. Opt. Soc. Am. B,* vol. 7, pp. 2006-2015, 1990.

[63] T. Musienko, V. Rudakov and L. Solov'ev, "On the application of Kramers-Kronig relations to media with spatial dispersion," *J. Phys. Condens. Matter,* vol. 1, p. 6745, 1989.

[64] Y. Tatsuo and T. Nobuo, "Far-Infrared difference-frequency generation by picosecond laser pulses," *Jpn. J. Appl. Phys.,* vol. 9, p. 1361, 1970.

[65] D. H. Auston, "Picosecond optoelectronic switching and gating in silicon," *Appl. Phys. Lett.,* vol. 26, pp. 101-103, 1975.

[66] R. A. Lewis, "Terahertz generation by optical rectification in GaAs and related materials," in *Conference on Lasers & Electro Optics & The Pacific Rim Conference on Lasers and Electro-Optics (CLEO/PACIFIC RIM '09)*, 2009.

[67] Q. Wu, M. Litz and X. C. Zhang, "Broadband detection capability of ZnTe electro-optic field detectors," *Appl. Phys. Lett.,* vol. 68, pp. 2924-2926, 1996.

[68] A. Bonvalet, M. Joffre, J. L. Martin and A. Migus, "Generation of ultrabroadband femtosecond pulses in the mid-infrared by optical rectification of 15 fs light pulses at 100 MHz repetition rate," *Appl. Phys. Lett.,* vol. 67, pp. 2907-2909, 1995.

[69] D. H. Auston, K. P. Cheung and P. R. Smith, "Picosecond photoconducting Hertzian dipoles," *Appl. Phys. Lett.,* vol. 45, pp. 284-286, 1984.

[70] P. R. Smith, D. H. Auston and M. C. Nuss, "Subpicosecond photoconducting dipole antennas," *IEEE J. Quant. Electron.,* vol. 24, pp. 255-260, 1988.

[71] C. Fattinger and D. Grischkowsky, "Point source terahertz optics," *Appl. Phys. Lett.,* vol. 53, pp. 1480-1482, 1988.

[72] M. van Exter, C. Fattinger and D. Grischkowsky, "High-brightness terahertz beams characterized with an ultrafast detector," *Appl. Phys. Lett.,* vol. 55, pp. 337-339, 1989.

[73] M. van Exter, C. Fattinger and D. Grischkowsky, "Terahertz time-domain spectroscopy of water vapor," *Opt. Lett.,* vol. 14, pp. 1128-1130, 1989.

[74] I. Pupeza, R. Wilk and M. Koch, "Highly accurate optical material parameter determination with THz time-domain spectroscopy," *Opt. Express,* vol. 15, pp. 4335-4350, 2007.

[75] F. Garet, "Generation optoelectronique d'impulsions electromagnetiques ultra-courtes ; applications a la spectroscopie THz," Institut national polytechnique de Grenoble, Grenoble, France, 1997.

[76] W. Zouaghi, M. D. Thomson, K. Rabia, R. Hahn, V. Blank and H. G. Roskos, "Broadband terahertz spectroscopy: principles, fundamental research and potential for industrial applications," *Eur. J. Phys.,* vol. 34, p. S179, 2013.

[77] F. G. Sun, G. A. Wagoner, D. Bentz and X. C. Zhang, "Measurement of free-space THz pulses via long-lifetime photoconductors," in *The 8th IEEE Annual Meeting Conference Proceedings Lasers and Electro-Optics Society Annual Meeting*, 1995.

[78] W. Withayachumnankul, "Engineering aspects of terahertz time-domain spectroscopy.," PhD Thesis, School of Electrical and Electronic Engineering, University of Adelaide, 2010.

[79]   P. U. Jepsen, R. H. Jacobsen and S. R. Keiding, "Generation and detection of terahertz pulses from biased semiconductor antennas," *J. Opt. Soc. Am. B,* vol. 13, pp. 2424-2436, 1996.

[80]   M. van Exter and D. Grischkowsky, "Characterization of an optoelectronic terahertz beam system," *IEEE Trans. Microw. Theory Tech.,* vol. 38, pp. 1684-1691, 1990.

[81]   J. Balakrishnan, "Developments in double-modulated terahertz differential time-domain spectroscopy," PhD Thesis, Electrical & Electronic Engineering, The University of Adelaide, Australia, Adelaide, 2005.

[82]   P. Sang-Gyu, M. R. Melloch and A. M. Weiner, "Analysis of terahertz waveforms measured by photoconductive and electrooptic sampling," *IEEE J. Quant. Electron.,* vol. 35, pp. 810-819, 1999.

[83]   H. C. B. Skjeie, "Terahertz Time-Domain Spectroscopy," Department of Electronics and Telecommunications, Norwegian University of Science and Technology, Trondheim, 2010.

[84]   X. Xu, L. Song, Y. Shi, Y. Yang, S. Xie and W. Li, "Light-induced dielectric transparency in single-walled carbon nanotube films," *Chem. Phys. Lett.,* vol. 410, pp. 298-301, 2005.

[85]   S. Sirbu, "Induced excitations in Some metal oxides," PhD thesis, 2008.

[86]   M. Perenzoni and D. J. Paul, *Physics and applications of terahertz radiation* vol. 173. New York, 2014.

[87]   M. Naftaly and R. Dudley, "Methodologies for determining the dynamic ranges and signal-to-noise ratios of terahertz time-domain spectrometers," *Opt. Lett.,* vol. 34, pp. 1213-1215, 2009.

[88]   L. Duvillaret, F. Garet and J. L. Coutaz, "A reliable method for extraction of material parameters in terahertz time-domain spectroscopy," *IEEE J. Sel. Top. Quantum Electron.,* vol. 2, pp. 739-746, 1996.

[89]   S. M. Sze, *Semiconductor Devices Physics and Technology*: John Wiley & Sons, 1985.

[90]   I. Ferain, C. A. Colinge and J.-P. Colinge, "Multigate transistors as the future of classical metal-oxide-semiconductor field-effect transistors," *Nature,* vol. 479, pp. 310-316, 2011.

[91]   ITRS. (2014). -*The International Technology Roadmap for Semiconductors. [Online]*. Available: http://www.itrs.net

[92]   D. S. Hecht, L. Hu and G. Irvin, "Emerging transparent electrodes based on thin films of carbon nanotubes, graphene, and metallic nanostructures," *Adv. Mater.,* vol. 23, pp. 1482-1513, 2011.

[93]   Michael F. L. De Volder, Sameh H. Tawfick, Ray H. Baughman and A. J. Hart, "Carbon nanotubes: present and future commercial applications," *Science.,* vol. 399, pp. 535-539, 2013.

[94]   S. Bae, H. Kim, Y. Lee, X. Xu, J.-S. Park, Y. Zheng, J. Balakrishnan, T. Lei, H. Ri Kim, Y. I. Song, Y.-J. Kim, K. S. Kim, B. Ozyilmaz, J.-H. Ahn, B. H. Hong, and S. Iijima, "Roll-to-roll production of 30-inch graphene films for transparent electrodes," *Nat. Nano,* vol. 5, pp. 574-578, 2010.

[95]   Z. Wu, Z. Chen, X. Du, J. M. Logan, J. Sippel, M. Nikolou, K. Kamaras, J. R. Reynolds, D. B. Tanner, A. F. Hebard, and A. G. Rinzler, "Transparent, conductive carbon nanotube films," *Science,* vol. 305, pp. 1273-1276, 2004.

[96]   S. Bae, H. Kim, Y. Lee, X. Xu, J.-S. Park, Y. Zheng, J. Balakrishnan, T. Lei, H. Ri Kim, Y. I. Song, Y.-J. Kim, K. S. Kim, B. Ozyilmaz, J.-H. Ahn, B. H. Hong, and S. Iijima, "Roll-to-roll production of 30-inch graphene films for transparent electrodes," *Nat. Nano.,* vol. 5, pp. 574-578, 2010.

[97]   P. Bandaru, "Electrical properties and applications of carbon nanotube structures," *J. Nanosci. Nanotechnol.,* vol. 7, pp. 1239-1267, 2007.

[98]   A. A. Balandin, "Thermal properties of graphene and nanostructured carbon materials," *Nat. Mater.,* vol. 10, pp. 569-581, 2011.

[99]   K. M. F. Shahil and A. A. Balandin, "Thermal properties of graphene and multilayer graphene: Applications in thermal interface materials," *Solid State Commun.,* vol. 152, pp. 1331-1340, 2012.

[100]   S. Iijima and T. Ichihashi, "Single-shell carbon nanotubes of 1-nm diameter," *Nature.,* vol. 363, pp. 603 - 605, 1993.

[101]   S. Iijima, "Helical microtubules of graphitic carbon," *Nature.,* vol. 354, pp. 56 - 58, 1991.

[102]   F. Schwierz, "Graphene transistors: status, prospects, and problems," *Proc. IEEE,* vol. 101, pp. 1567-1584, 2013.

[103]   M. Roldo and D. G. Fatouros, "Biomedical applications of carbon nanotubes," *Ann. Rep. Prog. Chem. Sect. C (Physical Chemistry).* vol. 109, pp. 10-35, 2013.

[104]   H. R. Byon and H. C. Choi, "Network single-walled carbon nanotube-field effect transistors (SWNT-FETs) with increased Schottky contact area for highly sensitive biosensor applications," *J. Am. Chem. Soc.,* vol. 128, pp. 2188-2189, 2006.

[105]   R. Ma, S. Kwon, Q. Zheng, H. Y. Kwon, J. I. Kim, H. R. Choi and S. Baik, "Carbon-nanotube/silver networks in nitrile butadiene rubber for highly conductive flexible adhesives," *Adv. Mater,* vol. 24, pp. 3344-3349, 2012.

[106]   P. L. McEuen, "Single-wall carbon nanotubes," *Physics World,* pp. 31-36, 2000.

[107]   R. Martel, T. Schmidt, H. R. Shea, T. Hertel and P. Avouris, "Single- and multi-wall carbon nanotube field-effect transistors," *Appl. Phys. Lett.,* vol. 73, pp. 2447-2449, 1998.

[108]   C. SeungNam, C. Jung Han, B. Chan Wook, S. Hyung Bin, C. Joonhyock, K. Ohyun and K. Jong Min, "Perspectives on nanotechnology for RF and terahertz electronics," *IEEE Trans. Microw. Theory Tech.,* vol. 59, pp. 2709-2718, 2011.

[109]   P. R. Wallace, "The band theory of graphite," *Phys. Rev.,* vol. 71, pp. 622-634, 1947.

[110]   H. P. Boehm, A. Clauss, G. O. Fischer and U. Hofmann, "Du¨nnste Kohlenstoff-Folien," *Z. Naturforschg,* vol. 17b, pp. 150-153, 1962.

[111]   J. W. May, "Platinum surface LEED rings," *Surf. Sci.,* vol. 17, pp. 267-270, 1969.

[112]   A. J. Van Bommel, J. E. Crombeen and A. Van Tooren, "LEED and Auger electron observations of the SiC(0001) surface," *Surf. Sci.,* vol. 48, pp. 463-472, 1975.

[113]   H.-P. Boehm, R. Setton and E. Stumpp, "Nomenclature and terminology of graphitic intercalation compounds," *Pure Appl. Chem.,* vol. 66, pp. 1893–1901, 1994.

[114]   M. C. Lemme, T. J. Echtermeyer, M. Baus and H. Kurz, "A graphene field-effect device," *IEEE Electron Device Lett.,* vol. 28, pp. 282-284, 2007.

[115] Y.-M. Lin, C. Dimitrakopoulos, K. A. Jenkins, D. B. Farmer, H.-Y. Chiu, A. Grill and P. Avouris, "100-GHz transistors from wafer-scale epitaxial graphene," *Science,* vol. 327, p. 662, 2010.

[116] L. Liao, Y.-C. Lin, M. Bao, R. Cheng, J. Bai, Y. Liu, Y. Qu, K. L. Wang, Y. Huang and X. Duan, "High-speed graphene transistors with a self-aligned nanowire gate," *Nature,* vol. 467, pp. 305-308, 2010.

[117] R. Cheng, J. Bai, L. Liao, H. Zhou, Y. Chen, L. Liu, Y.-C. Lin, S. Jiang, Y. Huang and X. Duan, "High-frequency self-aligned graphene transistors with transferred gate stacks," *Proc. Natl. Acad. Sci.,* vol. 109, 2012.

[118] R. Saito, G. Dresselhaus and M. S. Dresselhaus, *Physical properties of carbon nanotubes.* London: Imperial College Press, 1998.

[119] M. S. Dresselhaus, G. Dresselhaus, J. C. Charlier and E. Hernandez, "Electronic, thermal and mechanical properties of carbon nanotubes," *Phil. Trans. R. Soc. A,* vol. 362, pp. 2065-2098, 2004.

[120] E. F. H. Brittain, W. O. George and C. H. J. Wells, *Introduction to molecular spectroscopy: Theory and experiment.* London: Academic Press Inc., 1970.

[121] M. Dressel and G. Grüner, *Electrodynamics of Solids: Optical Properties of Electrons in Matter* Cambridge University Press, 2002.

[122] Y.-S. Lee, *Principles of terahertz science and technology.* New York: Springer US, 2009.

[123] N. E. Tielking and R. R. Jones, "Coherent population transfer among Rydberg states by subpicosecond, half-cycle pulses," *Phys. Rev. A,* vol. 52, pp. 1371-1381, 1995.

[124] J. Ahn, D. N. Hutchinson, C. Rangan and P. H. Bucksbaum, "Quantum phase retrieval of a Rydberg wave packet using a half-cycle pulse," *Phys. Rev. Lett.,* vol. 86, pp. 1179-1182, 2001.

[125] B. E. Cole, J. B. Williams, B. T. King, M. S. Sherwin and C. R. Stanley, "Coherent manipulation of semiconductor quantum bits with terahertz radiation," *Nature,* vol. 410, pp. 60-63, 2001.

[126] M. Schall, M. Walther and P. Uhd Jepsen, "Fundamental and second-order phonon processes in CdTe and ZnTe," *Phys. Rev. B,* vol. 64, p. 094301, 2001.

[127] H. Harde, R. A. Cheville and D. Grischkowsky, "Terahertz studies of collision-broadened rotational lines," *J. Phys. Chem. A,* vol. 101, pp. 3646-3660, 1997.

[128] E. Pickwell and V. P. Wallace, "Biomedical applications of terahertz technology," *J. Phys. D: Appl. Phys.,* vol. 39, pp. R301-R310, 2006.

[129] S. G. Carter, V. Birkedal, C. S. Wang, L. A. Coldren, A. V. Maslov, D. S. Citrin and M. S. Sherwin, "Quantum coherence in an optical modulator," *Science,* vol. 310, pp. 651-653, 2005.

[130] V. N. Shastin, R. K. Zhukavin, A. V. Muravjov, E. E. Orlova and S. G. Pavlov, "THz oscillators based on intraband transitions in bulk semiconductors," in *Proc. SPIE in Terahertz Spectroscopy and Applications II, 40*, 1999, pp. 40-51.

[131] V. A. Kukushkin, "Generation of frequency-tunable far-infrared and terahertz radiation by optical nutations at intraband transitions in asymmetric semiconductor nanoheterostructures," *Semiconductors,* vol. 46, pp. 1487-1492, 2012.

[132] M. Fox, *Optical properties of solids* 2nd Edition ed.: OUP Oxford, 2010.

[133] A. H. Castro Neto, "Graphene: phonons behaving badly," *Nat. Mater,* vol. 6, pp. 176-177, 2007.

[134] G. Jo, M. Choe, S. Lee, W. Park, Y. H. Kahng and T. Lee, "The application of graphene as electrodes in electrical and optical devices," *Nanotechnology,* vol. 23, p. 112001, 2012.

[135] S. Huh, J. Park, K. S. Kim, B. H. Hong and S. B. Kim, "Selective n-type doping of graphene by photo-patterned gold nanoparticles," *ACS Nano,* vol. 5, pp. 3639-3644, 2011.

[136] G. Giovannetti, P. A. Khomyakov, G. Brocks, V. M. Karpan, J. van den Brink and P. J. Kelly, "Doping graphene with metal contacts," *Phys. Rev. Lett.,* vol. 101, p. 026803, 2008.

[137] Z. Yu, Q. Zhang, L. Li, Q. Chen, X. Niu, J. Liu and Q. Pei, "Highly flexible silver nanowire electrodes for shape-memory polymer light-emitting diodes," *Adv. Mater.,* vol. 23, pp. 664-668, 2011.

[138] L. Cai-Hong and Y. Xun, "Silver nanowire-based transparent, flexible, and conductive thin film," *Nanoscale Res. Lett.,* vol. 6, p. 75, 2011.

[139] J. Kim, I. Maeng, J. Jung, H. Song, J.-H. Son, K. Kim, J. Lee, C.-H. Kim, G. Chae, M. Jun, Y. Hwang, S. Jeong Lee, J.-M. Myoung, and H. Choi, "Terahertz time-domain measurement of non-Drude conductivity in silver nanowire thin films for transparent electrode applications," *Appl. Phys. Lett.,* vol. 102, pp. 0111091- 0111094, 2013.

[140] X. Liu, F. Wang, R. Aizen, O. Yehezkeli and I. Willner, "Graphene oxide/nucleic-acid-stabilized silver nanoclusters: functional hybrid materials for optical aptamer sensing and multiplexed analysis of pathogenic DNAs," *J. Am. Chem. Soc.,* vol. 135, pp. 11832-11839, 2013.

[141] I. Ocsoy, M. L. Paret, M. A. Ocsoy, S. Kunwar, T. Chen, M. You and W. Tan, "Nanotechnology in plant disease management: DNA-directed silver nanoparticles on graphene oxide as an antibacterial against xanthomonas perforans," *ACS Nano,* vol. 7, pp. 8972-8980, 2013.

[142] D. Lee, H. Lee, Y. Ahn, Y. Jeong, D.-Y. Lee and Y. Lee, "Highly stable and flexible silver nanowire-graphene hybrid transparent conducting electrodes for emerging optoelectronic devices," *Nanoscale,* vol. 5, pp. 7750-7755, 2013.

[143] T. Low and P. Avouris, "Graphene plasmonics for terahertz to mid-Infrared applications," *ACS Nano,* vol. 8, pp. 1086-1101, 2014.

[144] T.-I. Jeon and D. Grischkowsky, "Nature of conduction in doped silicon," *Phys. Rev. Lett.,* vol. 78, pp. 1106-1109, 1997.

[145] U. W. Kim, S. J. Oh, I. Maeng, C. Kang and J. H. Son, "Terahertz electrical characteristics of heavily doped n-GaAs thin films," *J. Korean Phys. Soc.,* vol. 50, pp. 789-792, 2007.

[146] M. B. Zivanov and L. D. Zivanov, "Determination of electron mobility in heavily doped n-type GaAs using kp-model," *Proc. in the 20th International Conference on Microelectronics (Cat. No.95TH8108),* pp. 95-100 vol.1100 vol.1, 1995.

[147] J. Lloyd-Hughes and T. I. Jeon, "A review of the terahertz conductivity of bulk and nano-materials," *J. Infrared Millim. Terahertz Waves,* vol. 33, pp. 871-925, 2012.

[148] K. Thirunavukkuarasu, "Carbon nanostructures under high pressure studied by infrared spectroscopy " PhD Thesis, Mathematisch-Naturwissenschaftlichen Fakultät, Universität Augsburg, 2009.

[149] M. Weber, "Terahertz transmission spectroscopy of the organic polymer: PEDOT:PSS," PhD thesis, Department of Physics, Freie Universität Berlin, Berlin, 2009.

[150] Z. Da-xiang, E. P. J. Parrott, D. J. Paul and J. A. Zeitler, "Determination of complex refractive index of thin metal films from terahertz time-domain spectroscopy," *J. Appl. Phys.,* vol. 104, pp. 053110 - 053110-9, 2008.

[151] X. Zou, J. Shang, J. Leaw, Z. Luo, L. Luo, C. La-o-vorakiat, L. Cheng, S. A. Cheong, H. Su, J.-X. Zhu, Y. Liu, K. P. Loh, A. H. Castro Neto, T. Yu, and E. E. M. Chia, "Terahertz conductivity of twisted bilayer graphene," *Phys. Rev. Lett.,* vol. 110, p. 067401, 2013.

[152] M. Sentef, M. Kollar and A. P. Kampf, "DC conductivity of graphene with disorder," *arXiv:1203.2216,* vol. Mesoscale and Nanoscale Physics, p. 7, 2012.

[153] J. T. Hong, K. M. Lee, B. H. Son, S. J. Park, D. J. Park, J. Y. Park, S. Lee and Y. H. Ahn, "Terahertz conductivity of reduced graphene oxide films," *Opt. Express,* vol. 21, pp. 7633-7640, 2013.

[154] N. V. Smith, "Classical generalization of the Drude formula for the optical conductivity," *Phys. Rev. B,* vol. 64, p. 155106, 2001.

[155] D. G. Cooke, A. N. MacDonald, A. Hryciw, J. Wang, Q. Li, A. Meldrum and F. A. Hegmann, "Transient terahertz conductivity in photoexcited silicon nanocrystal films," *Phys. Rev. B,* vol. 73, p. 193311, 2006.

[156] A. Thoman, A. Kern, H. Helm and M. Walther, "Nanostructured gold films as broadband terahertz antireflection coatings," *Phys. Rev. B,* vol. 77, p. 195405, 2008.

[157] F. Bommeli, L. Degiorgi, P. Wachter, W. S. Bacsa, W. A. de Heer and L. Forro, "The optical response of carbon nanotubes," *Synt. Met.,* vol. 86, pp. 2307-2308, 1997.

[158] M. J. O. Connell, *Carbon Nanotubes Properties and Applications*: CRC Press Taylor & Francis Group, 2006.

[159] T. Yamabe, K. Fukui and K. Tanaka, *The science and technology of carbon nanotubes*: Elsevier, 1999.

[160] F. J. García-Vidal, J. M. Pitarke and J. B. Pendry, "Effective medium theory of the optical properties of aligned carbon nanotubes," *Phys. Rev. Lett.,* vol. 78, pp. 4289-4292, 1997.

[161] A. Lakhtakia, G. Y. Slepyan, S. A. Maksimenko, A. V. Gusakov and O. M. Yevtushenko, "Effective medium theory of the microwave and the infrared properties of composites with carbon nanotube inclusions," *Carbon,* vol. 36, pp. 1833-1839, 1998.

[162] L. Ren, Q. Zhang, C. L. Pint, A. K. Wójcik, M. Bunney, Jr., T. Arikawa, I. Kawayama, M. Tonouchi, R. H. Hauge, A. A. Belyanin, and J. Kono, "Collective antenna effects in the terahertz and infrared response of highly aligned carbon nanotube arrays," *Phys. Rev. B,* vol. 87, p. 161401, 2013.

[163] S. Kumar, N. Kamaraju, A. Moravsky, R. O. Loutfy, M. Tondusson, E. Freysz and A. K. Sood, "Terahertz time domain spectroscopy to detect low-frequency vibrations of double-walled carbon nanotubes," *Eur. J. Inorg. Chem.,* vol. 2010, pp. 4363-4366, 2010.

[164] T.-I. Jeon, J.-H. Son, K. H. An, Y. H. Lee and Y. S. Lee, "Terahertz absorption and dispersion of fluorine-doped single-walled carbon nanotube," *J. Appl. Phys.,* vol. 98, p. 034316, 2005.

[165] T. I. Jeon, K. J. Kim, C. Kang, S. J. Oh, J. H. Son, K. H. An, D. J. Bae and Y. H. Lee, "Terahertz conductivity of anisotropic single walled carbon nanotube films," *Appl. Phys. Lett.,* vol. 80, pp. 3403-3405, 2002.

[166] S. Kumar, N. Kamaraju, B. Karthikeyan, M. Tondusson, E. Freysz and A. K. Sood, "Terahertz spectroscopy of single-walled carbon nanotubes in a polymer Film: observation of low-frequency phonons," *J. Phys. Chem. C,* vol. 114, pp. 12446-12450, 2010.

[167] T. J. Antosiewicz, P. Wrobel and T. Szoplik, "Performance of scanning near-field optical microscope probes with single groove and various metal coatings," *Plasmonics,* vol. 6, pp. 11-18, 2011.

[168] P. B. Johnson and R. W. Christy, "Optical constants of the noble metals," *Phys. Rev. B,* vol. 6, pp. 4370-4379, 1972.

[169] M. A. Ordal, L. L. Long, R. J. Bell, S. E. Bell, R. R. Bell, R. W. Alexander and C. A. Ward, "Optical properties of the metals Al, Co, Cu, Au, Fe, Pb, Ni, Pd, Pt, Ag, Ti, and W in the infrared and far infrared," *Appl. Opt.,* vol. 22, pp. 1099-1119, 1983.

[170] S. Demoustier, E. Minoux, M. Le Baillif, M. Charles and A. Ziaei, "Review of two microwave applications of carbon nanotubes: nano-antennas and nano-switches," *Comptes Rendus Physique,* vol. 9, pp. 53-66, 2008.

[171] Y. Zhou, X. Xu, F. Hu, X. Zheng, W. Li, P. Zhao, J. Bai and Z. Ren, "Graphene as broadband terahertz antireflection coating," *Appl. Phys. Lett.,* vol. 104, pp. 051106-051106-5, 2014.

[172] M. Liang, Z. Wu, L. Chen, L. Song, P. Ajayan and H. Xin, "Terahertz characterization of single-walled carbon nanotube and graphene on-substrate thin films," *IEEE Trans. Microw. Theory Tech.,* vol. 59, pp. 2719-2725, 2011.

[173] M. V. Shuba, A. G. Paddubskaya, A. O. Plyushch, P. P. Kuzhir, G. Y. Slepyan, S. A. Maksimenko, V. K. Ksenevich, P. Buka, D. Seliuta, I. Kasalynas, J. Macutkevic, G. Valusis, C. Thomsen, and A. Lakhtakia, "Experimental evidence of localized plasmon resonance in composite materials containing single-wall carbon nanotubes," *Phys. Rev. B,* vol. 85, p. 165435, 2012.

[174] M. V. Shuba, A. G. Paddubskaya, P. P. Kuzhir, G. Y. Slepyan, D. Seliuta, I. Kašalynas, G. Valušis and A. Lakhtakia, "Effects of inclusion dimensions and p-type doping in the terahertz spectra of composite materials containing bundles of single-wall carbon nanotubes," *J Nanophotonics,* vol. 6, pp. 061707-061707, 2012.

[175] N. Akima, Y. Iwasa, S. Brown, A. M. Barbour, J. Cao, J. L. Musfeldt, H. Matsui, N. Toyota, M. Shiraishi, H. Shimoda, and O. Zhou, "Strong anisotropy in the far-infrared absorption spectra of stretch-aligned single-walled carbon nanotubes," *Adv. Mater.,* vol. 18, pp. 1166-1169, 2006.

[176] M. S. Dresselhaus, G. Dresselhaus, A. Jorio, A. G. Souza Filho and R. Saito, "Raman spectroscopy on isolated single wall carbon nanotubes," *Carbon,* vol. 40, pp. 2043-2061, 2002.

[177] G. B. Jung, Y. Myung, Y. J. Cho, Y. J. Sohn, D. M. Jang, H. S. Kim, C. W. Lee, J. Park, I. Maeng, J. H. Son, and C. Kang, "Terahertz spectroscopy of nanocrystal-carbon nanotube and graphene oxide hybrid nanostructures," *J. Phys. Chem. C,* vol. 114, pp. 11258-11265, 2010.

[178] Á. Pekker and K. Kamarás, "Wide-range optical studies on various single-walled carbon nanotubes: Origin of the low-energy gap," *Phys. Rev. B,* vol. 84, p. 075475, 2011.

[179] P. Bowlan, E. Martinez-Moreno, K. Reimann, T. Elsaesser and M. Woerner, "Ultrafast terahertz response of multilayer graphene in the nonperturbative regime," *Phys. Rev. B,* vol. 89, p. 041408, 2014.

[180] Y. Sano, I. Kawayama, M. Tabata, K. A. Salek, H. Murakami, M. Wang, R. Vajtai, P. M. Ajayan, J. Kono and M. Tonouchi, "Imaging molecular adsorption and desorption dynamics on graphene using terahertz emission spectroscopy," *Sci. Rep.,* vol. 4, 2014.

[181] S.-R. Berardi, Y. Rusen, M. K. Michelle, F. Tian, T. Kristof, H. Wan Sik, J. Debdeep, L. Lei and X. Huili Grace, "Broadband graphene terahertz modulators enabled by intraband transitions," *Nat. Commun.,* vol. 3, pp. 780-780, 2012.

[182] J. L. Tomaino, A. D. Jameson, J. W. Kevek, M. J. Paul, A. M. van der Zande, R. A. Barton, P. L. McEuen, E. D. Minot and Y.-S. Lee, "Terahertz imaging and spectroscopy of large-area single-layer graphene," *Opt. Express,* vol. 19, pp. 141-146, 2011.

[183] B. Yang, H. Su. and R. S. Donnan., "Vector network analysis of dielectric and magnetic materials in millimeter wave band," *J. Phys.: Conf. Ser,* vol. 286, p. 012019, 2011.

[184] P. U. Jepsen, D. G. Cooke and M. Koch, "Terahertz spectroscopy and imaging – Modern techniques and applications," *Laser Photon. Rev.,* vol. 5, pp. 124-166, 2011.

[185] C. K. O. L.F. Chen, C.P. Neo, V. V. Varadan and V. K. Varadan, *Microwave electronics: Measurement and Material Characterization*. England John Wiley & sons Ltd, England, 2005.

[186] F. M. Smits, "Measurement of sheet resistivities with the four-point probe," *Bell System Technical Journal,* vol. 34, pp. 711-718, 1958.

[187] J. Martin, N. Akerman, G. Ulbricht, T. Lohmann, J. H. Smet, K. von Klitzing and A. Yacoby, "Observation of electron-hole puddles in graphene using a scanning single-electron transistor," *Nat. Phys.,* vol. 4, pp. 144-148, 2008.

[188] J. D. Buron, D. H. Petersen, P. Bøggild, D. G. Cooke, M. Hilke, J. Sun, E. Whiteway, P. F. Nielsen, O. Hansen, A. Yurgens, and P. U. Jepsen, "Graphene conductance uniformity mapping," *Nano Lett.,* vol. 12, pp. 5074-5081, 2012.

[189] J. H. Strait, P. A. George, M. Levendorf, M. Blood-Forsythe, F. Rana and J. Park, "Measurements of the carrier dynamics and terahertz response of oriented germanium nanowires using optical-pump terahertz-probe spectroscopy," *Nano Lett.,* vol. 9, pp. 2967-2972, 2009.

[190] C.-S. Yang, C.-M. Chang, P.-H. Chen, P. Yu and C.-L. Pan, "Broadband terahertz conductivity and optical transmission of indium-tin-oxide (ITO) nanomaterials," *Opt. Express,* vol. 21, pp. 16670-16682, 2013.

[191] D. G. Schlom and L. N. Pfeiffer, "Oxide electronics: upward mobility rocks!," *Nat. Mater.,* vol. 9, pp. 881-883, 2010.

[192] J. M. Marulanda and A. Srivastava, "Carrier density and effective mass calculations for carbon nanotubes," in *Conference on IEEE International Integrated Circuit Design and Technology (ICICDT '07)*, 2007.

[193] J. Xia, F. Chen, J. Li and N. Tao, "Measurement of the quantum capacitance of graphene," *Nat. Nano,* vol. 4, pp. 505-509, 2009.

[194] C. Berger, Z. Song, X. Li, X. Wu, N. Brown, C. Naud, D. Mayou, T. Li, J. Hass, A. N. Marchenkov, E. H. Conrad, P. N. First, and W. A. de Heer, "Electronic confinement and coherence in patterned epitaxial graphene," *Science,* vol. 312, pp. 1191-1196, 2006.

[195] L. Liao, J. Bai, R. Cheng, Y.-C. Lin, S. Jiang, Y. Qu, Y. Huang and X. Duan, "Sub-100 nm channel length graphene transistors," *Nano Lett.,* vol. 10, pp. 3952-3956, 2010.

[196] Y. Wu, Y.-m. Lin, A. A. Bol, K. A. Jenkins, F. Xia, D. B. Farmer, Y. Zhu and P. Avouris, "High-frequency, scaled graphene transistors on diamond-like carbon," *Nature,* vol. 472, pp. 74-78, 2011.

[197] F. Xia, T. Mueller, Y.-m. Lin, A. Valdes-Garcia and P. Avouris, "Ultrafast graphene photodetector," *Nat. Nano,* vol. 4, pp. 839-843, 2009.

[198] M. Steiner, M. Engel, Y.-M. Lin, Y. Wu, K. Jenkins, D. B. Farmer, J. J. Humes, N. L. Yoder, J.-W. T. Seo, A. A. Green, M. C. Hersam, R. Krupke, and P. Avouris, "High-frequency performance of scaled carbon nanotube array field-effect transistors," *Appl. Phys. Lett.,* vol. 101, p. 053123, 2012.

[199] J. Zheng, L. Wang, R. Quhe, Q. Liu, H. Li, D. Yu, W.-N. Mei, J. Shi, Z. Gao and J. Lu, "Sub-10 nm gate length graphene transistors: operating at terahertz frequencies with current saturation," *Sci. Rep.,* vol. 3, 2013.

[200] L. Nougaret, H. Happy, G. Dambrine, V. Derycke, J.-P. Bourgoin, A. A. Green and M. C. Hersam, "80 GHz field-effect transistors produced using high purity semiconducting single-walled carbon nanotubes," *Appl. Phys. Lett.,* vol. 94, p. 243505, 2009.

[201] W. Withayachumnankul, B. Ferguson, T. Rainsford, S. P. Mickan and D. Abbott, "Material parameter extraction for terahertz time-domain spectroscopy using fixed-point iteration," in *Proc. SPIE in Photonic Materials, Devices, and Applications,5840,* 2005.

[202] T.-I. Jeon, "New applications of tHz time-domain spectroscopy," Degree of Doctor of Philosophy, Electrical Engineering, Oklahoma State University, Stillwater, Oklahoma, 1997.

[203] T.-R. Tsai, S.-J. Chen, C.-F. Chang, S.-H. Hsu, T.-Y. Lin and C.-C. Chi, "Terahertz response of GaN thin films," *Opt. Express,* vol. 14, pp. 4898-4907, 2006.

[204] A. Dergan, "Electronic and transport properties of carbon nanotubes," Faculty of Mathematics and Physics, University of LjubljanaOctober 2010.

[205] S. M.-M. Dubois, Z. Zanolli, X. Declerck and J.-C. Charlier, "Electronic properties and quantum transport in graphene-based nanostructures," *Eur. Phys. J. B,* vol. 72, pp. 1-24, 2009.

[206] E. Joselevich, "Electronic structure and chemical reactivity of carbon nanotubes: A chemist's view," *ChemPhysChem,* vol. 5, pp. 619-624, 2004.

[207] R. A. Jishi, D. Inomata, K. Nakao, M. S. Dresselhaus and G. Dresselhaus, "Electronic and lattice properties of carbon nanotubes," *J. Phys. Soc. Jpn.,* vol. 63, pp. 2252-2260, 1994.

[208] I.-T. Lin, "Optical Properties of Graphene from the THz to the Visible Spectral Region," Master thesis, Electrical Engineering, UCLA (University of California, Los Angeles), 2012.

[209] S. Das Sarma, S. Adam, E. H. Hwang and E. Rossi, "Electronic transport in two-dimensional graphene," *Rev. Mod. Phys.,* vol. 83, pp. 407-470, 2011.

[210] Y. Nakayama and S. Akita, *Nanoengineering of carbon nanotubes and the status of its applications* vol. 706. Warrendale: Materials Research Society, 2002.

[211] H. Kataura, Y. Kumazawa, Y. Maniwa, I. Umezu, S. Suzuki, Y. Ohtsuka and Y. Achiba, "Optical properties of single-wall carbon nanotubes," *Synt. Met.,* vol. 103, pp. 2555-2558, 1999.

[212] M. J. O'Connell, *Carbon Nanotubes: Properties and Applications*: CRC Press, 2006.

[213] A. C. Ferrari, J. C. Meyer, V. Scardaci, C. Casiraghi, M. Lazzeri, F. Mauri, S. Piscanec, D. Jiang, K. S. Novoselov, S. Roth, and A. K. Geim, "Raman spectrum of graphene and graphene Layers," *Phys. Rev. Lett.,* vol. 97, p. 187401, 2006.

[214] I. Calizo, I. Bejenari, M. Rahman, G. Liu and A. A. Balandin, "Ultraviolet Raman microscopy of single and multilayer graphene," *J. Appl. Phys.,* vol. 106, p. 043509, 2009.

[215] L. M. Malard, M. A. Pimenta, G. Dresselhaus and M. S. Dresselhaus, "Raman spectroscopy in graphene," *Phys. Rep.,* vol. 473, pp. 51-87, 2009.

[216] X. Li, W. Cai, J. An, S. Kim, J. Nah, D. Yang, R. Piner, A. Velamakanni, I. Jung, E. Tutuc, S. K. Banerjee, L. Colombo, and R. S. Ruoff, "Large-area synthesis of high-quality and uniform graphene films on copper foils," *Science,* vol. 324, pp. 1312-1314, 2009.

[217] G. H. Han, F. Güneş, J. J. Bae, E. S. Kim, S. J. Chae, H.-J. Shin, J.-Y. Choi, D. Pribat and Y. H. Lee, "Influence of copper morphology in forming nucleation seeds for graphene growth," *Nano Lett.,* vol. 11, pp. 4144-4148, 2011.

[218] S. Bhaviripudi, X. Jia, M. S. Dresselhaus and J. Kong, "Role of kinetic factors in chemical vapor deposition synthesis of uniform large area graphene using copper catalyst," *Nano Lett.,* vol. 10, pp. 4128-4133, 2010.